DEVELOPMENT OF SUPERCONDUCTING TUNNEL JUNCTION ARRAYS FOR ASTRONOMICAL OBSERVATIONS

Cover: S-CAM3 system assembled in laboratory (see Chapter 5) together with a micrograph of a 10×12 STJ array (MUL192.D2, see Chapter 3.2.2.1).

The work described in this Thesis was performed in the Science Payload and Advanced Concepts Office of the European Space Agency's Technology and Research Centre in Noordwijk, The Netherlands.

D. D. E. Martin
Development of Superconducting Tunnel Junction Arrays for Astronomical Observations
Proefschrift Universiteit Twente, Enschede

ISBN 978-90-365-2558-9

DEVELOPMENT OF SUPERCONDUCTING TUNNEL JUNCTION ARRAYS FOR ASTRONOMICAL OBSERVATIONS

PROEFSCHRIFT

ter verkrijging van
de graad van doctor aan de Universiteit Twente,
op gezag van de rector magnificus,
prof. dr. W. H. M. Zijm,
volgens besluit van het College voor Promoties
in het openbaar te verdedigen
op woensdag 7 november 2007 om 15.00 uur

door

Didier Dieudonné Elisabeth Martin

geboren op 21 december 1965

te Tongeren, België

Dit proefschrift is goedgekeurd door:

Promotor:	prof. dr. H. Rogala *Universiteit Twente*
Co-Promotoren:	dr. A.A. Golubov *Universiteit Twente* dr. A. Peacock *European Space Agency*

TABLE OF CONTENTS

Chapter 1

INTRODUCTION

For as long as history goes, man has had the urge to explore, extending his frontiers and understanding of the world. We know from many relics and artefacts that early civilizations already performed methodical observations of the night sky. Of course in these early days, the observations were focussed on the motion of objects and its predictions. Besides being used for ceremonies, it also allowed people to determine the length of a year and when it was time to plant crops.

Astronomy was able to develop into a modern science with the invention of the telescope in 1608 by Hans Lippershey and Zacharias Janssen, in Holland. Galileo Galilei was the first to produce one of sufficient quality and use it to observe the sky. His *Siderius Nuncius* (Sidereal Messenger), published in 1610, was the first scientific treatise on observations of the Moon, stars and the moons of Jupiter, using a telescope.

Since then, many more inventions were made that refined the art of celestial observations. In order to record the images of the sky, photographic plates, invented in the early 1830's by Joseph "Nicéphore" Niépce and Jacques Mandé Daguerre, had to be improved to record the faint sky images. The first daguerrotype of the moon was made by American physiologist and chemist John William Draper in 1840, involving a full 20 minute exposure. The first star, other than our sun, was not recorded until the night of July 16-17, 1850, when William Cranch Bond, the director of Harvard College Observatory, and John Adams Whipple, a photographer associated with the Massachusetts General Hospital, took a daguerrotype of Vega. By 1870, technology had improved enough to allow Jansen & Lockyer to discover the element Helium on a photograph of a solar spectrum. With the advent of photography, it became possible to overcome the fixed exposure time of the human eye, and to faithfully record detected photons for later analysis. It also became possible to record photons at wavelengths for which the human eye is insensitive, particularly toward shorter wavelengths (near-UV; but also X-rays and ionizing particles). Photographic emulsions sensitive to longer wavelengths (near-IR) were only developed later in the 20th century. The glass plates used as substrates for the emulsions were resistant to bending and distortion during the observations, and have proven extremely stable over time (a full century and counting). The two Palomar Observatory Sky Surveys (POSS completed in 1958, and POSS-II during the 1990s [1]) and the complementary UK Schmidt surveys in the southern hemisphere were made using photographic plates and are still being used in their currently available digitized format. Nevertheless, photographic plates have very low quantum efficiencies, of order 1-2% only, have a non-linear response to light intensity and limited dynamic range of typically ~100. Finally, quantitative analysis of photographs requires them to be scanned and digitized, a cumbersome and non-trivial task.

The first half of the 20th century saw the advent of vacuum-tube technology. The photo-multiplier tube (PMT) relies on the photo-electric effect and successive signal amplification. A photon striking the photocathode, deposited on the inside of the entrance window of the device, can eject a photo-electron. The electric field in the device will accelerate this electron towards the first of a set of electrodes, called dynodes, where it can eject additional electrons. At each stage, the number of electrons is thus increased before finally striking the anode(s) where it generates a small, sharp current pulse. PMTs are typically operated with bias voltages of 1-2kV and provide an electronic gain of ~10^6. Their quantum efficiency is much higher than that of photographic plates and can be up to ~40%, depending on wavelength and

photocathode material. PMTs have a very linear behaviour and can be operated in photon-counting mode. Together with their large dynamic range, they allow accurate photometry to be performed. Their main disadvantage, however, is that PMTs are typically single-element devices and are next to impossible to package into 1-D or 2-D imaging arrays. In the 1960's, a series of high-voltage imaging devices were constructed, combining the PMT photocathode with an electron scanning system or anode arrays, which preserved the position information of the incoming photon. Examples are the Vidicon, Reticon and Multi-Anode Microchannel Array (MAMA) detectors [2].

Charge Coupled Devices (CCDs), were originally developed at Bell labs as a solid-state memory device [3]. Their sensitivity to light, through the photoelectric effect, and their ability to store charge in a regular array format made them suitable for imaging applications. The excellent electro-optical performance of CCDs makes them currently the most ubiquitous detectors used in astronomy. Photons absorbed in the silicon semiconductor release photo-electrons which are confined in each pixel by potential barriers. These barriers are achieved row-wise by impurity implantations while isolated electrodes create potential wells in the columns, so that photoelectrons gather in each pixel's potential well. By alternating the voltages across the column electrodes, the potential wells can be shifted sideways, effectively moving the charge packets. In order to readout such a device, the charges are moved column by column into a readout column register. This register has a similar pixel structure but is clocked-out orthogonally at a much higher speed. The charges from each pixel are thus transferred sequentially into a final storage capacitor which forms the readout node and is amplified by a low noise source follower. For a more detailed overview on how CCDs work, we refer to [4]. Astronomy-grade CCDs can have a quantum efficieny in excess of 90%, when used with an appropriate anti-reflection coating, have a uniform response and achieve extremely low noise ($<1e^-$) and dark current. Although their individual physical size does not match the beams of large telescopes, they can be combined into large focal plane assemblies. The Gaia project, currently under construction, combines 106 CCDs for a total of almost 10^9 pixels in a $0.3m^2$ area [5]. Their major drawbacks are the limited readout speed and, for space applications, the dramatic charge transfer efficiency degradation under charged particle irradiation. Nevertheless, this technology is further being matured and faster readout systems are beginning their entry onto major telescopes. A notable example is ULTRACAM that was commissioned on the William Herschel Telescope at La Palma in 2002 and the VLT in Chile in 2005. The instrument is based on three CCDs behind dichroic filters and can achieve a maximum readout rate of 500Hz [6]. It should be noted however that although the detectors consist of 1024×1024 pixels CCDs, the maximum frame rate is only available on a very limited window consisting of 6×6 pixels (binned) for a total Field-of-View of $7\times7arcsec^2$. Particular care has to be taken also for aligning this window, as it has to be at the edge of the sensitive CCD area, directly adjacent to the storage area.

More recently, Active Pixel Sensors (APS), based on Complementary Metal Oxide Semiconductor (CMOS) technology, have started their entry in this domain. These devices also rely on semiconductor materials to convert light into charge [7],[8]. Unlike CCDs however, they include amplifiers and multiplexers in each pixel, which avoids charges to be transferred across the complete array before being read out. This allows them to be more radiation tolerant for space applications. The standard CMOS processes used to manufacture these devices enables more complex functions to be included on chip, e.g. analogue to digital conversion or electronic shutters. The ability to access each pixel individually allows one to read out selected areas at much higher rates then what is possible with CCDs. Finally, hybrid circuits can be built where the photo-conversion takes place in an optimized detector material (low- or high bandgap for X-ray/UV or IR detection, for instance GaAs, CdZnTe, HgCdTe, etc.) which is bump-bonded to a CMOS readout circuit. Examples of successful IR sensors are the InSb and

HgCdTe arrays from Raytheon [9] and Rockwell [10]. Both of which have already been successfully used on ground telescopes (ESO, CFHT at Hawaii, etc.) and similar sensors are currently being deployed for space missions as well, e.g. the MIRI [11] and NIRSpec [12] instruments on James Webb Space Telescope.

In order to make the next technological step in the development of sensors, our approach was to switch from semiconductor technology to superconducting materials. The major difference stems from the minimum energy required to produce excitations. In semiconductors, the bandgap is of the order of 1eV, depending on the materials used, but for traditional superconductors, the energy gap is three orders of magnitude lower, of the order of a meV. Conversely, measurements can also rely on the much reduced thermal fluctuations at the required low operating temperatures (typically ~100 mK) which allow the detection of extremely small temperature changes. The increased sensitivity of these superconducting materials allows efficient and noise-free photon-counting with high timing accuracy as well as simultaneous energy determination of the absorbed photons to take place [13].

There are currently mainly two technologies which are being pursued to exploit the properties of superconductors for photon detection. These are based on transition edge sensors and tunnel junctions. Kinetic induction sensors [14] are also being developed but efficient coupling of optical or X-ray radiation into these devices is more complicated and not yet mature.

Transition edge sensors are being developed by many research groups and have shown excellent detection properties, especially in the X-ray regime (2.4eV resolution at 5.9keV [15]). These superconducting sensors are almost thermally isolated from the substrate on which they are grown and function as a thermometer. The film is biased, usually with a small voltage that provides local heating. A weak thermal link to the bath keeps them at a slightly elevated equilibrium temperature, right in the transition from the superconducting to the normal conducting state. When a photon is absorbed, the film heats up and increases its electrical resistance. The signal is then measured from the drop in current passing through the device. The integration of this current pulse provides a measurement that is directly proportional to the absorbed photon's energy. The devices typically have low electrical resistance (<1Ω) and require a Superconducting Quantum Interference Device (SQUID) readout. Although this makes the readout apparently more complex than using traditional semiconductor based amplifiers, recent developments at NIST have made it possible to read out large arrays using SQUID multiplexers [16]. The challenge of this technology is now to increase the readout speed, currently limited by the delay in the flux-locked loop.

A small array of 6×6 pixels (of with only 2×3 were instrumented) of tungsten sensors deposited on a Silicon substrate has been used to perform measurements in the visible-near infrared on the Crab Pulsar [17],[18]. The theoretical energy resolution of Transition Edge Sensors is given approximately by [19]:

$$\Delta E_{FWHM} = 2.355\sqrt{4kT\sqrt{n/2}E_{\max}} \qquad 1\text{-}1$$

Where E_{max} is the maximum energy to be measured and n a thermal coupling parameter. In the case of the W-TES on Si used for optical photon detection, E_{max}=10eV; n=5 yields a theoretical energy resolution of 0.05eV, whereas in practice, a resolution of ~0.15eV is achieved [19].

Superconducting Tunnel Junctions (STJs) have been developed in our laboratory since the early 1990's. At first, the Niobium based devices were tuned to detect X-ray photons, but it was soon realized that optical photon detection should be possible [20] and a few years later indeed shown to be a fact [21]. The principle of operation of STJs shall be described in more detail in the following chapter, but basically relies on the generation of excitations, or

quasiparticles. The transfer of electric charge through electron tunnelling across a thin insulator then creates an excess current pulse which is proportional to the incoming photon's energy.

The theoretical ultimate energy resolution, or Fano limit ($\Delta E_{\mathrm{FWHM,\,Fano}}$) of an STJ is given by the statistical variations in the number of generated excitations in the following way:

$$\Delta E_{FWHM,Fano} = 2.355\sqrt{\varepsilon F E} \qquad 1\text{-}2$$

where $\varepsilon \approx 1.7\Delta$ is the mean energy required to generate one quasiparticle [22], Δ being the material's energy gap, F the Fano factor and E the detected photon's energy. Practical devices suffer from additional statistical variations. As we shall see later, the most limiting one is usually related to variations in the number of tunnel processes each quasiparticle undergoes. The resulting tunnel limited energy resolution is:

$$\Delta E_{FWHM,tunnel} = 2.355\sqrt{\varepsilon (F+G) E} \qquad 1\text{-}3$$

where the additional tunnel factor $G \leq 1$. Table 1-1 summarizes the critical temperature, energy gap and limiting energy resolutions achievable for various superconductors at two representative photon energies (2.48eV≡500nm in the visible and 5.9keV X-ray emission from ^{55}Fe). This is also captured in Figure 1-1, but now presented as energy resolving power ($E/\Delta E$), in the tunnel limit with $G=1$, as function of photon energy and for different materials. The dots represent actual resolution measurements taken on Ta/Al and Al STJs of various sizes. Note that the resolving power increases with energy.

Table 1-1: Critical parameters for different superconducting materials and the associated theoretically achievable resolutions for two representative photon energies.

	T_c	Δ	Fano limit		Tunnel limit	
			ΔE @ 2.48eV	ΔE @ 5.9keV	ΔE @ 2.48eV	ΔE @ 5.9keV
	[K]	[meV]	[meV]	[eV]	[meV]	[eV]
Nb	9.2	1.55	85	4.2	208	10.2
Ta	4.5	0.70	57	2.8	140	6.8
Re	1.7	~0.26	35	1.7	85	4.2
Al	1.2	0.18	29	1.4	71	3.5
Mo	0.92	0.14	26	1.2	63	3.1
Hf	0.13	0.019	9	0.46	23	1.1

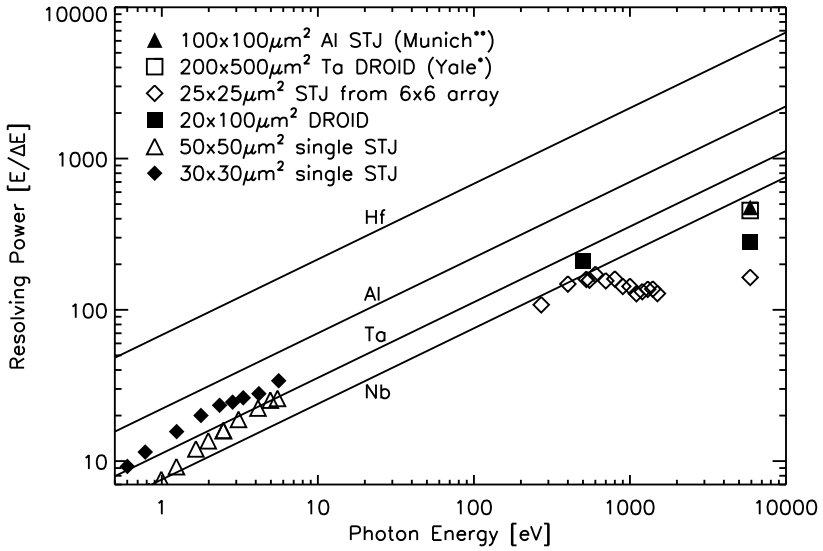

Figure 1-1: Theoretical energy resolving power ($E/\Delta E$) for various materials (solid lines) as well as measured resolutions of Ta/Al STJs of various sizes, also included are the results from the Munich** group on Al STJs [23] and Yale* results on Ta DROIDs [24].

1.1 Scope of thesis

Cryogenic detectors are being developed in order to exploit their high intrinsic energy resolving power, from the optical through X-ray wavelengths. Particularly in X-ray spectroscopy for astrophysical or material analysis purposes, these detectors could replace the relatively inefficient wavelength dispersive spectrometers or low-resolution, energy dispersive, semiconductor-based detectors. The X-ray observatories Chandra and XMM-Newton carry such grating-based spectrometers with CCD or MCP detectors, providing an energy resolving power of ~500-1000 at E=1 keV. Future potential X-ray missions such as Constellation-X [25] and XEUS [26],[27] intend to use cryogenic detectors in arrays of about 1000 pixels. These arrays should provide simultaneously imaging and spectroscopy with an energy resolution of ~2 eV in the E=0.5-7 keV band, with a detection efficiency in excess of 75% and a count rate capability of ~1000 cts/s. In summary, a cryogenic sensor array could well be the ideal detector for astronomy as it can deliver simultaneously timing, position and energy information for each individual photon.

Before being able to build a complex instrument for a future space mission, we embarked on the design, fabrication and exploitation of a ground-based instrument, which would enable us to better understand the problems and limitations related to cryogenic sensors. The essence of this thesis was to design, fabricate, calibrate and operate an optical camera based on Superconducing Tunnel Junctions. In order to fulfil this goal, it was necessary to further develop on the earlier work done on a superconducting tunnel junction camera for optical astronomy, called S-CAM. In particular, we set out to understand the resolution limitations of the superconducting devices, improve them and integrate a sizeable array into a practical instrument for use at a ground based optical telescope. In order to better understand the physical limitations on the energy resolution of these detectors, we had to fabricate sensors that did not suffer from imperfections. Only if the performance was nearly ideal could we refine our understanding of their physical behaviour. The improvements on the devices followed from the increased lifetime of the quasiparticles. At first we discovered that the tunnel limit mentioned previously could be overcome as quasiparticle lifetimes increase [28]. Further

improvements, yielding the best resolutions yet achieved with cryogenic sensors at optical wavelengths, revealed that the resolution is also limited by the finite thickness of the absorbing films and a theory was developed which could explain the functional dependence of the resolution as function of photon energy. The same theory was extended to explain the mediocre resolutions obtained with Aluminium devices. Indeed, from Table 1-1, we could infer that the energy resolution should be roughly twice as good as for Tantalum STJs. In practice however, we found rather similar results, that is, no improvement on resolution even though the energy gap of Al is much lower than that of Ta. Our new thin film theory can explain this behaviour as we will show.

As our long-term aim is to develop large arrays of superconducting tunnel junctions, we spent some time in investigating possible different readout methods. In particular, a matrix readout scheme was successfully fabricated and tested with optical and X-ray illumination. Secondly, an application specific integrated circuit (ASIC) was developed, which should reduce the required size and power consumption dramatically. Finally, we also investigated the role SQUIDs could play as the first amplifying stage. SQUIDs can be used as current sensors and are very efficient when coupled to low-impedance sensors, like TESs. STJs on the other hand have higher dynamic impedances and are more difficult to couple to the input coils of SQUIDs. Nevertheless, measurements were performed with a commercial SQUID and from that, parameters for an optimized SQUID design were deduced.

The first generation of S-CAM suffered from a number of problems that only became apparent as the system began to be used. The detector, a 6×6 array was found to be too small to perform accurate photometry; a larger detector had to be fabricated. We will show what the design parameters for this array are and present the results obtained from the various production runs. In the middle of this development our prime supplier of devices, Oxford Instruments Thin Film Group, stopped their activities in this domain and we had to transfer the knowledge to a new supplier. This turned out to be a blessing, because the alternative production route provided us with even better devices.

From an astronomer's point of view, the cut-off wavelength of the instrument has to be as large as possible. Intrinsically, the detectors can detect photons over a very large energy range. For ground based astronomy, the earth's atmosphere cuts off wavelengths shorter than about 300nm, effectively setting the lower limit. Above ~900nm, water and carbon-dioxide present a number of absorption bands but transmission windows up to ~30μm are present. In practice however, the 300K black-body radiation of the optical elements and sky extends down to ~2.5μm and would swamp the detector with photons if adequate filters were not used. In this work, we optimized these filters, increased the overall throughput, and extended the long wavelength cut-off while simultaneously increasing the IR rejection.

Finally, the cryogenic system had to be considerably improved, providing a stable environment for the detector. We shall show how this was achieved and the consequences this has for the calibration of the detector during observations.

In summary, our goals were to:

1) design, fabricate, calibrate and operate a practical optical camera for ground-based astronomy based on Superconducing Tunnel Junctions,
2) Increase the detector performance to obtain the best possible energy resolution achievable with Tantalum/Aluminium superconductors,
3) Improve the understanding of the detector's physics,
4) Increase the detector size to achieve true imaging, not to be limited by atmospheric conditions and obtain an as large a field of view as possible,
5) Optimize the IR rejection filters and extend the wavelength range,
6) Simplify and optimize the cooling system, providing a stable operating temperature for the detector throughout observing nights,
7) Improve the stability and speed of the electronics and software

1.2 Outline of the work

The work is split in four main chapters. We shall first start by briefly reviewing the superconducting state and describe the superconducting tunnel junction and how it works as a photon detector. In this part we shall present the best results obtained so far with Ta/Al devices for optical photon detection. We proceed by developing a new theory of energy down-conversion for thin films, where the statistical variations of phonon losses across boundaries can be significant and can explain the observed variations of resolution as function of wavelength.

We then proceed by presenting the fabrication processes used for the production of the S-CAM arrays. In particular, we shall show the mask designs for the different alternatives that were used in the camera. Each relevant detector chip will be presented with its key performance parameters as well as the selection criteria that were used for the 'flight' detectors.

In Chapter 4, we shall review the various elements required in the proximity electronics. In particular we shall analyse the noise levels for the various filtering techniques, analogue and digital, used in the laboratory and on S-CAM. We will present three alternative readout schemes which could be useful for the readout of future larger arrays. Starting by the matrix readout where only one amplifier per column and one per row is needed, drastically reducing the total number of circuits and connections required. Secondly we present a SQUID readout, which has the double benefit of easily providing stable biasing and can possibly be multiplexed, relaxing again the electronics volume required for large arrays. Finally, we present an ASIC developed specifically to readout 64 STJs. The main technical challenge was to provide on-chip compensation of the offset voltages of the various preamplifiers.

The S-CAM3 system is described in detail in Chapter 5. We start by the reflective and refractive optics, the filters used for calibrations and neutral density filters for flux attenuation. We present the optimized IR filters used inside the cryostat and the influence they have had on the final performance of the system. The cryogenic assembly is detailed, showing the capability to provide an extremely stable environment to the detector during the observing night, and throughout the observing campaign by keeping the detector below its critical temperature at all times. Finally the electronics system is presented and we show how it can sustain a constant rate in excess of ½ million events per second. The absolute timing calibration of the system is addressed here as well. We conclude this chapter by an analysis of the pile-up events and detector stability over time. We show how pile-up can be traded on-line against energy resolution by tuning the digital filtering algorithms, depending on the observing goal.

The one before last chapter is dedicated to some scientific results obtained during the various observation campaigns. We shall present measurements on cataclysmic variables and optical pulses from the Crab Pulsar, which require the accurate timing resolution of the instrument. This will be followed by a proof of principle in directly determining the red-shifts of distant quasars and direct stellar surface temperature measurements, based on the moderate spectroscopic capabilities of S-CAM. Finally, we present a topic which is currently of tremendous interest within the scientific community, namely the detection of extra-solar planets. The photometric capabilities of the instrument are being used to the full extend in order to detect planetary transits.

Finally, we present some concluding remarks and review ideas for further developments, some of which having started already.

Chapter 2

SUPERCONDUCTING TUNNEL JUNCTIONS AS PHOTON DETECTORS

Superconductivity was first discovered by Kammerlingh Onnes [29]. In his experiments to characterize metals at low temperatures, he noticed that the electrical resistance of mercury dropped below any measurable value below a temperature of 4.2K. Perfect conductivity was thus the first discovered property of superconductors. Perfect diamagnetism, the ability of a material to expel an external magnetic field from its interior, was discovered in 1933 by W. Meissner and R. Ochsenfeld [30]. Although a perfect conductor will expel a magnetic field as well, it would tend to trap the flux in during the transition from normal to perfect conductor. Indeed, from the Maxwell equations and the definition of electrical current we have:

$$\nabla \times \vec{H} = \vec{J} + \frac{\partial \vec{D}}{\partial t} \qquad \nabla \times \vec{E} = -\frac{\partial \vec{B}}{\partial t} \qquad \frac{\partial \vec{J}}{\partial t} = ne\frac{\partial \vec{v}}{\partial t} \tag{2-1}$$

Where n is the electron concentration and v, their velocity. By taking the curl of the time derivative of the first and using the other two equations as well as the equation of motion, we obtain:

$$\nabla^2 \frac{\partial \vec{H}}{\partial t} = \lambda^{-2} \frac{\partial \vec{H}}{\partial t} \qquad \lambda^2 = \frac{m}{ne^2 \mu_0} \tag{2-2}$$

From which we can see that the magnetic field remains unchanged with time below the characteristic penetration depth: λ. For a superconductor, however, a field in an originally normal sample will be expelled as the sample is cooled through its transition temperature T_c. A phenomenological description of superconductivity was first proposed by F. and H. London [31], by suggesting two equations which govern the microscopic electric and magnetic fields:

$$\vec{e} = \frac{m}{n_s e^2} \frac{\partial \vec{j}_s}{\partial t} \tag{2-3}$$

$$\vec{b} = -\frac{m}{\mu_0 n_s e^2} \nabla \times \vec{j}_s \tag{2-4}$$

Where the small vectors represent microscopic values of the fields and currents and n_s is the concentration of superconducting electrons, expected to range from 0 at $T=T_c$ up to the density of conduction electrons at T=0. Performing the same derivation as for equation 2-2, we find now that:

$$\vec{b} = \lambda^2 \nabla^2 \vec{b} \tag{2-5}$$

Which implies that a magnetic field will be exponentionally shielded from the interior of a superconductor with a penetration depth λ, independently of time, explaining the Meissner effect.

2.1 The BCS ground state

In 1957, J. Bardeen, L. Cooper and J. Shrieffer presented their microscopic theory of superconductivity commonly known as BCS theory [32], which revolutionized the understanding of the phenomenon. The basic idea relies on the observation that even a small attractive potential can bind electrons in pairs, called Cooper pairs. The attraction created by an otherwise repulsive Coulomb interaction between electrons can be understood as follows. In a crystal, if an electron moves in a certain direction, it polarizes the medium as it leaves behind positively charged ions which it will attract. In turn, these ions can attract another electron. This attraction, mediated by the ions can, for certain materials and below a certain temperature, overcome the screened repulsive Coulomb interaction between electrons.

The role of the electron-lattice interaction was experimentally shown by the isotope effect, where the critical temperature (and field) was found to be inversely proportional to the square root of the isotope mass of the same element. Since the attractive potential is mediated by interactions with the lattice, and in particular lattice vibrations or phonons, one can understand that superconductivity will be linked to characteristic phonon frequencies. As we shall see, the electron-phonon interaction is of primordial importance in determining the ultimate performance of Superconducting Tunnel Junctions.

In order to describe the quantum-mechanical nature of the superconducting state, the BCS theory relies on the concept of second quantization, which we will introduce shortly. The mathematics to describe a system consisting of many fermions uses the notion of Slater determinants. A Slater determinant is a wavefunction which simultaneously satisfies the Pauli exclusion principle and the anti-symmetry property of fermions. If $\phi(x_i)$ is the wavefunction of an individual electron, the combined wavefunction of N electrons can be approximated by a set of N×N Slater determinants, each of the form:

$$\psi(x_1, x_2, \cdots, x_N) = \frac{1}{\sqrt{N!}} \begin{vmatrix} \phi_1(x_1) & \phi_1(x_2) & \cdots & \phi_1(x_N) \\ \phi_2(x_1) & \phi_2(x_2) & \cdots & \phi_2(x_N) \\ \vdots & \vdots & & \vdots \\ \phi_N(x_1) & \phi_N(x_2) & \cdots & \phi_N(x_N) \end{vmatrix} \qquad 2\text{-}6$$

One can easily see that exchanging two particles only changes the wavefunction's sign, satisfying the condition of definite exchange energy, a property of indistinguishable fermions [33]. The Pauli exclusion principle which states that two particles can not occupy the same state is also readily verified ($\psi=0$ if $\phi_i=\phi_j, \forall i \neq j$).

This tedious description can be further simplified by introducing the concept of second quantization. This method was originally developed for quantizing classical fields, and is an extension of quantum mechanics dealing with quantum states of a system of a fixed number of particles. In quantum field theory, the classical field is replaced by a quantum operator acting on a quantum state to increase or decrease the number of particles by one. This allows us to work with a variable number of particles and is, as we will describe, of direct relevance to the creation and annihilation of excited quasiparticle states. Let $c^{+}_{\vec{k}\uparrow}$ and $c_{\vec{k}\uparrow}$ respectively represent the creation and annihilation operators of an electron of momentum $\vec{k}$ and spin up. Then,

starting from the Fermi sea $|F\rangle$, with all states filled up to k_F, the condensation of a single Cooper pair can be represented by:

$$|\psi_0\rangle = \sum_{|\vec{k}|>|\vec{k}_F|} g_k c^+_{\vec{k}\uparrow} c^+_{-\vec{k}\downarrow} |F\rangle \qquad 2\text{-}7$$

The most general N-electron wavefunction in terms of momentum eigenfunctions and Cooper pairs can be constructed from the vacuum state as follows:

$$|\psi_N\rangle = \sum g(\vec{k}_i, \cdots, \vec{k}_l) c^+_{\vec{k}_i\uparrow} c^+_{-\vec{k}_i\downarrow} \cdots c^+_{\vec{k}_l\uparrow} c^+_{-\vec{k}_l\downarrow} |0\rangle \qquad 2\text{-}8$$

This representation is still too cumbersome, given the many terms in the sum. Instead, BCS used the mean-field approach where the occupancy of each state is only dependent on the average occupancy of the other states. The BCS ground state is then given by:

$$|\psi_G\rangle = \prod_{\vec{k}_1 \cdots \vec{k}_M} (u_{\vec{k}} + v_{\vec{k}} c^+_{\vec{k}\uparrow} c^+_{-\vec{k}\downarrow}) |0\rangle \qquad 2\text{-}9$$

In which $|u_{\vec{k}}|^2 + |v_{\vec{k}}|^2 = 1$, $|v_{\vec{k}}|^2$ is the probability of the pair $(\vec{k}\uparrow, -\vec{k}\downarrow)$ being occupied and $|u_{\vec{k}}|^2$, the probability of it being empty.

Assuming now that we are only dealing with a free electron gas with a weak interaction potential between pairs of electrons, BCS used the pairing Hamiltonian:

$$\mathcal{H} = \sum_{\vec{k}\sigma} \varepsilon_{\vec{k}} n_{\vec{k}\sigma} + \sum_{\vec{k}\vec{l}} V_{\vec{k}\vec{l}} c^+_{\vec{k}\uparrow} c^+_{-\vec{k}\downarrow} c_{-\vec{l}\downarrow} c_{\vec{l}\uparrow} \qquad 2\text{-}10$$

which includes the interaction terms necessary for superconductivity but ignores all other interaction terms, which average out. The particle number operator, $n_{\vec{k}\sigma} = c^+_{\vec{k}\sigma} c_{\vec{k}\sigma}$, has an eigenvalue of unity (zero) when acting on an occupied (empty) state. The free electron energy relative to the Fermi energy is given by:

$$\varepsilon_{\vec{k}} = \frac{\hbar^2 \vec{k}^2}{2m^*} - E_F \qquad 2\text{-}11$$

The superconducting ground state can now be found by minimizing the total energy (obtained by operating the Hamiltonian 2-10 onto the ground state wavefuntion 2-9), while keeping the number of particles fixed. By substitution one finds that the interaction term given by:

$$\langle V \rangle = \langle \Psi_G | \sum_{\vec{k}\vec{l}} V_{\vec{k}\vec{l}} c^+_{\vec{k}\uparrow} c^+_{-\vec{k}\downarrow} c_{-\vec{l}\downarrow} c_{\vec{l}\uparrow} | \Psi_G \rangle = \sum_{\vec{k}\vec{l}} V_{\vec{k}\vec{l}} u_{\vec{k}} v^*_{\vec{k}} u^*_{\vec{l}} v_{\vec{l}} \qquad 2\text{-}12$$

shows that $V_{\vec{k}\vec{l}}$ scatters particles from state $(\vec{l}\uparrow, -\vec{l}\downarrow)$ to $(\vec{k}\uparrow, -\vec{k}\downarrow)$, which requires the initial $\vec{l}$ pair to be occupied and the $\vec{k}$ pair empty, and the reverse for the final state.

In order to solve the energy minimization equation, BCS introduced the two following quantities:

$$\Delta_{\vec{k}} = -\sum_{\vec{l}} V_{\vec{k}\vec{l}} u_{\vec{l}} v_{\vec{l}} \qquad 2\text{-}13$$

$$E_{\vec{k}} = \sqrt{\Delta_{\vec{k}}^2 + \varepsilon_{\vec{k}}^2} \qquad 2\text{-}14$$

$E_{\vec{k}}$ is the excitation energy of a quasiparticle of momentum $\vec{k}$, while $\Delta_{\vec{k}}$ is essentially independent of momentum and is the minimum excitation energy or energy gap. The $\Delta_{\vec{k}}$ can now be evaluated self-consistently by introducing equations 2-13 and 2-14 into 2-12.

In order to calculate the condensation energy as well as the probability coefficients u_k and v_k, the BCS theory assumes a constant negative interaction potential between pairs of particles up to a given energy and zero above:

$$V_{\vec{k}\vec{l}} = \begin{cases} -V & \text{if } \left|\varepsilon_{\vec{k}}\right|, \left|\varepsilon_{\vec{k}}\right| < \hbar\omega_c \\ 0 & \text{otherwise} \end{cases} \qquad 2\text{-}15$$

From this assumption, it is obvious that $\Delta_{\vec{k}}$, defined in 2-13, is independent of momentum and is further referred to as the gap energy, Δ. Furthermore, the self-consistency equation leads to a gap value of:

$$\Delta = \frac{\hbar\omega_c}{\sinh(N(0)^{-1}V^{-1})} \qquad 2\text{-}16$$

The occupation probabilities that minimize the total energy can then be calculated to be:

$$u_{\vec{k}}^2 = \frac{1}{2}\left(1 + \frac{\varepsilon_{\vec{k}}}{E_{\vec{k}}}\right) \qquad v_{\vec{k}}^2 = \frac{1}{2}\left(1 - \frac{\varepsilon_{\vec{k}}}{E_{\vec{k}}}\right) \qquad 2\text{-}17$$

For a more detailed description of this theory, we refer to chapter 3 of [34].

2.2 Quasiparticle excitations

In order to deal with excitations, above the BCS ground state, Bogoliubov [35] and Valatin [36] introduced a linear pair of orthonormal operators which could diagonalize the BCS Hamiltonian, which are defined as:

$$\gamma_{\vec{k}0}^{+} = u_{\vec{k}}^{*} c_{\vec{k}\uparrow}^{+} - v_{\vec{k}}^{*} c_{-\vec{k}\downarrow} \qquad 2\text{-}18$$

$$\gamma_{\vec{k}1}^{+} = u_{\vec{k}}^{*} c_{-\vec{k}\downarrow}^{+} + v_{\vec{k}}^{*} c_{\vec{k}\uparrow} \qquad 2\text{-}19$$

These operators correspond to the creation of excitations from the BCS ground state. Equation 2-18 represents the creation operator of an electron with momentum $\vec{k}$ and spin up if the pair state $\left(\vec{k}\uparrow, -\vec{k}\downarrow\right)$ was empty or destroys an electron with momentum $-\vec{k}$ and spin down in case that initial pair state was occupied, effectively creating an excitation with momentum $\vec{k}$ and spin up. The second operator is similar, but for the opposite momentum and spin. These excitations are termed quasiparticles and as we shall see later, form the essence of the photo detection principle of superconducting tunnel junctions. As mentioned in the

previous paragraph, the energy of these quasiparticles is given by equation 2-14. The quantity Δ therefore plays the role of an energy gap, below which no excitations can exist. It should be noted that excitations can only come in pairs if one wants to conserve the number of electrons in the system. The minimum energy required to create excitations in a superconductor is thus 2Δ. Furthermore, each Cooper pair that is destroyed yields a pair of quasiparticles with opposite free electron energy relative to the Fermi energy corresponding to an electron-like ($k>k_F$) and a hole-like excitation ($k<k_F$). These two quasiparticle branches are thus equally populated. Tunnelling processes can create an imbalance between the two branches, however this is quickly restored and will not be considered further in this work.

The superconducting density of states can be found by equating:

$$N_s(E_{\vec{k}})\,dE_{\vec{k}} = N_n(\varepsilon_{\vec{k}})\,d\varepsilon_{\vec{k}} \qquad 2\text{-}20$$

Assuming $N_n(E)=N(0)$ constant around the Fermi energy, we find:

$$N_s(E_{\vec{k}}) = N(0)\frac{d\varepsilon_{\vec{k}}}{dE_{\vec{k}}} = \begin{cases} \dfrac{E_{\vec{k}}}{\sqrt{E_{\vec{k}}^2-\Delta^2}} & E_{\vec{k}} > \Delta \\ 0 & E_{\vec{k}} < \Delta \end{cases} \qquad 2\text{-}21$$

This density of states is derived for a pure bulk superconductor. In our practical devices, we will use bi-layers of Tantalum and Aluminium. The proximity of two thin films of superconducting materials with different gap energy results in a film with an intermediate gap energy and position dependent density of states [37], confining the quasiparticles preferably in the lower gap material. For our tunnel junctions the lower gap material (Al) will naturally be in contact with the tunnel barrier and will enhance the tunnelling probability [38].

2.3 Tunnelling processes

Superconducting tunnel junctions consist of a sandwich of two thin superconducting films, separated by a very thin insulating barrier. Through a quantum-mechanical process, charge carriers can tunnel across this insulator and form a current that can be sensed by an external circuit. This process was discovered by Giaever [39], [40] while Nicol, Shapiro and Smith [41] showed that the observed non-linearity in the slope of the current to voltage characteristic (I-V curve) was directly related to the quasiparticle density of states, as described by BCS. Tunnelling structures thus present a powerful tool to probe the microscopic nature of superconductivity [42].

When applying a potential V ($<2\Delta/e$) across a junction, Quasiparticles can undergo four distinct tunnel processes as sketched in Figure 2-1. For process 1, a quasiparticle tunnels directly from layer 1 into layer 2, physically moving an electron in the same direction. For that process to happen, the QP state at the left has to be initially filled and the state on the right, empty. This is valid for electron-like as well as hole-like quasiparticles and if one neglects the dependence of the Tunnelling matrix on the QP wavevector, both contributions are equal. Using the Fermi distribution, f, this process generates a current which is proportional to:

$$I_1 \propto \int N_s(E_{\vec{k}})\,f(E_{\vec{k}})\,N_s(E_{\vec{k}}+eV)\left[1-f(E_{\vec{k}}+eV)\right]\,dE_{\vec{k}} \qquad 2\text{-}22$$

The exact opposite process is of course also possible, creating an opposite current, which partly cancels the previous one. However, due to the positive bias applied (as in the figure), the occupancy of higher energy levels in film 2 which can tunnel to available states in film 1 is

much lower due to the exponential Fermi distribution. The current resulting from process 2 is proportional to:

$$I_2 \propto \int N_s(E_{\bar{k}} + eV) f(E_{\bar{k}} + eV) N_s(E_{\bar{k}}) \left[1 - f(E_{\bar{k}})\right] dE_{\bar{k}} \qquad 2\text{-}23$$

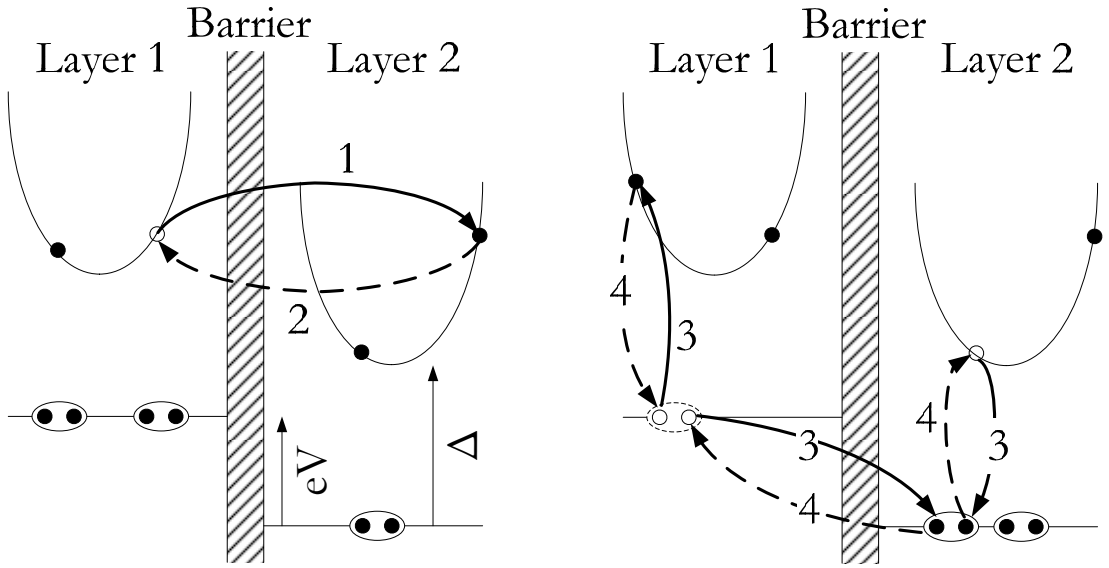

Figure 2-1: The four tunnelling processes in an biased STJ, assuming a bias voltage, V which is smaller than the gap energy Δ.

The following two processes are slightly more complex as they involve the creation and annihilation of Cooper pairs. In process 3, an electron still moves from Layer 1 to Layer 2, as for process 1. In a simplistic view, a Cooper pair needs to be annihilated in Layer 1; one of the two quasiparticles is created in that same layer, while the other one tunnels to Layer 2 and recombines with an available quasiparticle into a Cooper pair. It therefore appears as if the original QP in Layer 2, transited into Layer 1 while the effective electron flow is from left to right, creating a positive current through a process called 'back-tunnelling' and which is proportional to:

$$I_3 \propto \int N_s(E_{\bar{k}} + eV) \left[1 - f(E_{\bar{k}} + eV)\right] N_s(E_{\bar{k}}) f(E_{\bar{k}}) \, dE_{\bar{k}} \qquad 2\text{-}24$$

Process 4 is the opposite of process 3 and partially cancels that current. Again, for positive bias this process will be rapidly vanishing as it requires QPs with energies larger than eV+Δ. The tunnel rate will be proportional to:

$$I_4 \propto \int N_s(E_{\bar{k}} + eV) f(E_{\bar{k}} + eV) \, N_s(E_{\bar{k}}) \left[1 - f(E_{\bar{k}})\right] dE_{\bar{k}} \qquad 2\text{-}25$$

The process of 'back-tunnelling' provides the equivalent of an internal amplification in the device, and is particularly important for the detection of optical photons; for as long as quasiparticles survive in the films, they can tunnel back and forth while providing a useful signal [43].

The total tunnel current is then given by the sum of the four contributions and amounts to the traditional result, where G_{nn} is the normal state conductance of the junction:

$$I_T = I_1 - I_2 + I_3 - I_4 = G_{nn} \int N_s(E_{\bar{k}}) \, N_s(E_{\bar{k}} + eV) \left[f(E_{\bar{k}}) - f(E_{\bar{k}} + eV)\right] dE_{\bar{k}}$$

2.4 Josephson tunnelling

Starting from the vacuum state and progressively adding Cooper pairs, the BCS theory was able to construct a wave function, ψ, describing a large number of interacting Cooper pairs. This function has a similar meaning as the order parameter introduced by Ginzburg and Landau, where $|\psi(\vec{r})|^2$ is proportional to the density of superconducting electrons at position $\vec{r}$. A typical Cooper pair has a wave function that overlaps with many other Cooper pairs. Cooper pairs find it energetically favourable to lock all their phases. Therefore, $\psi(\vec{r})$ can be seen as a macroscopic wave function. The signature of a superconductor is thus its condensed many-particle wave function $\psi(\vec{r}) = |\psi(\vec{r})| e^{j\phi}$ which maintains its phase coherence over macroscopic distances.

The tunnelling of Cooper pairs at zero bias is a process that was first predicted by Josephson [44]. If φ is the phase difference between the condensates' wavefunctions across the tunnel junction and V is the applied voltage, it can be shown that [45]:

$$\frac{d\varphi}{dt} = \frac{2e}{\hbar} V \qquad 2\text{-}26$$

$$J = J_c \sin\varphi \qquad 2\text{-}27$$

$$J_c = \frac{4eK\sqrt{n_{s1} n_{s2}}}{\hbar} \qquad 2\text{-}28$$

where J_c is the Josephson current density, n_{s1} and n_{s2} are the Cooper pair densities in both films and K is a coupling constant. In the practical application of photon detection with STJs, this Josephson current may prohibit stable biasing of the junction as well as excess noise and needs to be suppressed.

The suppression can be achieved by applying a magnetic field parallel to the junction's surface. Assuming that the junction area is defined in the $[x,y]$ coordinate plane and $f(x,y)$ defines the junction area, the field dependence of the Josephson current can be calculated from the following relations [46]:

$$\nabla_{x,y}\varphi = \frac{2ed_{eff}}{\hbar} \vec{B} \times \vec{e}_z \qquad 2\text{-}29$$

$$I_c = \iint dxdy\, J_{c,0} \sin\varphi\, f(x,y) \qquad 2\text{-}30$$

For film thicknesses of the order of the London penetration depth, the effective magnetic thickness is given by:

$$d_{eff} = t + \lambda_1 \tanh\frac{d_1}{2\lambda_1} + \lambda_2 \tanh\frac{d_2}{2\lambda_2} \qquad 2\text{-}31$$

where t is the barrier thickness and d_i, λ_i the layer 'i' thickness and London penetration depth, respectively. Equations 2-29 and 2-30 show that the Josephson current is related to the two-dimensional Fourier transform of the junction's shape. Special geometries, like e.g. quartic or raised-cosine [47],[48], can thus be designed to have a fast suppression of the Josephson current as function of magnetic field. Let us now consider a few junction shapes which are

relevant to this work, as they are easy to assemble in compact arrays. Figure 2-2 shows four variations on the standard theme; the magnetic field is always in-plane with the junctions. Shape A is a square junction with the magnetic field applied parallel to one side. Shape B is identical but for the field which is at 45 degrees. Shape C corresponds to a pixel from a closed-packed array. The cut-outs, of size α×δ, are for the base-film plugs (see paragraph 3.2.1). Shape D is identical to B, however, there is a cut-out and protrusion which could be caused by a misalignment, by α, of the Mesa-etch mask (see paragraph 3.2).

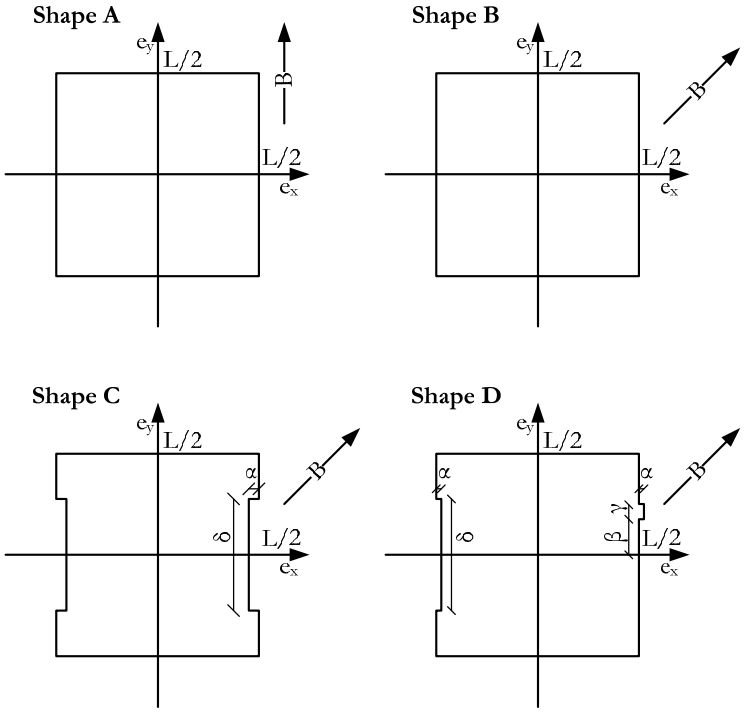

Figure 2-2: Various STJ shapes that are used in the calculation of the Josephson current suppression as function of magnetic field, see text for details.

If $J_{c,0}$ is the maximum Josephson current density at zero field, the Josephson current for shape A can be readily calculated from 2-29 and 2-30:

$$I_c = \frac{J_{c,0} L \hbar}{e d_{eff} B} \sin \frac{e d_{eff} B L}{\hbar} \qquad 2\text{-}32$$

This current decreases as 1/B. A faster suppression as function of magnetic field can be achieved by turning the junctions 45 degrees with respect to the magnetic field, as in shape B. In this case, integrating the same equations yield:

$$I_c = \frac{2 J_{c,0} \hbar^2}{e^2 d_{eff}^2 B^2} \sin^2 \frac{e d_{eff} B L}{\sqrt{2}\hbar} \qquad 2\text{-}33$$

Although a bit more cumbersome, the integration is readily carried out for shape C as well and gives:

$$I_c = \frac{2 J_{c,0} \hbar^2}{e^2 d_{eff}^2 B^2} \sqrt{\sin^4 \frac{e d_{eff} B L}{\sqrt{2}\hbar} + 2 \sin^2 \frac{e d_{eff} B \alpha}{\sqrt{2}\hbar} \sin^2 \frac{2 e d_{eff} B \delta}{\sqrt{2}\hbar} \sin^2 \frac{e d_{eff} B (L - \alpha)}{\sqrt{2}\hbar}} \qquad 2\text{-}34$$

As we will see in the next chapter, the latest S-CAM arrays are based on a closed-packed design, which deviates from the regular square pattern. In order to judge the influence of this novel shape, Figure 2-3 compares the Josephson current suppression for shape B (dashed curve) to this new shape C (solid curve). For the calculations, we took the dimensions as they appear on the mask design: L=33.19, α=1.06 and δ=13.44μm and for the magnetic thickness, we used a value that shall later be derived by fitting, d_{eff}=103nm. The overall behaviour of the different pixel designs are similar, with an identical main periodicity and overall $1/B^2$ fall-off. As it is also modulated by α and δ, the closed-packed design appears more erratic in shape but in particular lacks many of the deep suppression regions. In practice, this turns out not to be a problem and these detectors are just as easy to bias as the squared devices.

Figure 2-4 shows measurements of the Josephson current in an array pixel. The device is from MUL192.C2 (see for details on this design paragraph 3.2.1) and has a standard 'square' design with L=33.19μm. As one can see from the figure, equation 2-33 can not truthfully reproduce the measurements. In particular, the maxima recorded around 34 and 43 Gauss cannot be explained. Various causes can be considered, like the non-uniformity of the barrier, the roughness of the device's edges caused by the etch process, the self-screening effect, misalignment of the magnetic field, etc. We suggest rather a misalignment of the Mesa-etch mask during the production process. If this mask is shifted by a small amount in the x direction, it would have the effect of causing an additional cut-out on one side of the junction while keeping a small protrusion of tri-layer on the other; see shape D in Figure 2-2.

The resulting Josephson current can be evaluated as before and one finds:

$$I_c = \frac{2J_{c,0}\hbar^2}{e^2 d_{eff}^2 B^2}\sqrt{\left[\begin{aligned}&\sin^2\frac{ed_{eff}BL}{\sqrt{2}\hbar} + \cos\frac{ed_{eff}B(L+\alpha-2\beta-\gamma)}{\sqrt{2}\hbar}\sin\frac{ed_{eff}B\alpha}{\sqrt{2}\hbar}\sin\frac{ed_{eff}B\gamma}{\sqrt{2}\hbar}\\ &\quad - \cos\frac{ed_{eff}B(L-\alpha)}{\sqrt{2}\hbar}\sin\frac{ed_{eff}B\alpha}{\sqrt{2}\hbar}\sin\frac{ed_{eff}B\delta}{\sqrt{2}\hbar}\end{aligned}\right]^2 + \left[\begin{aligned}&\sin\frac{ed_{eff}B(L+\alpha-2\beta-\gamma)}{\sqrt{2}\hbar}\sin\frac{ed_{eff}B\alpha}{\sqrt{2}\hbar}\sin\frac{ed_{eff}B\gamma}{\sqrt{2}\hbar}\\ &+\sin\frac{ed_{eff}B(L-\alpha)}{\sqrt{2}\hbar}\sin\frac{ed_{eff}B\alpha}{\sqrt{2}\hbar}\sin\frac{ed_{eff}B\delta}{\sqrt{2}\hbar}\end{aligned}\right]^2} \qquad 2\text{-}35$$

From the mask design, we impose L=33.19, β=3.53, γ=4.25 and δ=23.19μm and fitted d_{eff} and α. The values that minimized the χ^2 are α=0.74μm and d_{eff}=103nm. From this and assuming a symmetrical junction with 130nm thick films on either side of the barrier, we find an equivalent London penetration depth of λ_L=70nm.

Note that the zero-field Josephson current could not be directly evaluated as no measurements could be taken at field values below 27Gauss due to the breakdown of superconductivity in the connecting wires. However, the fit can be extrapolated to zero and we find I_{c0}=5.4mA, or a current density J_{c0}=490A/cm^2. From theory we know that this is related to the barrier normal resistance as $J_{c,0} = \frac{\pi\Delta}{2eR_{NN}}$. Using this relation, we infer a normal state resistance R_{NN}=1.6μΩ.cm^2, consistent with the value of 2μΩ.cm^2 measured on test structures of the same wafer.

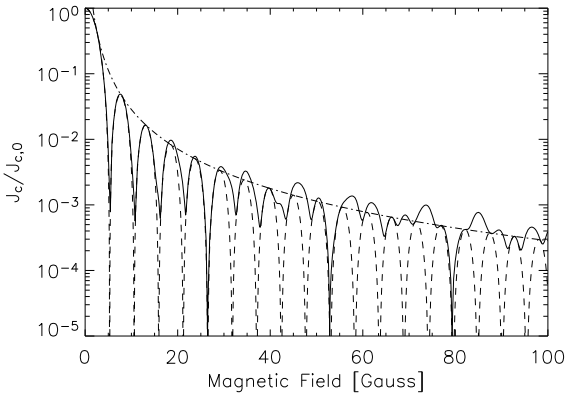

Figure 2-3: Josephson current as function of magnetic field for shape B (dashed) and C (solid).

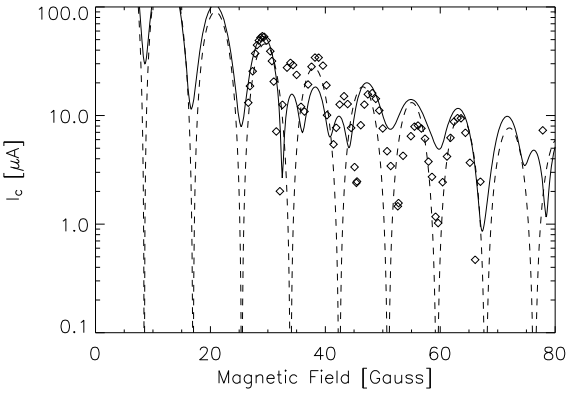

Figure 2-4: Josephson current measured for device MUL192.C2 T01 (symbols). The solid line is a fit using shape D, while the dashed line is obtained for shape B.

2.5 Theoretical detector performance analysis

2.5.1 Photo-absorption and energy down-conversion in STJs

The process of photo-absorption in superconducting films has been described in [49], [50], [51] and will be briefly summarized here, following the schematic representation of Figure 2-5. As an energetic photon is absorbed in a superconducting material, its complete energy is transferred to an initial photo-electron. Through secondary ionization, plasmon emission and decay, this electron will very rapidly (tens of femtoseconds) share its energy with other electrons. This process will result after a fraction of a picosecond into an original cloud of electrons each with a typical energy E_1 ~1eV, which is formally defined as the energy at which the electron-electron scattering and electron-phonon scattering rates are equal:

$$\tau_{e-e}^{-1}(E_1) = \tau_s^{-1}(E_1) \qquad 2\text{-}36$$

Although the phonon scattering rate will be higher from this energy onwards, the energy loss through electron-electron collisions, on average about half the electron's energy, will still be much higher than through electron-phonon scattering, as E_1 is much larger than the Debye energy Ω_D. A second energy level, E'_1, can thus be defined below which the electron-phonon interaction controls both the electron energy and momentum relaxation, and can be expressed as:

$$\tau_{e-e}(E'_1) = \frac{E'_1}{2\Omega_D}\tau_s \qquad 2\text{-}37$$

Which expresses the fact that it takes an electron as long to decay to half its energy through a single e-e collision as it takes to generate $E'_1/2\Omega_D$ Debye phonons. Assuming that the e-e scattering rate is proportional to the energy squared, we obtain,

$$E'_1 = 2^{1/3} E_1^{2/3} \Omega_D^{1/3} \qquad \left(>> \Omega_D\right) \qquad 2\text{-}38$$

The time, t_{dc}, it takes to down-convert from E_1 to Ω_D can be evaluated as follows. Assuming that electrons lose about half their energy during each e-e collision, the time taken by the first sub-stage $E_1 \rightarrow E'_1$, can be calculated backwards to be:

$$\tau_{e-e}(2E_1') + \tau_{e-e}(4E_1') + \cdots = \tau_{e-e}(E_1')\left(\frac{E_1'}{2E_1'}\right)^2 + \tau_{e-e}(E_1')\left(\frac{E_1'}{4E_1'}\right)^2 + \cdots = \frac{1}{3}\tau_{e-e}(E_1') \qquad 2\text{-}39$$

The second sub-stage, $E'_1 \rightarrow \Omega_D$ will take another $\tau_{e\text{-}e}(E'_1)$ as there are two equally competing channels to convert $E'_1 \rightarrow E'_1/2$ each at a rate of $\tau_{e\text{-}e}(E'_1)^{-1}$ and a further $\tau_{e\text{-}e}(E'_1)/2$ for phonon emission to relax the electron energy from $E'_1/2 \rightarrow \Omega_D$. So that the down-conversion time t_{dc} is given by:

$$t_{dc} = \frac{4}{3}\tau_{e-e}(E_1') = \frac{4}{3}\tau_s\left(\frac{E_1}{E_1'}\right)^2 = \frac{1}{3}\tau_s\left(\frac{4E_1}{\Omega_D}\right)^{2/3} \qquad 2\text{-}40$$

This quantity marks the start of the next phase with a sharp phonon distribution peaked around the Debye energy, called the phonon bubble. We shall later on evaluate the size of this phonon bubble as it will subsequently be used in the analysis of photo-absorption in thin films.

Now the phonon down-conversion begins. This phase is characterized by the fact that phonons control the dynamics and the quasiparticle distribution rapidly readjusts itself accordingly. This phase persists until the phonons reach the energy Ω_1, at which time the variations are again controlled by the, now much slower, electronic transitions while on that time scale, phonons break Cooper pairs almost instantly. In this stage, lower energy quasiparticle generation takes place, until the energy remaining of the excitations is too low to generate further quasiparticles. It is during this last stage that quasiparticle tunnelling will effectively start and create an excess current which is proportional to the energy of the original absorbed photon.

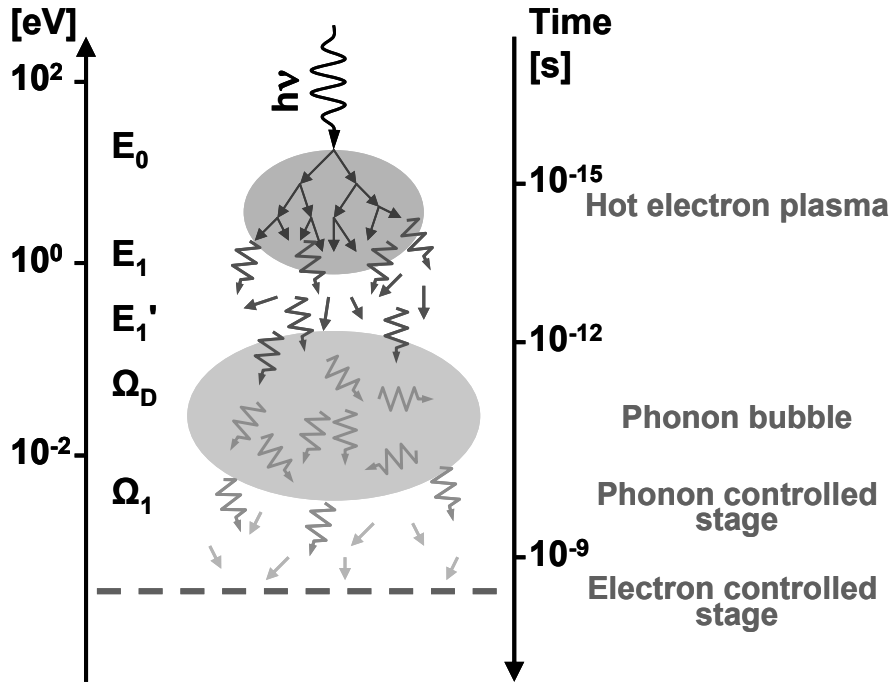

Figure 2-5: Photon absorption and energy down-conversion in a superconducting film.

The energy levels and associated scattering rates are schematically represented in Figure 2-6. As the energy (ε) of individual electrons fall during the down-conversion process, the electron-electron scattering rate (τ_{e-e}^{-1}) first scales as ε^2. Below some energy ($\hat{E}$), the e-e

collision rate becomes dominated by elastic scattering in the thin disordered film and the energy dependence now becomes proportional to $\varepsilon^{3/2}$. The electron-phonon scattering rate is constant above the Debye energy and scales as ε^3 below it. The first cross-over of these two rates occurs at E_1, as previously discussed, however a second cross-over point occurs at a much lower energy (E*). Phonon-electron scattering scales linearly with energy and dominates the electron-phonon scattering at energies below Ω_1. Depending on the material, Ω_1 can be larger or smaller than E*.

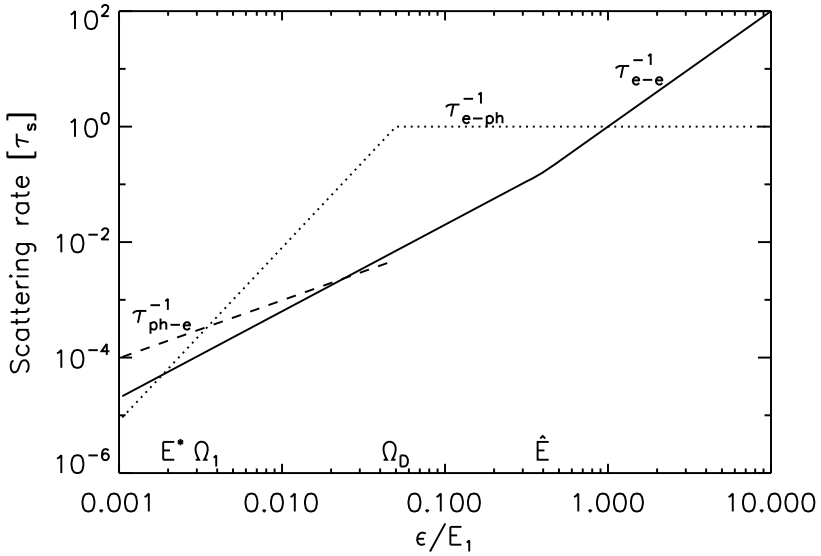

Figure 2-6: Schematic representation of electron-electron, electron-phonon and phonon-electron scattering rates, normalized to τ_s^{-1} as function of energy (normalized to E_1).

2.5.2 Theoretical Energy resolution

The theoretical performance of STJs has been reported extensively in literature and up to now was considered to be limited by six factors. The most fundamental one is related to the creation of quasiparticles. As the absorbed photon's energy is gradually converted into excitations, some energy is lost to sub-gap phonons which cannot break any Cooper pairs. This is the reason why it takes on average ~1.7Δ to create one quasiparticle. The average number of excess carriers is thus $N_0(E) \approx E/1.7\Delta$. Since this is a statistical process, there will be some variance on the number of quasiparticles created which limits the energy resolution to:

$$\delta E_{Fano} = 2.355\sqrt{1.7\Delta F E} \qquad 2\text{-}41$$

Where E is the photon's energy and F the Fano factor, which has been evaluated at ~0.2 [52], [53].

For as long as quasiparticles live, they can tunnel back and forth between the two electrodes and contribute to a usable signal. The average number of times each quasiparticle will tunnel is given by $\langle n \rangle = \Gamma_{tunnel}/\Gamma_{loss}$, where Γ_{tunnel} and Γ_{loss} are the tunnel and loss rates respectively. For multiple tunnelling junctions, it can be shown that the tunnel resolution limit is given by [54], [55]:

$$\delta E_{tunnel} = 2.355\sqrt{1.7\Delta E\left(1+\frac{1}{\langle n \rangle}\right)} = 2.355\sqrt{1.7\Delta G E} \qquad 2\text{-}42$$

It should be noted that the tunnel noise contribution given in [2-42] is for an infinite pulse integration time. It turns out that this noise component is non-stationary and can be partially suppressed if the electronics integration time can be chosen smaller than the quasiparticle lifetime [56].

As we have seen in the previous paragraph, quasiparticles can also tunnel such as to produce a current opposite to the useful signal current. Statistical variations on the ratio of direct to cancellation tunnel events further broaden the measured pulse height distribution. The cancellation noise contribution to the energy resolution has also been shown to be proportional to the square root of the energy and is given by [57]:

$$\delta E_{cancel} = 2.355\sqrt{1.7\Delta E\frac{4\sigma}{\langle n\rangle(\sigma-1)^2}} = 2.355\sqrt{1.7\Delta HE} \qquad 2\text{-}43$$

Where σ is the average ratio of direct tunnel events per quasiparticle $<n_{tun}>$ to cancellation tunnel events per quasiparticle $<n_{can}>$ and $<n>=<n_{tun}>+<n_{can}>$ is the total average number of tunnel events. In practice, this contribution to the total pulse height dispersion is only important at X-ray energies and for low-energy gap devices, where the thermalization of the quasiparticles to the gap is slow compared to the tunnel time.

In a practical application, the detectors are optically coupled to the external world. Since the energy gap of these devices is very low, photons down to the sub-mm wavelength range will cause excess quasiparticles to be generated, when absorbed. In practice, the background infrared photons, originating from warmer parts of the instrument, cannot be individually detected and its flux will have to be severely suppressed if one wants to measure single optical or X-ray photons. The energy resolution degradation induced by IR photons is related to the Poissonian arrival statistics of such photons as well as the shot noise from the increased sub-gap current and is given by:

$$\delta E_{IR} = 2.355\sqrt{\langle E_{IR}^2\rangle\Gamma_{IR}\tau} \qquad 2\text{-}44$$

Where $<E^2_{IR}>$ represents the mean squared energy of the background photon energy distribution, Γ_{IR} is the background photon flux and τ is the electronics integration time [58].

Like any detector, STJs are non-ideal devices. Regions with slightly suppressed gap energy or trapping sites can cause local variations in measured charge output. This spatial non-uniformity in the responsivity of the superconducting device will lead to a variance which is proportional to the photon's energy. This effect is usually negligible for optical photons, but plays a major role in X-ray detection. Using an arbitrary scaling factor α [59],

$$\delta E_{non-unif} = 2.355\sqrt{\alpha E^2} \qquad 2\text{-}45$$

In addition to the effects related to quasiparticle dynamics, the photon energy resolution of STJs will be hampered by electronics noise. A detailed noise analysis will be presented in chapter 4.3. In a practical set-up, the IR and electronic noise can be measured independently of all other contributions by injecting electronic pulses into the preamplifer and measure their pulse height distribution width.

As all these contributions to the measured energy variance are independent, they can be added quadratically so that the total energy resolution is given by:

$$\delta E_{tot} = \sqrt{\delta E_{Fano}^2 + \delta E_{tun}^2 + \delta E_{cancel}^2 + \delta E_{IR}^2 + \delta E_{non-unif}^2 + \delta E_{el}^2} \qquad 2\text{-}46$$

For what follows, we will define the intrinsic energy resolution as:

$$\delta E_i = \sqrt{\delta E_{Fano}^2 + \delta E_{tun}^2 + \delta E_{cancel}^2 + \delta E_{non-unif}^2} \qquad 2\text{-}47$$

This quantity can be obtained experimentally by quadratically subtracting the measured electronic and IR induced noise contribution from the measured total resolution.

The energy resolving power is a measure of the ability to distinguish different energies in the pulse height distribution and is usually defined as the full width at half maximum (FWHM) of the pulse height distribution from a mono-chromatic illumination of the sensor. The (measured) total and intrinsic resolving powers are given respectively by:

$$R_{tot} = \frac{E}{\delta E_{tot}} \qquad 2\text{-}48$$

$$R_i = \frac{E}{\delta E_i} \qquad 2\text{-}49$$

2.5.3 Photo-absorption in thin films

In the latest generation of Ta/Al STJs, produced for ESTEC by Cambridge MicroFab Ltd (see chapter 3.2), a significantly higher resolving power, around 24 at 2.5eV, has been achieved compared to previous devices. As we improved the quality of our detectors, two effects were noticed. First, the longer lifetime of the quasiparticles in our Ta/Al STJs enabled a substantial suppression in tunnel noise, without compromising the electronics signal-to-noise ratio. This then led to the discovery of additional resolution limiting factors which we shall discuss now.

The measurements that we will report here were carried out in an Oxford Instruments Heliox cryostat at a temperature of 285mK. Figure 2-7 shows a collection of I-V curves for the different sized devices available on the science chip MUL169.D3. The chip consists of a symmetrical lay-up of 100nm Ta, 30nm Al, Al oxide barrier, 30nm Al and 100nm Ta, identical to that of the S-CAM3 devices. For all detectors, except the smallest one, the sub-gap current is of order 100fA/μm^2. The values are measured at 100μV, except for the 100μm device, where it is evaluated at 150μV due to the presence of a Fiske step.

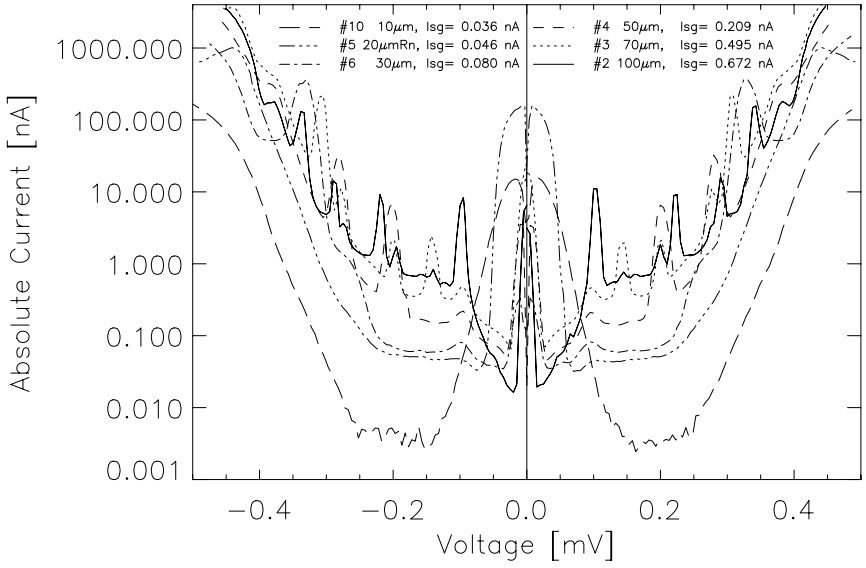

Figure 2-7: IV curves for the different sized devices (10×10 – 100×100μm^2) of the MUL169.D3 chip.

Figure 2-8 presents a collection of three spectra obtained with device MUL169.D3 #6, a $30\times30\mu m^2$ STJ that will also be used later in this chapter as illustration of the newly discovered effects. A micrograph of the detector is given in Figure 2-9. For the optical measurements, light was coupled in through an optical fibre connected to a light source which consisted of an Oriel Xenon lamp and a double grating monochromator. The optical light was directed through the sapphire substrate into the junction's Tantalum base film.

The gap energy for these proximized films is measured to be ~0.5meV, which should yield about 1180 quasiparticles per eV photon energy. The responsivity, which is a measure of the registered number of tunnel events per photon energy, is about $2\times10^5 e^-/eV$, with an associated pulse decay time of 85μs. From this, we estimate the average number of tunnels per quasiparticle $\langle n\rangle=170$ and a tunnel rate $\Gamma_{tunnel} = 2\times10^6 s^{-1}$.

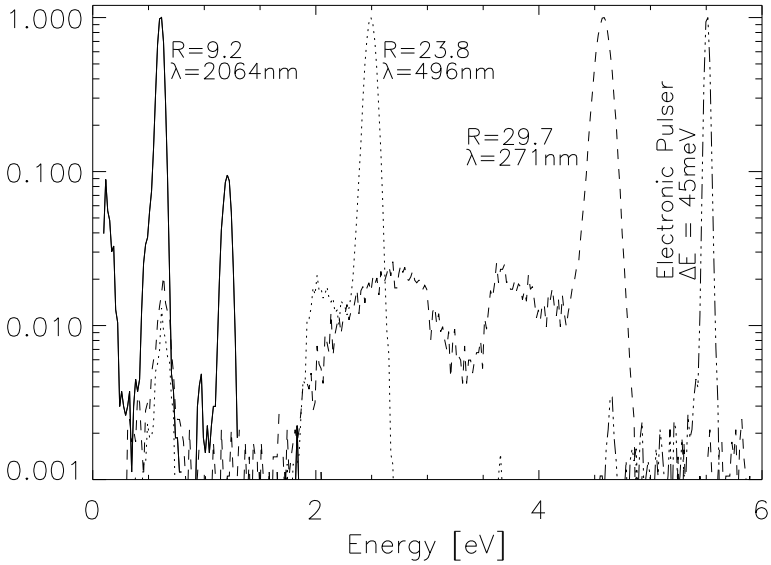

Figure 2-8: Spectra obtained with MUL169.D3 device #6, for different illumination wavelengths.

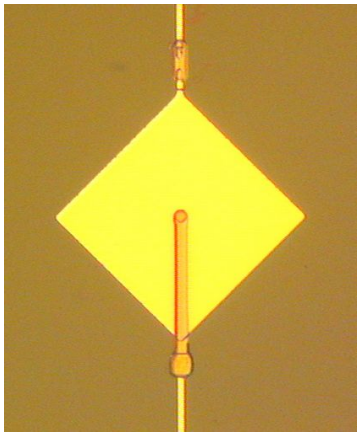

Figure 2-9: $30\times30\mu m^2$ device #6 of MUL169.D3. Notice the Nb top contact and plug in the base lead.

The spectra show the excellent resolving power obtained with this device, R=9.2, 23.8 and 29.7 at 2064, 496 and 271nm respectively. A few features can be identified:

1. For the lowest energy spectrum (λ=2064nm) the threshold was lowered, such that some noise counts start to be visible below 0.24eV.
2. For that same spectrum, the second-order of the monochromator is also visible.
3. For the 496 and 271nm spectra, a 'shoulder' is present at lower energies. This has been identified to correspond to photon-absorption in unproximized Ta film, which has a larger energy gap. The ratios of counts in the mean peak to those in the 'shoulder' are consistent with a small stub in the base lead before the Nb plug and a 0.45μm Al over-etch at the perimeter of the device.
4. The 'bump' clearly visible from 1.7-3.3eV for the shortest wavelength illumination is due to fluorescence of the coupling fibre or the sapphire substrate.
5. The spectrum obtained from an electronic pulser is added, from which we deduce 45meV noise contribution.

Figure 2-10 shows the measured (diamonds) and intrinsic (triangles) resolving power as function of photon energy for the $30\times30\ \mu m^2$ Ta/Al detector. We assume now that H is negligible in our devices; the IR and electronic noise terms are removed for the intrinsic resolution by subtracting the noise contribution measured with the electronic pulser from the measured energy variance and the non-uniformity term only plays a significant role at X-ray

energies. We are therefore left with only the Fano and tunnel noise contributions. To highlight the inadequacy of equations 2-41 and 2-42, we have overlaid the results of these equations using F+G=0.7 (dashed curve) and 1.0 (dot-dashed curve) on the measurement points in Figure 2-11. From these comparison plots, we see that the trend of the measurements seems to inflect between 2 and 3eV, which corresponds to the energy range where the absorption length in Tantalum decreases drastically.

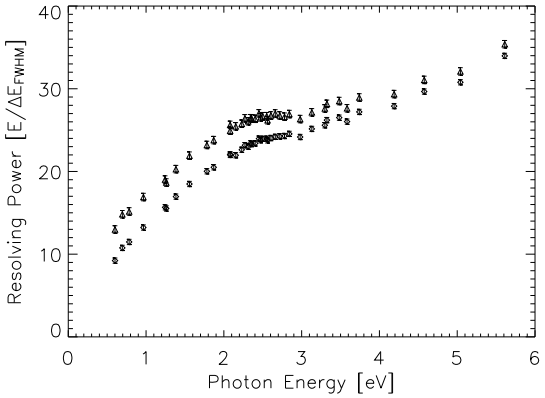

Figure 2-10: Measured (diamonds) and intrinsic (triangles) resolving power as function of photon energy for a 30×30μm^2 Ta/Al junction.

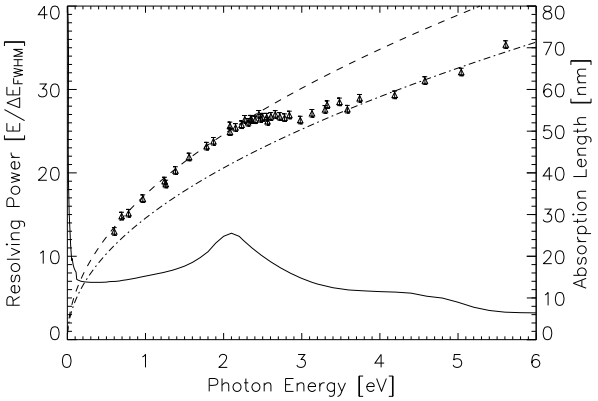

Figure 2-11: Intrinsic resolution and theoretical resolutions for two values of F+G (see text). Continuous line is the absorption length in Ta.

We believe this correlation is a strong evidence that vertical inhomogeneity – the distribution of photon absorption sites in the direction of the incident photon flux – plays a role in the limiting resolving power of high quality STJs, mediated by the processes of productive (that is, having energies greater than 2Δ) phonon losses to the substrate.

In order to understand this correlation, consider the following. At some point during the down-conversion process, we know that a phonon bubble will be created. This ensemble of phonons will propagate and progressively loose energy by breaking Cooper pairs, but as their energy decreases, their mean-free path will also increase from several to hundreds of nanometers. For thin films, or photon absorption in the vicinity of a boundary, phonons incident on this interface can be lost from the superconductive film, effectively removing energy from the system. Indeed, the relative soft electrode metal is deposited on a substrate of much higher acoustic impedance, which creates a critical cone for phonon transmission across this boundary. Productive phonons incident on the barrier at angles of incidence less than the critical value can thus be transmitted and constitute a loss of energy.

Two effects can now be distinguished. Angular fluctuations in the distribution of emitted phonons close to the limiting incident angle of the cone give rise to variations in the number of phonons lost from the sensor. In addition, the number of phonons reaching the interface depends on their distance to that interface as their probability to interact with the condensate increases with distance. Even if phonons reach the interface they will have a certain probability of crossing it and being lost from the system. We will call these combined effects the phonon escape noise. Secondly, the exponential distribution of absorption depths in the material naturally leads to a vertical inhomogeneity of the response, as the mean energy loss depends on the distance of the absorption site to the interface.

The phonon escape noise and vertical inhomogeneity can be described in terms of contributions to the broadening of the detector's response. We shall now derive a model that describes these effects as function of photon energy.

First we will start by evaluating the electron and phonon distribution functions once the phonon bubble is created. The non-equilibrium state of interacting quasiparticles and phonons can be described by the following set of coupled equations [60]-[64]:

$$\frac{\partial n}{\partial t} - D\Delta n = I_{ep}\{n,N\} + I_{ee}\{n\} + Q(\varepsilon,\vec{x},\vec{x}_0,t)$$
$$\frac{\partial N}{\partial t} = I_d\{N\} + I_{pe}\{N,n\} \qquad 2\text{-}50$$

The phonon and quasiparticle distribution functions are given respectively by $n = n(\varepsilon,\vec{x},t)$ and $N = N(\Omega,\vec{x},t)$, as function of qp energy, ε, phonon energy, Ω, position and time. D is the quasiparticle diffusion constant and $I_{ep}\{n,N\}$, $I_{ee}\{n\}$, $I_d\{N\}$ and $I_{pe}\{N,n\}$ are the collision integrals for qps and phonons, electron-electron interactions, phonon loss into the substrate and phonon-qps interactions. Q is the source term, also depending on the absorption site $\vec{x}_0$.

During the period $E_1 \rightarrow \Omega_D$, the electrons diffuse outward from the absorption site, releasing an energetic phonon at each scatter. This stage is so fast (~0.38ps in Ta) that during this time, the phonons are quasi immobile and do not decay. Under these conditions, the phonon distribution can be derived from the qp distribution. By solving the second differential equation in [2-50], we obtain:

$$\frac{\partial N(\varepsilon,\vec{x},t)}{\partial t} = \frac{2}{\pi\tau_{ph}}\int_{\Delta}^{\infty}\frac{d\varepsilon'}{\Delta}\rho(\varepsilon')\rho(\varepsilon+\varepsilon')\left(1-\frac{\Delta^2}{\varepsilon'(\varepsilon+\varepsilon')}\right)n(\varepsilon+\varepsilon',\vec{x},\vec{x}_0,t) \approx \alpha\, n(\vec{x},\vec{x}_0,t) \qquad 2\text{-}51$$

Here, τ_{ph} is the phonon pair-breaking time, ϱ a dimensionless superconducting density of states and $n(\vec{x},\vec{x}_0,t) = 2N_0\int_{\Delta}^{\infty} d\varepsilon\,\rho(\varepsilon)\,n(\varepsilon,\vec{x},t)$, the qp density of states with N_0 the normal state density of states per spin at the Fermi level. The parameter α will be defined later.

It can be shown [65], [66] that electrons diffusing in a layer of thickness d ($-d/2<z<d/2$) with normal along the z-axis have the following distribution:

$$n(\vec{x},t) = \frac{1}{2d\pi Dt}\sum_{m=0}^{\infty}\frac{1}{1+\delta_{m,0}}\cos\left[m\pi\left(\frac{1}{2}+\frac{z}{d}\right)\right]\cos\left[m\pi\left(\frac{1}{2}+\frac{z_0}{d}\right)\right]\exp\left[-\frac{m^2\pi^2 Dt}{d^2}-\frac{(\vec{r}-\vec{r}_0)^2}{4Dt}\right] \qquad 2\text{-}52$$

Where $\delta_{m,n}$ is the Kronecker symbol and $\vec{r}$, the position vector in the x-y plane. The phonon distribution at the end of the $E_1 \rightarrow \Omega_D$ phase can now be calculated by integrating [2-51] from $t=0 \rightarrow t_{dc}$. Since we are only interested in the vertical distribution, we can integrate [2-52] over area of the interface, A, in the x-y plane. The resulting averaged phonon distribution is:

$$\tilde{N}(\Omega,z,z_0,t) = \frac{8E}{A\Omega_D^4\beta d}\sum_{m=0}^{\infty}\frac{1}{1+\delta_{m,0}}\cos\left[m\pi\left(\frac{1}{2}+\frac{z}{d}\right)\right]\cos\left[m\pi\left(\frac{1}{2}+\frac{z_0}{d}\right)\right]\frac{1-\exp\left[-\frac{m^2\pi^2 Dt_{dc}}{d^2}\right]}{\frac{m^2\pi^2 Dt_{dc}}{d^2}} \qquad 2\text{-}53$$

The result has been normalized such that the energy at the end of this phase remains equal to the initially deposited energy E, effectively removing parameter α used in [2-51]. We are now in a position to evaluate the average energy loss due to phonon transmission through the interface as well as the fluctuations around its mean. We shall assume that phonons incident on the escape interface are reflected or transmitted with probabilities according to the acoustic

mismatch laws [67]. Phonons which are incident to the interface at an angle larger than the critical angle θ_c=arcsin(c_s/c), where c_s and c are the mean velocities in the superconductor and substrate respectively, will undergo total internal reflection and remain in the superconductor. If $l_{pb}(\varepsilon)$ is the phonon mean free path with respect to pair breaking and is related to the pair breaking length for Debye phonons as $l_{pb}(\varepsilon)=l_{pb,D}\Omega_D/\varepsilon$, ξ the cosine of the incidence angle to the interface, $\eta(\xi)$ the transmission coefficient across that interface, we find the average energy loss for an absorption at depth z_0 to be:

$$E_{loss}(z_0) = 4E\sum_{m=0}^{\infty}\frac{\cos m\pi\left(\frac{1}{2}+\frac{z_0}{d}\right)}{1+\delta_{m,0}}\frac{1-\exp\left[-\frac{m^2\pi^2 D t_{dc}}{d^2}\right]}{\frac{m^2\pi^2 D t_{dc}}{d^2}}\int_0^1 \xi\,\eta(\xi)\,\theta(\xi-\xi_c)\,d\xi$$
$$\int_0^{\Omega_D}\left(\frac{\varepsilon}{\Omega_D}\right)^3\frac{l_{pb}(\varepsilon)}{d}\frac{1-(-1)^m\exp(-d/l_{pb}(\varepsilon)\xi)}{1+(m\pi l_{pb}(\varepsilon)\xi/d)^2}\frac{d\varepsilon}{\Omega_D} \qquad 2\text{-}54$$

Considering now that the probability of absorbing a photon at depth z_0, is exponentially related to the ratio of z_0 and the absorption depth $L(E)$, we can average over the various absorption depths to find:

$$E_{loss} = 4E\sum_{m=0}^{\infty}\frac{1}{1+\delta_{m,0}}\frac{1-\exp\left[-\frac{m^2\pi^2 D t_{dc}}{d^2}\right]}{\frac{m^2\pi^2 D t_{dc}}{d^2}}\frac{1-(-1)^m\exp(-d/L(E))}{[1+(m\pi L(E)/d)^2][1-\exp(-d/L(E))]}$$
$$\int_0^1 \xi\,\eta(\xi)\,\theta(\xi-\xi_c)\,d\xi\int_0^{\Omega_D}\left(\frac{\varepsilon}{\Omega_D}\right)^3\frac{l_{pb}(\varepsilon)}{d}\frac{d\varepsilon}{\Omega_D}\frac{1-(-1)^m\exp(-d/l_{pb}(\varepsilon)\xi)}{1+(m\pi l_{pb}(\varepsilon)\xi/d)^2}\frac{d\varepsilon}{\Omega_D} \qquad 2\text{-}55$$

In order to evaluate the fluctuations on the energy loss, we have to take a step back and consider the number of phonons, dM, in the energy range [ε,ε+dε], and their energy dM_ε. As we briefly discussed before, the fluctuations of the energy loss can be attributed to three random processes:

1. the number of phonons emitted into the critical cone
2. the statistical nature of the interaction of phonons with the condensate on their way to the interface
3. the transmission of phonons across the interface

These three effects are independent and their variances can be added to find the total variance of energy loss:

$$\overline{(\delta dM_\varepsilon)^2} = \overline{(\delta dM_\varepsilon)^2}\Big|_c + \overline{(\delta dM_\varepsilon)^2}\Big|_i + \overline{(\delta dM_\varepsilon)^2}\Big|_t \qquad 2\text{-}56$$

If we consider the first term, the probability, p, of being emitted inside the critical cone is binomially distributed and $\overline{(\delta dM_\varepsilon)^2}\Big|_c = p(1-p)\,dM$ with $p=\sin^2(\theta_c/2)$. Similar expressions can be derived for the other two terms and we find:

$$\overline{(\delta E_{loss})^2} = \frac{1}{2}\int_{-d/2}^{d/2} \frac{\exp\left[-(z_0 + d/2)/L(E)\right]}{L(E)\left[1-\exp\left[-d/L(E)\right]\right]} dz_0 \int_{-d/2}^{d/2} dz \int_0^{\Omega_D} \varepsilon^4 \beta \, d\varepsilon$$
$$\int_{\xi_c}^{1} \eta(\xi) \exp\left[-(d/2+z)/l_{pb}(\varepsilon)\xi\right]\left[1 - p\,\eta(\xi)\exp\left[-(d/2+z)/l_{pb}(\varepsilon)\xi\right]\right] \widetilde{N}(\varepsilon, \xi, z, z_0, t_{dc})\, d\xi$$

2-57

To follow the form of equation [2-41], we will represent the variance of the energy loss as $\overline{(\delta E_{loss})^2} = 1.7\Delta J_v E$ and find:

$$J_v = \frac{4\Omega_D}{1.7\Delta} \sum_{m=0}^{\infty} \frac{1}{1+\delta_{m,0}} \frac{1-\exp\left[-\dfrac{m^2\pi^2 D\, t_{dc}}{d^2}\right]}{\dfrac{m^2\pi^2 D\, t_{dc}}{d^2}} \frac{1-(-1)^m \exp(-d/L(E))}{[1+(m\pi L(E)/d)^2][1-\exp(-d/L(E))]}$$
$$\int_0^{\Omega_D} \left(\frac{\varepsilon}{\Omega_D}\right)^4 \frac{l_{pb}(\varepsilon)}{d} \frac{d\varepsilon}{\Omega_D}$$
$$\int_{\xi_c}^{1} \xi\,\eta(\xi)\left[\frac{1-(-1)^m \exp(-d/l_{pb}(\varepsilon)\xi)}{1+(m\pi l_{pb}(\varepsilon)\xi/d)^2} - 2\eta(\xi)\, p(\xi) \frac{1-(-1)^m \exp(-2d/l_{pb}(\varepsilon)\xi)}{4+(m\pi l_{pb}(\varepsilon)\xi/d)^2}\right] d\xi$$

2-58

Let's now turn to the vertical inhomogeneity. As we have seen from equation [2-54], we know that the mean energy loss is dependent on the depth of the absorption site. As photons are absorbed according to an exponential distribution of depth, this will result in a further broadening of the measured photon energy distribution. The measured spectrum of a monochromatic source will be the convolution of Gaussian distributions weighted by the absorption depth profile. This additional line-broadening due to vertical inhomogeneity can be approximated by a Gaussian with characteristic parameter $K_v(E)$ which also therefore depends on photon energy. Such an approximation is justified as long as the broadening does not significantly distort the Gaussian line-shape. One can show that the variance of the energy distribution due to this effect can be expressed as [66]:

$$\overline{(\delta Q)^2} = K_v \overline{Q}^2$$
$$K_v = \frac{\overline{E_{loss}^2(z_0)} - \overline{E_{loss}(z_0)}^2}{\left[E - \overline{E_{loss}(z_0)}\right]^2}$$

2-59

With $E_{loss}(z_0)$ given by equation [2-54].

2.5.3.1 Comparison with measurements – the Tantalum-Aluminium case

Following the ideas developed above, we modelled the intrinsic resolving power of a Ta/Al STJ for comparison with the measurements presented above. Retaining only those terms relevant to our Ta/Al films and for optical photon detection, the detector's intrinsic resolving power is given by:

$$R_i = \frac{E}{2.355\sqrt{1.7\Delta\, E\left(F + G + J_v(E)\right) + K_v(E)\, E^2}}$$

2-60

The list of parameters used in equations [2-58] and [2-59] are given in Table 2-1. The electron diffusion constant during the phonon bubble formation, *D*, and the tunnel noise factor *G* were used as fitting parameters in a χ^2 minimizing routine. The resulting best-fit values were $D = 4.5\times10^{-5}$ m^2s^{-1} and $G = 0.11$. The product of the pair-breaking time for Debye phonons, $\tau_{pb,D}$ and the electron diffusion constant play a direct role in the size of the phonon bubble and the probability for phonons to reach the interface; the larger these two values are, the less energy-dependent the resulting loss and variance will be. Our value of the diffusion constant is much lower than that which can be inferred from residual resistance measurements or diffusion experiments in absorbers. However, this coefficient relates to excited electrons with energy well above the Fermi level, for which scattering is dominated by spontaneous and stimulated emission of Debye phonons and is significantly stronger than elastic scattering at low temperature.

The tunnel noise factor G found here appears to be considerably suppressed from its asymptotic value of 1, however the value is fully consistent with that obtained from Figure 2 in reference [28].

Table 2-1: List of parameters used in fitting the measured resolution.

Symbol	Name	Value	Comment
d	Detector base film thickness	130nm	Measured
Δ	Film energy gap	0.5meV	Measured
Ω_D	Debye energy	20.7meV	From [65]
E_1/Ω_D	Characteristic down-conversion energy	47	From [65]
τ_s	Electron-phonon scattering time ($\varepsilon > \Omega_D$)	35fs	From [65]
τ_{ph}	Characteristic pair breaking time	22ps	From [68]
$\tau_{ph,D}$	pair breaking time for Debye phonons	2.4ps	From [68]
t_{dc}	$E_1 \rightarrow \Omega_D$ down- conversion time	0.38ps	From equation [2-40]
c_s	Speed of sound in Ta	$2.33 km.s^{-1}$	From [68]
c	Speed of sound in sapphire	$7.14 km.s^{-1}$	From [67]
θ_c	Critical angle	19°	Acoustic mismatch
D	Electron diffusion constant during down-conversion	$0.45 cm^2.s^{-1}$	Fitting parameter
G	Tunnel noise factor	0.11	Fitting parameter

Figure 2-12 compares our best fit with the measured resolving power. Error bars on the measurement points are statistical 1-sigma values. It is seen that the modelled curve (dashed) follows the measured intrinsic resolution closely, and in particular displays the inflection around 2-2.5eV as well as the increasing degradation towards higher energies. Figure 2-13 shows the energy dependence of the phonon escape noise and vertical inhomogeneity parameters. For photon energies in the range 0.1-6eV, the values of $J_\nu(E)$ and $K_\nu(E)$ are found to lie within the range 0.26-0.55 and $4.3\text{-}3.1\times10^{-5}$ respectively.

As our model predicts an energy dependent loss of productive phonons, this should also be visible in the normalized responsivity curves. Figure 2-14 shows the responsivity loss for all measurements relative to an average value. The first observation is that the scatter seems larger than any consistent effect. Any such effect would have to be smaller than a percent and the overlaid curve, derived from equation [2-55] with the previously determined best fit values for *D* and *G*, confirms this. The explanation for the scatter is thought to be due to the variations of responsivity observed from measurement run to measurement run and is thus purely instrumental. Even within a single run, (triangular symbols), scatter can result from e.g. bath temperature variations. Nevertheless, the fitted curve seems to follow this selected set of points to some extent, falling within most of the error bars.

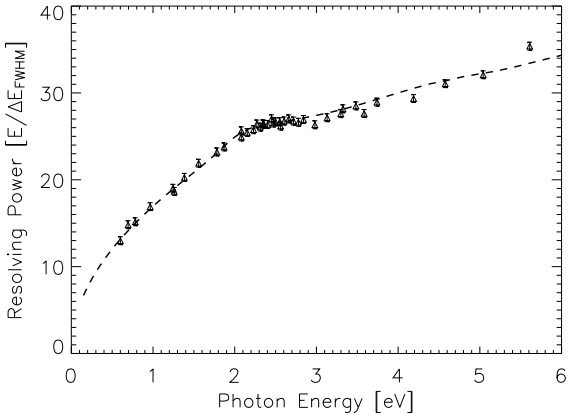

Figure 2-12: Best fit resolving power overlaid on the measurement points.

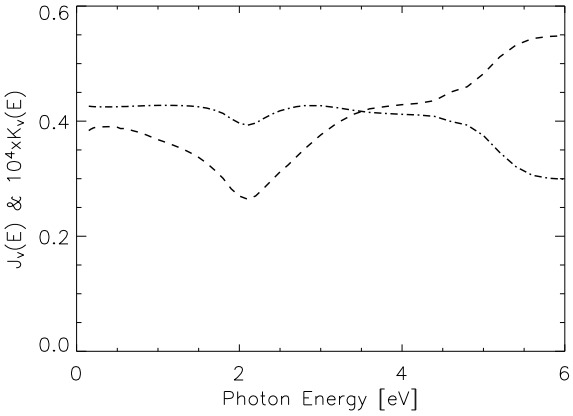

Figure 2-13: Angular (dashed curve) and inhomogeneity (dash-dot curve) noise parameters for the best fit.

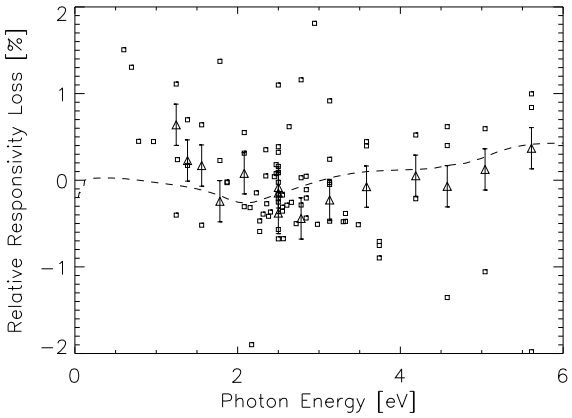

Figure 2-14: Relative responsivity variations as function of energy. The triangles are from a single measurement run, results from several additional runs are added as squares. The dashed curve is the expected responsivity variation obtained through our new model.

2.5.3.2 Comparison with measurements – the pure Aluminium case

As our new model predicts further energy resolution degradation compared to previous models, we also tried to apply it to earlier work in our group, based on pure Aluminium devices [59], [69], [70].

The experiments were also carried out in the optical region using a $30\times30\mu m^2$ Al STJ, with 100nm base and 50nm top films. Although the reduced energy-gap of Aluminium compared to Tantalum would predict an energy resolving power increase over these last devices, measurements to-date could not confirm this. Figure 2-15 shows the measured intrinsic resolving power of such a device together with the limiting resolution predicted by [2-47] with $F+G+H=5.5$ for the dashed line and 8.0 for the dot-dashed curve.

Previous publications of these results attributed this discrepancy to non-uniformity of the response across the device. We believe that it can now better be explained by the angular noise and vertical inhomogeneity parameters deduced here. If we fix the tunnel noise parameter to a value estimated from [28] and the cancellation noise term to the value calculated in [70] and only fit the electron diffusion coefficient, we obtain the best fit plotted in Figure 2-16. The complete list of parameters used is given in Table 2-2.

For photon energies in the range 0.1-6eV, the values of $J_\nu(E)$ and $K_\nu(E)$ are found to lie within the range 4.6-4.8 and $3.9\text{-}6.7\times10^{-5}$ respectively. Compared to the Ta junctions, the

photon absorption coefficient in Al does not vary considerably in the energy range covered by the measurements points and therefore no distinct feature is available to corroborate the theory. Nevertheless, the high values obtained for J_v can easily explain why the resolving power is not as high as one could hope for based on the energy gap value alone.

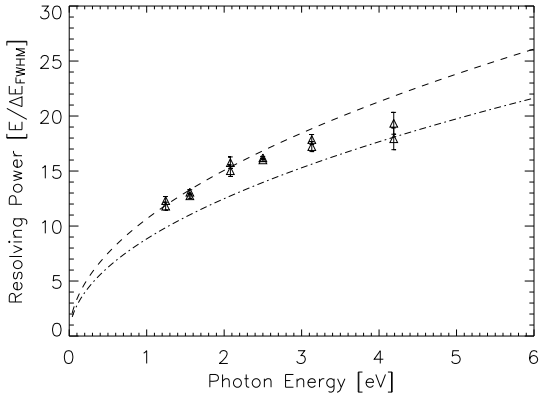

Figure 2-15: Intrinsic resolving power measured with the Al device and overlaid predicted curves using equation [2-47] with F+G+H=5.5 and 8.0.

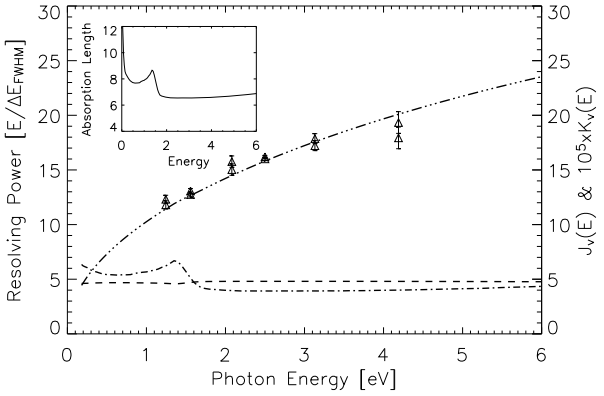

Figure 2-16: Best fit resolving power superimposed on measurement points. Jv (dashed) and Kv (Dot-dashed) noise parameters are plotted against the right-hand vertical axis. Inset shows the photon absorption length in Al.

Table 2-2: List of parameters used in fitting the measured resolution of the Al device.

Symbol	Name	Value	Comment
d	Detector base film thickness	100nm	Measured
Δ	Film energy gap	0.17meV	Measured
Ω_D	Debye energy	36.9meV	From [65]
E_1/Ω_D	Characteristic down-conversion energy	67	From [65]
τ_s	Electron-phonon scattering time ($\varepsilon > \Omega_D$)	29fs	From [65]
τ_{ph}	Characteristic pair breaking time	242ps	From [68]
$\tau_{ph,D}$	pair breaking time for Debye phonons	3.5ps	From [68]
t_{dc}	$E_1 \rightarrow \Omega_D$ down- conversion time	0.47ps	From equation [2-40]
c_s	Speed of sound in Al	$3.66 km.s^{-1}$	From [68]
c	Speed of sound in sapphire	$7.14 km.s^{-1}$	From [67]
θ_c	Critical angle	30.8°	Acoustic mismatch
D	Electron diffusion constant during down-conversion	$3.9 cm^2.s^{-1}$	Fitting parameter
G	Tunnel noise factor	0.35	Estimated from [28]
H	Cancellation noise factor	0.12	Calculated [70]

Chapter 3

DETECTOR ARRAY FABRICATION AND PERFORMANCE

We have just seen how STJs can be used as photon detectors and what their intrinsic energy resolution limitations are. We will now focus on the fabrication of these devices and specifically describe the processes used for array production. The characterization of devices was first carried out at the level of sub-gap leakage current. Responsivity measurements using 500nm photons from a monochromator were taken on those arrays that had a sufficient number of good pixels. Both these sets of measurements were made in our Oxford Instrument's Heliox refrigerator. In this section we shall also explain which arrays were chosen for the various S-CAM campaigns and present their energy resolution using the complete S-CAM system.

3.1 TFG STJ Fabrication

The fabrication of our S-CAM devices started at Oxford Instruments' Thin Film Group in Cambridge (TFG [71]). They were contracted to produce S-CAM detectors until 2002, when the group was dismantled. The detector array work performed at TFG heavily relied on previous Tantalum work, during which mostly science chips were produced. These were based on the mask set called 'MNYA' and consisted of a series of 10 STJs ranging in size from 10 to 100μm on a side, with two devices of each type. In addition, this mask provided six 50×50 and two 10×10μm^2 devices, without Nb plugs in the base leads. A separate mask set, M1.2a, was used for producing resistors in the base layer. For each trilayer deposition, a least one chip was fabricated using this mask to measure the residual resistance ratio (RRR) of the base layer, verifying the epitaxial quality of the film.

The processing at TFG was done on 2" diameter and 0.5mm thick Sapphire wafers. The trilayer deposition was done under ultra-high vacuum (base pressure ~10^{-9}mbar) and started with the growth of an epitaxial Tantalum layer at high temperature, typically 850ºC, followed by an Aluminium layer deposition at liquid Nitrogen temperature. The process was followed by oxidation of the Aluminium to create the tunnel barrier. We then proceeded with the growth of another Aluminium layer, followed by a thin Niobium deposition. This was at first thought to be necessary to produce a good quality top Tantalum film, but detailed studies of devices produced with and without this Nb seed layer did not show any difference in performance. Finally, the tri-layer was completed by a top Tantalum cap. This complete process was done in a single run, without breaking vacuum. The deposition rates were typically 0.53Å/s, 1.1Å/s and 0.69Å/s for Ta, Al and Nb, respectively. Deposition rate and temperature for the base Ta layer was optimized in earlier work for best RRR.

After tri-layer depositions, the wafers were sawn in chips, each 13.5×7.5mm^2 for further processing. So post-processing was performed at chip, rather then wafer level. The basic processing route was as follows (see for a schematic representation Table 3-1):

a) **Base Etch** which defines the STJs and leads. This turned out to be the most critical step in the process. The chip was manually stirred in a wet chemical etchant for a short, fixed time and then immersed in an etch stop and rinsed. The etching step lasted for about 7 seconds but the impression was that it was not very

well controlled, partly because of the very short etching time and because of the exact stoichiometry required for the etchant. In order to improve the repeatability of this process, a dry Reactive Ion Etch (RIE) route was tried but never resulted in good low-leakage devices. The base-etch step was concluded by an O_2 ash, which removed the remaining photoresist.

b) **Mesa etch** which removes the top layers and oxide barrier to form the leads and was achieved by RIE using CF_4/O_2 for 45 seconds. Resist was then removed by flood-exposure with UV light and developing.

c) **Snip** which is an etch of the base film, in preparation of the Nb plug deposition. It interrupts the Ta contact in the base film between pixels. This step was achieved by CF_4 RIE for 48 seconds.

d) **Passivation** is done by sputter deposition of Silicon Oxide over the complete chip. For good insulation, the SiO_2 thickness is equal to the trilayer thickness plus 150-200nm typically. Deposition time for S-CAM arrays is 85 minutes.

e) **Vias** are etched in the SiO_2 to allow for top contacts and bridges between base contacts. This is done with CHF_3 reactive ion etching for 8.5 minutes.

f) **Niobium** is deposited, patterned by lift-off technique for top and basefilm contacts. Prior to the deposition, the chip is cleaned for 30 seconds by ion beam milling. The Nb is sputtered for 45 minutes at room temperature. The step is completed by a CF_4 reactive ion etch for 94 seconds.

g) **AuCu** is deposited for top contacts. Prior to both depositions, the chip is cleaned by ion beam milling for 30 seconds. The AuCu is sputtered at room temperature for 2 minutes. Patterning is done by lift-off.

h) **AuCu** is deposited for back-chip coating on some chips. As previously, the chip is first cleaned by ion beam milling for 30 seconds. The AuCu is sputtered at room temperature for 2 minutes. Patterning is done by lift-off.

Table 3-1: Schematic representation of the TFG post-processing route.

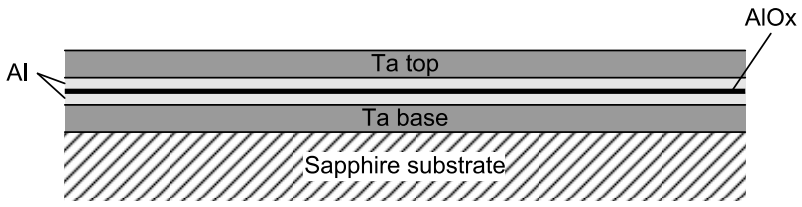

Trilayer

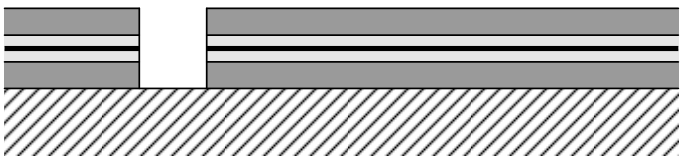

a) Base Etch

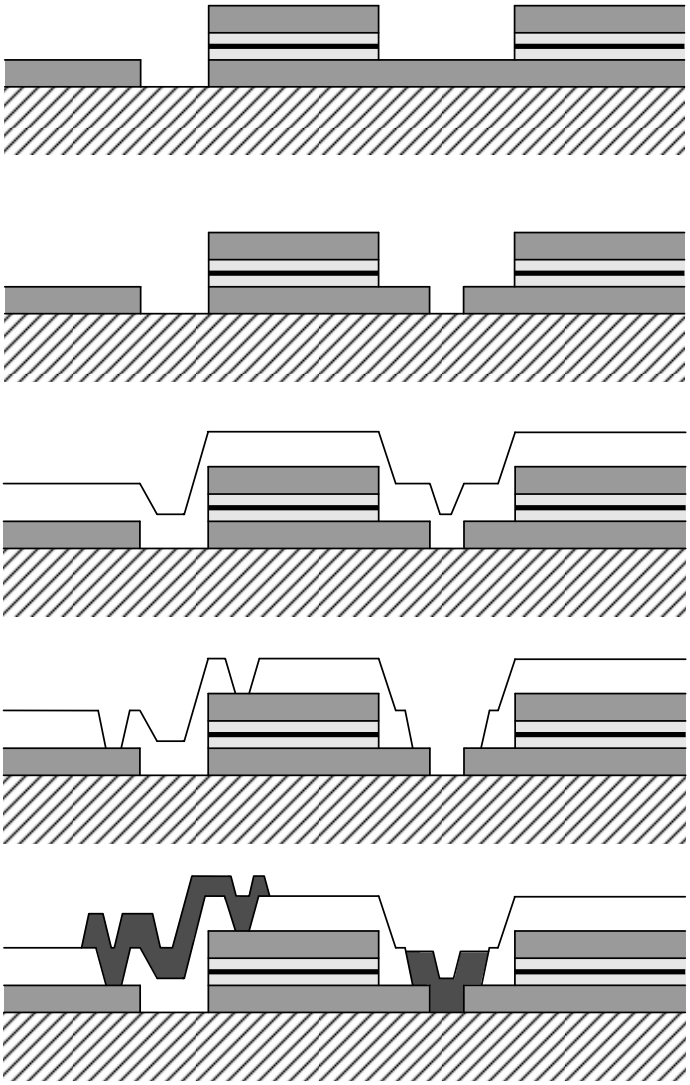

b) Mesa Etch

c) Snip

d) SilOx insulation

e) Vias

f) Nb Contacts and plugs

3.1.1 S-CAM3 mask details

Three mask iterations were required to finalize the design. All were based on our initial 12×10 closed-packed array concept of Ta/Al junctions with SiO_2 insulation and Nb wiring and plugs in base lead. The final mask set, M5.4c, has some modifications in wire widths to improve the yield. The original designs had too thin leads which lead to top and base lead loss during the Mesa stage and was caused by undercut during the base etch.

Besides the actual active pixel array, the masks contain various additional structures. For process diagnostics, Talystep, TEM and AFM structures are available. Alignment features are available on each mask layer and are designed such that they don't interfere with the first, base-etch, mask (e.g. through deposition of additional opaque material during the process). The backside of the chip can be coated with Au, one of the mask layers provides a 2mm diameter hole, centred around the detector area. This back layer is aligned with the front by means of an interrupted circle of 2mm outer diameter and 100μm width. The Au back layer can easily be aligned with the front base layer to within a few tens of micrometers.

All mask features are designed to snap to the MEBES format grid of 0.125μm. The array consists of four electrically separated blocks of 30 pixels. Each block is divided into three columns of 10 pixels and has one common base electrode. Each pixel has a separate top

contact. Electrical connection to the chip is made through 124 pads, 62 on each long side of the chip. The pads each have a dimension of 875×180μm^2 and are separated by 10μm. The contact pads are usually Au coated, although some chips were fabricated without Au deposition. The chip also has two gold coated clamping areas, each 1800×3500μm^2 in size, which allow, together with the golden back side for a good thermal contact to the detector holder.

The array junctions are square and measure 33.941×33.941μm^2. They are turned by 45° with respect to the main axes of the chip to provide easier supercurrent suppression. The separation between pixels is governed by the need to have Nb bridges in the base leads and amounts to 3.536μm. The gap is identical in the two directions, although it could have been reduced in the axis orthogonal to the base lead interconnects.

A snapshot of the corner of the array is given in Figure 3-1. The pixel is thus placed on a pitch of 37.477 which yields an 82% fill factor by design. The actual processing, in particular the base etch, will over-etch the trilayer edges by an amount of 0.5-0.7μm. The resulting fill factor is then 78±0.6%.

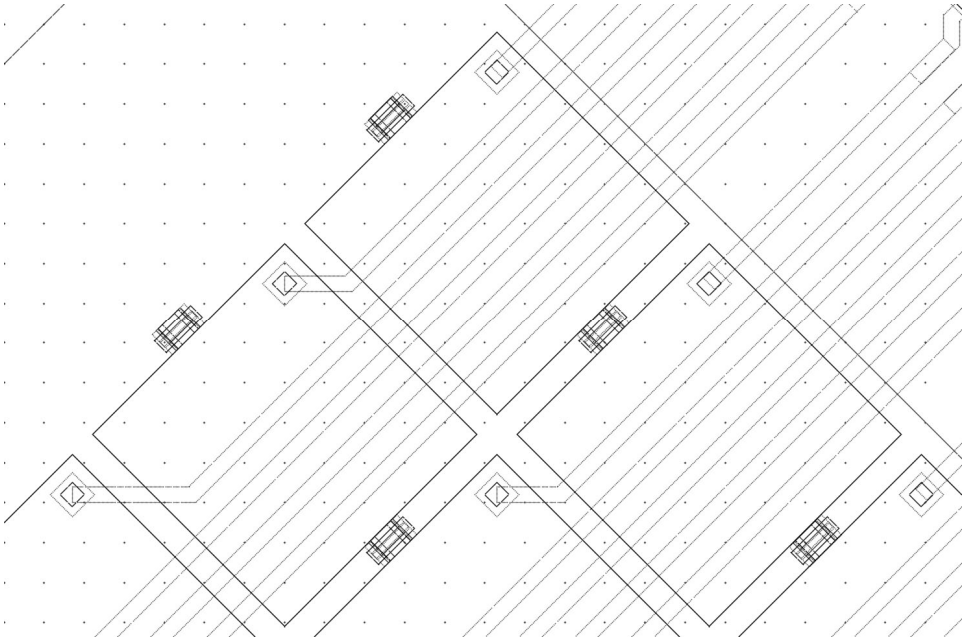

Figure 3-1: M5.4c mask details of the corner of the array. All layers are displayed.

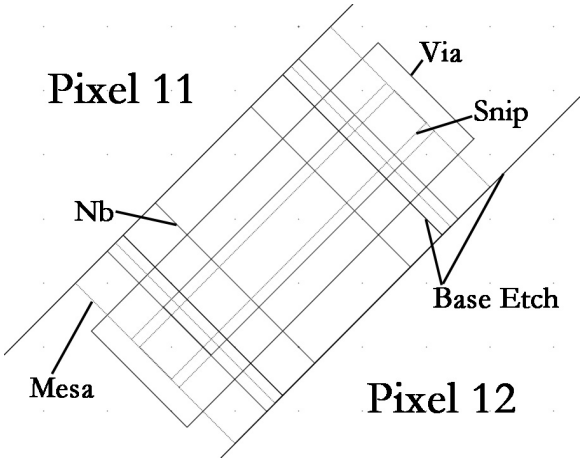

Figure 3-2: M5.4c mask details of the Niobium stub in the base lead.

Figure 3-2 shows the details of the base lead plug. The top left and bottom right areas are the edges of two adjacent pixels of a same column. The labels refer to the edges of the various process steps. For instance, the base etch will define a 3.536μm wide trilayer interconnect. The Mesa etch spans the complete interpixel gap and is 5.657μm wide, to allow for some mask misalignment (±1μm will be tolerated). The snip is as wide as the Mesa, but only 0.707μm long. After Silox deposition, a 6.364×2.121μm^2 Via is opened. Finally, a small Nb strip will provide the electrical contact between the two base layers.

3.1.2 TFG Array performance

Five trilayers were produced for the development of the S-CAM3 arrays, KJL410, KJL439, KJL476, KJL477 and KJL480. All trilayers consisted of 100nm base Ta film, 30nm Al, ~1nm AlOx, 30nm Al, 5nm Nb seed layer and 100nm top Ta film, with the exception of KJL410 which did not have the Nb seed.

A summary of the film properties of the three relevant runs is given in Table 3-2. The residual resistance ratios are corrected for the film thickness, and normalized to 100nm thickness. The normal resistance values are a direct measure of the barrier transmisivity. The chips were tested for leakage at the manufacturer's. In order to save testing time, only 16 pixels of the arrays were measured. Devices were classified as low-leakage if at least 15 of the 16 detectors had low sub-gap currents. These were then fully measured and analysed in our laboratories. In summary, a total of 18 arrays were produced, of which 16 were completely processed and only 6 showed good sub-gap current behaviour.

Table 3-2: Summary of S-CAM3 film depositions and chip production.

Multilayer	RRR	R_{nn}	Number of chips produced/completed			Number of low leakage arrays
			M1.2a	MNYa	M5.4C	M5.4C
KJL476	34	$2.9\times10^{-10}\Omega.m^2$	1/1	2/2	5/3	2
KJL477	33	$2.8\times10^{-10}\Omega.m^2$	1/1	1/1	8/8	3
KJL480	31	$3.2\times10^{-10}\Omega.m^2$	1/1	1/1	5/5	1
Total			3/3	4/4	18/16	6

We shall now review the detailed performances of these six arrays. We chose to display all the devices to show the variability of the various performance indicators. For each of them, we summarize the responsivity map in e^-/eV (black areas are dead pixels); the correlation between responsivity and subgap current measured at 600mK; the responsivity per pixel; the responsivity distribution, the pulse decay time versus responsivity and the pulse decay time distribution. The measurements were performed in our test cryostat, where only 32 pixels could be characterized at a time, hence the four sets of points in the scatter plots.

3.1.2.1 KJL476.8

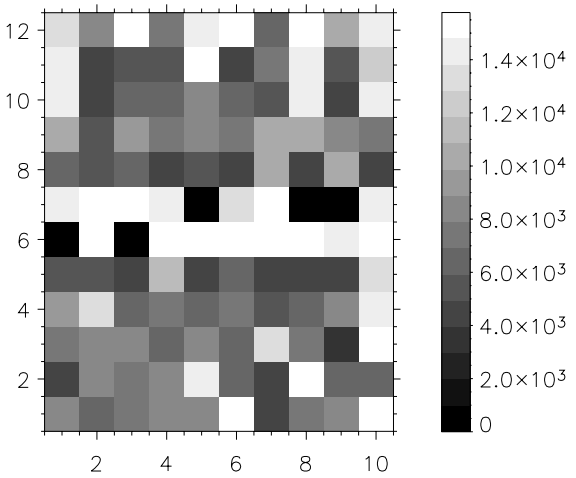

Figure 3-3: Responsivity map in e^-/eV.

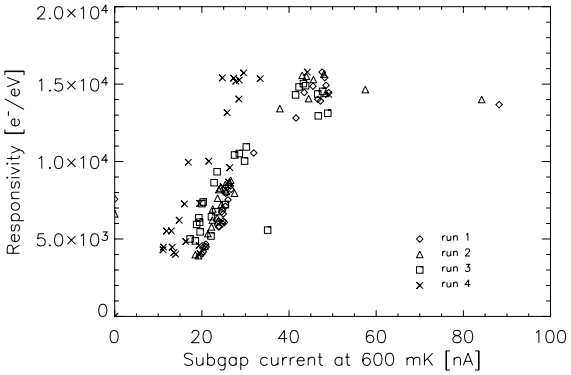

Figure 3-4: Correlation of responsivity and subgap current for all pixels.

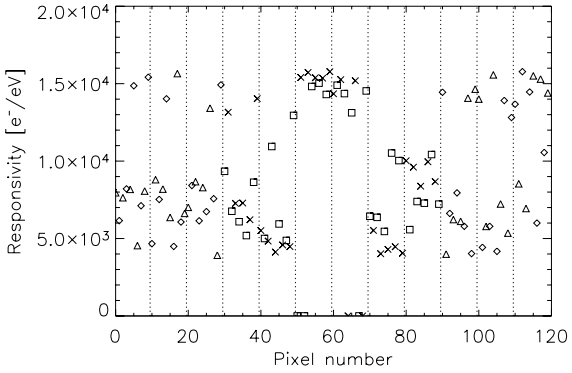

Figure 3-5: Responsivity of all pixels.

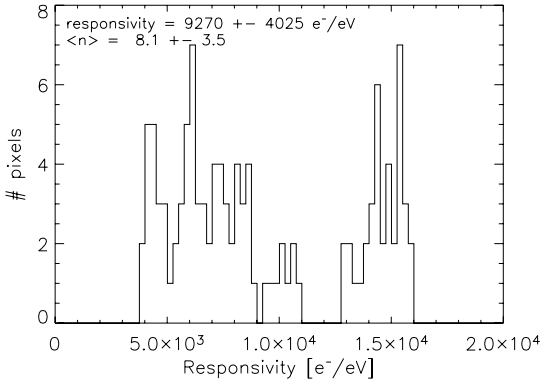

Figure 3-6: Histogram of pixel responsivity.

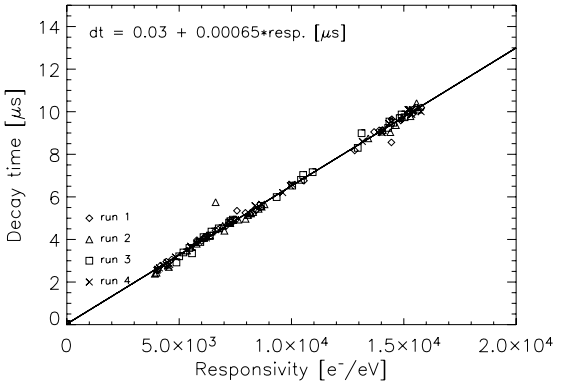

Figure 3-7: pulse decay time versus responsivity for all pixels.

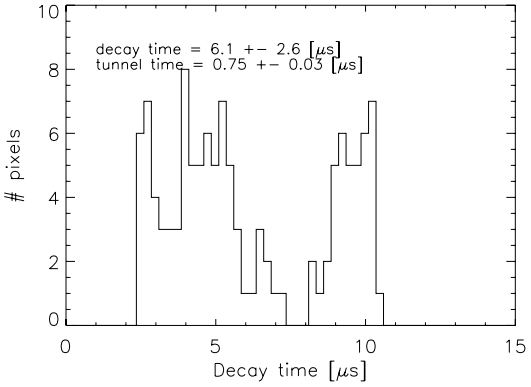

Figure 3-8: Histogram of pixel pulse decay time.

This device has five bad pixels and two interconnected pixels. The bad pixels are all concentrated in the middle two lines. The responsivity distribution is broad and shows two separate regions, where it appears that the higher responsivities are mostly situated in the centre two lines. The two interconnected pixels appear in Figure 3-4 at twice the nominal current, as expected. The same figure shows that the responsivity is correlated with the subgap current at 600mK, a good explanation for this has not been identified yet. Figure 3-7 shows an excellent

correlation (ρ=0.9988) between pulse decay time and responsivity, indicating a constant tunnel time and uniform tunnel barrier.

3.1.2.2 KJL476.9

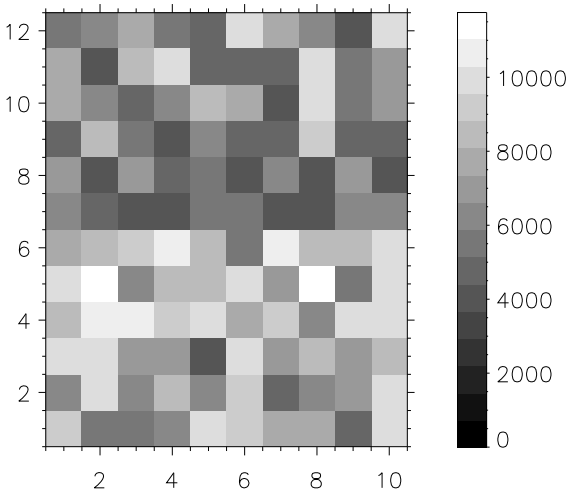

Figure 3-9: Responsivity map in e^-/eV.

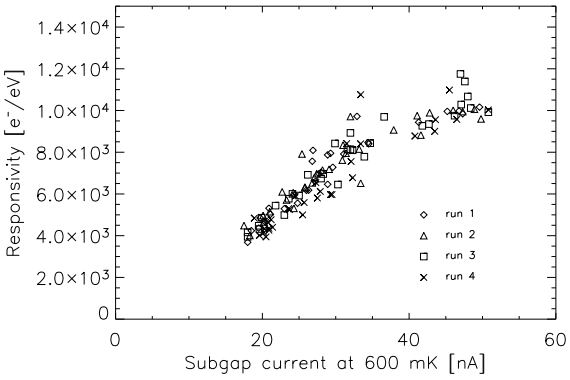

Figure 3-10: Correlation of responsivity and subgap current for all pixels.

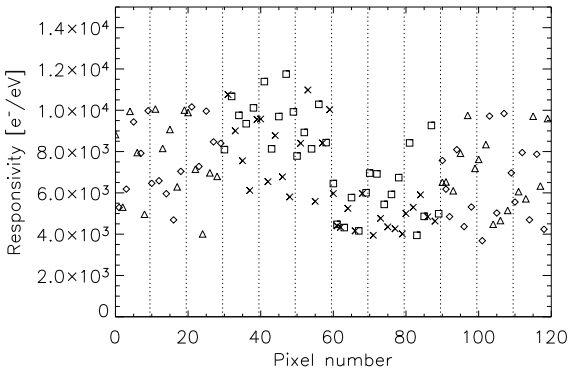

Figure 3-11: Responsivity of all pixels.

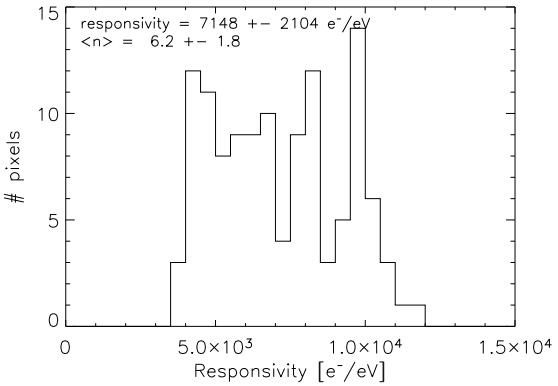

Figure 3-12: Histogram of pixel responsivity.

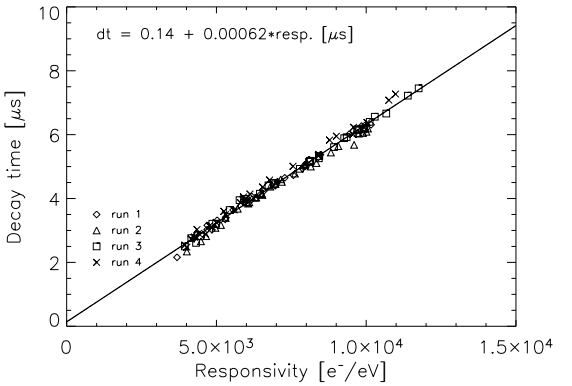

Figure 3-13: pulse decay time versus responsivity for all pixels.

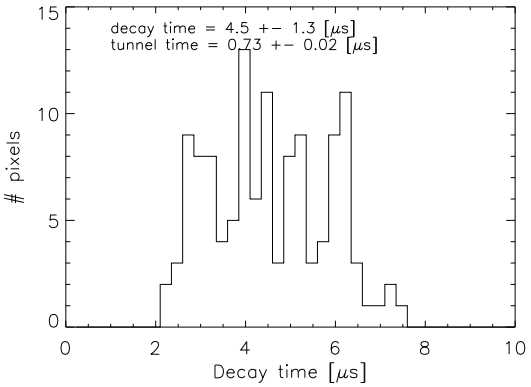

Figure 3-14: Histogram of pixel pulse decay time.

KJL476.9 is fully functional and has no interconnected pixels. The responsivity distribution is again broad and the top half has clearly a lower average than the bottom half. Responsivity is again correlated with the subgap current at 600mK and pulse decay time.

3.1.2.3 KJL477.5

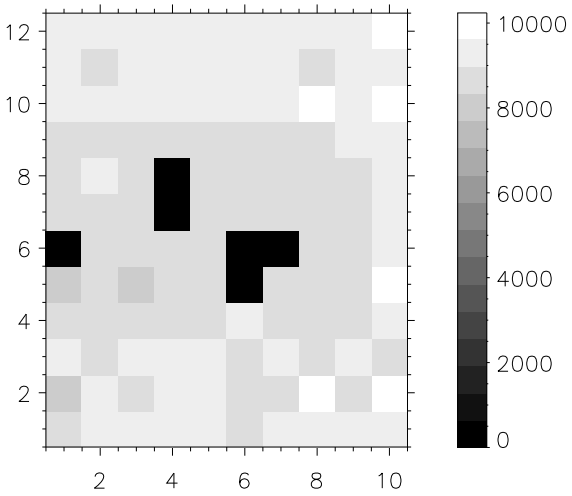

Figure 3-15: Responsivity map in e^-/eV.

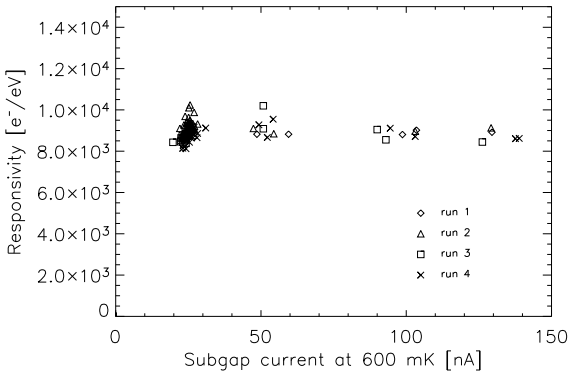

Figure 3-16: Correlation of responsivity and subgap current for all pixels.

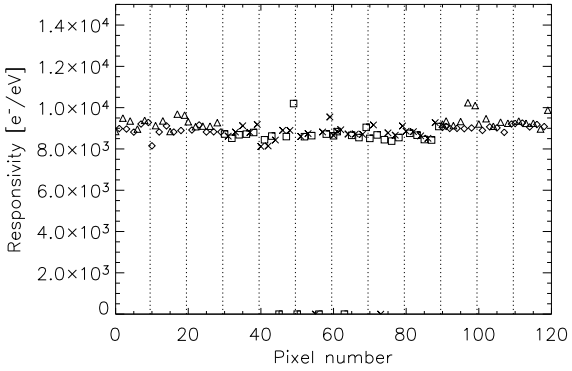

Figure 3-17: Responsivity of all pixels.

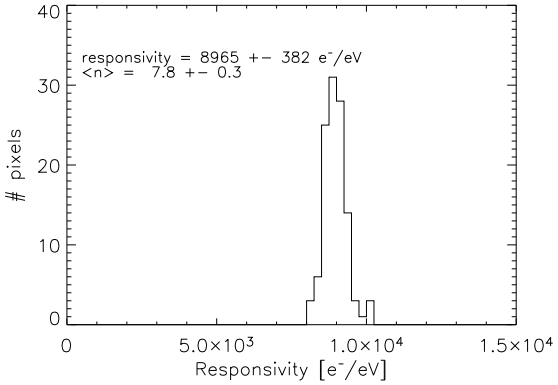

Figure 3-18: Histogram of pixel responsivity.

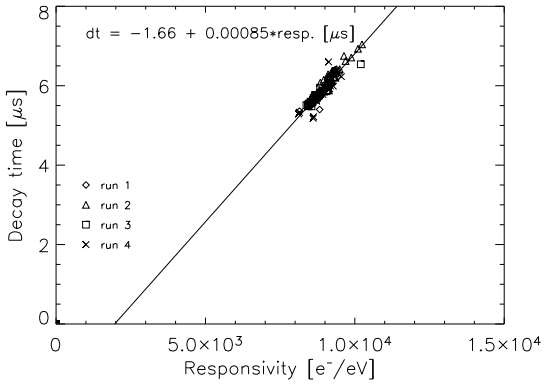

Figure 3-19: pulse decay time versus responsivity for all pixels.

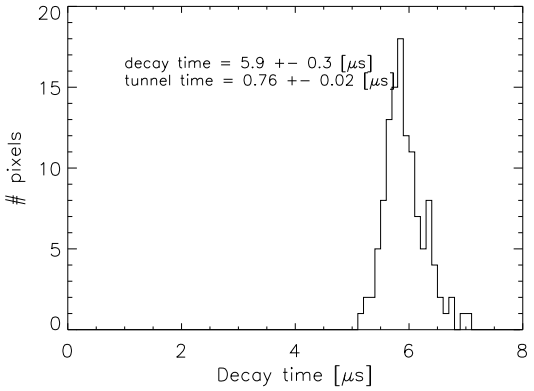

Figure 3-20: Histogram of pixel pulse decay time.

This device has six defective pixels, again concentrated in the middle of the array. In addition, it has one group of five, two groups of four and five groups of two connected pixels. These are recognizable as separate clusters at twice, four and five times the nominal sub-gap current in Figure 3-16. The responsivity is, however, much more uniform with a standard deviation of only 4.3%. The average responsivity value is similar to KJL476.8.

3.1.2.4 KJL477.8

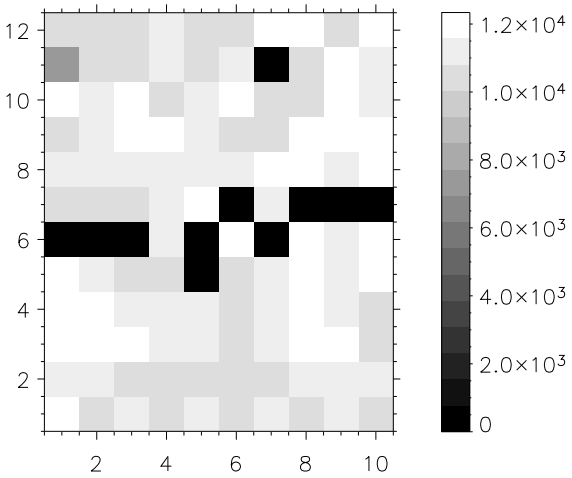

Figure 3-21: Responsivity map in e^-/eV.

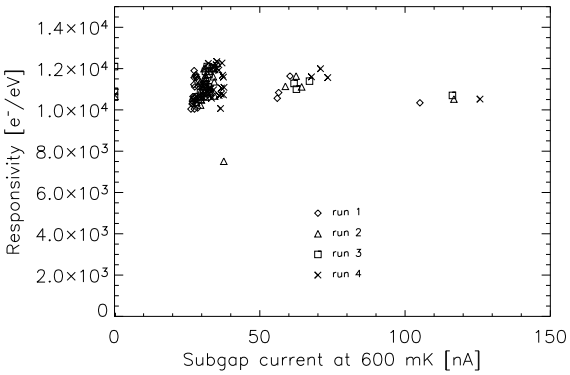

Figure 3-22: Correlation of responsivity and subgap current for all pixels.

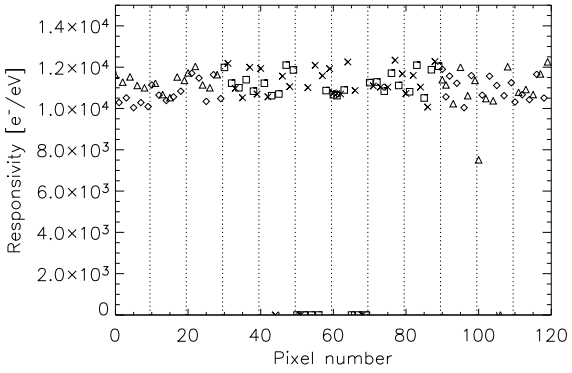

Figure 3-23: Responsivity of all pixels.

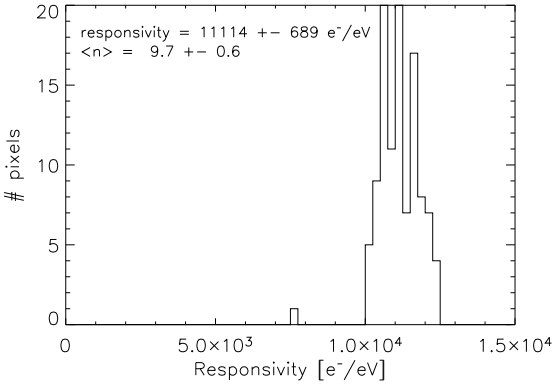

Figure 3-24: Histogram of pixel responsivity.

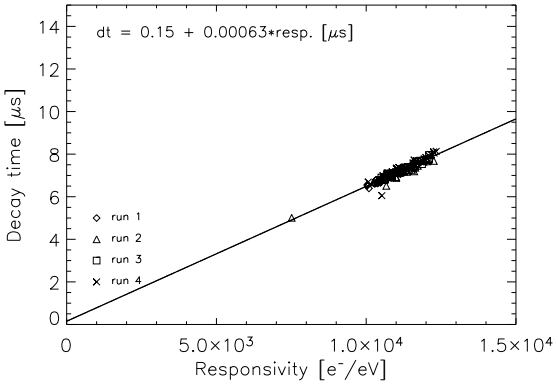

Figure 3-25: pulse decay time versus responsivity for all pixels.

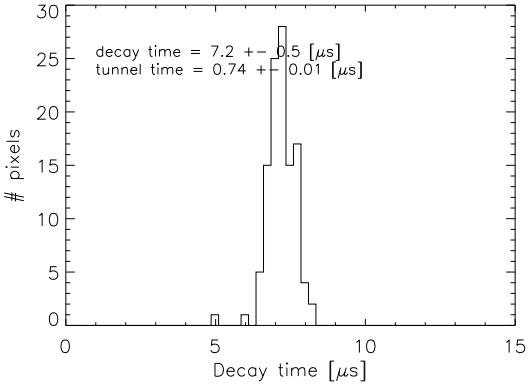

Figure 3-26: Histogram of pixel pulse decay time.

This chip has 11 bad pixels, also concentrated around the middle lines. There are six groups of two and one group of four interconnected pixels. The responsivity distribution is again narrow (6.2% standard deviation). Because of this narrow distribution, there is no correlation to be found between the subgap current at 600mK and the responsivity. It should be noted that the average subgap current at 600mK is 30.5nA, almost half the value of KJL476.9 pixels of similar responsivity.

3.1.2.5 KJL477.10

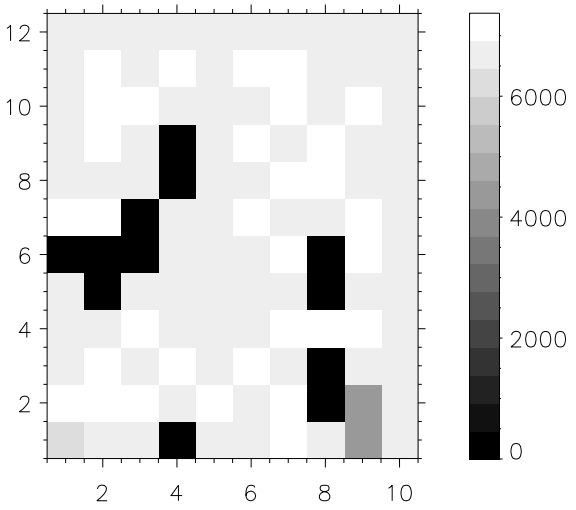

Figure 3-27: Responsivity map in e^-/eV.

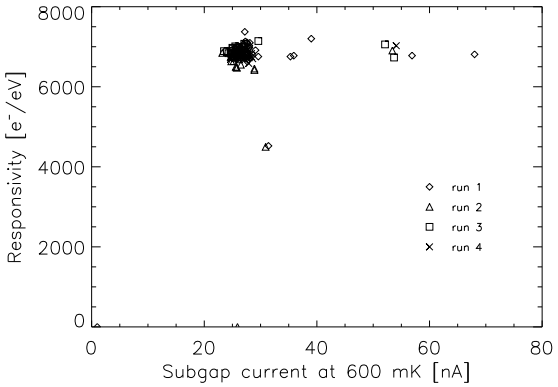

Figure 3-28: Correlation of responsivity and subgap current for all pixels.

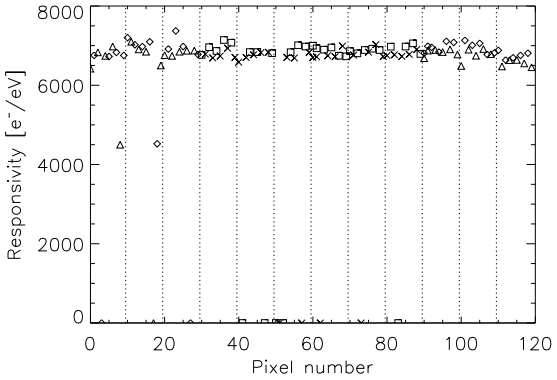

Figure 3-29: Responsivity of all pixels.

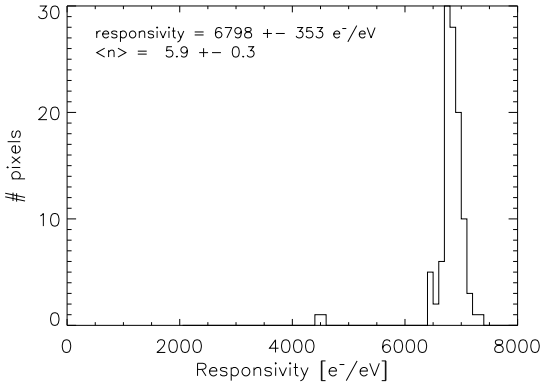

Figure 3-30: Histogram of pixel responsivity.

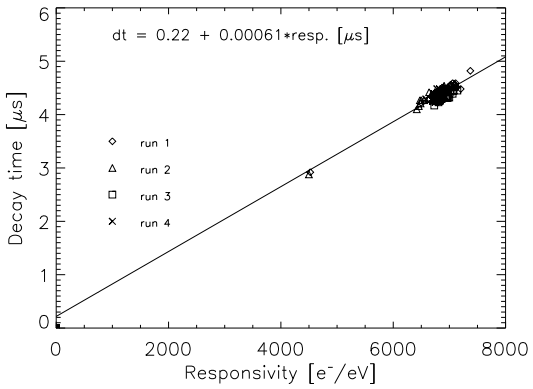

Figure 3-31: pulse decay time versus responsivity for all pixels.

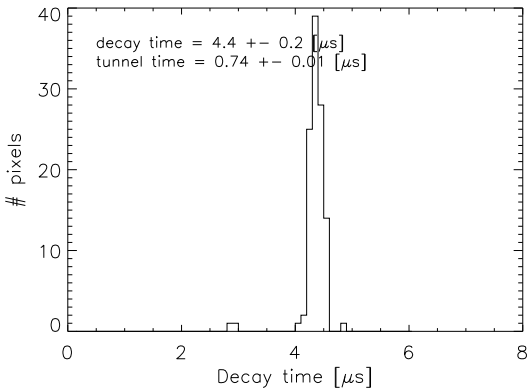

Figure 3-32: Histogram of pixel pulse decay time.

KJL477.10 has 10 bad pixels and three groups of two interconnected pixels. Although the responsivity is rather low, the lowest of this set, it is very uniform with a standard deviation of 5%.

3.1.2.6 KJL480.5

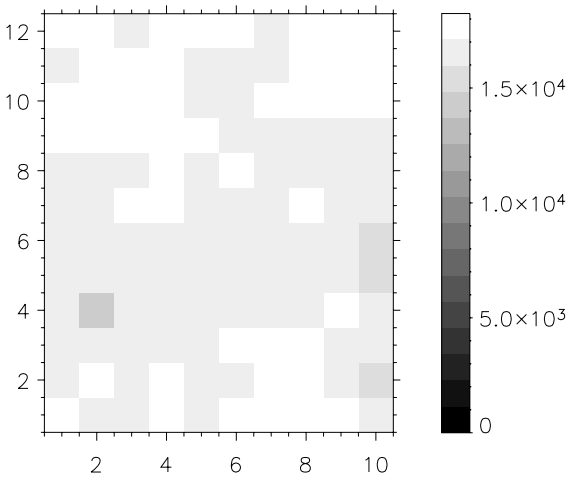

Figure 3-33: Responsivity map in e^-/eV.

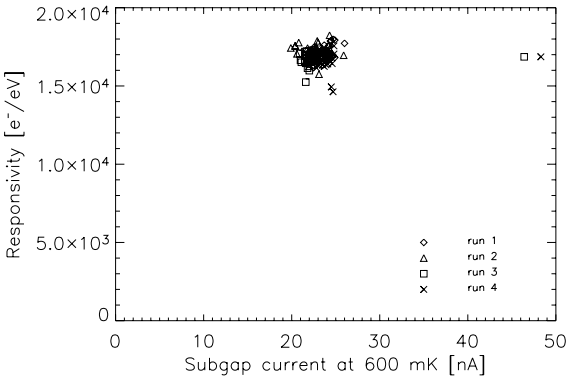

Figure 3-34: Correlation of responsivity and subgap current for all pixels.

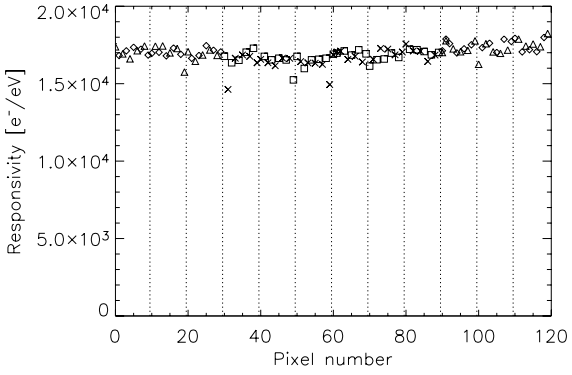

Figure 3-35: Responsivity of all pixels.

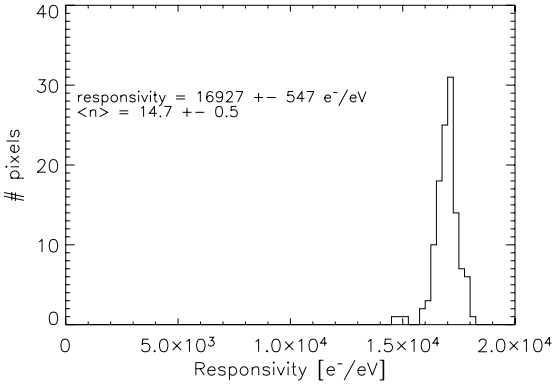

Figure 3-36: Histogram of pixel responsivity.

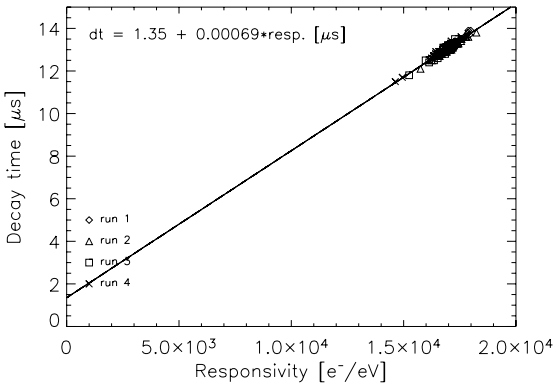

Figure 3-37: Pulse decay time versus responsivity for all pixels.

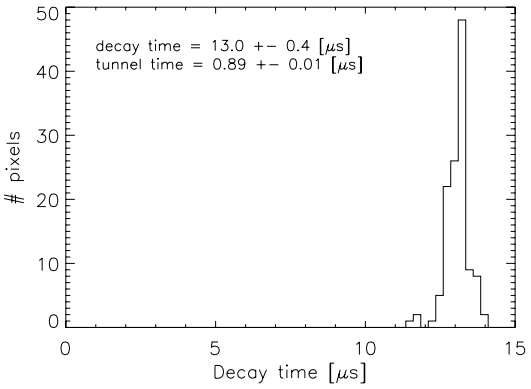

Figure 3-38: Histogram of pixel pulse decay time.

KJL480.5 was by far the best array produced by TFG. It was fully functional with only 2 interconnected pixels. The responsivity was highest and the most uniform of the set.

3.1.2.7 Performance summary and Array selection

A summary of the performances of all arrays is given in Table 3-3. At this stage, the choice of the array to be used for S-CAM3 was rather obvious: KJL480.5 had 120 functional pixels, the highest responsivity, guaranteeing the best possible energy resolution, and best responsivity uniformity. A micrograph of the array is shown in Figure 3-39. Details of the pixels, top wiring and base Niobium plugs are clearly visible in Figure 3-40.

Table 3-3: Summary of array characteristics.

	KJL476.8	KJL476.9	KJL477.5	KJL477.8	KJL477.10	KJL480.5
# of bad pixels	5	0	6	11	10	0
# of interconnected pixels	2	0	23	16	6	2
# of bad pixels, after FIB	n/a	n/a	5	11	n/a	45
# of interconnected pixels, after FIB	n/a	n/a	20	2	n/a	0
Responsivity [e^-/eV]	9270±4025	7148±2104	8965±382	11114±689	6798±353	16927±547
Decay time [μs]	6.05±2.62	4.56±1.31	5.93±0.35	7.19±0.46	4.35±0.23	13.04±0.39
Tunnel time [μs]	0.75±0.03	0.73±0.02	0.76±0.02	0.74±0.015	0.74±0.012	0.89±0.007
<n>	8.1±3.5	6.2±1.8	7.80±0.33	9.67±0.60	5.91±0.31	14.73±0.48

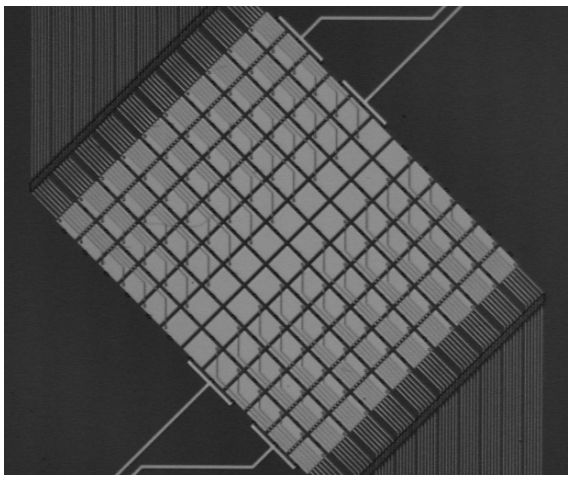

Figure 3-39: Micrograph of KJL480.5.

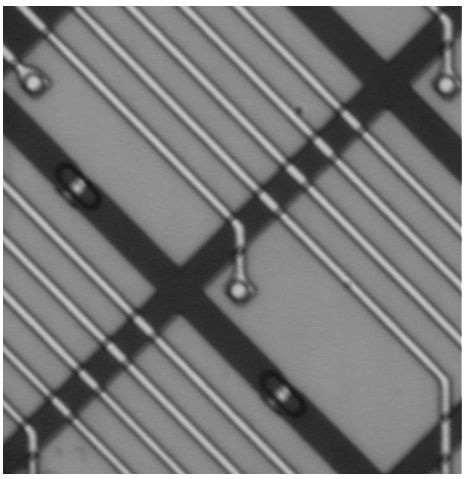

Figure 3-40: Detail of pixels where top wiring and base Nb plugs are visible.

KJL480.5 only had one small beauty stain: it had two interconnected pixels, due to a piece of Niobium shorting the contact pads (see Figure 3-41). Presumably, this piece was not properly removed during the lift-off and was later covered by the AuCu. In order to fix that small error, we investigated various possibilities of removing the short.

Although we had good experience with a pulsed laser, which we used in previous repairs, this was not available after being dismantled. Mechanically scratching the metal was considered too difficult because of the small, 10μm gap between pads. The remaining option was the use of a Focussed Ion Beam (FIB). Because of the risk of charging and eventual breakdown of the sensitive junctions, we manufactured a special sample holder and screen. The metal screen was fixed close to the surface of the chip and covered the active area, effectively protecting the array and most of the wiring.

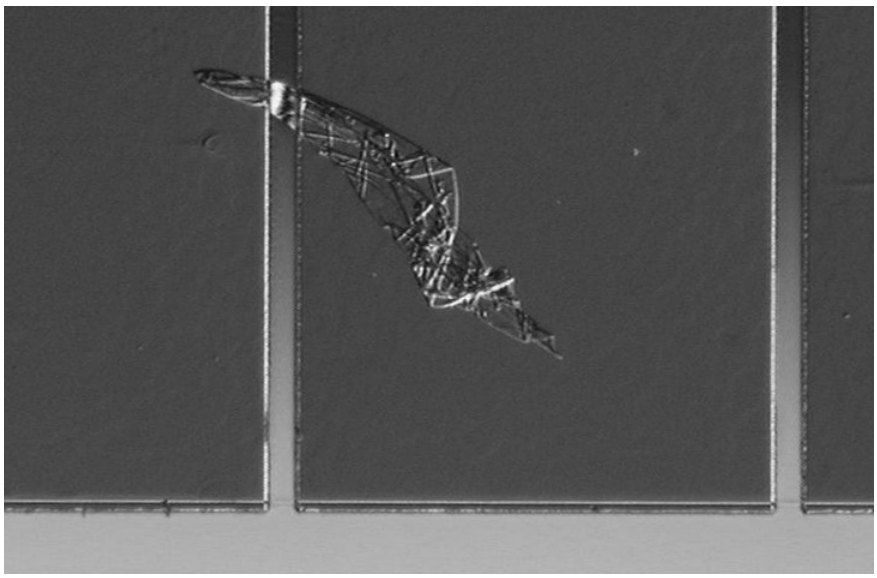

Figure 3-41: Niobium short between KJL480.5 contact pads.

In order to validate the procedure, we first tried it out on two devices: KJL477.5 and KJL477.8. We successfully removed 3 shorts on KJL477.5, but measured a responsivity degradation of ~10%. Since more than a year had elapsed between the first screening and the post-FIB measurement, we could not conclude whether this was due to the FIB milling or an ageing effect. We therefore subjected a second device to the FIB milling procedure. Most of the shorts on device KJL477.8 were due to a scratch over a large fraction of the pads on one side of the chip. Figure 3-42 shows an example of such a short. Figure 3-43 is the result after FIB treatment of the area. In total, 31 suspected areas were treated, successfully removing 8 shorts. One short was too close to the array and could not be repaired. Prior to the FIBM, 24 pixels of the array were screened and the responsivity was found to have decreased from the original June 2002 screening value of 11154±527e^-/eV (average and standard deviation of these 24 pixels) to 8457±516 e^-/eV immediately prior to and 8695±567 e^-/eV, after the FIBM in October 2003. We concluded therefore that the FIBM had not caused any degradation and proceeded with the processing of KJL480.5.

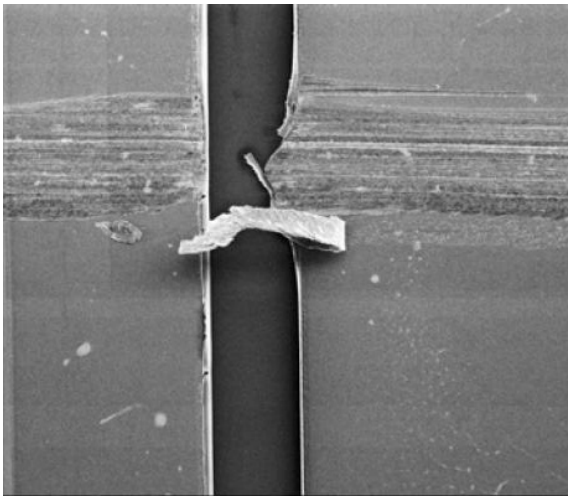

Figure 3-42: Short between tracks on KJL477.8, induced by scratching of the surface.

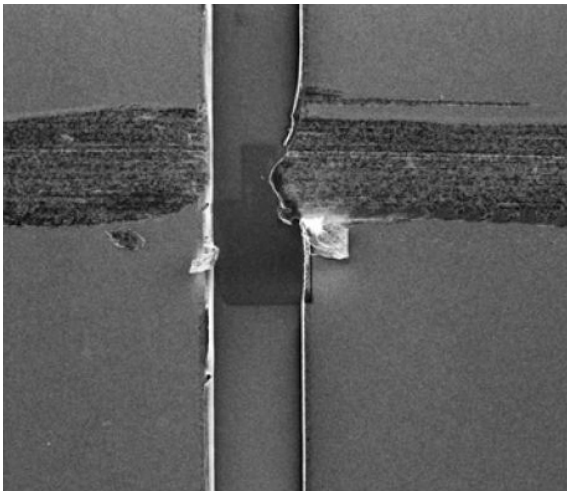

Figure 3-43: Same area on KJL477.8, after removing the metallic short by FIB.

Although we took all precautions as for our trial runs, the result of the FIBM on this device was dramatic. The FIB itself was most likely not the problem, but rather a static discharge during handling, as a consequence of which we lost a vast amount of the array. A micrograph of the chip's active area, seen in transmission through the substrate is shown in Figure 3-44. The metallic contact between the pads was successfully removed but at an exorbitant cost: 45 pixels were lost. A static discharge evaporated their base lead interconnects or top contact wires.

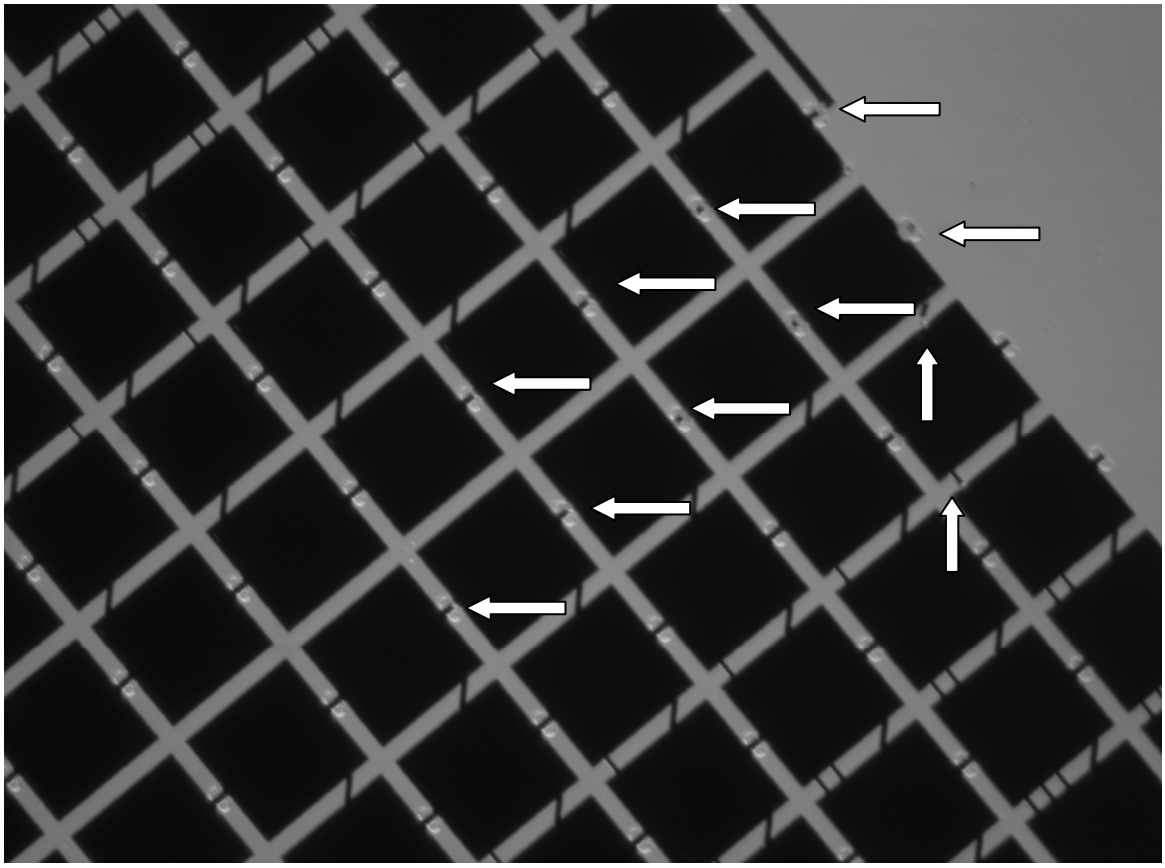

Figure 3-44: Interrupted base lead contacts after FIBMilling KJL480.5.

The area affected can be identified by the black pixels in Figure 3-45, which is a responsivity map measured after the FIB surgery. The array is now split into two functional blocks. The responsivity, plotted for each pixel in Figure 3-46, has dropped on average by 23%. Theoretically, this drop could be explained by ageing, as for KJL477.8. Figure 3-47, however, shows a double distribution while Figure 3-45 clearly locates the lower responsivity pixels in the vicinity of the dead pixels. We must conclude that, while ageing has most likely affected the device, the FIB milling caused additional responsivity decrease and spread. A summary comparison of the performance of the array pre- and post-FIB milling is given in Table 3-4.

A real cause of the responsivity degradation has not been identified. Nevertheless, Figure 3-48 still shows a clear correlation of pulse decay time with responsivity. The calculated tunnel times before and after surgery are virtually equal, indicating that the tunnel barrier is not affected, but rather a reduction of quasiparticle lifetime is the sole contributor to the decrease of responsivity. The cause for this effect could possibly be found in material electro-migrating into the sensitive area of individual STJ pixels, creating more local traps. This effect could have been more severe in the vicinity of the broken wires where more current has flown, affecting more the devices in the periphery of the dead pixels. A similar but slower effect, namely contact material diffusion, could explain the uniform ageing of these devices as well.

Table 3-4: Performance summary of KJL480.5, pre- and post-FIB Milling

	Responsivity [e⁻/eV]	Pulse decay time [μs]	Tunnel time [μs]	<n>
Original 2002 screening	16927±547	13.04±0.39	0.89±0.007	14.73±0.48
Post-FIB milling 2003	13093±2503	9.97±1.79	0.88±0.014	11.4±2.2

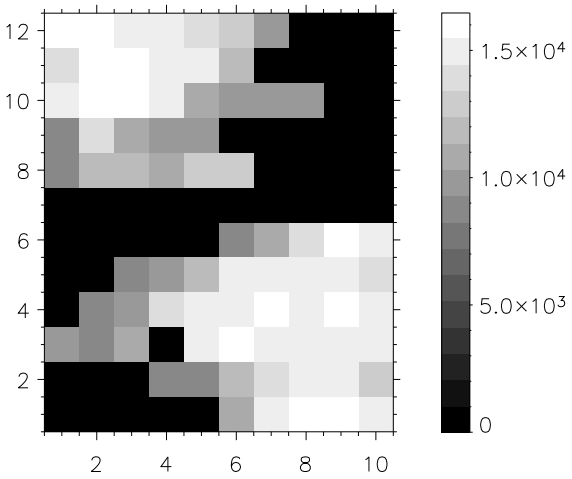

Figure 3-45: Responsivity map of KJL480.5, after FIBM.

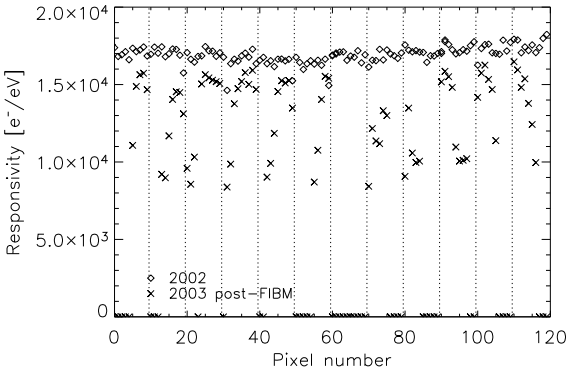

Figure 3-46: Responsivity per pixel, before (diamonds) and after (crosses) FIBM.

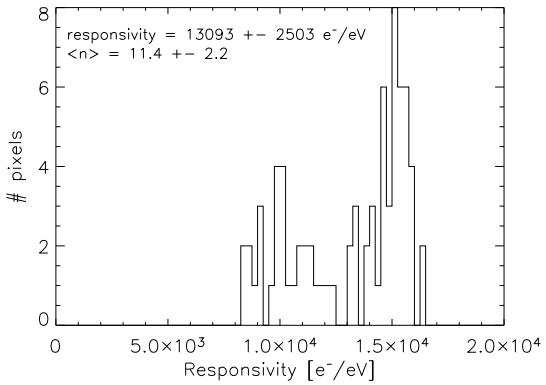

Figure 3-47: Responsivity distribution, post FIBM.

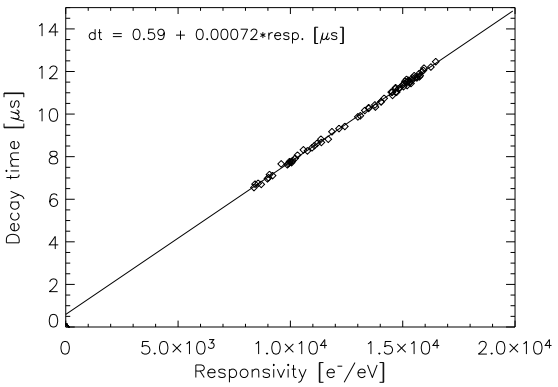

Figure 3-48: Pulse decay time as function of responsivity.

We now had the dilemma of still using this chip, or opt for the backup array KJL476.9. In order to understand why KJL480.5 was used as the first device on S-CAM3, we have to explain two more factors which influenced our choice. As we have seen in the introduction, it was important to increase the field of view of S-CAM. While our favourite array was now crippled, it still had a considerably larger field of view than our previous devices in S-CAM2. In particular, the two sensitive areas of the array could be used for source and background measurements, delimited by pixel coordinates ([6,1],[10,6]) and ([8,1],[5,12]) respectively. In addition, there was an area on the chip which had hardly been affected and still showed high resolution (pixel coordinates [6,2] to [9,5]); and would be used as the target area in the S-CAM observation campaign.

In order to compare the devices in terms of resolving power, both chips were measured in the S-CAM system. For each array, the magnetic field and bias voltage yielding the best average resolution were used. As we shall describe in paragraph 4.2, the S-CAM electronics allows the detector signals to be filtered with different filter frequencies. Figure 3-49 shows the resolving power obtained with KJL480.5 at a wavelength of 495nm as function of filter

frequency. The triangles represent the average over all pixels, whereas the squares are averages over the selected 4×4 source region mentioned above. The diamonds are the average noise values determined with an electronic pulser signal and should be referred to the right-hand scale. Error bars represent the standard deviation, while the lines are only a guide to the eye. A peak resolution of 10.0±0.6 is obtained for the selected area at a filter centre frequency of 9kHz. The average over the complete chip is then 9.0±1.2, with a minimum and maximum of 6.2 and 11.0 respectively. The electronics noise contribution is 0.22±0.04eV.

A similar plot is given in Figure 3-50 for device KJL476.9. The best average resolution of 6.0±1.1 is obtained at the filter centre frequency of 6kHz. The minimum and maximum pixel resolutions are 4.0 and 8.9 for this chip. The electronics noise had a value of 0.38±0.09eV. This higher value compared to KJL480.5 is a direct consequence of the reduced responsivity of this array.

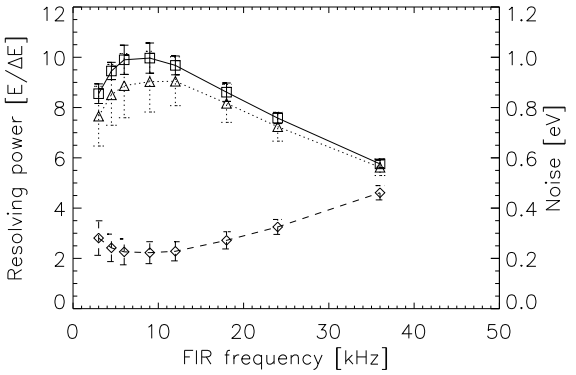

Figure 3-49: Resolving power as function of filter frequency for KJL480.5, averaged over all pixels (triangles) and a selected area (squares). Diamonds are average noise levels (right hand scale).

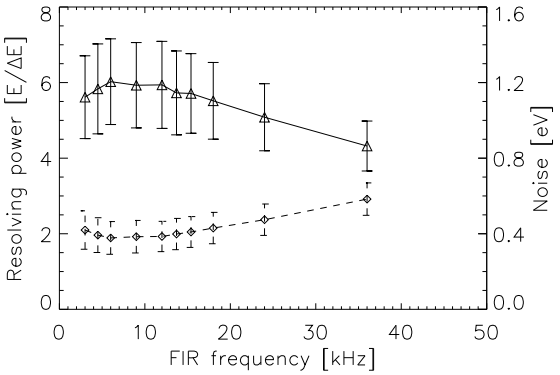

Figure 3-50: Resolving power as function of filter frequency for KJL476.9, averaged over all pixels (triangles). Diamonds are average noise levels (right hand scale).

Figure 3-51 shows the resolution of KJL480.5 as function of wavelength (triangles), using the best settings for all parameters, bias voltage, magnetic field and filter frequency. Let us now consider the empirical resolution function:

$$R = \frac{E}{\Delta E} = \frac{\lambda}{\Delta \lambda} = \left[2.355 \sqrt{\frac{\varepsilon F'}{E} + \frac{\sigma_n^2}{E^2}} \right]^{-1} \qquad 3\text{-}1$$

where E is the incident photon energy, σ_n the noise variance and F' an equivalent noise factor which encompasses Fano and tunnel noise (F+G). Using the measured resolution and noise values, a best-χ^2 fit yields a value F'=2.45. As we have seen in the derivations of chapter 2.5, this value is considerably higher than what would be theoretically expected. A possible explanation could be the presence of local traps causing a non-uniform response over the pixels [72]. The result of the fit is represented by the dash-dot line in the plot.

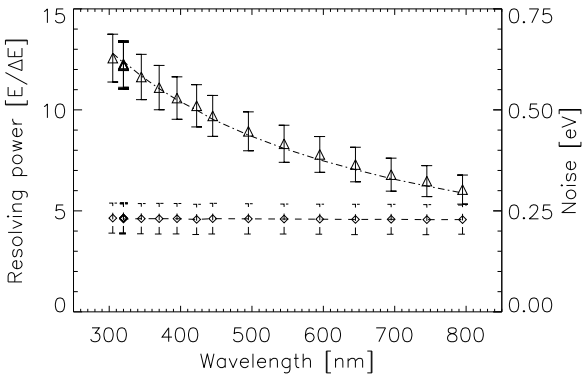

Figure 3-51: Wavelength dependency of resolving power for KJL480.5 (triangles). Diamonds are electronic noise measurements using the right-hand scale.

The last determining factor for device selection had to do with bias stability. As we shall see in section 4.1, the electronic circuits need to bias the devices with a stable voltage between the Josephson current and Fiske resonances. A superposition of I-V curves of all pixels in KJL480.5 and KJL476.9 are given in Figure 3-52 and Figure 3-53 respectively. The first Fiske resonance for the KJL480.5 devices is at about 300μV, while for the KJL476.9 devices, it is 50μV lower. In addition, the Josephson suppression is slightly more effective for KJL480.5. This lead to a wider bias range (75-250μV, compared to 90-180μV for KJL476.9) and more stable operating conditions for this array.

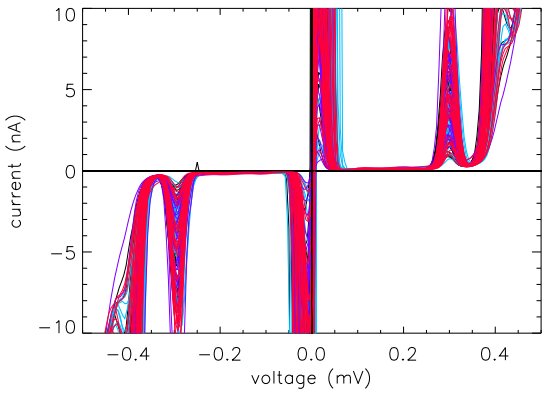

Figure 3-52: IV curves of all KJL480.5 pixels.

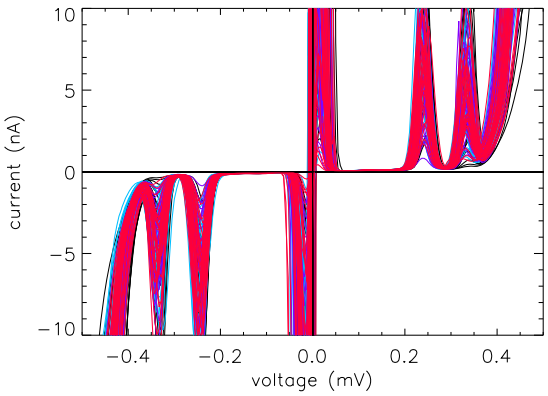

Figure 3-53: IV curves of all KJL476.9 pixels.

In summary, KJL480.5 was used for the first S-CAM3 campaign, S-CAM3a. During this observing run it was noticed that, although we now had a good simultaneous source and background sampling, it was still difficult to perform accurate photometry as some light could spill over the selected detector area. It became obvious that a larger active FOV was more important a parameter than resolution. KJL476.9 was therefore chosen for the second campaign, S-CAM3b.

3.2 MFab STJ Fabrication

As we were notified in 2002 that OI TFG would stop their activities in STJs, we turned to Cambridge MicroFab Ltd (MFab [73]) also located near Cambridge, UK for further detector developments. Mfab was a natural choice at the time, since they had been involved for many years in our STJ programme and in particular in the development of STJs with alternative, lower energy-gap materials. With the combined past experience at MFab as well as in ESTEC, it was relatively easy to start up a Tantalum/Aluminium processing route.

The processing at MFab is also done on 2" diameter and 0.5mm thick r-plane Sapphire substrates from Kyocera. The multilayer is deposited under ultra-high vacuum in a dedicated deposition system using DC-magnetron sputtering. This system contains four processing stations, three of which are loaded with high purity Tantalum, Niobium and Aluminium targets respectively while the last station is equipped with an Ion Beam Miller. The Ta and Nb targets are from Plansee [74], while the Al target is purchased from TMI [75]. Epitaxial Tantalum is deposited on a substrate heated to 810ºC at a rate of 0.39Å/s. Growth rate and substrate temperature were optimized for best RRR values. The Argon pressure was also optimized by depositing Ta on Kapton films at room temperature and selecting the setting for least stress. Film growth proceeds with an Aluminium layer deposition at -120ºC and 0.5Å/s. Barrier oxidation is then performed at 60ºC for two hours under 187mbar oxygen pressure. Cap Aluminium is then deposited under the same conditions as for the base Al film and is then followed by the cap Tantalum growth at 0ºC. Following the experience with TFG, a Niobium seed layer is not used.

The post-processing of the chips is done at wafer level. The general process is very similar to the TFG one, except that there is no specific 'snip' step, as this is included in the base etch (step 'c' in Table 3-1) and there is no gold coating on either side of the chips.

a) **Base Etch** defines the STJs and leads. The areas are defined using a Shipley S1813 [76] photoresist and UV exposure with mask layer 1. The actual etch is split in three parts. First the top Tantalum is removed using plasma etching. The etchstop is optically determined, after which the wafer is rinsed and dried. The Aluminium and barrier layers are then removed using a wet etch for a total of ~45s. The surface is then cleaned using Ion Beam Milling for 3m before the base Tantalum is plasma etched. Finally, the resist is removed using SVC-14.

b) **Mesa etch** removes the top layers and oxide barrier to form the leads. This is achieved using the same process as for the base etch, but stopping at the base Tantalum.

c) **Passivation** is done by reactively sputtering Silicon from a high purity target in an O_2 atmosphere. The SiO_2 is typically grown to a thickness equal to the trilayer thickness plus ~160nm. Deposition time is 75 minutes.

d) **Vias** are etched using CHF_3 reactive ion etching for 22 minutes, for an oxide thickness of 440nm.

e) **Niobium** is deposited for top and basefilm contacts and patterned by lift-off technique. The Nb is sputtered for about 100 minutes at room temperature for a total thickness of ~230nm.

3.2.1 S-CAM3 Mask details

Since MFab processes at wafer level, we designed a mask set which encompassed various options. The full wafer mask, MF2K5, is represented in Figure 3-54. It includes two identical science chips (positions B2 and F2), eight arrays and several additional alignment and process verification structures. The science chips consist of a total of 29 STJs, ranging in size from 20×20 to 100×100μm^2. There are four different arrays:

a) Three off 10×12 pixel arrays (positions C3, D3 and E3), similar to the TFG arrays with a maximum of 6 wires crossing a device. The Nb wires are 1.5μm wide in the array area, on a pitch of 5.3μm. Each pixel is 33.25μm with an interpixel gap of 4.25μm, yielding a fillfactor of 78.6% (drawn). A corner of this standard array mask is represented in Figure 3-55. Notice that the plugs in this design are elongated in the direction of the channel between pixels. The base leads consists of small mesa'd stubs, 4.25μm wide and 2.82μm long, interconnected by a 2.25×16μm^2 Nb plug.

b) Two off 10×12 pixel arrays with alternative wiring (positions C2 and E2). It was thought that the wire density crossing the detectors would be problematic and this array design only has a maximum of 5 wires crossing a pixel. The wires are 1.5μm wide but now on a pitch of 6.2μm. In order to achieve this lower wire density, the array is organized in four blocks of 5×6 pixels. The disadvantage of this design is that it requires an interruption of the base contact between two blocks achieved by omitting the Nb plugs in the middle of the array. This implies that the pixels in the middle are not exact copies of the other pixels in the array. Nevertheless, since the other arrays were functional, we never tested this design in depth.

c) One close-packed 10×12 pixel array (position D2). Wire density is similar to the C3, D3 and E3 chips. In this case however, the interpixel gap was reduced to a minimum achievable with the current technology: 2.125μm. Because the base leads require a Niobium plug, the lithography required a 1.06×13.44μm^2 cut-out in the pixels at the level of the plug, leaving as much space as in the standard pixel case. Using the same pitch as before, the pixel width is now 35.38μm. The fillfactor of this array is thus 87% (drawn). Figure 3-56 shows a corner of the array design.

d) One double 8×8 pixel array (position F3), which could be used for a potential fibre-fed instrument (see section 7.3). The pixel design is essentially identical to the standard array. The only difference is the wiring separation of 6.3μm.

e) One DROID array consisting of four electrically isolated sections of 15 DROIDs each (position B3). Each DROID is 360μm long and 33.25μm wide, including the 33.25μm junctions at both ends. Device separation is 4.25μm in both directions. Each of the four groups is assembled as 5×3 DROIDs, which together form an array of 20×3 devices, covering a total area of 746×1089μm^2. For a description of the DROID structures, see section 7.1.

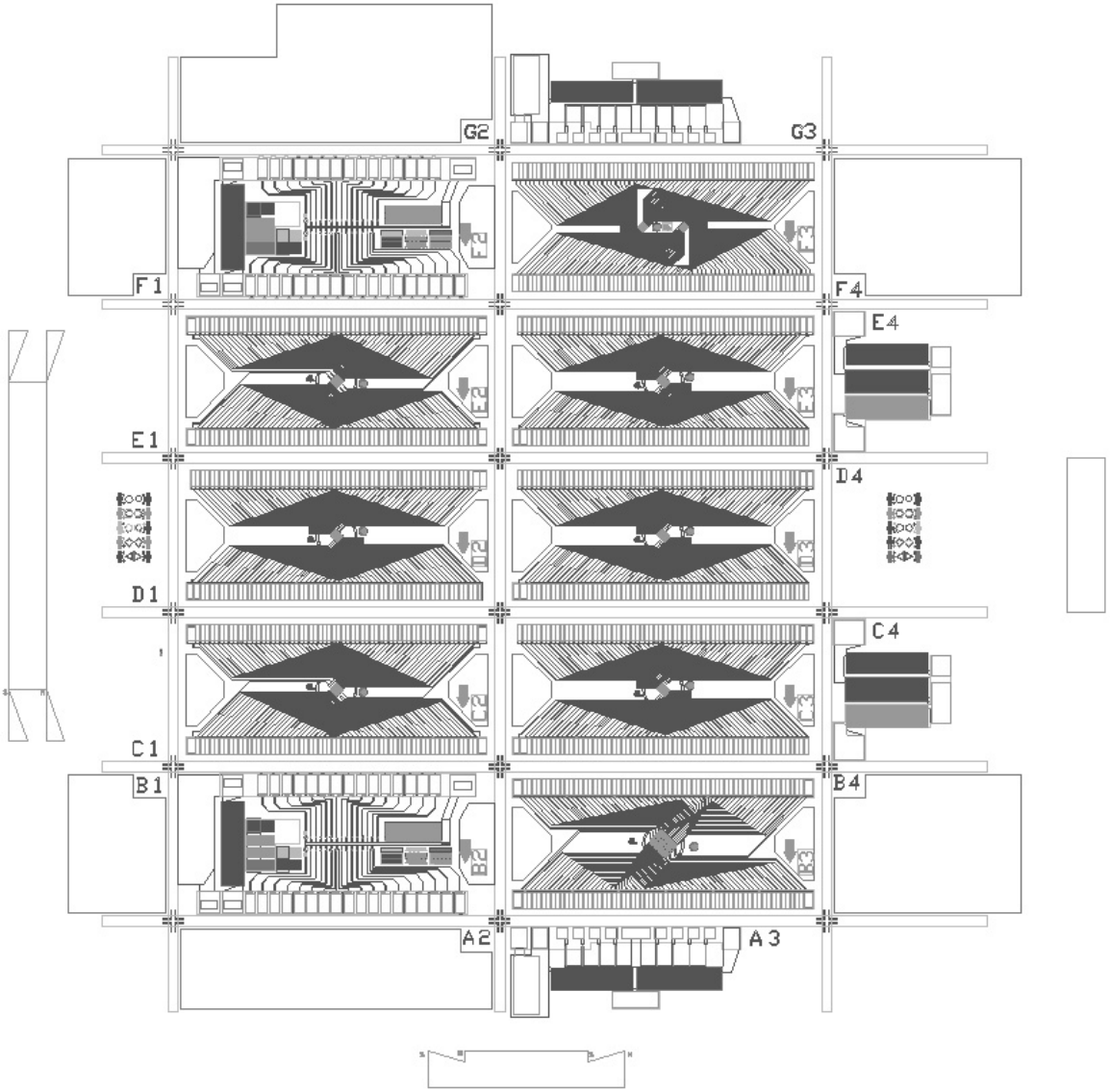

Figure 3-54: Full wafer mask set, all layers are displayed. Included are eight arrays, two science chips and additional process verification and alignment structures

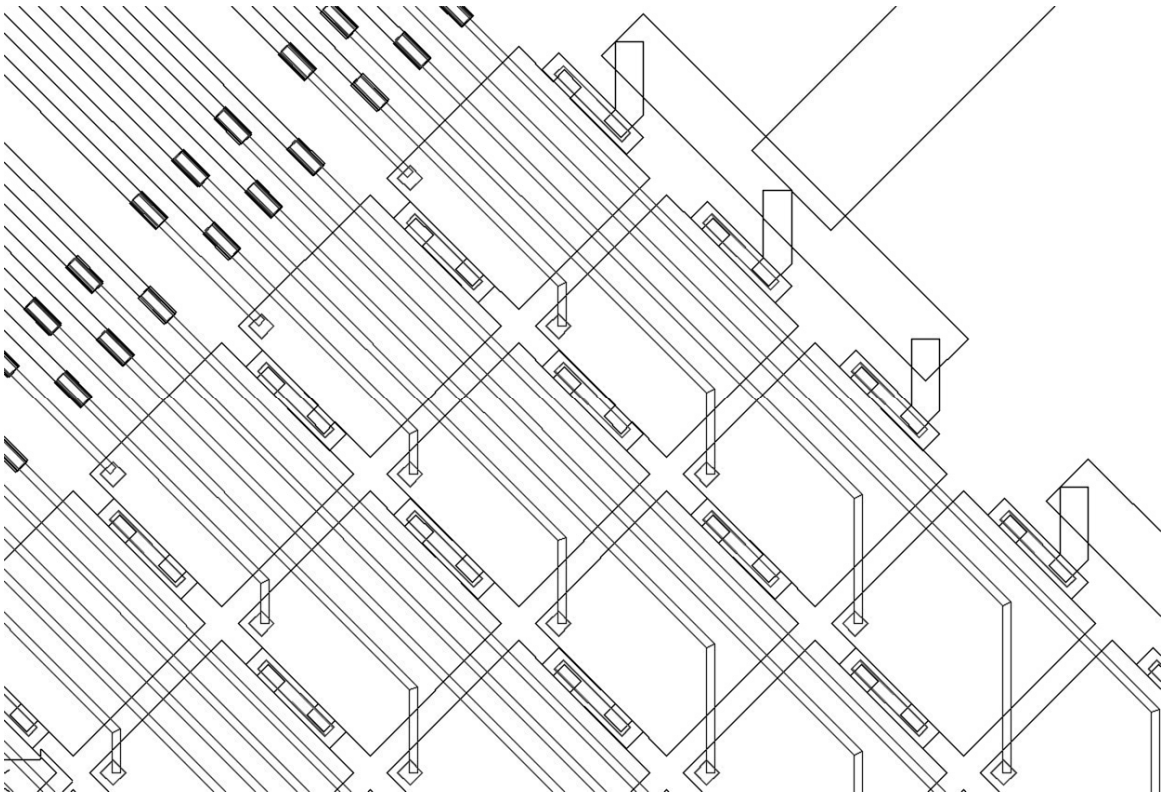

Figure 3-55: Mask detail of the standard 10×12 array.

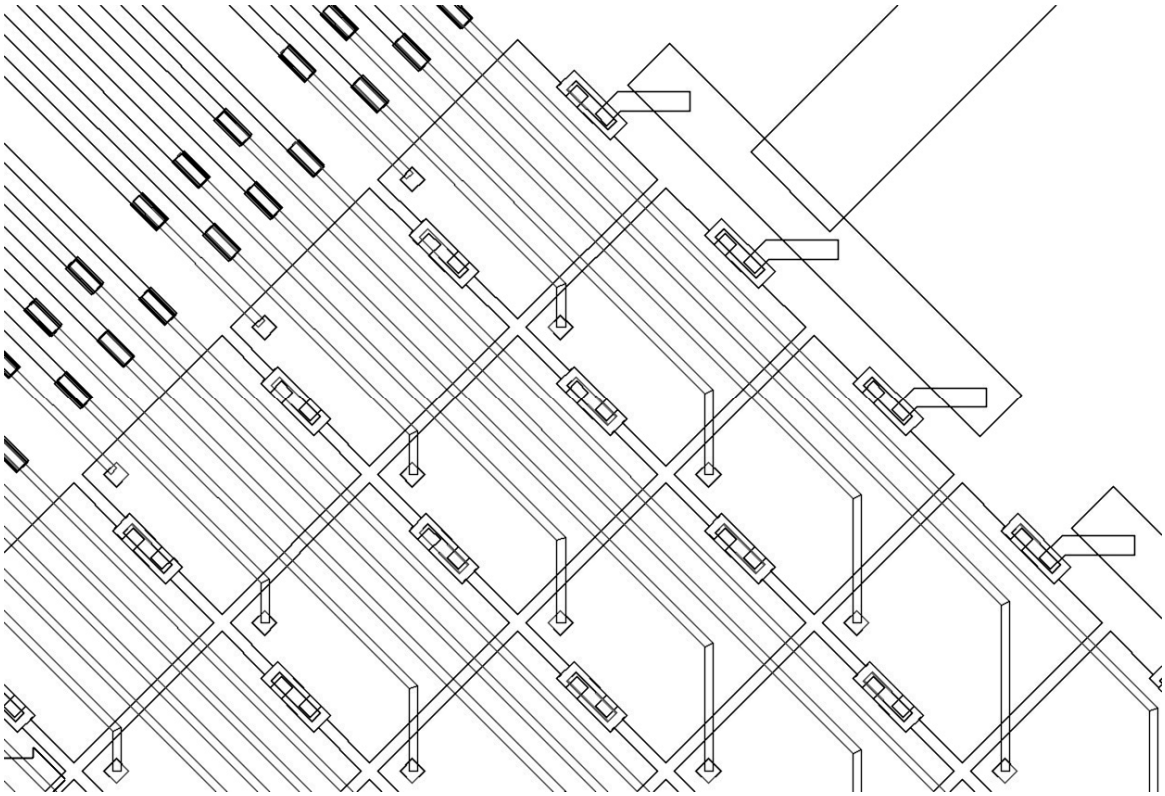

Figure 3-56: Mask detail of the close-packed array. The pixel pitch is similar to the standard array, but the interpixel gap is smaller, leading to higher fill factor. Notice the particular plug structure.

In order to improve the process, we regularly perform focussed ion beam milling and imaging on our devices. Figure 3-57 is a SEM micrograph of a test structure used in this context. The dark grey area is sapphire substrate. Trilayer, Mesa, via and Nb areas are indicated. The vertical line shows the zone were FIB milling was performed. The various numbers correspond to areas which were investigated. Figure 3-58 corresponds to region 1 on the SEM image and shows the edge of the trilayer. Note that the sample was covered with Platinum prior to FIB milling, to avoid excessive charging of the films. The picture shows that the top Ta film is ~150nm shorter than the base film. In addition, the Al layers are further etched back for a total of 350nm, which explains the slight downward bending of the edge of the top Ta film, indicating the criticality of the base edge. Figure 3-59 corresponds to region 7 of the SEM. Here, we see a via through the Silox and a Niobium deposition, mimicking a top contact. One can clearly see the difference between a uniform base Ta layer, and the grainy top Aluminium, and top Tantalum. The crystallographic orientation of the Al carries through to the Niobium. By simply measuring the widths of the structures, we find a grain column width of 150±90nm.

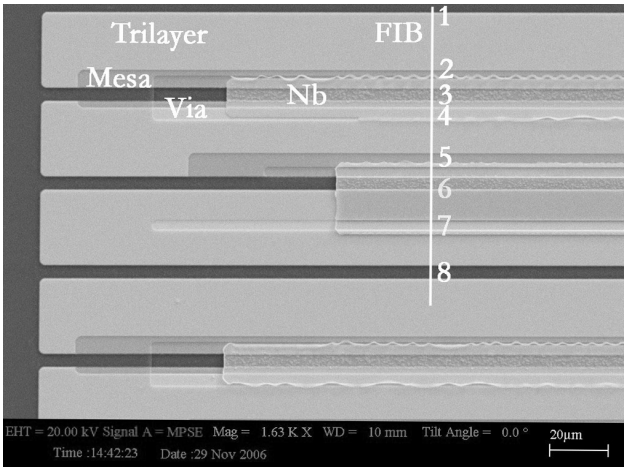

Figure 3-57: SEM of test structures, indicating the FIB milling line and the various regions that were investigated.

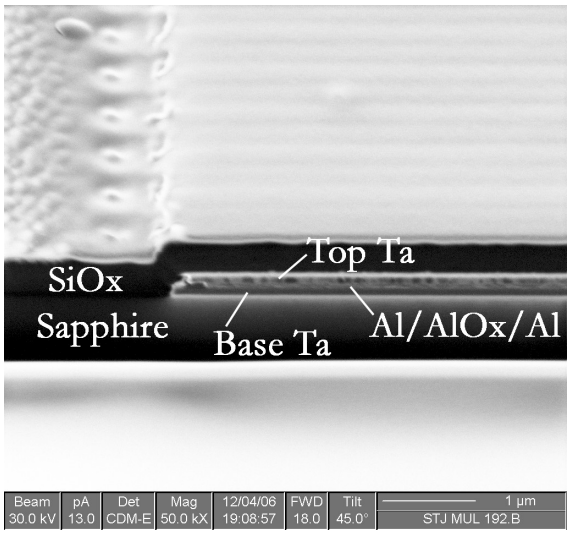

Figure 3-58: FIB imaging of region 1, where one can clearly see the junction edge. The area is covered with Pt to avoid charging of the device.

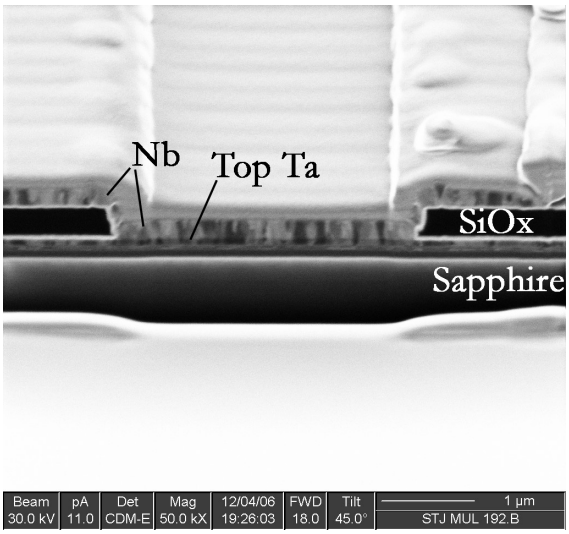

Figure 3-59: FIB imaging of region 7, clearly showing a via through the Silox and a Nb top contact.

3.2.2 MFab Array performance

Although the Tantalum process at MFab is not yet fully optimized, the very first processing using mask set MF2K5 was successful in delivering working arrays. Two were fully characterized for the S-CAM3 project, MUL192.C3 and MUL192.D2. Figure 3-60 shows a micrograph of a closed-packed array, while Figure 3-61 is close-up on MUL192.D2. The RRR value of the MUL192 wafer was 38.5 (normalized to 100nm), better than the TFG devices (see Table 3-2).

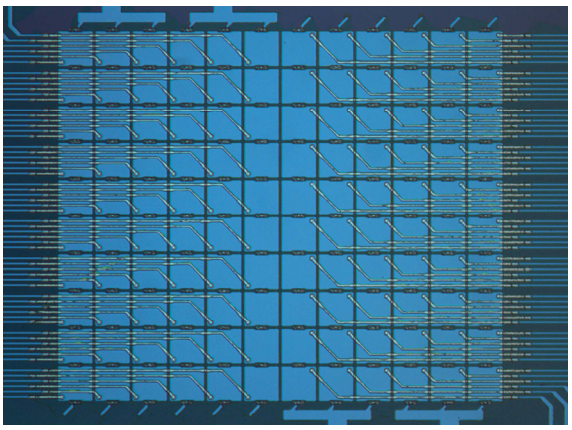

Figure 3-60: Micrograph of a closed-packed 10×12 array.

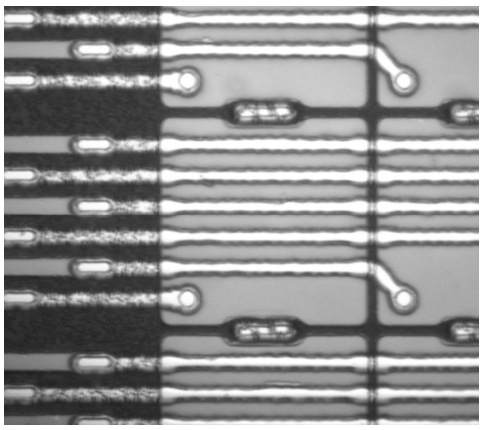

Figure 3-61: Close-packed Pixel and wiring details of MUL192.D2.

3.2.2.1 MUL192.D2

This array only has two non-functional pixels. Since these are located in corners ([1,1] and [1,12]), this is not a major problem. The responsivity map, shown in Figure 3-62, indicates a slightly lower responsivity for the upper half of the array, compared to the lower part. The average responsivity is high, at 61380 e^-/eV, however the scatter is large, with a standard deviation of 28%. Nevertheless, the lowest responsivity pixel is still considerably better than any of the KJL devices. The pulse decay time is again well correlated with the responsivity, as can be seen in Figure 3-65. This leads to a uniform tunnel time across the array, with a value of 0.39±0.01μs.

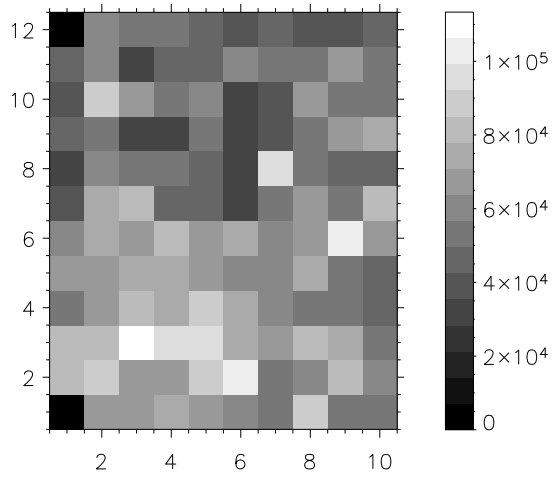

Figure 3-62: Responsivity map of MUL192.D2.

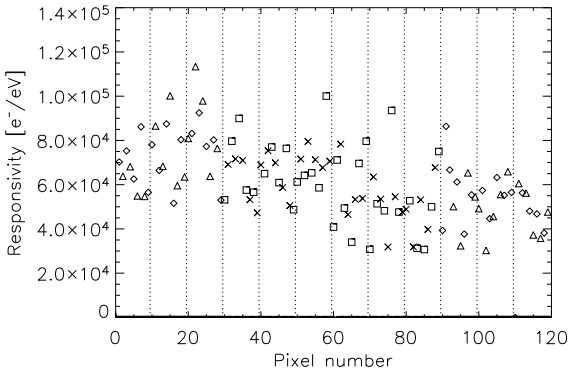

Figure 3-63: Responsivity of all pixels.

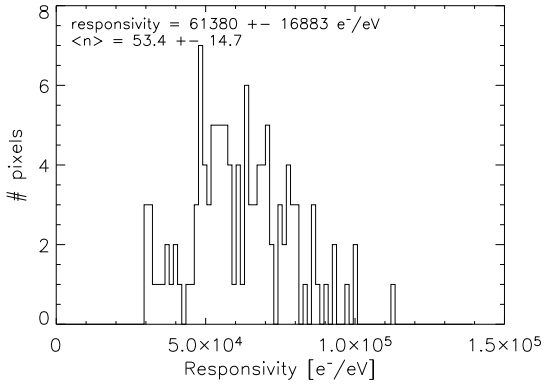

Figure 3-64: Histogram of pixel responsivity.

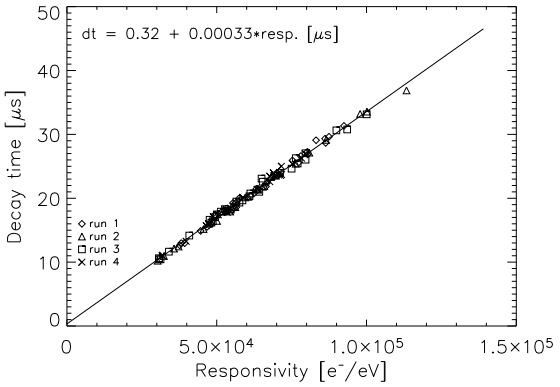

Figure 3-65: Pulse decay time versus responsivity for all pixels.

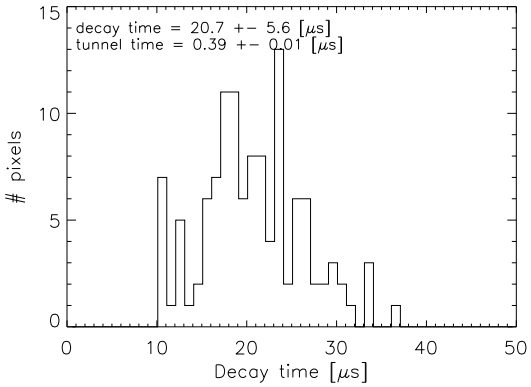

Figure 3-66: Histogram of pixel pulse decay time.

3.2.2.2 MUL192.C3

A second device (C3) from the same wafer was fully functional but the design has a smaller fillfactor compared to the closed-packed array. Nevertheless, responsivity is on average even higher than device D2. As the tunnel times are equal within error bars, this difference is directly attributable to the longer quasiparticle decay times. A summary of the devices' characteristics is given in Figures 3-67 to 3-71.

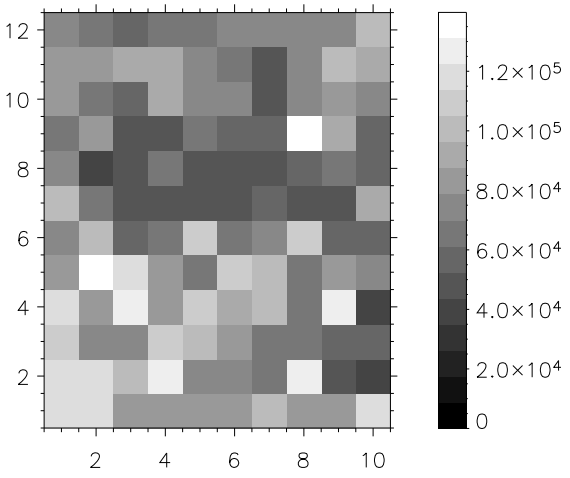

Figure 3-67: Responsivity map of MUL192.C3.

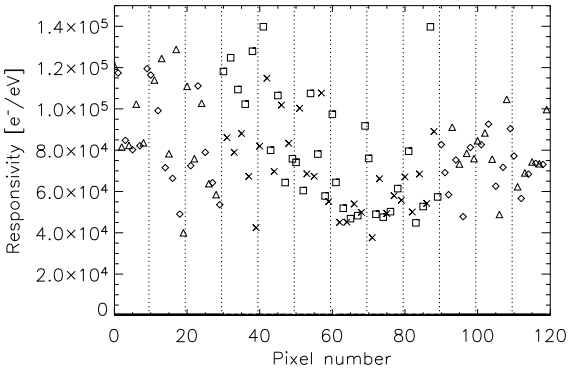

Figure 3-68: Responsivity of all pixels.

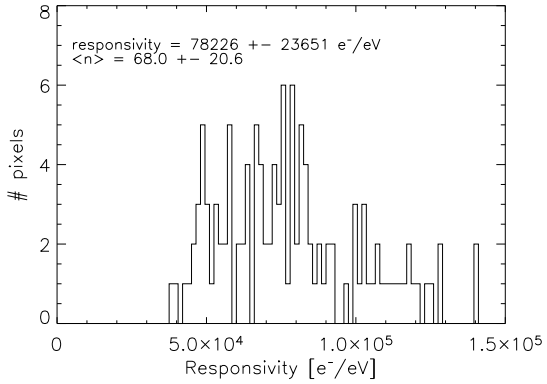

Figure 3-69: Histogram of pixel responsivity.

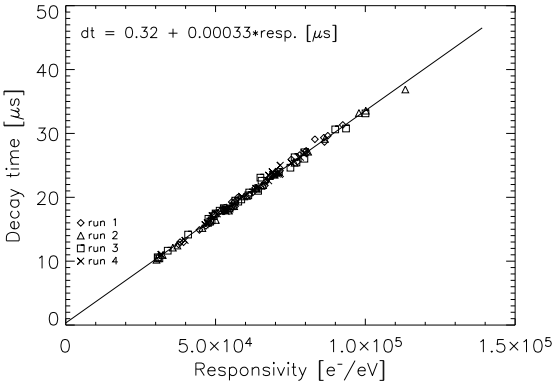

Figure 3-70: Pulse decay time versus responsivity for all pixels.

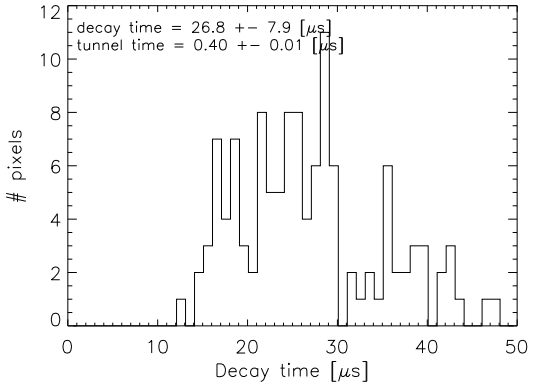

Figure 3-71: Histogram of pixel pulse decay time.

3.2.2.3 Performance summary and Array selection

At the time of writing, not all devices from this wafer were fully characterized, although it was clear that at least half of the wafer showed large amounts of defective pixels. The limited number of produced wafers and tested devices therefore does not allow for a good yield characterization to-date.

Since we now had two functioning arrays, the criterion used for selection was again based on resolving power. Figure 3-72 shows the resolution obtained with MUL192.D2 at a wavelength of 632.8nm (using a HeNe laser) as function of filter frequency. The triangles represent the average over all pixels and the diamonds are the average noise values determined with an electronic pulser signal (right-hand scale). Error bars represent the standard deviation, while the lines are only a guide to the eye. The best resolution is obtained at a filter centre frequency of 18kHz and has a value of 11.7±0.9. The minimum and maximum resolutions are 7.7 and 13.8 respectively. The electronics noise contribution is 0.126±0.014eV.

A similar plot is given in Figure 3-73 for device MUL192.C3, measured at the same wavelength. A best average resolution of 10.4±1.4 is obtained at the filter centre frequency of 24kHz. The minimum and maximum pixel resolutions for this chip are 7.3 and 13.2. The electronics noise had a value of 0.154±0.025eV. Both devices are considerably better than the TFG devices. One should also notice that the best resolution is obtained at a considerably higher filter frequency. This allows, as we shall see in section 5.4, for a higher count-rate capability.

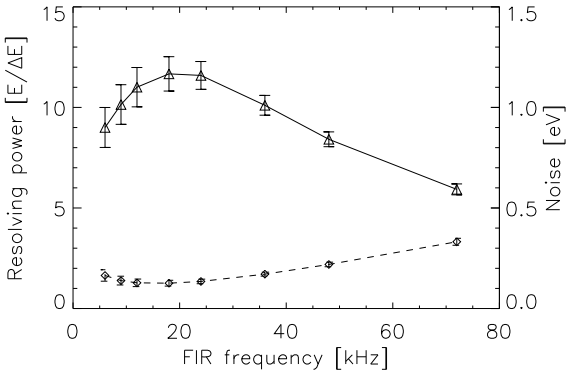

Figure 3-72: Resolving power as function of filter frequency for MUL192.D2, averaged over all pixels (triangles). Diamonds are average noise levels (right hand scale).

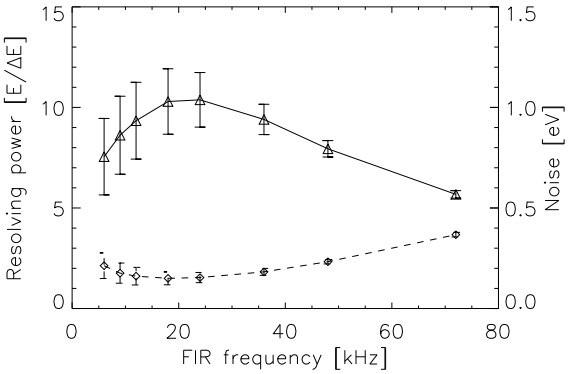

Figure 3-73: Resolving power as function of filter frequency for MUL192.C3, averaged over all pixels (triangles). Diamonds are average noise levels (right hand scale).

Figure 3-74 shows the resolution of MUL192.D2 as function of wavelength (triangles), using the best settings for all parameters, bias voltage, magnetic field and filter frequency. Using again equation 3.1, a best-χ^2 fit yields a value F'=1.34, closer to the expected theoretical value than that derived for the TFG array. The result of the fit is represented by the dash-dot line in the plot. Note the resolution of 14.2±1.0 at the wavelength of 495nm, which is to be compared to the best resolving power of 10 for KJL480.5.

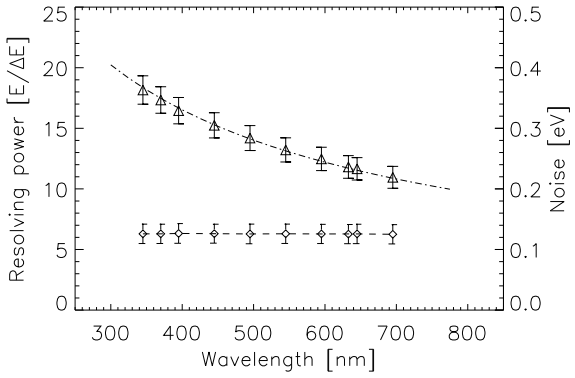

Figure 3-74: Average resolving power as function of photon wavelength (triangles). The curve passing through the measurement points is a best fit. Diamonds are the measured noise values.

A summary of the performances of both MFab arrays is given in Table 3-5. Besides the better energy resolution of MUL192.D2, this device also has a better fill factor (86.6%, inferred from micrographs) than MUL192.C3 (78.6%) and has been used for all S-CAM3 campaigns as of May 2006 (S-CAM3c).

Table 3-5: Summary of MFab array characteristics.

	MUL192.D2	MUL192.C3
# of bad pixels	2	0
# of interconnected pixels	0	0
Responsivity [e^-/eV]	61380±16883	78226±23651
Decay time [μs]	20.7±5.6	26.8±7.9
Tunnel time [μs]	0.39±0.01	0.40±0.01
<n>	53.4±14.7	68.0±20.6
E/ΔE at 632.8nm	11.7±0.9	10.4±1.4
E/ΔE at 495nm	14.2±1.0	

Chapter 4

READOUT ELECTRONICS FOR SUPERCONDUCTING TUNNEL JUNCTIONS

Signals produced by detectors are usually electrical quantities, which are generally not directly useful for human interpretation. Furthermore, they require amplification before any processing can be performed on them. An electronic signal chain therefore always consists of 6 main components: device biasing; low noise amplification; signal conditioning; sampling and conversion to the digital domain; digital processing and storage. With the advent of fast and accurate analogue-to-digital converters (ADCs) as well as powerful digital processors, the boundary between the analogue and digital domains is rapidly moving closer to the pre-amplification stage. Nevertheless, the first four components of the electronics signal chain are still always present. While the complete S-CAM electronics chain will be described in the following chapter, we will present here some details of the front-end circuits necessary to readout STJ detectors.

We have seen in chapter 2 that the absorption of a photon will create excess quasiparticles, which can tunnel across the barrier of an STJ. In order to extract a useful signal, the device needs to be biased with a constant voltage. If the applied voltage is too small, tunnelling occurs in both directions, effectively cancelling a fraction of the signal. Too large a voltage will eventually induce thermal currents. In addition, the device should not be biased near the Josephson current or Fiske resonances. These additional currents would otherwise induce excess shot noise.

When a Ta/Al STJ is properly biased, around 150μV, the signal generated by a photon absorption event is an excess tunnel current of order 500pA for each eV of incident photon energy. This current is, to first order, decaying exponentially with a time constant equal to the lifetime of the qps, of order 20μs. The integrated charge, which represents a measure of the photon's energy will depend on the lifetime of the qps but is of order 5×10^4 e^-/eV. From this we can summarize that our generic front-end electronics should be capable of stably biasing the device at a voltage of about 100-200μV. In order to reach a resolving power of >10, its noise will have to be less than a few $1000\,e^-_{rms}$. Finally, if we want to sample the signal efficiently, a bandpass of order $BW \approx (2\pi\tau_d)^{-1} \approx 10kHz$ is required.

The most commonly used circuit for these applications is based on a junction-field effect transistor (JFET) charge sensitive preamplifier (CSA), originally invented by Walter Kistler [77]. We shall describe next the particular circuit used in S-CAM and review the filters used and analyze their noise performance. We will also present a few alternatives that were studied in in the course of this work. In an attempt to simplify the readout of a large number of junctions, an alternative readout scheme, called matrix readout, was developed and successfully tested. A second alternative is based on Superconducting QUantum Interference Devices (SQUIDs) which could be very promising in the X-ray regime. Finally, we also integrated a set of 64 amplification channels onto a CMOS ASIC and will present the results.

4.1 JFET based preamplifiers

Figure 4-1 shows the schematic of a preamplifier circuit. This layout is conceptually identical to the S-CAM3 electronics developed by A. van Dordrecht, but was tailored for the Matrix readout which will be described in section 4.4. Two amplifiers are hosted on each side of a $9\times11cm^2$ printed circuit board. This could be achieved by using an 8 layer PCB and surface mounted components. Extreme care was taken to shield the input node, by using a separate, 'clean', ground for the input stage. The two sides of the PCB were shielded through the power and ground planes. The amplifier is powered by a ±12V supply and has a total power consumption of ~200mW/channel.

Each individual amplifier can be switched on or off by remote control through Q1. The switching circuit (including Q4) is tailored for a soft start which minimizes charge injection into the STJ, which could otherwise lead to instabilities or even flux trapping.

The input stage consists of a cascode configuration (Q6 and Q5) with an N-channel JFET as input transistor. The Intersil IF9030 is rated at $0.5nV/Hz^{1/2}$ for a bias current of 5mA. Its gate leakage current and 1/f noise are negligible for this application. For power consumption reasons, the transistor is biased at 3mA, which degrades slightly its noise performance. The transistor's common-source input capacitance is C_{iss}=60pF. The cascade stage is followed by the operational amplifier U2, which provides additional open-loop gain. The CSA's output is AC-coupled to the output buffer U4. Opamp U3 is DC-coupled to the output and, after low-pass filtering, provides an image of the detector's bias current.

The feedback circuit consists of a 500MΩ resistor in parallel to a 1pF integrating capacitor. Since the output swing of U2 is limited to ~5V, the maximum current that can be provided at the input node is ~10nA. This is an important factor that needs to be taken into consideration in the choice of the feedback resistor. A high value, required for low-noise operation is only feasible with good quality and uniform junction arrays. In order to provide additional current to the STJ, e.g. in case of instability, Q7 was added. This transistor acts as a switch, lowering the feedback resistance to 1MΩ and proportionally increasing the current handling capability at the input node to 5μA. Q7 can be commanded via S/W through transistor Q3, which provides the level shift.

As we know, STJs need to be biased at a precise, stable and very low bias voltage. Standard discrete components do not offer this capability; in particular Q6's V_{gs} can vary from device to device by a much larger factor. Also, any circuit placed at the input node will affect the noise performance. That is the reason of using the electrometer Opamp U1. It samples the input (DC) voltage and through a DC feedback-loop, will regulate Q6's gate voltage. The inverting input of U1 is connected to a digital-to-analog converter (DAC) through a resistive divider. This allows S/W control of the amplifier's bias voltage in the range ±1mV. Although the offset voltage of the AD549 is laser trimmed, it residual value can still be of order 200μV and 5μV/ºC, and can be compensated through calibration using the DAC.

By combining the functionality of Q3, U1 and U3, and through S/W control it is now also possible to diagnose the detector. By scanning the DAC values and monitoring the output of U3, a complete I-V curve can be obtained automatically from all channels.

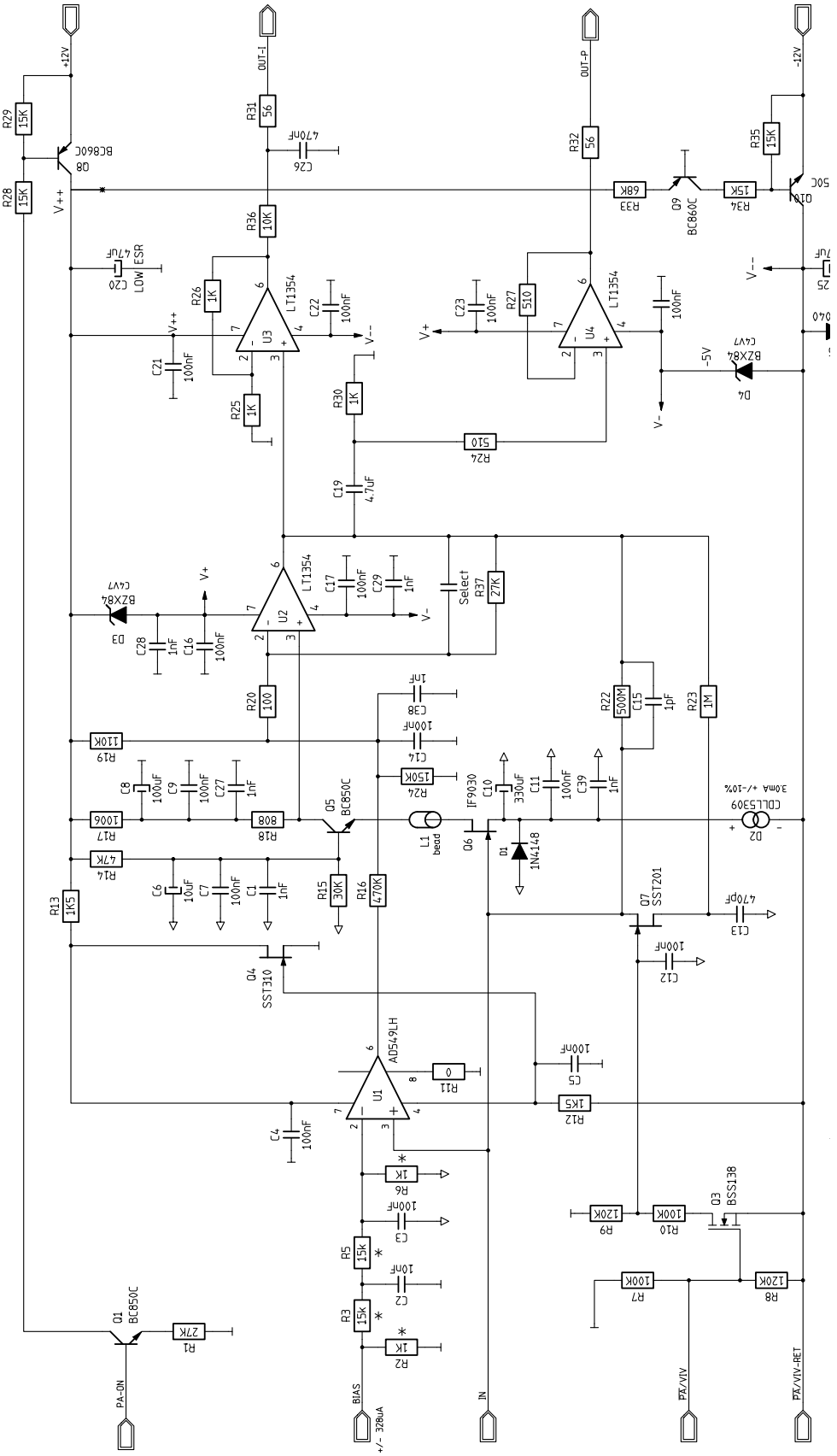

Figure 4-1: Preamplifier schematic

4.2 Filtering techniques

For photon detection, we are not only interested in detecting the absorption of the photon, but also measure its energy. A commonly used method is to process the output of the CSA through a (uni-polar) Semi-Gaussian filter [78],[79]. This filter consists of a differentiator and 'n' integrators and its transfer function is given by:

$$H(\omega) = \frac{j\omega\tau_0}{(1+j\omega\tau_0)}\frac{1}{(1+j\omega\tau_0)^n} \qquad 4\text{-}1$$

The output of this filter is a bell-shaped curve, resembling a Gaussian, hence its name, with a well defined peak. The peak value can then be sampled and is an image of the original charge injected by the detector and integrated by the CSA. The purpose of the filter is two-fold, it will allow an optimization of the signal-to-noise ratio (SNR) and at the same time provide a well defined pulse shape, limited in time to avoid pulse pile-up. In our laboratory set-up we have used a small modification to this filter by adding an additional differentiation stage, which allows easier AC-coupling. The additional circuit also contains a pole-zero compensation, which effectively compensates for the CSA's pole. This avoids unnecessary undershoot of the signal and thus restricts it's extend in time. The result is a bi-polar signal with a well defined maximum and minimum peak, of which only the former is measured. Its transfer and impulse response functions are given by:

$$H(\omega) = \frac{j\omega\tau_0(1+j\omega\tau_{CSA})}{(1+j\omega\tau_0)^2}\frac{1}{(1+j\omega\tau_0)^n} \qquad 4\text{-}2$$

$$h(t) = \frac{1}{n+1}\frac{t^n}{\tau_0^{n+2}}e^{-t/\tau_0}(n+1-t/\tau_0).1(t) \qquad 4\text{-}3$$

To characterize STJs, our standard acquisition electronics contains 2 filters, of order n=2, with different time constants (e.g. τ_0= 6 and 21μs). The fast filter is used as trigger circuit while the slow filter, with best SNR, measures the signal's amplitude. A ratio of slow versus fast filter outputs can also be used to measure the detector's pulse decay time.

For S-CAM, we chose a different route. Here the signals are converted into the digital domain at a sampling frequency f_s, and digitally filtered. The Finite Impulse Response (FIR) filter consists of 3 contiguous sections, each performing a running average over n_{taps} samples which are then combined. The transfer function and impulse response of the filter are given by:

$$H(\omega) = 1 - 3e^{-jT\omega} + 3e^{-j2T\omega} - e^{-j3T\omega} \qquad 4\text{-}4$$

$$h(t) = 1(t) - 3\cdot 1(t-T) + 3\cdot 1(t-2T) - 1(t-3T) \qquad 4\text{-}5$$

Where 1(t) is the Heaviside function, t is time and $T = n_{taps}/f_s$ is the filter's time constant. The filter resembles a bipolar semi-Gaussian filter in that its step response will have a well defined positive and negative peak and zero DC value. For S-CAM, both peaks are sampled and stored. For pulse-height analysis, a weighted sum is calculated offline for best signal-to-noise ratio.

The magnitude of the filter's transfer function is plotted as a solid line in Figure 4-2. The dashed-dotted line is the response of the combined CSA and filter. In this example, the signal is sampled at 40MHz and n_{taps}=511, yielding a centre frequency of 24kHz and bandwidth of

26.5kHz. For comparison, the response of a bipolar semi-Gaussian filter and CSA, of equal bandwidth, is plotted in dashed line.

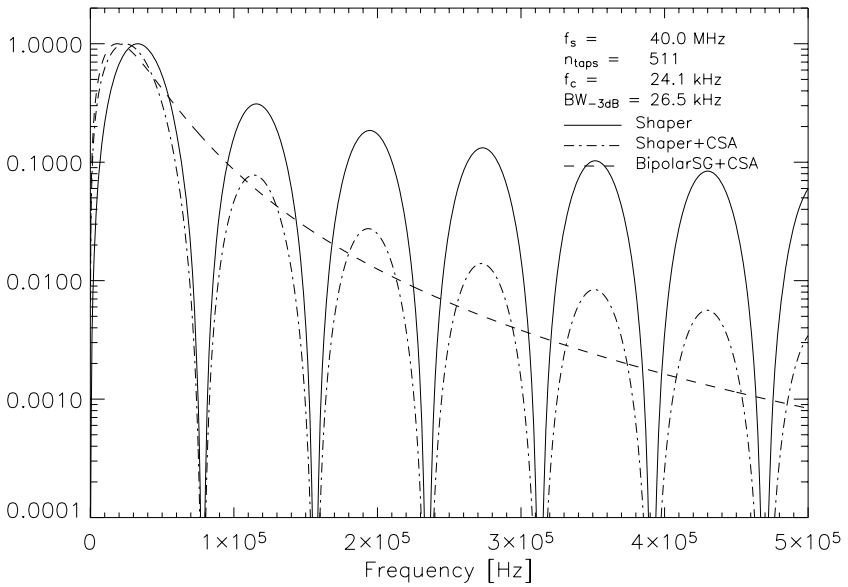

Figure 4-2: FIR (solid) and FIR+CSA (dash-dot) frequency response, $|H(f)|$. Dashed line is the Bipolar semi-Gaussian filter + CSA response.

In Figures 4-3 and 4-4, we represent the output of the digital filter to STJ pulses of various decay times, normalized to the response to a Dirac pulse. For this simulation, the total charge in the input pulse is kept constant. Obvious is the decrease of signal amplitude as the pulse decay time increases.

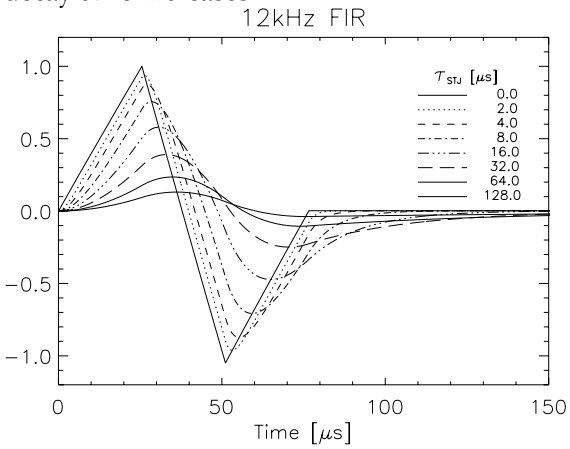

Figure 4-3: 12kHz FIR response to STJ pulses with different decay times; n_{taps}=511, f_s=20MHz.

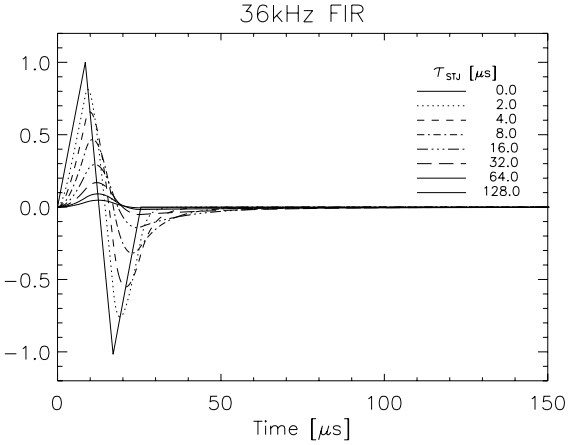

Figure 4-4: 36kHz FIR response to STJ pulses with different decay times; n_{taps}=340, f_s=40MHz.

To illustrate this further, Figures 4-5 and 4-6 show the amplitudes of the positive and negative peaks as function of pulse decay time; the different curves are for different FIR frequencies. Again, these plots are normalized to the response to a Dirac pulse and are computed for equal charge injection ($I_{in}=Q_0/\tau_{STJ}.\exp(-t/\tau_{STJ}).1(t)$). Figure 4-7 shows the ratio between positive and negative peaks, where a clear, almost linear dependence on pulse decay time (τ_{STJ}) can be noticed.

In an STJ, however, the thickness of the oxide barrier is rather constant from batch to batch and thus is also the tunnel time. However, the quasiparticle lifetimes are still variable from production run to production run. It is therefore more representative to compare signals

with varying responsivity, keeping the tunnel time constant. The integrated charge from these devices is then directly proportional to the quasiparticle lifetime. Under this assumption, the signals available at the output of the FIR filter are plotted in Figures 4-8, 4-9 and 4-10.

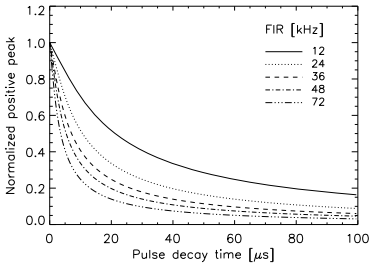

Figure 4-5: Positive peak amplitude for fixed total charge at input, as function of pulse decay time.

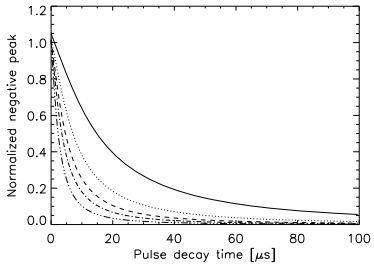

Figure 4-6: Negative peak amplitude; same legend as in Figure 4-5.

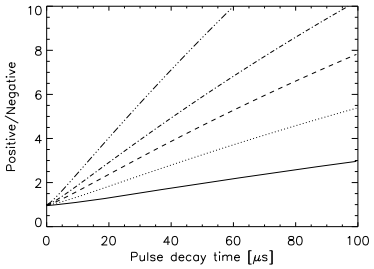

Figure 4-7: Ratio between positive and negative peaks.

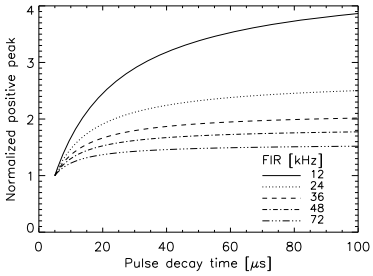

Figure 4-8: Positive peak amplitude for fixed tunnel time, as function of pulse decay time.

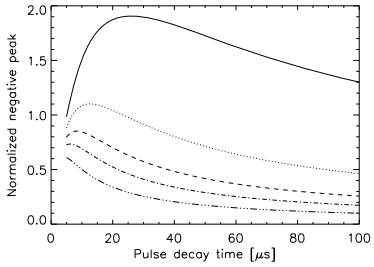

Figure 4-9: Negative peak amplitude, same legend as in Figure 4-8

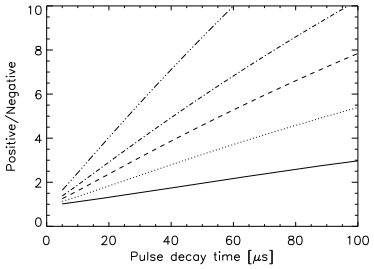

Figure 4-10: Ratio of positive and negative peaks.

4.3 Noise analysis

For electrical modelling purposes, an STJ can be represented by a capacitor in parallel with a dynamic resistance. The dynamic resistance can be estimated from I-V curves and in practice is always larger than the leakage current at the bias point divided by the bias voltage. The capacitance is estimated as that of a parallel plate capacitor of identical size using a relative electrical permittivity ε_r of 10.5. The detector's corner frequency above which it can be modelled by a pure capacitor is given by:

$$f_c = \frac{1}{2\pi}\frac{J_b l^2}{V_b}\frac{d}{\varepsilon_0 \varepsilon_r l^2} \qquad 4\text{-}6$$

In Ta based devices, we currently achieve leakage current densities (J_b) better than 50fA/μm^2 at a temperature of 0.3K and at a bias voltage (V_b) of 100μV; the oxide thickness (d) is of order 1nm which yields a corner frequency, f_c, of 860Hz. For pulse height analysis, traditional semi-Gaussian or FIR pulse shaping is used with time constants of order 10μs [80], this is an order of magnitude shorter than the detector's equivalent RC time given by 4-6. For a wide range of detector sizes (l×l), the STJ can therefore be represented electrically by a capacitor.

Let us consider now a single STJ connected to a JFET charge-sensitive pre-amplifier. The major noise sources are represented in Figure 4-11 [80],[81]. The JFET's series noise (e_n), physically generated in its channel, consists of white Gaussian noise and '1/f' noise and is referred to the input node provided the transistor's input capacitance (gate-to-source, C_{gs} and

gate-to-drain, C_{gd}) is added to the input node capacitance (C_{stray}) [82],[83]. The input referred current noise from the transistor can be shown to be negligible [83]. The parallel noise (i_n) consists of the detector bias current which is responsible for shot noise ($i_{n,sh}$) and Johnson noise from the feedback resistor ($i_{n,Rf}$). The shot noise can usually be neglected since we routinely manufacture extremely high quality barriers with consistently very low leakage currents. The noise contribution from the feedback network can also be made small by choosing an appropriate high resistor value.

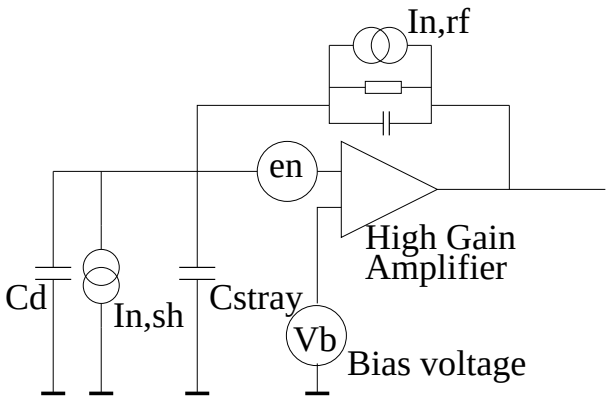

Figure 4-11: Noise sources in a charge sensitive preamplifier connected to an STJ.

Equation 4-7 shows the total noise power spectrum density at the output of a charge sensitive amplifier where C_d, C_w, C_f and C_{gs} and C_{gd} are the detector, wiring, feedback and input transistor's capacitances respectively:

$$\left|v_0\right|^2 = \left|\frac{C_d + C_w + C_f + C_{gs} + C_{gd}}{C_f}\right|^2 e_n^2 + \left|\frac{1}{j\omega C_f}\right|^2 \left(i_{n,sh}^2 + i_{n,\mathrm{R}f}^2\right) \qquad 4\text{-}7$$

The first term is called the series noise power (single-sided) spectral density of the input transistor; e_n is of order $1\mathrm{nV/Hz^{1/2}}$ for the JFETs in use. The transistor's $1/f$ and gate leakage noise components can be neglected. The second term in 4-7 is the parallel noise component where the noise current (single-sided) spectral densities are given by:

$$i_{n,sh} = \sqrt{2qI_l} \qquad 4\text{-}8$$

$$i_{n,\mathrm{R}f} = \sqrt{4kT/\mathrm{R}_f} \qquad 4\text{-}9$$

In order to calculate the noise equivalent charge (ENC) at the input, we must first evaluate the rms noise voltage at the output of the shaping filter. Since all noise frequency components are orthogonal to each other, the noise voltage at the output of a filter is given by:

$$v_n^2 = \int_0^\infty \left|v_0(j2\pi f)\right|^2 \left|H(j2\pi f)\right|^2 df \qquad 4\text{-}10$$

The ENC is then obtained by dividing this v_n by the voltage created at the filter's output by a single electron injected at the input as a Dirac pulse. We will now first recall the ENC for the semi-Gaussian filters and then present the results for the S-CAM3 FIR filter.

4.3.1 Semi-Gaussian filters

The signal from the unipolar shaper will peak at time t=n.τ_0. Using equations 4-1, 4-7 and 4-10, one can show that the response to a single electron Dirac pulse and ENCs related to series and parallel noise are given respectively by [81]:

$$v_{o,1e} \propto \frac{q}{C_f \tau_0} \frac{n^n e^{-n}}{n!} \qquad 4\text{-}11$$

$$ENC_{u,s}^2 = e_n^2 C_t^2 \frac{B(3/2, n-1/2)}{q^2 4\pi\tau_0} \frac{n!^2 e^{2n}}{n^{2n}} \qquad 4\text{-}12$$

$$ENC_{u,p}^2 = i_n^2 \frac{\tau_0 B(1/2, n+1/2)}{q^2 4\pi} \frac{n!^2 e^{2n}}{n^{2n}} \qquad 4\text{-}13$$

Where *B(a,b)* is the Beta function and C_t is the total capacitance at the amplifier's input node. In the practical case of e_n=1nV/Hz$^{1/2}$, n=2, τ_0=10µs, C_t =220pF, R_f=500MΩ, we find $ENC_{u,s}$ = 283e$^-_{rms}$ and $ENC_{u,p}$ =128e$^-_{rms}$, total ENC_u =311e$^-_{rms}$. The total input node capacitance is assuming 100pF from the STJ, 60pF from the wiring and 60pF for the JFET.

A similar analysis can be performed for the bipolar semi-Gaussian shaper. This time, the first peak will occur at $t = (1+n-\sqrt{1+n})\tau_0$. The results are:

$$v_{o,1e} \propto \frac{q}{C_f \tau_0^2} \frac{(1+n-\sqrt{1+n})^n e^{-(1+n-\sqrt{1+n})}}{(n+1)!} \qquad 4\text{-}14$$

$$ENC_{b,s}^2 = e_n^2 C_t^2 \frac{B(5/2, n-1/2)}{q^2 4\pi\tau_0} \frac{(n+1)!^2 e^{2(1+n-\sqrt{1+n})}}{(1+n-\sqrt{1+n})^{2n}(1+n)} \qquad 4\text{-}15$$

$$ENC_{b,p}^2 = i_n^2 \frac{\tau_0 B(3/2, n+1/2)}{q^2 4\pi} \frac{(n+1)!^2 e^{2(1+n-\sqrt{1+n})}}{(1+n-\sqrt{1+n})^{2n}(1+n)} \qquad 4\text{-}16$$

For the same numerical case as treated previously, we now obtain $ENC_{b,s}$ =416e$^-_{rms}$ and $ENC_{b,p}$ =109e$^-_{rms}$, yielding a total ENC_b =430e$^-_{rms}$, which is very close to the experimentally obtained 500 e$^-_{rms}$.

4.3.2 S-CAM3 FIR

For S-CAM, the analysis is a little more complex. Indeed, here we do not only sample the first peak, but we perform a weighted sum of the two peaks. Also, the simplicity of the FIR implementation does not allow for a pole-zero cancellation. Let τ_f be the time constant of the preamplifier's feedback network ($\tau_f = R_f.C_f$). We can easily show that the noise at the output of the FIR filter for series and parallel noise is given respectively by:

$$v_{o,rms,s}^2 = 3e_n^2 T (1 - C_t/C_f)^2 \qquad 4\text{-}17$$

$$v_{o,rms,p}^2 = \frac{i_n^2 T^3}{2C_f^2} \qquad 4\text{-}18$$

The two peak values corresponding to a 1e- input Dirac pulse are given by:

$$v_{\max} = qR_f\left(e^{-T/\tau_f} - 1\right) \approx qT/C_f \qquad 4\text{-}19$$

$$v_{\min} = -qR_f\left(e^{-2T/\tau_f} - 3e^{-T/\tau_f} + 2\right) \approx -qT/C_f \qquad 4\text{-}20$$

The ENC of both peaks due to series noise is then given by:

$$ENC_{+,s} = \sqrt{3T}\,\frac{e_n(1-C_t/C_f)}{qR_f(e^{-T/\tau_f}-1)} \approx \frac{C_t e_n}{q}\sqrt{\frac{3}{T}} \qquad 4\text{-}21$$

$$ENC_{-,s} = \sqrt{3T}\,\frac{e_n(C_t/C_f-1)}{qR_f(e^{-2T/\tau_f} - 3e^{-T/\tau_f} + 2)} \approx \frac{C_t e_n}{q}\sqrt{\frac{3}{T}} \qquad 4\text{-}22$$

And for parallel noise:

$$ENC_{+,p} = \frac{i_n T^{3/2}}{2qR_f C_f(1-e^{-T/\tau_f})} \approx \frac{i_n}{q}\sqrt{\frac{T}{2}} \qquad 4\text{-}23$$

$$ENC_{-,p} = \frac{i_n T^{3/2}}{2qR_f C_f(e^{-2T/\tau_f} - 3e^{-T/\tau_f} + 2)} \approx \frac{i_n}{q}\sqrt{\frac{T}{2}} \qquad 4\text{-}24$$

If we combine both peaks linearly as follows, $v_t = \alpha v_{\max} + (1-\alpha)v_{\min}$, we not only add correlated signals but also correlated noise and thus need to evaluate the noise autocorrelation function. From the Wiener-Khinchin theorem, we know that the noise autocorrelation function is related to the noise power spectral density by a Fourier transform. If we assume that the input signal is a Dirac pulse, and this is correct for the evaluation of the response to a single electron, the sampling times for the two peaks are T and 2T. Since the noise is stationary, we only need to evaluate the noise autocorrelation function, $R(\tau)$, for τ=T. The autocorrelation function for series and parallel noise is easily found to be given by:

$$R_s(\tau) = e_n^2 T(1-C_t/C_f)^2 \qquad 4\text{-}25$$

$$R_p(\tau) = \frac{i_n^2 T^3}{6C_f^2} \qquad 4\text{-}26$$

These values are both a third of the square of the respective noise voltages. By equally adding the two samples (α=0.5), we find that the total noise is given by:

$$v_{o,n,tot}^2 = \alpha^2 v_{o,n}^2(T) + (1-\alpha)^2 v_{o,n}^2(2T) + 2\alpha(1-\alpha)R(T) \cong \frac{1}{2}v_{o,n}^2 + \frac{1}{6}v_{o,n}^2 = \frac{2}{3}v_{o,n}^2 \qquad 4\text{-}27$$

This is only 15% higher than for uncorrelated noise samples. In the practical case, comparable to our calculation for the bipolar semi-Gaussian filter, of e_n=1nV/Hz$^{1/2}$, n_{taps}=511, f_s=20MHz, T=25.5μs, C_t=220pF, R_f=500MΩ and α=0.5, we find ENC_s = 383e$^-_{rms}$ and ENC_p =105e$^-_{rms}$, with a total ENC=400e$^-_{rms}$.

As we have seen in Figure 4-7, the negative peak will always be smaller than the positive peak for real STJ pulses. This is particularly true for τ_{STJ}>>T. So we can anticipate that the best signal to noise ratio will have α>0.5. If we let ξ be the ratio of peaks (v_{min}/v_{max}), the SNR can be expressed as:

$$SNR = \frac{\alpha + (1-\alpha)\xi}{\sqrt{1-\frac{4}{3}\alpha(1-\alpha)}} \frac{v_{\max}}{v_{o,n}} \qquad 4\text{-}28$$

This relation is plotted in Figure 4-12, normalized to α=1. The optimum SNR is obtained for:

$$\alpha = \frac{3-\xi}{2(1+\xi)} \qquad 4\text{-}29$$

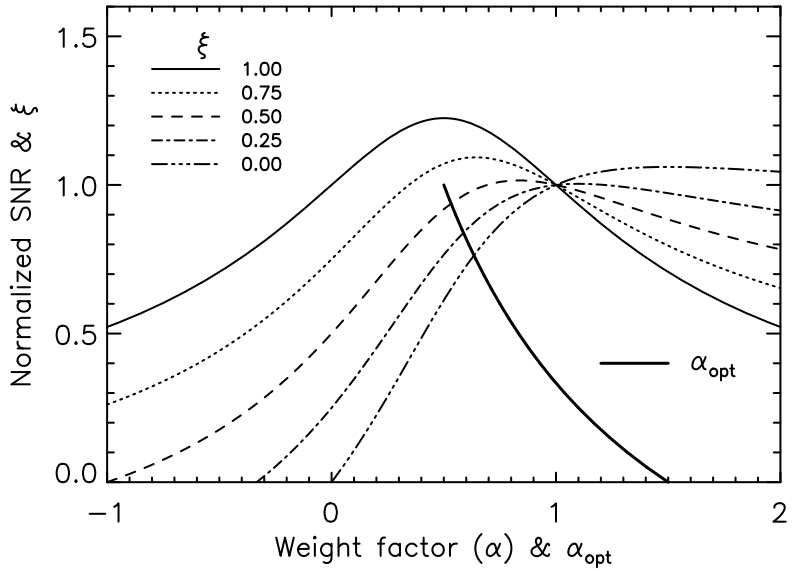

Figure 4-12: Normalized SNR as function of weight factor α. Thick line is the optimum α for a given ξ (vertical axis).

For ξ<0.3, the optimum α is larger than one, indicating that it's better to subtract a fraction of the second sample and is a direct consequence of the correlation between the two noise samples. This result is merely an indication that the noise can be reduced slightly by optimum filtering of the signals. From signal analysis, we know that this can be achieved through whitening the noise following by correlation with the signal template. In practice, however, there are two limitations. Firstly, an optimal filtering algorithm is much more computing intensive and could not be implemented in the S-CAM analysis. Secondly, we have seen in section 2.5 that STJ pulses contain non-stationary noise related to their tunnel statistics. So, in practice, an optimal α is obtained through measurement.

4.4 Matrix readout scheme

As we have seen, STJ detectors are read out using individual acquisition chains for each pixel. This severely limits the number of pixels for three main reasons:

1. The detectors require very low operating temperatures and the most serious problem is related to heat load onto the cryogenic cooler through the wiring between the room-temperature electronics and the detector. Current amplifier designs based on JFETs or CMOS are not adequate at the required detector temperature. SQUID based multiplexing schemes are now becoming available for TESs [84],[85] but these still suffer from limited speed both in terms of photon flux and in pulse sampling. A modified SQUID architecture, applicable to STJs will be discussed in the next section [86].
2. The second concern relates to the specific case of the application to space instruments, where power consumption and mass are to be minimised. Indeed, each pixel requires an individual readout chain comprising a biasing circuit and a preamplifier, shaping filter, low-level threshold detector, sample-and-hold and analog-to-digital converter circuits.
3. In the specific case of front illumination by soft X-rays, the amount of wiring crossing the detectors effectively suppresses the low energy response.

We will review here an alternative method for reading out large format arrays of pixel detectors which drastically reduces the number of wires on chip as well as between the detector and the acquisition electronics and reduces by the same amount the number of electronic channels [87],[88]. With this new method, an array of N×N pixels can be read-out by 2×N amplifier chains instead of the normally required N^2. We will describe the pixel array interconnection principle, which we shall refer to as matrix read-out, and evaluate its advantages and disadvantages. We demonstrate the approach through the use of a two-by-two array of STJs. We will report on the results obtained with Tantalum devices illuminated by optical photons [89].

4.4.1 The Pixel Array Interconnection Principle

The principle is based on interconnecting the pixels in rows and columns as shown in Figure 4-13. The base electrodes are interconnected in rows and the top electrodes in columns. Each row and each column is connected to a separate bias and amplification circuit. When a pixel has been hit by a photon, the excess tunnel current will produce a signal proportional to the photon's energy simultaneously in its corresponding row and column. A coincidence measurement between rows and columns can therefore determine which pixel recorded the photon event. The photon's energy can be derived in the usual way by filtering the integrated charge output from the charge sensitive preamplifier using a pulse shaper followed by a peak detector. Figure 4-14 shows a possible implementation using conventional JFET charge sensitive amplifiers.

Voltage biasing of the detectors is achieved by creating a virtual ground on all columns and a virtual bias voltage on each row. This can be implemented using a high open loop gain amplifier with negative feedback and a very low offset voltage operational amplifier controlling the amplifier's input JFET DC operating point, as described earlier. Another type of readout implementation which uses SQUIDs as a first stage amplification will be presented in the next section.

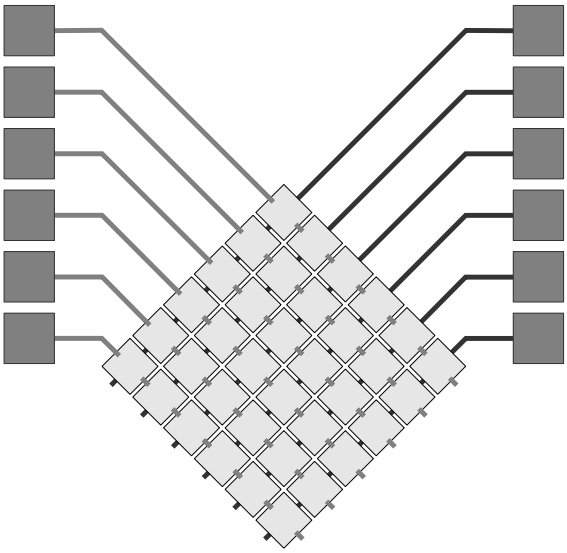

Figure 4-13: Layout of the matrix read-out scheme as applied to a 6×6 STJ array. The 2 side columns are the contact pads. The 36 detectors are interconnected in rows and columns by their top and base electrodes respectively.

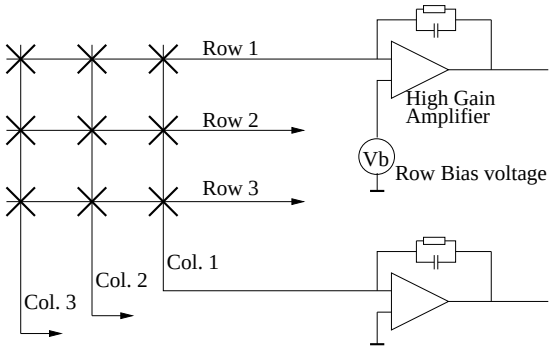

Figure 4-14: Schematic representation of a traditional semiconductor amplifier chain connected to the detector matrix. The high open loop gain amplifiers ensure the row and column biasing voltages through the feedback network

4.4.2 Advantages of the Readout Approach

Obviously, with the proposed readout approach, the number of wires and circuits for reading out a large format array can be reduced drastically. A conventional approach would currently limit the number of pixels to a few hundred and with major development (particularly related to the cryogenic cabling) possibly to 10^3 due to excessive heat load on the cryogenic system. We can now however envisage arrays of 10^4 to 10^6 pixels. Such large format arrays open up the possibility to develop large format, large field-of-view imaging spectrometers for UV-optical astronomy and high-energy X-ray astrophysics.

Since the number of connections to the detector chip has decreased and because the contacts are intrinsically available at the border of the array (see Figure 4-13), no complex routing is necessary to connect the array pixels to the reduced number of contact pads. Bonding can be achieved by traditional wire bonding, i.e. no bump-bonding is necessary.

This scheme does not require additional processing steps in the fabrication of the array chips. In fact, it can actually reduce the processing complexity. Indeed, in the case of STJs, the detectors are usually covered with SiO_2 and vias patterned so as to create contacts onto the top electrodes. This is not necessary for our proposed scheme since there are no tracks that need electrical isolation from the top electrodes. In addition, the traditional pixel addressing method requires a separate top electrode contact for each detector and therefore the number of tracks required increases rapidly with the array size. At some point, one would have to move to multiple layers of routing metal, increasing the processing complexity for the traditional readout even further.

The tracks covering the top electrodes also mask the detector in the case of illumination from the top. This is a major problem when used for X-ray detection. For optical or UV photons, the illumination can be through the transparent sapphire or Magnesium Fluoride substrate. The new addressing scheme alleviates this problem by first and foremost avoiding having tracks across the top electrodes.

4.4.3 Possible Drawbacks with the Readout Approach

4.4.3.1 Noise considerations

Let us consider a single STJ connected to a FET charge-sensitive pre-amplifier. We have shown that the total noise power spectrum density at the output of a charge sensitive amplifier is given by:

$$\left|v_0\right|^2 = \left|\frac{C_d + C_w + C_f + C_{gs} + C_{gd}}{C_f}\right|^2 e_n^2 + \left|\frac{1}{j\omega C_f}\right|^2 \left(i_{n,sh}^2 + i_{n,Rf}^2\right) \qquad 4\text{-}30$$

Where the series noise (e_n) is the transistor's input voltage noise and the parallel noise consists of the detector bias current which is responsible for shot noise ($i_{n,sh}$) and Johnson noise from the feedback resistor ($i_{n,Rf}$). The shot noise can usually be neglected since we routinely manufacture extremely high quality barriers with consistently very low leakage currents. The noise contribution from the feedback network can also be made small by choosing an appropriate high resistor value. C_d, C_w, C_f and C_{gs} and C_{gd} are the detector, wiring, feedback and input transistor's capacitances respectively.

In the new read-out scheme, each amplifier senses a parallel combination of N detectors as sketched in Figure 4-15, for a N×N array. The parallel noise power density due to the detectors' leakage currents will increase by a factor N compared to the single detector case, but should remain negligible with high quality barriers. The new read-out scheme does not, a priori, influence the value to be chosen for the feedback resistor and therefore its noise contribution remains unchanged. However, it affects in two ways the output noise related to the FET's input referred (series) voltage noise. Firstly, this component is directly influenced by the input node capacitance as is seen in equation 4-30. The detector's capacitance C_d has now increased to $N \times C_d$ as perceived at the output of a N×N detector array. Secondly, each row (column) is connected to each column (row) amplifier through the detectors (Figure 4-16).

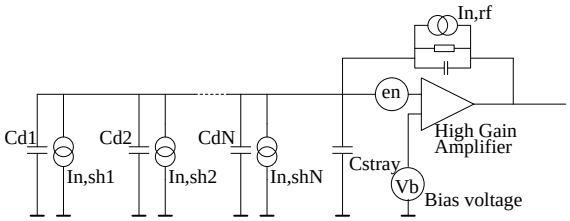

Figure 4-15: Schematic of the noise sources resulting from the parallel connection of STJs in rows and columns.

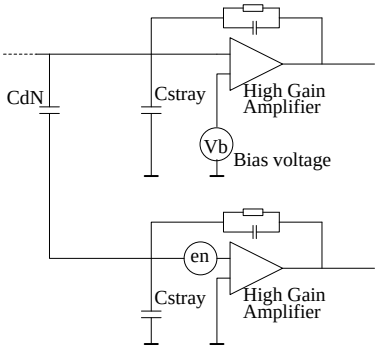

Figure 4-16: Schematic representation of the influence on the row's amplifier by the column's amplifier noise.

The series noises related to the column (row) amplifiers are therefore also coupled in through the detectors' capacitance. One can easily show that these noise voltage sources add quadratically (since they are uncorrelated) so that the total noise power spectrum density at the output of the charge sensitive amplifier is now given by:

$$\left|v_0\right|^2 = \left[\left|\frac{N.C_d + C_w + C_f + C_{gs} + C_{gd}}{C_f}\right|^2 + N.\left|\frac{C_d}{C_f}\right|^2\right] e_n^2 + \left|\frac{1}{j\omega C_f}\right|^2 \left(N.i_{n,sh}^2 + i_{n,Rf}^2\right) \qquad 4\text{-}31$$

If the noise is dominated by the series component and assuming we use the same preamplifier (i.e. having the same e_n), the equivalent noise charge will increase for this new matrix readout method over the traditional case by a factor ξ given by:

$$\xi = \sqrt{\frac{\left(N.C_d + C_w + C_f + C_{gs} + C_{gd}\right)^2 + N.C_d^2}{\left(C_d + C_w + C_f + C_{gs} + C_{gd}\right)^2}} \qquad 4\text{-}32$$

Consider a practical example where we assume that the parallel noise is negligible; C_d=60pF (25×25μm^2 detector); C_w=90pF; C_{gs}+C_{gd}=30pF; C_f=1pF. The equivalent noise charge will increase by a factor ~4 for a 10×10 array of detectors when using the matrix read-out. If we consider an array of 10^4 STJs each of size 10×10μm^2, C_d is lowered to 9.6pF, N=100, ξ becomes 8.3.

The degradation in noise performance can be compensated slightly by realising that each detector is read-out using an independent row and column amplifier. Since their series noise components are to a large extent uncorrelated, their signals can be combined thereby lowering the series noise component by a factor ~$\sqrt{2}$. In the above examples, ξ can be lowered to 3 and 6 respectively.

4.4.3.2 FET optimisation

In the previous section, we compared the noise performances using the same amplifier. Since the noise increase is mainly due to an increased input node capacitance, the pre-amplifier's input FET can be optimised. Since CMOS technology is more readily available for custom integrated circuit (ASIC) design we will consider a MOS input transistor, the analysis for a JFET being similar. Assuming operation in saturation, the transistor's transconductance (g_m) and related white series noise voltage (e_n) are given by:

$$g_m = \sqrt{2.\mu.C_{ox}.\frac{W}{L}.I_D} \qquad 4\text{-}33$$

$$e_n = \sqrt{4.k.T.\frac{2}{3.g_m}} \qquad 4\text{-}34$$

where μ, C_{ox}, W, L, I_D, k and T are the carrier mobility, gate oxide capacitance, effective channel width, length, drain bias current, Boltzmann's constant and temperature respectively. The transistor's gate capacitance is given by $2/3C_{ox}WL$.
If I_d and L are kept constant because of power and processing technology considerations, the optimum gate widths, which minimise the series noise power density, are:

$$W_{opt} = \frac{C_d + C_w + C_f}{2.C_{ox}.L} \qquad 4\text{-}35$$

$$W_{opt} = \frac{N.C_d + C_w + C_f}{2.C_{ox}.L}\sqrt{4 + \frac{3.N.C_d^2}{\left(N.C_d + C_w + C_f\right)^2}} \qquad 4\text{-}36$$

in the cases of standard and matrix readout respectively. The previously defined parameter ξ becomes:

$$\xi_{opt} = \left\{ \frac{N.C_d^2 + \left[N.C_d + C_w + C_f\right]^2 \left[1 + \frac{1}{3}\left[\sqrt{4 + \frac{3.N.C_d^2}{\left(N.C_d + C_w + C_f\right)^2}} - 1\right]\right]^2}{\sqrt{N.C_d + C_w + C_f}\sqrt{\sqrt{4 + \frac{3.N.C_d^2}{\left(N.C_d + C_w + C_f\right)^2}} - 1}} \frac{9}{16\left[C_d + C_w + C_f\right]^{3/2}} \right\}^{1/2} \quad 4\text{-}37$$

If $NC_d^2 << (NC_d+C_w+C_f)^2$, equation 4-37 can be simplified to:

$$\xi_{opt} = \left[\frac{N.C_d + C_w + C_f}{C_d + C_w + C_f}\right]^{3/4} \quad 4\text{-}38$$

Further applying the √2 improvement by signal combination, the noise degradation factors for the 2 examples given in the previous section are 2.3 and 4.1 respectively. This optimisation did not take the '1/f' noise into account. A '1/f' noise optimisation would require a 3 times larger input transistor compared to the 'white' noise optimisation [81]. An analytical solution including both 'white' and '1/f' series noise is not possible to derive since it depends on device parameters. Any real values for ξ will therefore likely be somewhat higher than those reported here. This analysis only shows what the maximum gain in signal-to-noise ratio can be achieved by optimising the input transistor's size.

4.4.3.3 Biasing issues

A more serious problem is related to the biasing of STJs. The Josephson current at zero bias voltage and the Fiske resonances are normally suppressed with a magnetic field of about 200 Gauss so as to ensure stable biasing. The suppression is very effective for single devices but is not perfect for all devices in an array. This is thought to be related to small geometrical differences between each junction and small magnetic field non-uniformities. When biasing an array, a sub-optimum magnetic field (for individual devices) has to be chosen and some residual Josephson current will persist. In order to bias the junctions this Josephson current has to be surpassed, i.e. the biasing network has to be able to provide sufficient current during the bias settling time and every time the junction is disturbed from its equilibrium bias point. Since our connection scheme involves a single bias circuit for each row (and column), it has to provide sufficient current to overcome the sum of all Josephson currents in a row (and column). As can be seen in Figure 4-14, this current has to be provided by the feedback resistor in the charge sensitive amplifier. A difficulty arises from the fact that a high value is needed for low parallel noise and a low value is required for providing sufficient bias current. Using an active feedback element as proposed for leaky semi-conductor detectors could probably solve this problem [90],[91].

4.4.3.4 Count rate issue

A photon absorbed in a particular junction has to be localized by a simultaneous detection in the corresponding row and column. If another photon is absorbed in another junction within the electronic response time, position ambiguity and possible pile-up can result. The position ambiguity can be resolved by using a fast threshold detection circuit. In principle, sub-microsecond response times are possible since a slow shaping time (optimized for best signal-

to-noise ratio) is not required for detection purposes. Therefore >1MHz rates are theoretically feasible.

To illustrate the effects, Figure 4-17 shows a scatter plot of the charge measured from a row versus that read from a column. Pile-up will occur if two events are absorbed either in the same junction or in the same row or column. Pile-up within the same junction is, of course, identical to the individual read-out case (regions 1 in Figure 4-17).

If two or more photons are absorbed within the same row or column but not in the same junction, they can be detected and analyzed separately since there will be no pile-up in the columns respectively rows (regions 3 and 2 in Figure 4-17). In this case however, the row and column signals cannot be combined for improving the signal-to-noise ratio since they will contain pile-up.

Another problem related to pile-up is the issue of infrared (IR) flux. Any heat source in the field of view of the detector will produce IR events in the detectors. These will see a base-line current increase together with a variance due to the statistical arrival of the photons. This variance can significantly reduce the resolution [92]. Each electronic chain will record the total IR flux received on its line as additional noise, which is N times higher than for the traditional read-out under the same illumination circumstances. Extreme care has to be taken in the design of baffling and filters for an instrument using these extremely sensitive detectors.

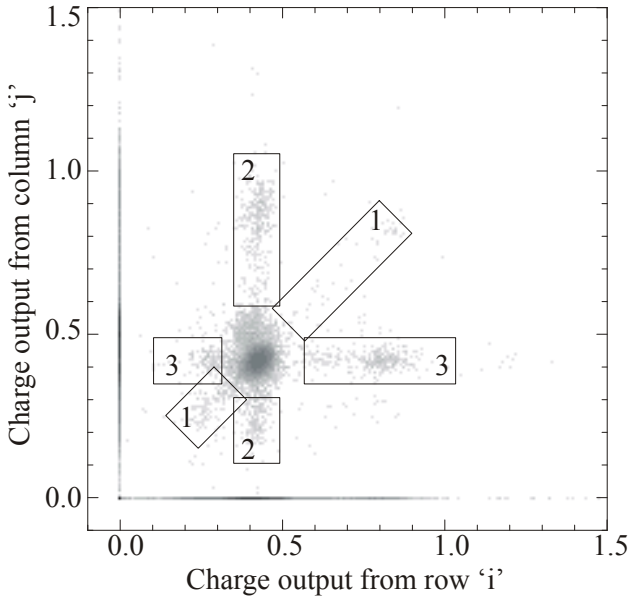

Figure 4-17: Scatter plot of the charge measured from a row versus that read from a column. Pile-up regions are delimited by rectangles. Regions 1 correspond to pile-up events in the junction at row 'i' and column 'j'. Regions 3 are pile-up in row 'i' only while regions 2 are pile-up in column 'j'

4.4.3.5 Diagnostics and yield

STJs are normally diagnosed by tracing their current versus voltage (IV) characteristic. Due to the fact that all junctions are interconnected in the matrix scheme, it becomes impossible to diagnose individual detectors. However, an IV curve is still a good analysis tool in that it will provide upper limits to the Josephson and sub-gap currents of the devices.

Note however that if a junction has a short, cannot be biased or is too noisy, it will spoil the complete row and column. This could pose a serious yield problem for large arrays.

4.4.4 Test Results

A Tantalum based 6×6 array produced by Oxford Instruments was used to test the matrix readout concept. A micrograph of the chip is shown in Figure 4-18. It has a lay-up of 100nm of Tantalum, 30nm Aluminium, an Aluminium oxide barrier followed by 30nm of Aluminium and again 100nm Tantalum. Each STJ is 25×25μm^2. For comparison reasons, a similar chip using the same trilayer, was fabricated with individual pixel access, see Figure 4-19.

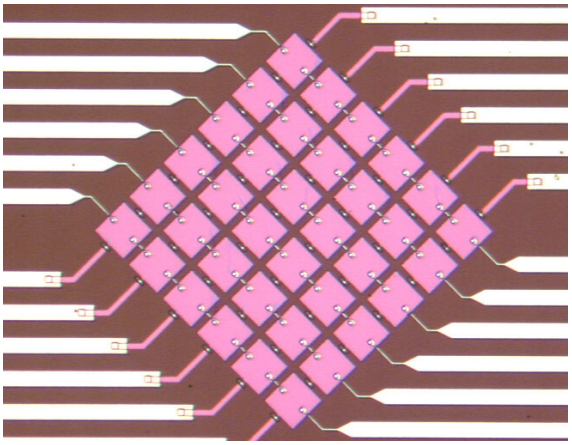

Figure 4-18: Micrograph of 6x6 Tantalum STJ array – Matrix read-out.

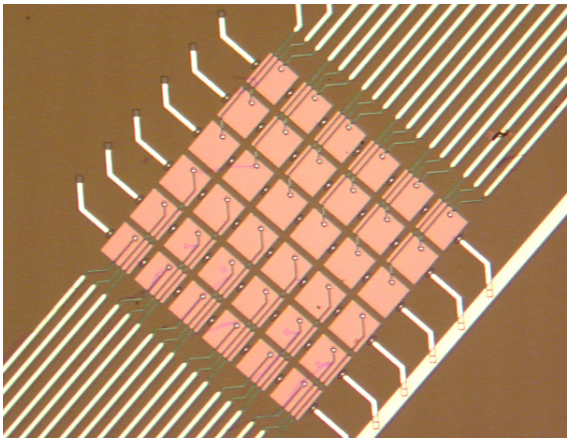

Figure 4-19: Micrograph of 6x6 Tantalum STJ array – Individual pixel read-out. Note the increased wiring complexity.

The measurements reported here were performed in an Oxford Instrument's Heliox system at a base temperature of 0.31K and with a magnetic field of 167 Gauss. At the time of the tests, only a 4-channel data acquisition system was available. Two channels (1 and 2) were used to bias and read the middle two lines while the other two channels (3 and 4) were connected to the middle two columns. The other four lines were biased at a fixed voltage while the four remaining columns were grounded. For the spectral measurements, the junctions were biased at 80μV (on Ch1 and 2 while Ch3 and 4 were kept at Ground potential). A connection diagram is given in Figure 4-20.

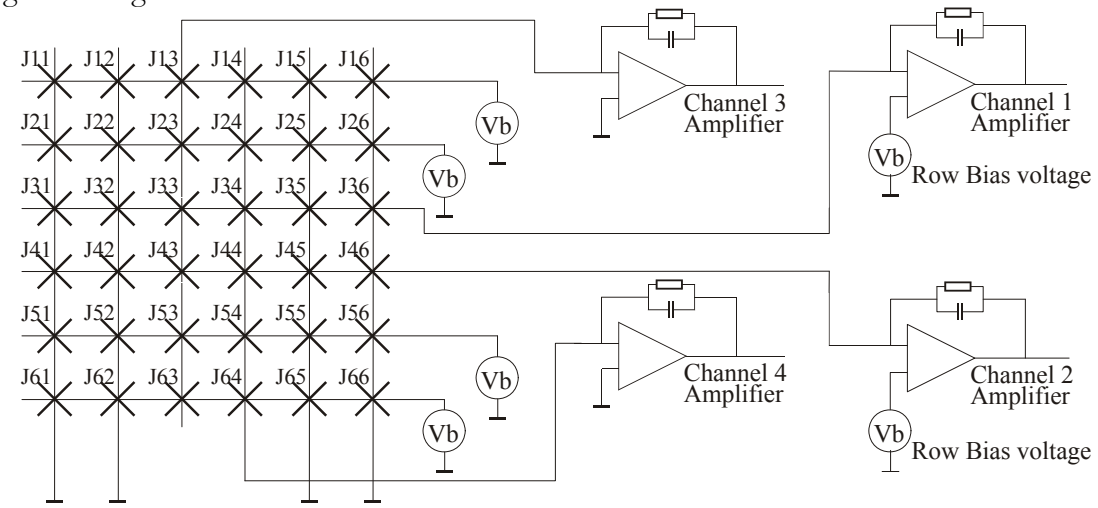

Figure 4-20: Schematic of test set-up; All lines are biased at V_b while all columns are at ground potential

4.4.4.1 The I-V Curve

As was discussed in section 4.4.3.5, individual STJs cannot be diagnosed but the curves can show upper limits on the sub-gap currents and residual Josephson currents. They will also show that no detector is damaged or has trapped flux. With all the columns grounded, each line was separately measured while sweeping the voltage between –500 and +500μV. The I-V curve for line 1 is given as an example in Figure 4-21. An enlarged plot is given in Figure 4-22 to show the leakage current. The sub-gap currents for all lines were below 0.5nA. This implies an average leakage current of 0.13pA/μm^2 at 100μV. The curves show lower currents at even lower bias voltage and it was found that the highest signal-to-noise ratio could be obtained at a bias of 80μV. The Josephson currents for all junctions were well suppressed at a magnetic field strength of 167 Gauss. All values were below 80nA for a complete line of 6 junctions. This is an important factor to ensure easy and stable biasing of the junctions during normal operations.

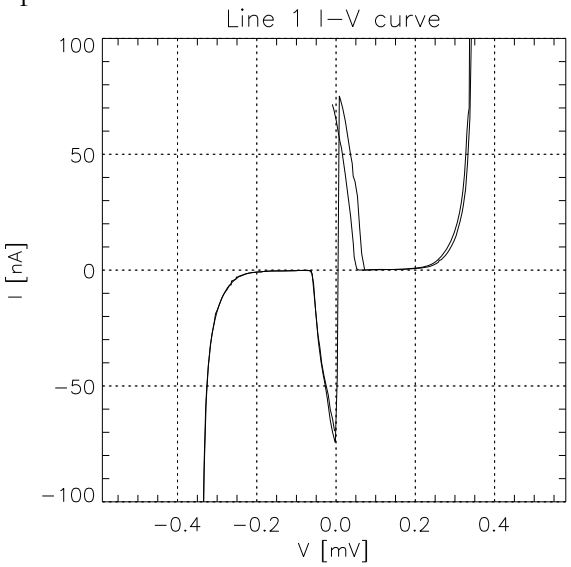

Figure 4-21: I-V curve for line 1, all columns grounded; residual Josephson current and first Fiske resonance onset visible.

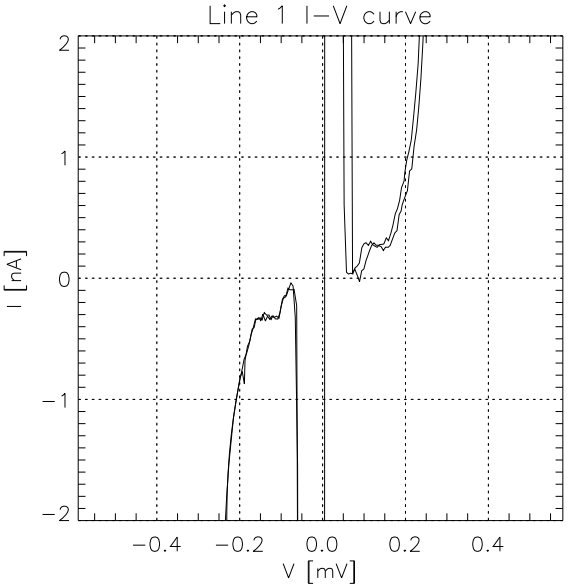

Figure 4-22: Zoom of Figure 4-21, shows sub-gap current.

4.4.4.2 Response to Photons

In order to detect photons, each pre-amplifier channel is followed by a slow[1] and a fast[2] shaping filter. The fast filter is used for triggering and time stamping the events while the slow filter is optimised for accurate pulse amplitude measurements (PHA). Data files contain an event list of the fast and slow samples of all 4 channels and a time stamp for each trigger. A Xenon lamp with a double monochromator was used as a light source and coupled to the detector array via an optical fibre. Illumination was through the sapphire substrate. Measurements were performed at 225, 250, 300, 400, 500, 600 and 800nm wavelength (5.5, 5, 4.1, 3.1, 2.5, 2.1 and 1.6eV photon energy resp.). The responsivity of the detectors was found to be of order 4800 electrons per eV, while the pulse decay time was about 3μs. Using an energy gap, Δ, of 0.52meV, we find that each quasiparticle tunnels on average ~4 times.

[1] Filter centre frequency = 16kHz
[2] Filter centre frequency = 65kHz

4.4.4.3 Channel Correlation

Figures 4-23 and 4-24 show grey-scaled 2-D histograms of one (slow-PHA-) channel against another when the detector was illuminated with 300nm (4.1eV) photons. Clear correlation can be seen between channels sharing a common STJ (Figure 4-23, J_{34}). Channels which do not share a detector only have a few points off the axes. In the case of channel 1 versus channel 2 (Figure 4-24), these correspond to pile-up events and represent only ~0.17% of the total amount of recorded events in this particular case, in agreement with the expectation for a photon flux of ~400Hz in each channel and the acquisition electronics' characteristics. The ratio of total number of events recorded in a particular channel to the number of correlated events between 2 channels was systematically 1/6. This implies that each line and each column was indeed recording the events from all its corresponding 6 detectors.

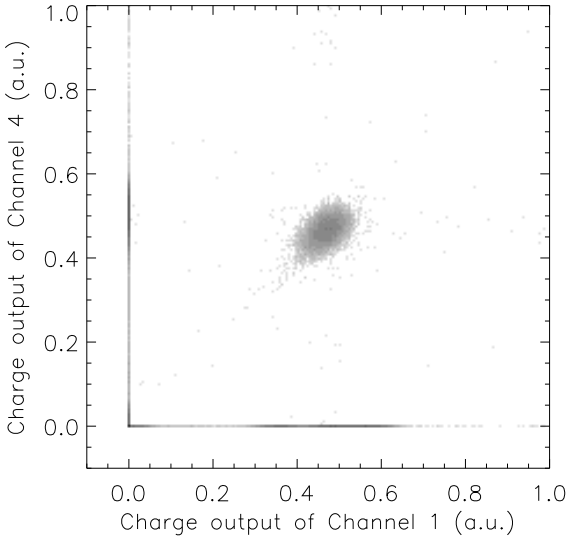

Figure 4-23: 2-D histogram of CH1 vs. CH4.

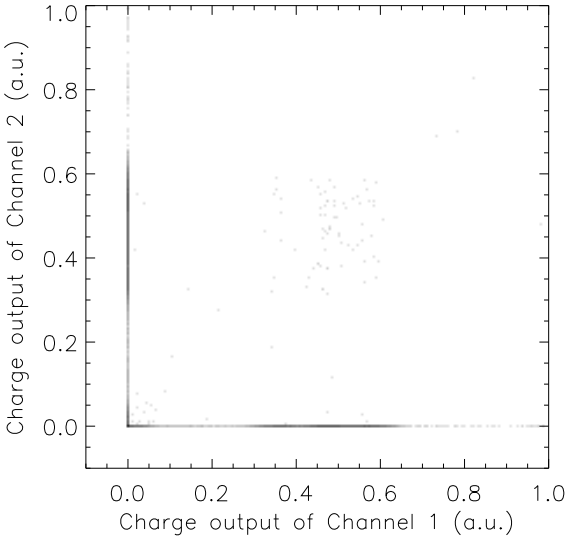

Figure 4-24: 2-D histogram of CH1 vs. CH2.

4.4.4.4 Spectra

For each junction, events were retained by selecting those, which had a non-zero signal in both its corresponding channels. For instance for junction J_{33}, valid events were those for which channels 1 and 3 were simultaneously triggered within the coincidence window of 5μs. Figure 4-25 shows the spectra accumulated with the channels connected to junction J_{34} while illuminating the array with 500nm (2.5eV) photons. The plots include the fits used for calculating the resolution.

For each junction, the line resolution was computed on each of its corresponding acquisition channels. The average resolution, Full Width at Half Maximum (FWHM, in eV) for each pair of channels is plotted in Figure 4-26 as a function of photon energy as well as the average of all pixels.

As mentioned in section 4.4.3.1, combining the line and column values for each pixel, the electronic noise contribution can be reduced. This is shown in Figure 4-27 together with the measured electronic noise. Also shown in this plot is the calculated intrinsic detector resolution, obtained by quadratically subtracting the electronic noise from the measured line resolution.

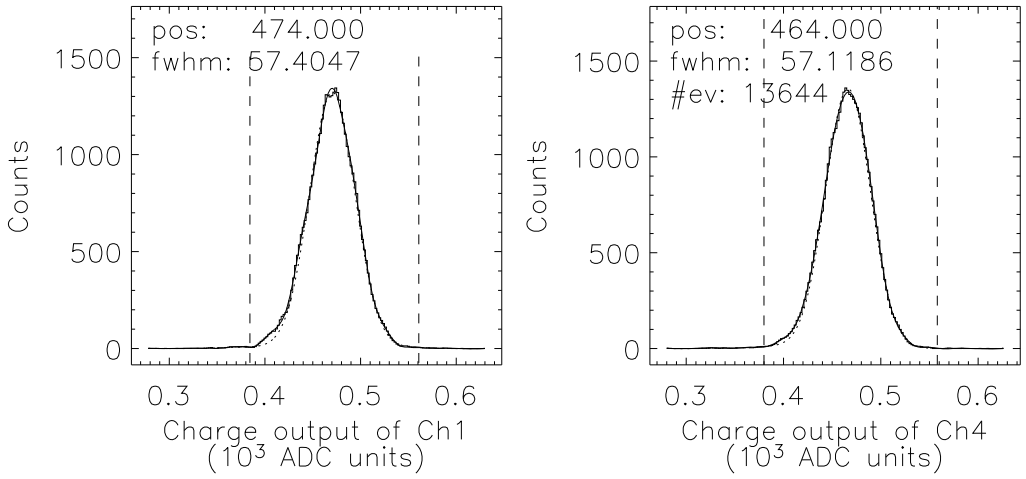

Figure 4-25: Spectra obtained for J_{34}, 500nm (2.5eV) illumination.

In order to verify the hypothesis of electronic noise reduction, we compared a predicted FWHM resolution to the actual measurement. The predictions were in all cases within ~6% of the actual value. To take an example, consider λ=500nm (2.5eV), junction J_{34}. The measured spectral line widths on CH1 and CH4 were 0.439eV and 0.485eV respectively. The electronic noise on CH1 was measured at 0.406eV. Unfortunately, no direct noise measurement was available on channels 3 and 4 because of their signals inverted polarity. An additional inverting amplifier had to be inserted between the preamplifier and the pulse height analyzer for those channels. This also inverted the test pulses used for noise measurements, which consequently went undetected. By making the assumption that the intrinsic detector resolution must be identical in both channels, we can derive the electronic noise on CH4 to be:

$$\sqrt{\left[0.485^2 - \left(0.439^2 - 0.406^2\right)\right]} = 0.455\text{eV}$$

The expected resolution obtained by summing the signals from CH1 and CH4 is then:

$$\sqrt{\left[\left(0.439^2 - 0.406^2\right) + \left(0.406^2 + 0.455^2\right)/4\right]} = 0.348\text{eV},$$

which is close to the measured value of 0.366eV.

The resolution enhancement obtained by combining row and column measurements is a function of energy since it depends on the ratio of the intrinsic detector's resolution to the electronic noise. The gain in resolution was found to increase from 18% at 5.5eV (225nm) to 29% at 1.55eV (800nm).

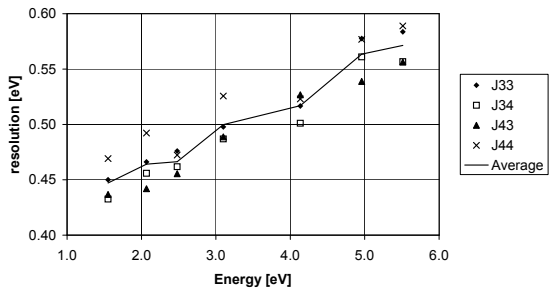

Figure 4-26: Line resolution (FWHM [eV]) as a function of energy for all 4 junctions. The average resolution from both channels is used for each junction.

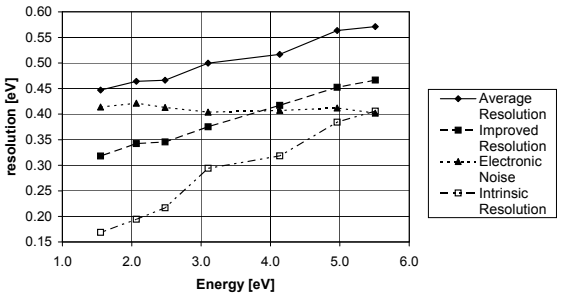

Figure 4-27: Average Line resolutions (FWHM [eV]) as a function of energy including improved resolution obtained by row and column signal combination. The electronic noise and resulting intrinsic resolution of the detector are also shown.

4.4.5 Comparison with traditional pixel readout

A comparison chip (pixel chip) with individual pixel connections was processed in parallel to the matrix chip. The layers thickness and pixel sizes were identical which allowed us to compare basic characteristics like charge output and resolution between the two readout concepts. The average leakage currents on the pixel chip were ~0.3nA per pixel. One of the devices (J_{16}) was clearly better than the others with 0.1nA leakage current at 200μV and was used for all further measurements. The pixel chip had an average responsivity slightly larger than the matrix chip at 6000 electrons per eV, versus 4800. The larger responsivity can in part be explained by the higher bias voltage used for the pixel array and from the manufacturing process. The pulse decay times (3μs) were identical to within a measurement error of 10%.

Spectra were taken with the pixel chip at the same photon energies as previously. For these, the best junction available was used at its optimal magnetic field of 166G and bias voltage of 100μV. The average electronic noise for this pixel was found to be 0.277eV, while the matrix chip had 0.411eV electronic noise averaged on each channel and over all energies. By combining row and column data, the matrix chip's electronic noise could be lowered to 0.26eV on average, similar to the pixel array, within the error bars.

A comparison plot of energy resolutions obtained with both chips is given in Figure 4-28. It shows the Matrix chip's resolution averaged over all junctions and channels as well as its improved resolution by adding row and column signals. The resolutions can be compared to that of the best available single pixel from the pixel array. The matrix chip's improved resolution is slightly worse than the individual pixel chip, ranging from 0% at 800nm (1.6eV) to 10% at 225nm (5.5eV). This degradation can partly be explained by the lower responsivity of that device. Note that a degradation of 20% is recorded at 250nm (5eV).

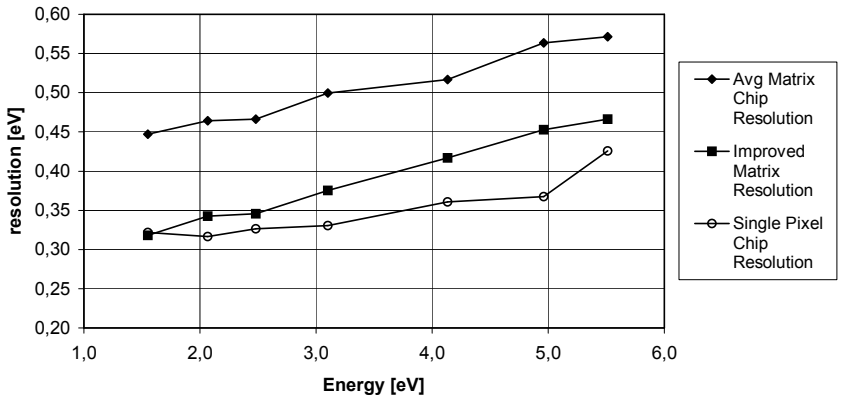

Figure 4-28: Comparison of energy resolutions between matrix and pixel chips.

4.4.6 Conclusions

We have presented a novel connection scheme for arrays of pixelated detectors. This scheme drastically reduces the number of wires and circuitry necessary for reading out large array detectors. We have presented results obtained on a 6×6 array of STJs using optical photon excitation. We have shown that these devices can be properly biased and show good spectral resolution. We also confirmed that the signals from rows and columns could be combined to improve the signal-to-noise ratio. The energy resolutions obtained are on average only 10% worse when compared to the traditional individual single-channel readout measured on the best available pixel device of the same process batch. We attribute this difference to sub-optimal magnetic field and bias voltage settings in the matrix channel read-out.

4.5 SQUID based preamplifiers

If we want to develop larger focal plane arrays, the excessive number of wires required with room temperature electronics will be rather prohibitive and a different solution will need to be sought. As we have seen in the previous chapter, the matrix readout scheme could help, but a more elegant solution would be to perform preamplification together with multiplexing close to the detector array. In previous paragraphs, it became clear that the traditional CSA has some shortcomings when used in conjunction with STJs. For one, semiconductor amplifiers are difficult to operate cryogenically without suffering considerable excess noise, kink and hysteresis effects [93]. Only recently have there been some interesting developments at IMEC, using a standard CMOS process [94]. Secondly, STJs need to be stably biased at voltages much lower than typical offset voltages occurring in electronic circuits. Finally, the circuits presented above would cause unacceptable power dissipation at these low temperatures. For example, the IMEC circuit, while achieving an impressive $200e^-_{rms}$ noise, dissipates 4.5μW per channel at 4.2K and does not have any features for offset compensation to the level required, nor the necessary bandwidth to readout STJs.

Instead, we investigated the possibility of using SQUIDs as preamplifiers. An amplifier and multiplexing SQUID circuit has already been used to readout large IR focal plane arrays based on transition edge sensors [85]. For optical and X-ray detection, faster closed-loop solutions are now also being developed [95],[96]. Although several SQUID configurations could be used in combination with STJs, such as RF, DC, DROS etc., our focus has been on the commercially available high speed DC-SQUID from Hypres [97] which was originally developed at NIST [98].

A DC-SQUID consists of two Josephson junctions connected in parallel in a superconducting loop. In order to suppress the junctions' hysteretic behaviour, they are shunted by very low valued resistors. If biased above the junctions' critical current, the SQUID presents a periodic voltage to flux relation (for details see for instance [99]). The basic SQUID loop is often tightly coupled to an input coil, which converts the current to be measured into flux. For our setup we used a Hypres single-stage series SQUID model M236-4 2904D29. In this design, a series connection of 100 SQUIDs are coupled to a 0.3μH input coil and a smaller feedback coil. The series design has the advantage of being able to connect the SQUID array directly to a room temperature voltage amplifier eliminating the need for AC flux modulation with lock-in detection as well as an output flux transformer. Lower noise current densities than those reported for the Hypres SQUIDs are achievable but those designs either lack the large bandwidth required for STJ current pulses or require much more sophisticated lock-in techniques, impractical for large format STJ array read-out.

Figure 4-29 shows the I-V curve of the device. The vertical axis is the current through the device with a 50μA/div. scale. Figure 4-30 is a typical V-Φ curve. The horizontal axis is the current through the input coil (6.7μA/div.), while the vertical axis is the output voltage after the ×100 room temperature amplifier. While the manufacturer reports 10mV maximum modulation depth when all devices are in phase, our measured modulation depth is nearly ideal at 8mV. The input coil coupling is as specified at $24\mu A/\Phi_0$.; the gain is 1300V/A on the positive slope of the V-Φ curve. The white noise levels at the SQUID output were measured at $4.5nV/Hz^{1/2}$, which translates to $3.5pA/Hz^{1/2}$ at the input coil.

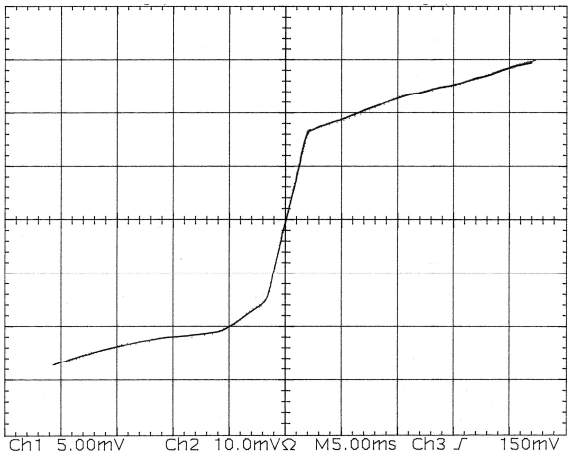

Figure 4-29: SQUID I-V curve. Vertical scale is 50μA/div; Horizontal axis is the applied voltage at 5mV/div.

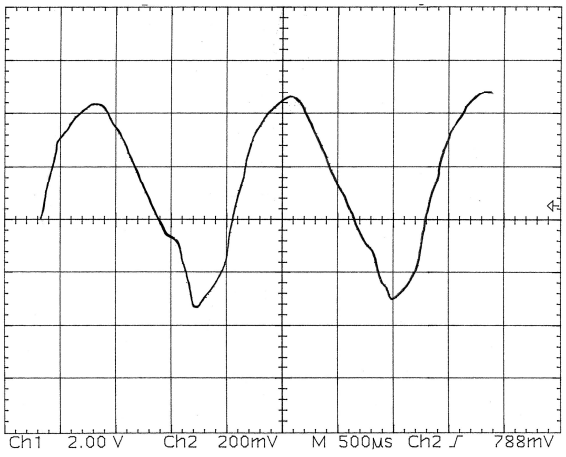

Figure 4-30: SQUID V-Φ curve. Horizontal scale is 6.7μA/div input coil current. Vertical scale is 2mV/div output voltage.

4.5.1 SQUID pre-amplifier configuration

The SQUIDs are coupled to the STJ as shown in Figure 4-31 [100]. Resistor R_d and capacitor C_d model the detector. Typical values are >100kΩ and 900pF for a 100×100μm² detector. Resistor R_2 effectively produces a voltage bias to the STJ. Its value should be low (compared to R_d) to provide good voltage biasing and low Johnson noise. Resistor R_1 forms in conjunction with the SQUID's input coil a low pass filter and should be tuned for an optimal damping of the L_{sq}-C_d circuit. Conflicting requirements arise here since R_1 should be small to provide sufficient low-pass filtering but at the same time high to reduce the effects of thermal noise. In our case it is designed to have a cut-off frequency of several MHz and a damping coefficient of 0.7. In our design for a 100×100 μm² STJ detector with 900pF capacitance, R_1 is 10 Ω and R_2 is 5 Ω. The resulting R-L-C filter has a cut-off frequency of 8 MHz ($\omega_0^2 = \frac{R_2}{L_{sq}C_d(R_1+R_2)}$) and a damping coefficient ($\xi = \frac{L_{sq}+R_1R_2C_d}{2\sqrt{L_{sq}C_dR_2(R_1+R_2)}}$) of 0.85. The voltage noise induced by R_2 onto the STJ ($\sqrt{4.k.T.R_2.BW}$) is $2.5\times10^{-8} V_{rms}$ (at 0.3K) and is well below the requirement. The noise current density generated by R_1 is 1.3pA/Hz$^{1/2}$ (at 0.3K), which is less than the SQUID's noise. The detector's dynamic resistance has not been included in the calculations since its value is much larger than the other resistors involved. The SQUID array is coupled to a room-temperature voltage amplifier followed by appropriate filtering and sampling. For a single STJ readout, a minimum of six wires are required; ground return, STJ bias resistor current, SQUID bias and read-out, feedback coil (flux bias) and the on-chip heater (flux de-trapping). The number of connections per STJ to room temperature can be reduced for arrays, since the bias resistor R_1 and ground return can be shared amongst many STJs and the SQUID heaters can be connected in parallel. This all will make only sense in a real application if a cryogenic multiplexing scheme is implemented as well.

The SQUID chip was mounted on an alumina substrate, fixed in a Niobium can. The wiring was twisted and shielded in lead-tin solder tubes, after removing the solder flux. This configuration guaranteed a flawless operation, without any need to de-trap magnetic flux. A picture of the assembly is given in Figure 4-32.

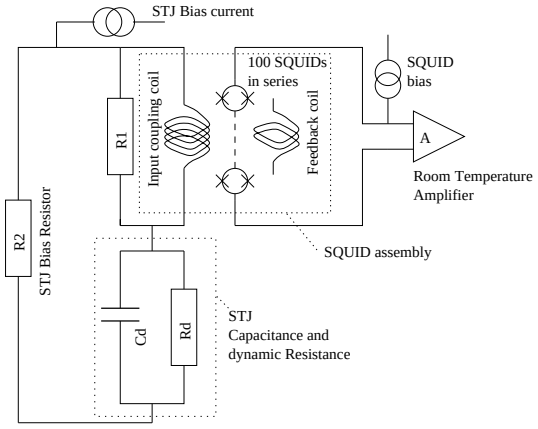

Figure 4-31:Electrical schematic of the SQUID, biasing and STJ assembly.

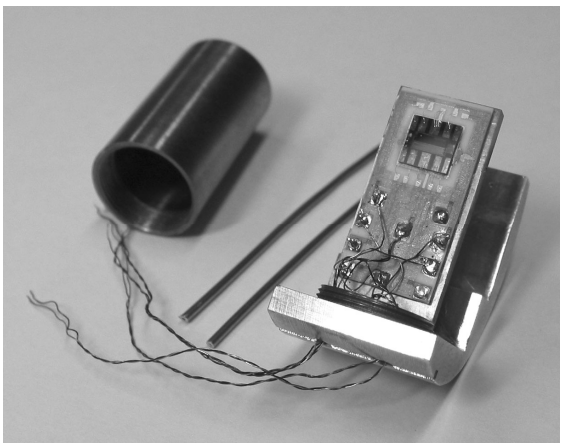

Figure 4-32: SQUID assembly: the chip is mounted on a ceramic substrate which is glued to a Cu strip. The whole assembly is enclosed in a Nb can (left cylinder).

For the experiment, we used a 100×100μm^2 Niobium STJ operated at 1.2K. Operation of a Tantalum STJ at 0.3K was not possible due to the use of Molybdenum shunt resistors in the SQUID array, which would become superconducting. Later versions of the SQUIDs used Palladium resistors, but these were not available at the time of this work. A typical STJ current pulse measured with this SQUID is depicted in Figure 4-33; the rise time is of order 100ns, decay time ranges between 5 and 30 microseconds depending on the particular detector design and the peak value is of order 1mA for a 6keV photon. Although the feedback coil can be used in a closed loop configuration (flux locked loop technique) to increase linearity and dynamic range, we only use it to position the operating point in the middle of a V-Φ cycle for maximum amplification. The detector's peak current of about 1mA is well below the 5 mA needed for reaching the maximum of the V-Φ modulation curve.

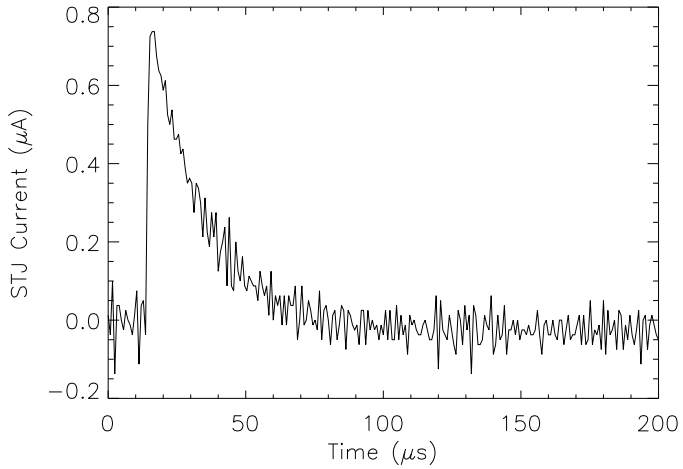

Figure 4-33: Typical current pulse from a 6keV photon absorbed in a Niobium STJ

4.5.2 Noise evaluation

For the present equivalent noise charge (ENC) calculations, we have considered the above mentioned design example for the 100×100μm^2 detector. The reported noise current of the SQUID array is 2pA/Hz$^{1/2}$ with a 1/f corner frequency of 1 kHz. Actual noise performance depends however very significantly on the environment. The transfer function is about

2000V/A which implies an output noise voltage density of 4nV/Hz$^{1/2}$. In order not to degrade the signals further, the follow-on amplifier therefore still needs to have a very low noise voltage. To evaluate the equivalent noise charge at the input of the SQUID and compare it to previous results with traditional CSAs, we considered a SQUID amplifier followed by a voltage amplifier (gain A_1) and an n-stage integrator (shaper) with time constant τ_1 and DC-gain A_2. In principle, a differentiator is not needed since the current amplifying SQUID replaces the integrating CSA. In a real application however, a high-pass filter needs to be implemented to reduce the effects of low frequency noise. For analysis purposes, we only considered the SQUID's white noise of current density i_w. Our goal was to determine the optimum shaping time and compare this with ENC values obtained for JFET CSAs. Clearly, if we consider a Dirac impulse at the SQUID's input, the optimum shaping time would be as small as possible. However, the pulses from the STJ have finite rise and decay times. Since the rise times are at least an order of magnitude smaller than the decay times, we only considered the latter, τ_0. The output voltage's Laplace transform for a single electron charge at the input is given by equation 4-39, while the rms noise voltage ($V_{n,o}$) at the output is given by equation 4-40. Total ENC is obtained by calculating the ratio of the noise voltage to the peak of the inverse Laplace transform of 4-39.

$$V_0 = A_1 A_2^n R_{sq} \left(\frac{1}{1+s\tau_1} \right)^n \frac{e}{1+s\tau_0} \qquad 4\text{-}39$$

$$\left|V_{n,0}\right|^2 = A_1^2 A_2^{2n} R_{sq}^2 \int_0^\infty \left|i_w\right|^2 \left| \frac{1}{1+j2\pi\tau_1 f} \right|^{2n} df \qquad 4\text{-}40$$

A first order approximation is given by 4-41, where B_f is the bandwidth of the shaping filter, $i_{n,sq}$ is the SQUID noise current density and $i_{n,sh}$ the detector's leakage current's shot noise.

$$ENC_{rms} \approx \sqrt{\frac{i_{n,sq}^2 + i_{n,sh}^2}{4\pi^2 B_f}} \qquad 4\text{-}41$$

The ENC (FWHM) has been calculated for a noise current density of 2pA/Hz$^{1/2}$ and different pulse decay times, using equations 4-39 and 4-40. The results as a function of shaping time (τ_1) are plotted in Figure 4-34. Table 4-1 gives the minimum ENC in electrons (FWHM) and the corresponding optimum shaping time for each of the pulse decay times considered (τ_0). The Hypres series SQUID shows no improvement over the JFET CSA. Qualitatively, the low impedance SQUID is not well matched to the high impedance detector. A real advantage could occur if the detector's capacitance is larger than 70nF (900×900μm^2 STJ), in that case, the white voltage noise of the JFET by itself would induce an ENC equal to 10^5 electrons. On the other hand, the SQUID amplifier is very tolerant with regard to detector leakage currents since a 12mA current is required to reach the SQUIDs white noise floor.

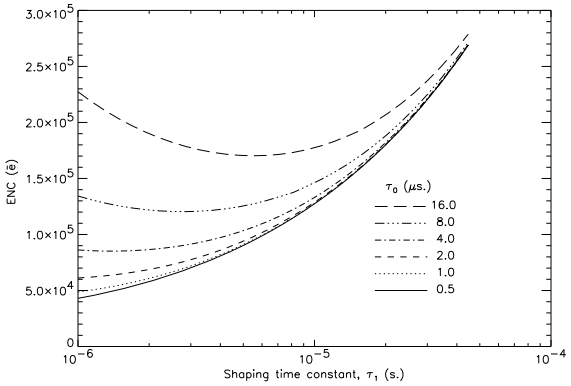

Figure 4-34: ENC as function of filter shaping time, for different pulse decay times.

Table 4-1: Min ENC as function of pulse decay time

ENC min (e^-)	τ_1 at min [μs]	τ_0 [μs]
$< 4.3\times10^4$	< 1	0.5
$< 4.9\times10^4$	< 1	1.0
$< 6.1\times10^4$	< 1	2.0
8.5×10^4	1.3	4.0
1.2×10^5	2.9	8.0
1.7×10^5	5.5	16.0

4.5.3 SQUIDs in the Matrix readout scheme

As we have just shown, the current generation of SQUIDs will have better noise performance than CSAs if the detector's capacitance is large. An obvious example is in the Matrix readout scheme where we have seen that noise will degrade as we add more junctions to the lines and columns. Figure 4-35 shows the matrix readout scheme using SQUIDs. In this case, each SQUID senses a line or column and the shot noises of all corresponding detectors add quadratically (see Figure 4-36). Additionally, the row amplifiers sense the noise sources in the column amplifiers (and vice-versa). This is illustrated in Figure 4-37.

For an N×N matrix, the noise current spectral density and the ENC at the input of the SQUID can be approximated to first order by:

$$i_{n,in} \approx \sqrt{\left(i_{n,\mathrm{R1}}^2 + i_{n,sq}^2\right)\left(1+\omega^4 L_{sq}^2 C_d^2 N\right) + i_{n,\mathrm{R2}}^2 \omega^2 R_2^2 C_d^2 + N i_{n,sq}^2} \qquad 4\text{-}42$$

$$ENC_{rms} \approx \sqrt{\frac{i_{n,sq}^2 + N.i_{n,sh}^2}{4\pi^2 B_f}} \qquad 4\text{-}43$$

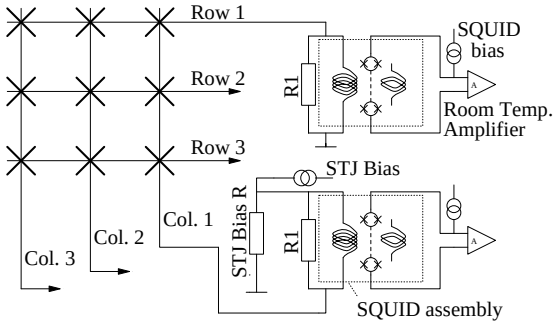

Figure 4-35: STJ array with SQUID amplifiers connected in Matrix scheme.

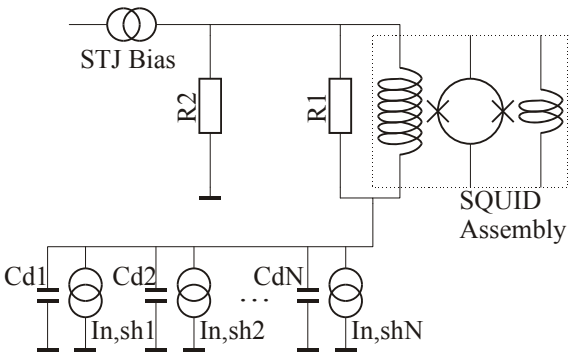

Figure 4-36: Schematic of the noise sources resulting from the parallel connection of STJs in rows and columns.

Contrary to what was the case with a JFET amplifier, the noise level will not increase by the matrix connection scheme other than the expected rise in shot noise from the detectors' leakage currents.

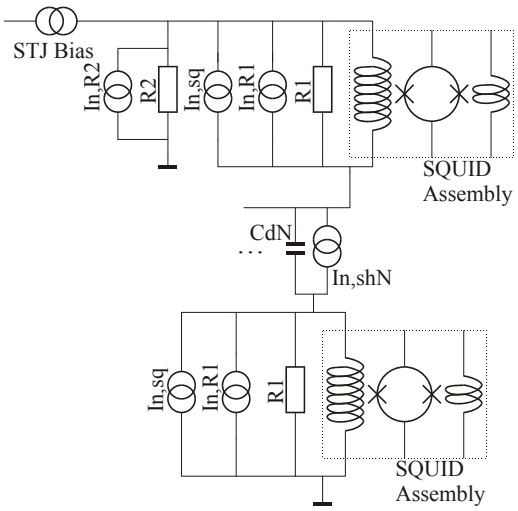

Figure 4-37: Schematic representation of the influence on the row's amplifier by the column's amplifier noise.

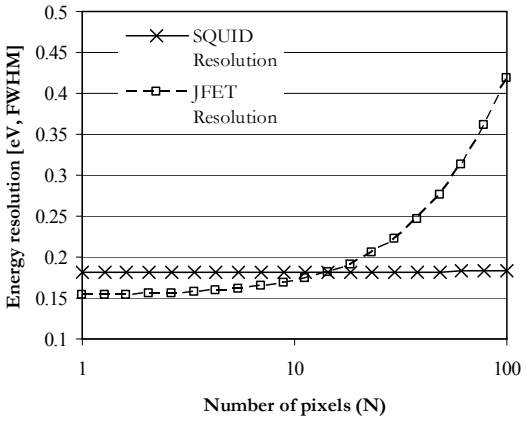

Figure 4-38: Energy resolution [eV, FWHM] as a function of array size (matrix readout of a NxN array); Comparison between the JFET and SQUID preamplifiers.

4.5.4 Optical photon detection

We shall derive now some noise specifications for the SQUID in the case of optical photon detection. For this purpose we shall assume a 200×200μm^2 detector or, for noise analysis otherwise equivalent, a 100×100 array of 20×20μm^2 STJs connected in matrix. For optical photon detection, a practical upper limit to the photon's wavelength might be ~1μm. This is set by the need to adequately filter the infrared background which would otherwise compromise the detector's energy resolution. At that wavelength, a tunnel-limited resolution of 0.1eV is achievable for Ta devices. Using a detector's responsivity of 10^4 e$^-$/eV, the SQUID's noise contribution should be less than about 400e$^-_{rms}$. If one further assumes a filter bandwidth of ~26kHz (equivalent to a 6μs shaping time), a current spectral density less than 70fA/Hz$^{1/2}$ is required from the SQUID. Currently available SQUIDs have current noise levels of the order of ~1pA/Hz$^{1/2}$ [97],[101] and are therefore not suitable. Although quantum-limited SQUIDs have been demonstrated over the last few years, their coupling to STJs is not optimal. A redesign of the coupling transformers as well as a lowered operating temperature (0.3K versus the more common 4.2K) should however make the goal achievable.

Figure 4-38 is a comparison of the energy resolution one can expect for a JFET amplifier and a SQUID amplifier as applied to an N×N Matrix array of STJs. In this particular case, the SQUID (with 70fA/Hz$^{1/2}$ white noise level) will be better than an optimum JFET for N>14. From the curve, one can also verify that the leakage current of even a large number of detectors hardly degrades the energy resolution.

4.5.5 X-ray photon detection

For X-ray detection and in particular for an application like XEUS, ESA's potential next X-ray observatory, the photon energy range of interest would be about 100-2000eV. The lower limit is being imposed by the use of aluminium filters to block UV/optical and IR flux. The higher limit is set by the reduced blocking efficiency of high energy X-rays by the thin superconducting STJ films.

The noise criterion of the SQUID can be relaxed compared to the optical case since the tunnel-limited detector resolution is ~0.9eV at the lowest X-ray energy. This yields a requirement of 0.6pA/Hz$^{1/2}$ as a maximum SQUID current noise power density. As for the matrix readout of optical photons, a similar calculation can be performed for the individual

readout of an STJ, this time as a function of detector size. Using the same parameters, one finds that the SQUID performs better than an optimised JFET for a detector larger than ~80×80μm^2.

For X-rays, the current generated by the STJ is likely to cause the SQUID to loose lock. This is particularly true since we have shown here that the input inductance of the SQUID needs to be increased considerably. For this application, a flux lock loop design is a must. A digital Double Relaxation Oscillation SQUID, as proposed by Podt et al. [102] could be a way to reduce the number of wires to room temperature.

4.5.6 Slew rate and damping

Although the rising edge of the current generated by an STJ following a photo-absorption is rather steep, slew rate should not be a real problem. The signal is effectively low-pass filtered by the SQUID's input inductance. The fact that the SQUID does present a finite impedance at higher frequencies could be a problem for the stability of the detector's voltage bias. During the pulse's rising edge, the voltage across the detector will vary, causing potential non-linear effects. The real impact of this has to be studied in detail in a practical implementation.

The STJ/SQUID assembly is an L-C tank circuit that needs to be damped. This is the role of resistor R_1 in Figure 4-31. For a critically damped system, the value of this resistor should be $0.7\sqrt{L_{sq}/C_d}$. For the inductance and capacitance values quoted in this study, the resistor should have a value of the order of tens of Ohms. This is compatible with the noise requirement for X-ray detection, but not necessarily for optical photons. In this case, one can calculate that for its Johnson noise to be sufficiently low, its value should be in excess of 3500Ω. Additional damping should therefore be provided by R_2 and a larger L_{sq}. Again, in a practical design these values shall have to be optimised.

4.5.7 Conclusions

Current SQUIDs are difficult to couple to the high impedance STJs because of the specific design of their coupling coils. With a redesign of the coupling coil, effectively increasing the flux for a given input current, and lowering their operating temperature to that of Ta STJs, we have shown that SQUIDs can be good competitors to CSAs.

The advantages of the SQUIDs can be summarized as follows:

1. the SQUIDs are coupled to the STJs by means of inductive transformers and, hence, the STJ current rather than the charge is measured. Since SQUIDs only exhibit parallel noise, the detector's capacitance doesn't play a direct role in the ENC and therefore these devices could be used in conjunction with large area, large capacitance junctions, or for matrix readout.
2. SQUIDs need to be cooled to cryogenic temperatures as well and can be placed directly next to the STJs, avoiding the necessity of coupling the STJs to the first amplification stage by means of very long, and again capacitive, wires. These wires remain a necessity, of course, but will carry larger signals from a lower impedance source and be less sensitive to microphonic noise pick-up.
3. The lower output impedance of the SQUID array will reduce the crosstalk between pixel wire connections to room-temperature for STJ array read-outs.
4. STJ biasing is simpler since this can be achieved by current biasing a small fixed resistor located next to the STJ. Several STJs can actually be biased in parallel by the same circuit, drastically simplifying the circuitry for STJ array read-out.
5. SQUIDs could be used to multiplex the signals from a large number of array pixels, drastically reducing the number of connections to room temperature electronics.

4.6 SARA64 – a 64-channel preamplifier ASIC

As we have seen, the major complexity associated with reading out STJs is related to providing a low and stable bias voltage in the range of ~100μV while minimizing noise sources. Until now, this is achieved by using amplifiers built from discrete components.

Since a 120-pixel device has already been deployed on S-CAM3, it is clear that any future generation will require many more readout channels. Even though the discretely built system can be further expanded with additional channels and could be conceived for ground applications, eventually, its volume would become excessive and impractical. This is even more so for a space application where mass and power need to be minimized and another solution needs to be sought. Clearly there is a need to develop highly integrated readout electronics. For this purpose, we attempted a development of two ASICs with the help of the Norwegian company IDEAS [103].

The concept was to integrate as many analog chains as possible into a CMOS ASIC [104]. The final architecture comprised two chips which are schematically represented in Figure 4-39. The principle of these chips can be traced back to Si microstrip readout ASICs developed at CERN [105]. The system was complemented by multiplexers (MUX), ADCs and digital signal processors capable of reading out 128 channels, see Figure 4-40. The ADC card has 16 channels running at 20MHz with 12 bits resolution; each is connected to a MUX serving eight preamplifier outputs, effectively sampling each channel at 2.5Msamples/s. In the case of an event, the trigger chip signals the ADC card which then directs the relevant data samples, including pre-trigger samples, to a DSP card. The commercial DSP card (Eagle Mango) consists of 12 ADSP-21062 SHARC processors. The S/W is set up such that a central DSP controls the data flow based on interrupts and manages the other processors such as to distribute the filtering tasks evenly between the processors.

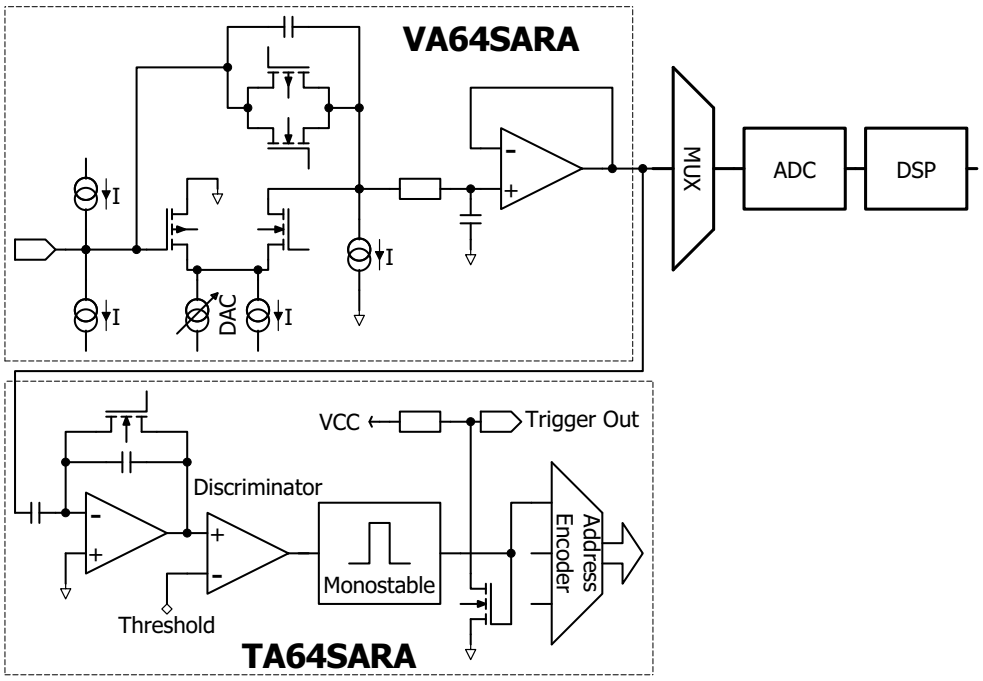

Figure 4-39: VA64SARA and TA64SARA functional description. The VA chip provides bias and pre-amplification while the TA chip detects events above threshold.

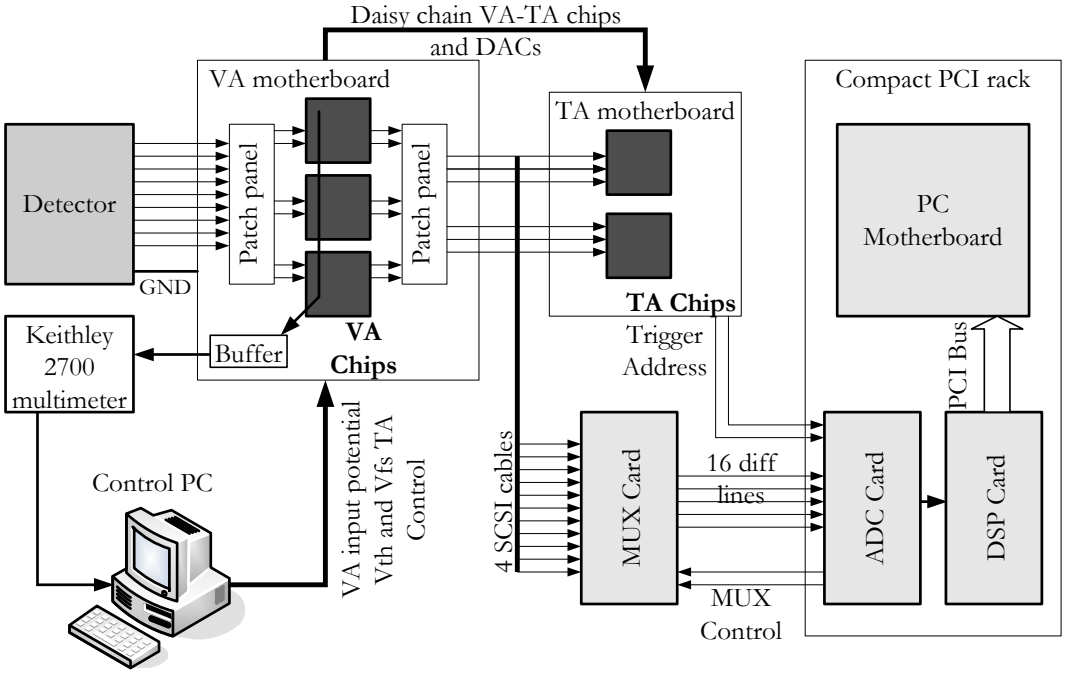

Figure 4-40: Schematic representation of the complete readout system used for characterizing the ASICs

4.6.1 The VA64SARA

The VA64SARA ASIC is a 64-channel low-noise, low-power charge sensitive preamplifier circuit. This chip was specifically designed to readout STJs operating as photon detectors in the visible and UV wavelength range. Each amplifier channel further includes a low-pass (anti-aliasing) filter, output buffer, input bias voltage control and a leakage current compensation circuit. The ASIC occupies an area of ~8.2×7.3mm² and is implemented in a 0.8µm N-well CMOS double poly, double metal AMS process [106].

In the micrograph shown in Figure 4-41, analog input and output pads are on the left and right respectively. Top and bottom pads are reserved for the digital signals and chip bias voltages. The chip requires separate ±2V supplies for the analog and digital parts. Total nominal power consumption is 400mW or ~6mW/channel.

Only about one third of the chip's area (left in the picture) is needed for the actual amplifiers, whereas the rest of the chip consists of the digital-to-analog converters (DACs) used for controlling the input offset voltage and detector bias. These current DACs, one for each channel, have 10 bits resolution and control the Drain current of the input transistor. This allows for a nominal offset adjustment range of ±5mV and a resolution of ±5µV. The actual range and resolution is externally controllable by a bias current.

A calibration routine is executed after power-up, which measures the input offset values and corrects the DAC settings. Since changing a particular DAC value has a small influence on the others, due to different drawn current values, an iterative procedure is required. Typically, 5-6 iterations are required to reduce the offset voltages below 10µV. Figure 4-43 shows the results obtained after 15 iterations for each of the 64 channels on 2 separate chips.

The left axis is the residual offset voltage while the right axis shows the digital DAC values. Chip 2 can clearly be compensated correctly (only 1 bad channel) while many DAC values saturate (at 0) for chip 1, hence this ASIC is not usable. Offset voltages are very stable over time and are primarily dominated by temperature fluctuations. Less than ±15µV drifts have been observed in the laboratory over a period of >15 hours, without taking special

precautions for stabilizing the environment's temperature. The chip also contains 4 dummy channels which can be used to monitor the offset voltage across the chip and allow fine trimming of the DACs for e.g. varying temperature conditions. This feature has not been tested yet.

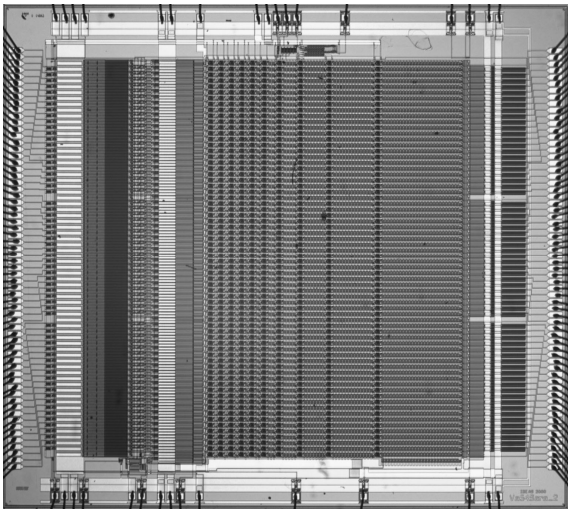

Figure 4-41: Micrograph of the VA64SARA chip.

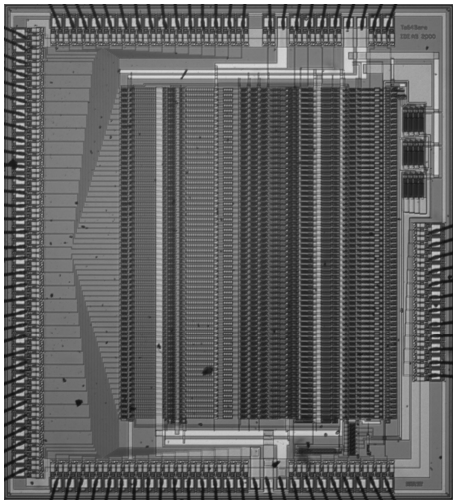

Figure 4-42: Micrograph of the TA64SARA chip.

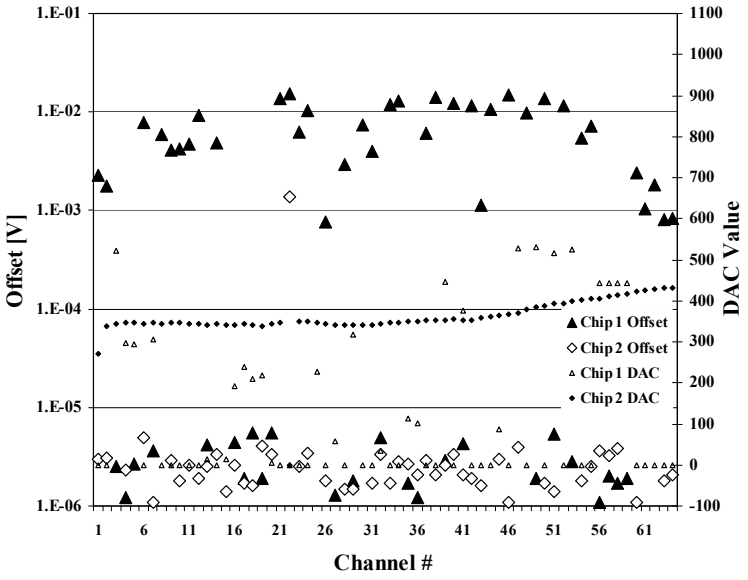

Figure 4-43: Offset voltages of each channel of two typical circuits. Chip 1 is clearly not adequate, while Chip 2 only has one channel which cannot be compensated.

The equivalent input noise charge (ENC) measured with a 10μs peaking time shaping filter is $250e^-_{rms}$ with a noise slope of $2.9e^-_{rms}$/pF. For a typical detector and wiring capacitance of 160pF, the ENC is $714e^-_{rms}$. These low noise values are obtained by using a folded cascode input stage with a W/L=12000μm/1.4μm PMOS input transistor. The bias current for this transistor is set to 2.2mA which yields a simulated transconductance of ~30mS. With a total current of 2.5mA in the input cascode pair, most of the power is dissipated in these transistors.

A schematic of the input stage is given in Figure 4-44. The charge integrator contains a 200fF feedback capacitance. In parallel to the capacitor, there are two long transistors, an NMOS (W/L=127/2) and a PMOS (W/L=15/2); a logic bit allows one to select one of these transistors, enabling both input current polarities to be measured. This feature is important for

e.g. the matrix readout scheme. The feedback transistors are operated in the sub-threshold region, acting as a high valued resistor.

An additional circuit will measure the voltage difference between node 'Out_I' and the input. Should that be larger than a predefined threshold, it will switch a current source or sink, providing additional bias current to the detector.

Combined with an additional gain stage, the chip's gain is 13mV/fC. Its dynamic range is ~100fC. Digital settings are programmed into the chip using a shift register. The last element of this register is also available on an output pad. This allows a control of the chip's status but also to daisy-chain a number of chips.

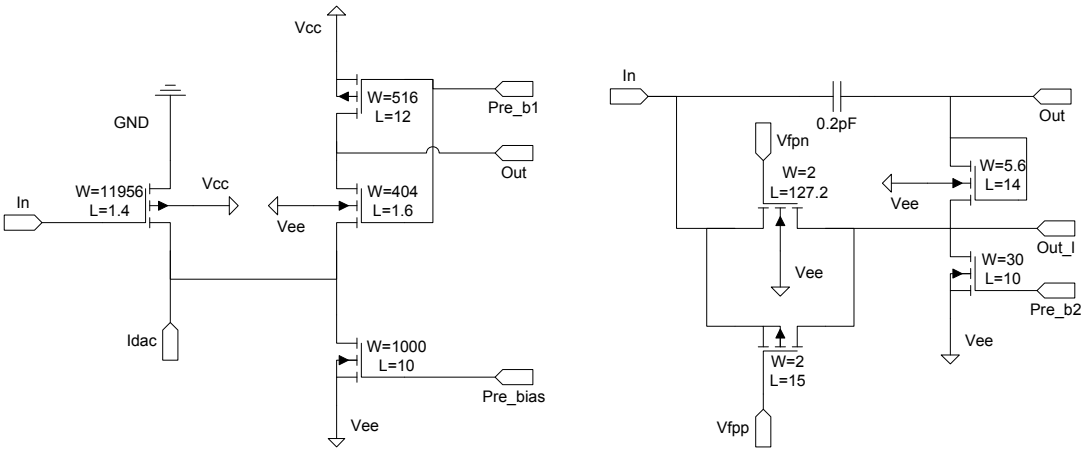

Figure 4-44: VA64SARA input stage schematics.

4.6.2 The TA64SARA

In order to separate fast digital transients from the very sensitive front-end amplifiers, a separate chip was designed for detecting signals above threshold. The TA64SARA contains 64 parallel triggering circuits that can be directly matched to the VA64SARA. A single channel schematic of both ASICs is given in Figure 4-39 and a micrograph in Figure 4-42.

The TA64SARA is based on IDEAS series of timing chips [107] and includes for each channel, a CR-RC shaper followed by a level-sensitive discriminator and address encoder. Once a signal is detected above threshold, the chip generates a trigger and the channel's address is loaded onto the address bus. The trigger signals from all channels are wire-or'ed to a single trigger signal.

This circuit also requires separate ±2V supplies for the analog and digital parts. Power consumption is ~1mW/channel. The chip has an area of 4.7×5.2mm^2 and is implemented in the same CMOS process as the VA64SARA.

The shaping amplifier has a tunable peaking time in the range 3-9μs. This allows for matching the filter's bandwidth to the STJ signals. In the particular application of optical photon detection with STJs, the recorded signals for the longest wavelengths are so low that the trigger level needs to be set to very low values, near the noise edge. In order to provide uniform and the lowest possible threshold setting, the offset of each discriminator can be compensated by a 3-bit DAC. The resolution of these DACs is tunable by an external current source. Furthermore, each channel can be enabled or disabled individually by a bit mask.

As for the VA chip, the digital settings are programmed into the ASIC using a shift register. The last element of this register is again available on an output pad, allowing a status check and daisy-chaining.

4.6.3 Test results summary

The two ASICs, each having 64 independent channels, have been designed and integrated into a complete readout system. The first chip provides detector biasing and low noise signal amplification while the threshold detection and trigger logic is implemented in the second one. Although a standard CMOS process was used, the design allows for input offset voltage compensation to within ±10μV. The low noise operation has been verified with open input (~250e^-_{rms}) and with various input load capacitors (~700e^-_{rms} for 160pF). The noise performance is comparable to our state-of-the-art discrete amplifiers and should allow optical photon detection from Superconducting Tunnel Junctions.

However, when we tried to connect the ASIC to an STJ array, we were not able to provide stable biasing. The most probable cause is the cross-talk between the various channels resulting from the close proximity of the interconnection wires in the dewar.

In comparison to traditional discrete amplifiers, the compactness of the chips and their low power consumption (factor 30 smaller than discrete amplifiers) are a major step forward to readout large format STJ arrays. Nevertheless, further work is clearly necessary and would be beneficial to a wider acceptance of this technology.

Chapter 5

THE S-CAM3 SYSTEM

The S-CAM system consists of four distinct subsystems, each of which will be described in some detail in this chapter:

1. The optical sub-system, which relays the telescope beam and focuses the image onto the detector
2. The dewar and its associated cooler, which provide the required cryogenic environment for the superconducting detector
3. The superconducting detector array, previously described
4. The electronics and software sub-system, which amplify, detects and stores the individual photon signals and commands all other sub-systems.

The assembled S-CAM3 system is depicted in Figure 5-1. Light from the telescope enters at the bottom right and follows the arrow path. Only the proximity front-end electronics is visible in this picture and consists of four identical units. The focussing lens is mounted directly on the dewar and is hidden in this view by the filter wheel.

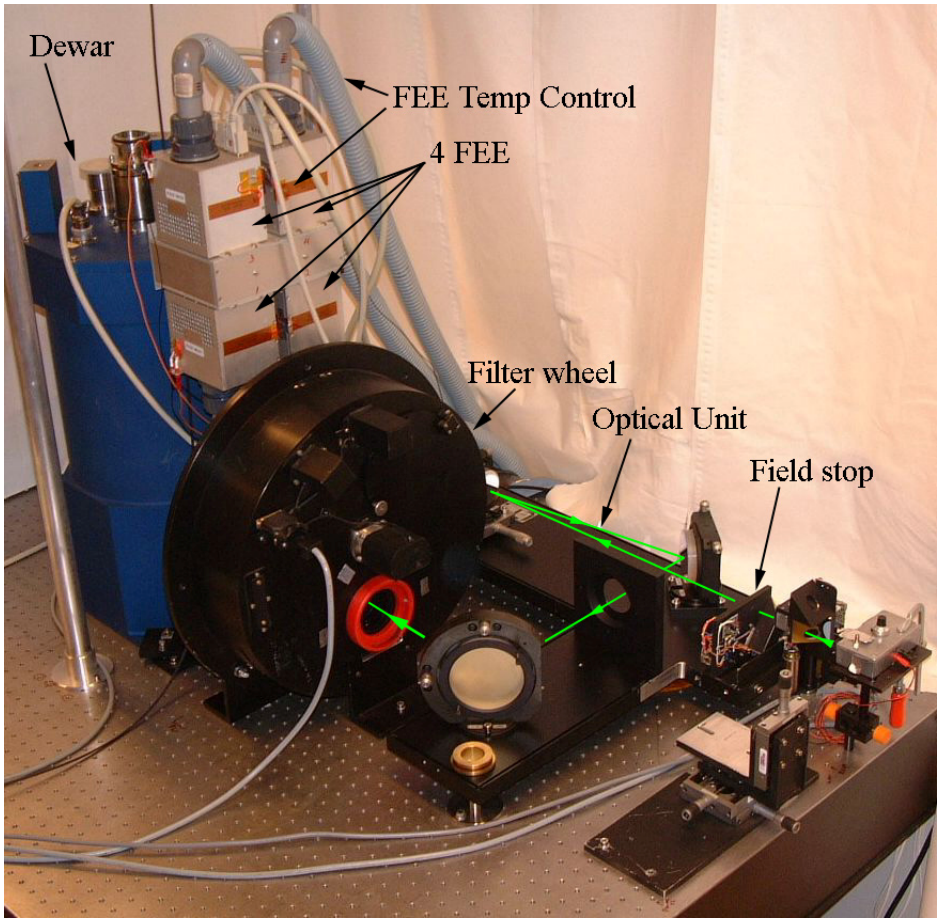

Figure 5-1: S-CAM3 assembly. Light enters at the bottom right and follows the arrow line.

The system was originally conceived to fit on one of the Nasmyth foci of the 4.2m William Herschel Telescope (WHT [108]) of the Isaac Newton Group of Telescopes (ING), see Figure 5-2.

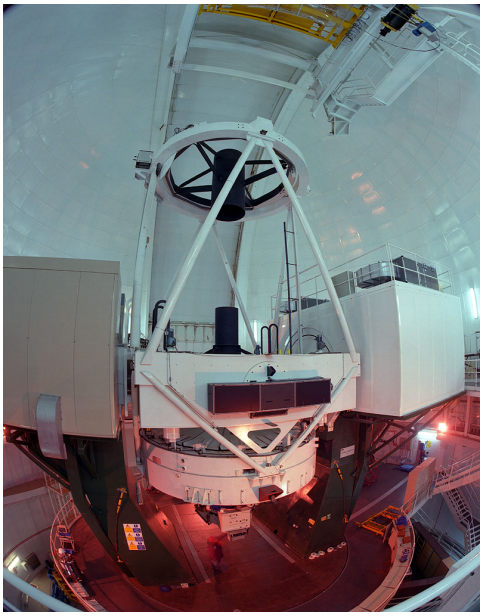

Figure 5-2: Outside and inside views of the William Herschel Telescope at La Palma. Photos Courtesy of the Isaac Newton Group of Telescopes, La Palma.

S-CAM3 was later adapted to also fit the 1m Optical Ground Station (OGS [109]) telescope at Tenerife, see Figure 5-3. This telescope is primarily used for monitoring space debris and for optical telecommunication tests, but its access is easy for the S-CAM team, since it is ESA owned. The optical configuration of the Coudé focus is presented in Figure 5-4.

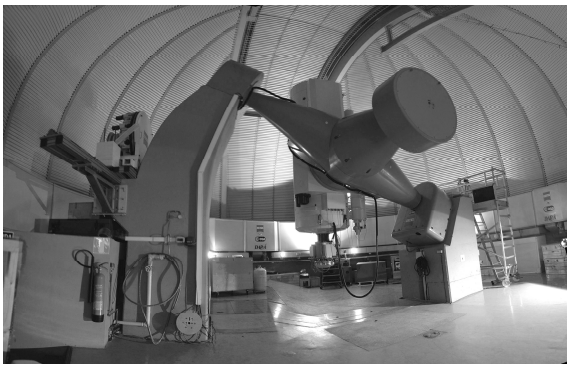

Figure 5-3: Optical Ground Station at Tenerife.

To date, six observing campaigns were performed with S-CAM3; all are listed in Table 5-1. The actual observations typically would span a week. In addition, we would require about 6 days for setting-up and 2 days for disassembly.

Table 5-1: Summary of observing campaigns

Run	Campaign duration	Observations	Telescope
S-CAM3a	29/06/2004-15/07/2004	05/07/2004-12/07/2004	WHT
S-CAM3b	02/11/2005-17/11/2005	08/11/2005-14/11/2005	OGS
S-CAM3c	28/04/2006-13/05/2006	04/05/2006-10/05/2006	OGS
S-CAM3d	30/07/2006-15/08/2006	04/08/2006-12/08/2006	OGS
S-CAM3e	07/05/2007-24/05/2007	13/05/2007-21/05/2007	OGS
S-CAM3f	07/09/2007-23/09/2007	12/09/2007-21/09/2007	OGS

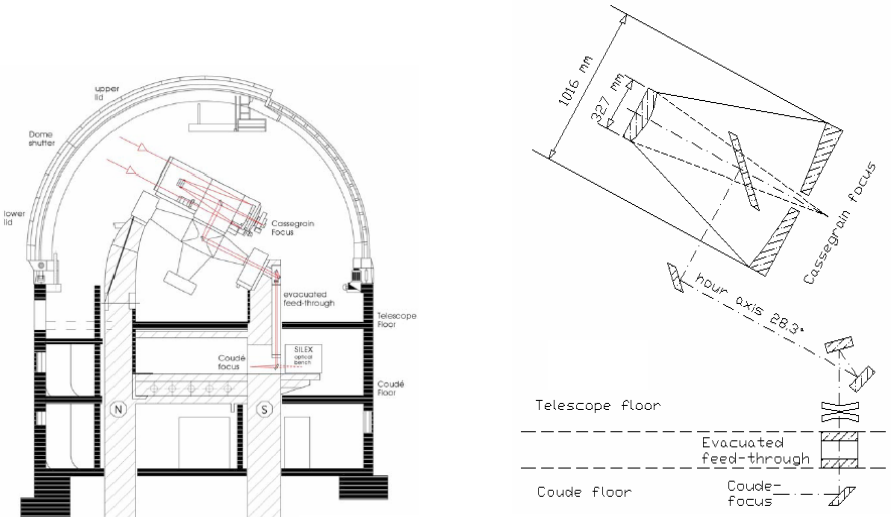

Figure 5-4: Optical configuration of the Coudé focus at the OGS.

5.1 The optics sub-system

As we explained in the introduction, the S-CAM system was designed to fit the Nasmyth focus of the WHT at La Palma. With a focal length of 46.5m, the plate-scale at the Nasmyth focus is 225µm/arcsec. While the original S-CAM1 and 2 arrays only had 36, 25µm pixels, a re-imaging optical system was designed to achieve 0.6arcsec/pixel plate-scale at the detector, oversampling the typical ~1arcsec point-spread function of the telescope. This re-imaging of the focal plane is realized by the combination of a reflective and refractive optical unit, schematically represented in Figure 5-5. After passing the entrance pupil stop, the incoming telescope beam is collimated by reflective optics. The beam then passes a filter wheel and is focused by the lens assembly into the cryostat. In the cryostat, a set of four filters provide the necessary IR rejection. Both reflective optics unit and the lens were originally designed by SESO [110] for S-CAM1&2.

For the larger S-CAM3 detector, it was decided to keep the same optical design. The 35µm pixels on a 37.5µm pitch provide a 0.9arcsec/pixel plate-scale at the WHT. Given the limited amount of pixels, this provides a larger field-of-view (10.8"×9") and a better match to the seeing conditions at the La Palma site. The larger field-of-view, however, required a redesign of the lens system to avoid vignetting of the beam.

After the first S-CAM3 campaign at the WHT, it was decided to adapt the system to ESA's Optical Ground Station. This 1-m class telescope has a fixed optical bench at the Coudé focus with a 39.1m focal length, similar to the WHT. Since the f-number of the OGS system is considerably larger than that of the WHT, the optical quality of the optical unit is not adversely affected and did not require any redesign. Actually, the collimated beam diameter is now ~13mm, versus ~45mm at the WHT, yielding lower aberrations from the lens assembly. For the OGS set-up, the plate-scale at the detector is 1.07arcsec/pixel for a total FOV of 12.8"×10.7".

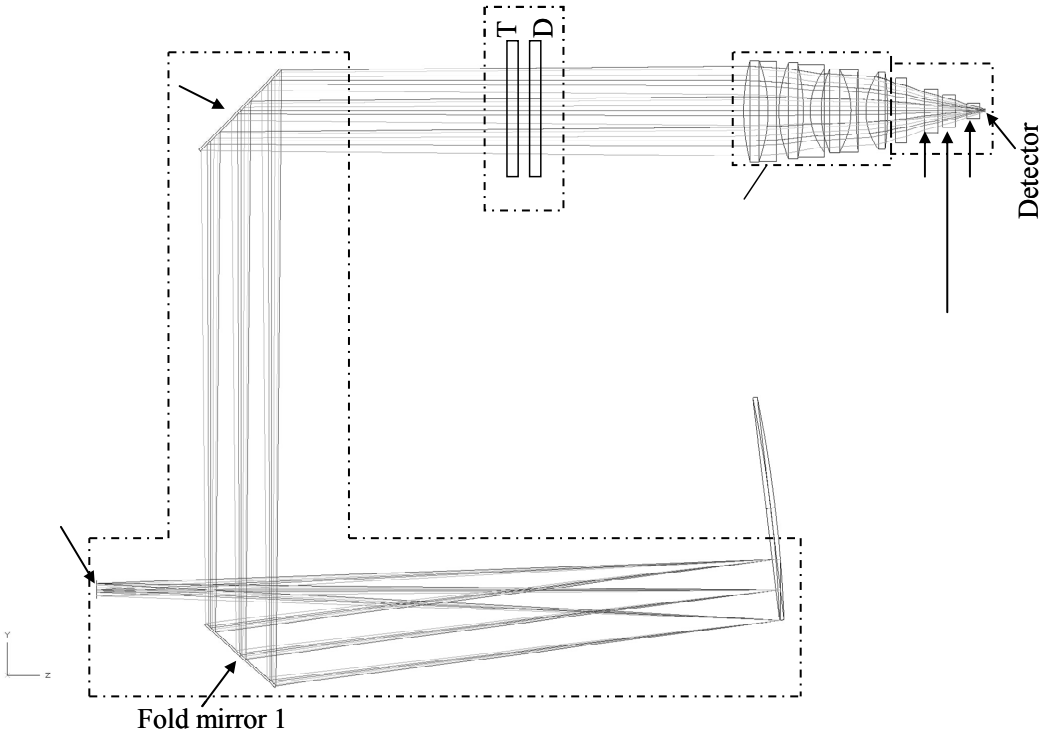

Figure 5-5: Schematic of the S-CAM3 optical set-up.

5.1.1 Reflective optics

After passing the entrance pupil stop, the incoming telescope beam is collimated by a 500mm focal length off-axis parabola. The collimated beam is then folded twice, to exit the reflective unit in a direction parallel to the incoming beam. This assembly is mounted on its own optical bench and can be adjusted in height and tilt by three mounting feet.

The entrance field stop of this unit has been modified to serve several purposes. Two motorized vertical translation stages were inserted. The first one allows one to select between three field stops:

1. Fully open; used to find the beam during set-up.
2. 3.4mm diameter field stop, matched to the detector size, and used during observations.
3. 200μm pinhole, used for focussing and alignment.

The second motorized stage allows the insertion of calibration sources and simultaneously moving of a 45º tracking mirror. The calibration sources are threefold:

1. Pulsed red (630nm) LED. Pulses can be synchronized with a GPS receiver for absolute timing calibration.
2. HeNe laser for wavelength calibration, coupled through an optical fibre. During laboratory calibration of the instrument, the monochromator light source can be coupled in using this same interface.
3. A "white" LED (HLWW-L51), λ~380-800nm with peaks at 440 and 580nm and a UV LED (RTL365-525) peaking at λ=367nm and which has a bandwidth $\Delta\lambda$=16nm.

The tracking mirror consists of a plane mirror with a 16mm diameter hole to allow an unobstructed view of the telescope beam over the complete S-CAM3 field-of-view. The off-axis light is reflected at 90 degrees to a CCD guiding camera in the WHT configuration. During

target acquisition, the mirror can be shifted upwards to allow the on-axis light, basically the S-CAM image, to be redirected to the guiding camera. Once the target is acquired and centred, the hole is put back in place and the CCD camera used for off-axis guiding.

Both translation stages and calibration sources can be remotely controlled and monitored by the S/W.

5.1.2 Filter wheel

The filter wheel was scavenged from an earlier project and consists of a double wheel, each with eight 80mm holes, in which 64mm diameter filters will fit. The unit is used to hold neutral density filters (ND), to observe bright objects, and interference filters (CAL) which, together with the LEDs, allow for wavelength calibration of the instrument during observing campaigns. In addition, two cross-polarization filters (POL1 and POL2) are also incorporated. The filter arrangement of S-CAM3 is given in Table 5-2. Any combination of the two wheels is possible in principle. For ease of operational purposes, we separated these in three categories: observations, calibrations and diagnostics. In observation mode, this allows for instance for all neutral densities to be selected in steps of $10^{0.5}$ from 1.0 to 10^5 (with the exception of $10^{4.5}$).

The calibration filters consist of Comar Instruments and Fairlight narrowband interference filters and are used, in combination with the aforementioned LEDs for wavelength calibration of the instrument during observation campaigns. Four sets of CAL filters are foreseen, although only CAL2 is used in practice. In this assembly, three filters are combined into the same holder, as sketched in Figure 5-6. Position 1 holds a 25mm diameter 365.7nm filter, positions 2 and 5 hold the 12.5mm diameter 488.2 and 669.6nm filters respectively. Positions 3 and 4 are blanked. The filter wavelengths, diameters as well as the electrical power delivered to the LEDs are tailored to provide three nicely separated lines of about equal amplitude. An example of a single pixel spectrum obtained during a 103sec exposure during one of the observing campaigns is given in Figure 5-7. The three calibration lines are clearly separated and allow the verification of the instrument's gain and offset (PHA channel versus photon energy). The dashed lines are a triple Gaussian fit to the data. The fitted peak values and widths are summarized in Table 5-4.

The polarizers are available in diagnostics mode. All filters' transmissions as function of wavelength were characterized prior to integration.

Table 5-2: Filter positions. *

Filter Position	Wheel 1	Wheel 2
8	Open	Open
7	ND 0.5	ND 1.0*
6	ND 2.0_D	ND 0.6**
5	ND 2.0*	POL2
4	CAL2	ND 1.0
3	CAL3	ND 2.0_T
2	CAL4	ND 3.0
1	POL1	Closed

*50×50mm^2 filters from an earlier project
** 55mmØ filter

Table 5-3: Calibration filters. Nominal transmission wavelengths at 20°C; $\Delta\lambda$~0.1nm/K

Name	Filters	Wavelengths [nm]
CAL1	515IL12	514.1±3.0***
CAL2	365FS02	365.7±5.2****
	488FS02	488.2±0.9****
	670IL12	669.6±2.6***
CAL3	532IL12	532.1±2.9***
CAL4	633IL12	632.2±2.3***

*** Measured
**** @23°C; $\Delta\lambda$~0.015nm/K

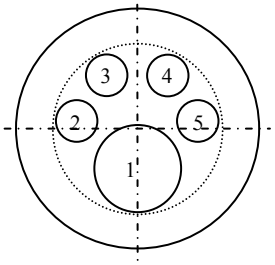

Figure 5-6: CAL2 configuration.

Table 5-4: Peak fits for Figure 5-7

λ [nm]	Peak	FWHM
365.7	4421.4±1.1	248.2±1.9
488.2	3337.4±0.7	215.8±1.1
669.6	2439.3±0.8	202.3±1.4

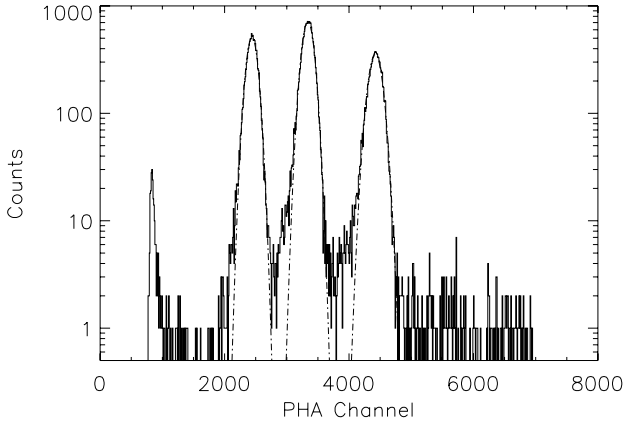

Figure 5-7: Calibration spectrum example for pixel [6,6].

5.1.3 Lens Assembly

The lens assembly was redesigned by Winlight System [111] to fit the larger S-CAM3 field of view. In fact the design was done to accommodate an even larger field of view, as foreseen for our next generation detectors, see chapter 7.1. The unvignetted field of view of the lens is 47" in diameter. The lens is mounted, via a two-axis translation table, onto the cryostat allowing alignment of the beam with the detector. Focus is adjusted by means of a thread on the lens assembly housing.

The optics consists of three doublets and a singlet lens. In combination with the reflective optics unit, the complete system has a demagnification factor of 5.42±0.02. The optics was designed to provide a back focal length of 72mm; a minimal distance of 71mm is required to reach the detector sitting behind the IR filters.

The lens compensates the aberrations with all the IR filters, cryostat window and detector substrate taken into account. At the design wavelengths of 365, 525 and 700nm, the 90% encircled energy diameter is 15.7±0.6μm, well under the pixel size. Even for the full 47" FOV, the 90% encircled energy is smaller than the pixel size.

All exposed lens surfaces have been AR coated and the total transmission efficiency of the lens is at worst 82% at 300nm, while it is larger than 90% in the band 310-700nm.

5.1.4 Infrared shielding and filtering

The rejection of thermal infrared photons is of crucial importance. The low energy gap of Ta/Al STJs makes them sensitive to wavelengths up to ~1mm. Since the detector is optically coupled to a 300K environment, the IR rejection filters have very tight requirements. In S-CAM2 this problem was solved by baffling and by using KG2 and KG5 glasses from Schott.

Simple calculations of attenuation factors in the vicinity of the peak of the 300K blackbody radiation could, however not explain the excess in sub-gap current (~0.4nA or 0.6pA/μm^2) measured on the S-CAM2 detector. We concluded that we were suffering from residual very long wavelength radiation. In order to suppress this even further in S-CAM3, we first replaced the innermost filters by thick pieces of normal glass (each 10mm thick) and experimented with various combinations of glasses, various combinations of Schott KG2, KG4, KG5, BK7 and plain SiO_2. A summary of the optimal IR rejection filter configuration inside the dewar is given in Table 5-5.

Additionally, we closed every possible aperture between the various thermal shields in the dewar and on the detector holder. We believe that most of the long-wavelength radiation arose

from photons scattering inside the dewar and leaking through the various small remaining apertures onto the detector. With the improvements, we reduced the IR load by more than an order of magnitude.

Table 5-5: Summary and comparison of IR rejection filters and glasses used in S-CAM2 and S-CAM3. * The sapphire entrance window is now coated with an anti-reflection coating rather than an IR reflection coating.

	Location	**Entrance Window**	**Thermal Shield**	**Magnet**	**Detector holder**	**Detector substrate**
	Temperature	*300K*	*~12K*	*2 or 4K*	*0.3K*	*0.3K*
S-CAM2	**Glass type**	*Sapphire*	*Schott KG2*	*Schott KG5*	*SiO_2*	*Sapphire*
	thickness	*8mm*	*9.5mm*	*3mm*	*1mm*	*0.5mm*
S-CAM3	**Glass type**	*Sapphire **	*Schott KG2*	*Schott BK7*	*SiO_2*	*Sapphire*
	thickness	*8mm*	*10.0mm*	*9.5mm*	*10mm*	*0.5mm*

Figure 5-8 shows the effect of the S-CAM3 IR filters in the long wavelength range. The dotted curve is the amount of photons collected by our STJ size from a 300K blackbody radiator. The dashed line shows what is left after this radiation passes the detector's sapphire substrate. The dot-dashed curve is the final flux arriving on the detector after passing the complete set of IR filters and substrate. These calculated curves are based on optical properties but do not, however, take into account the efficiency with which long wavelength electromagnetic radiation couples into a comparatively small detector. If one assumes 100% absorption efficiency up to the cut-off wavelength, the photocurrent generated without any filters would be of order 260μA for KJL480. The sapphire substrate would attenuate this by three orders of magnitude, but the current would still be far too large for optical photon detection. The IR filters finally would theoretically reduce the photocurrent to less than 0.4pA. The fact that the measured subgap current is ~100pA, indicates that some IR is still leaking, most likely through the remaining venting orifices.

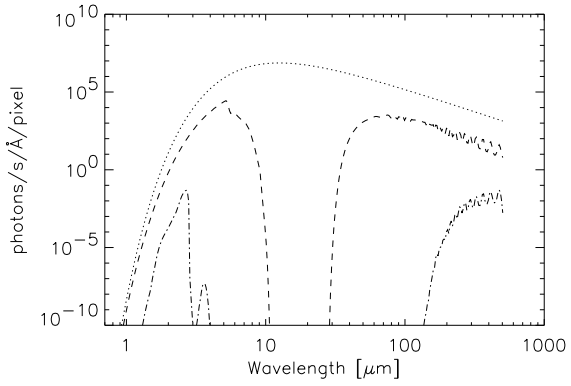

Figure 5-8: Dotted curve is photon flux emanating from a 300K blackbody radiator. Dashed curve is remaining photon flux from 300K BB passing through the detector's sapphire substrate. Dot-dashed curve is remaining 300K BB flux passing through S-CAM3 optical path (IR filters + substrate).

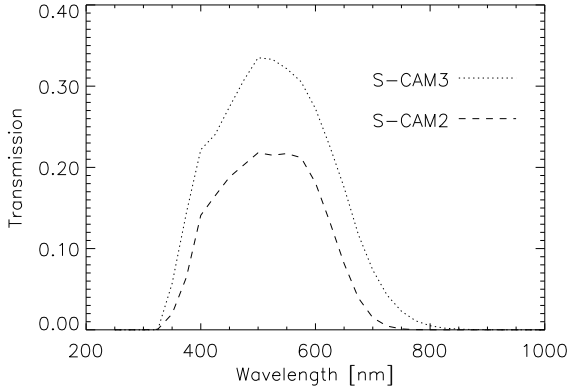

Figure 5-9: Optical transmission curves for S-CAM2 (dashed) and S-CAM3 (dotted). The curves include all the optical elements (imaging optics, IR filters, windows etc.) as well as the detector's efficiency. The plots are based on measurements of the various components.

Figure 5-9 is a comparison of the total efficiency of S-CAM2 versus S-CAM3. These curves take into account the measured transmissions of all optical elements as well as the detector's efficiency. One can easily notice that the peak efficiency has increased from ~22% in S-CAM2 to ~34% in S-CAM3. The bandwidth (at 10% of peak) has also increased from 350–700nm to 340–740nm. We were not able to achieve the goal of reaching 1000nm but, in

combination with the much increased efficiency, we have been able to clearly extend the red response.

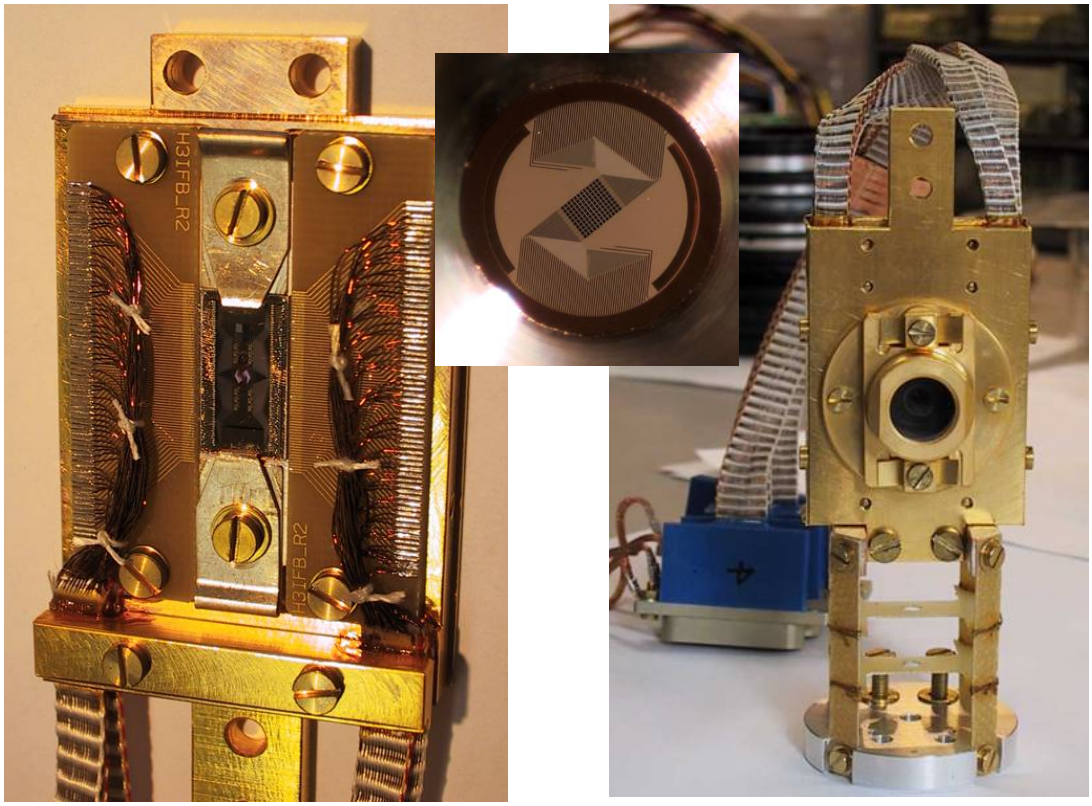

Figure 5-10: Cold finger assembly. Left: detector front view with superconducting wiring. Right: complete assembly with view on the last (10mm SiO_2) IR filter. Inset: view of the detector through the IR filter and sapphire substrate.

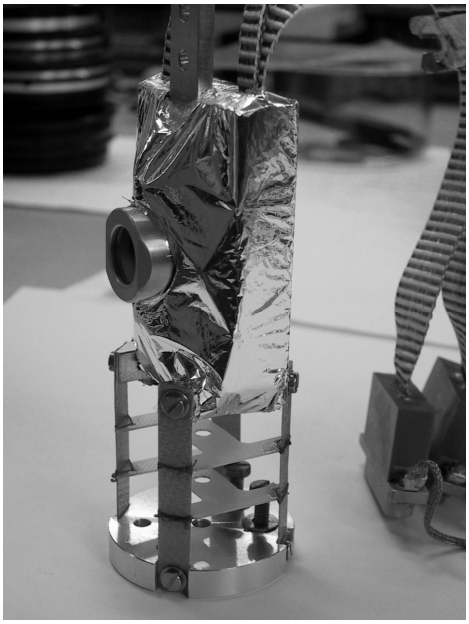

Figure 5-11: Complete cold finger assembly with multilayer insulation, lowering the heat load. Care has been taken to close off all direct optical (IR) paths to the detector.

Figure 5-10 gives an impression of how the cold finger and detector are assembled. The structure is fabricated from Cu and is gold-plated. To avoid residual magnetic remanence, the usual Ni buffer layer was not applied and all screws are made of brass. The detector is electrically connected with Al wirebonds to two standard printed-circuit boards. From there each group of 30 pixels is connected to a 32-wire loom made of 100μm superconducting Nb wires, fabricated by Tekdata [112], which provide low electrical resistance and simultaneously a high thermal impedance. Per group, two wires are used for the ground return and each detector has its own 'signal' wire to the room temperature electronics. The ~20cm long looms are thermally and mechanically anchored at one end to the liquid Helium cold plate (at 4K) and at an intermediate position, thermally anchored to the ^{4}He sorption cooler (see next Section).

In order to reduce the IR flux onto the detector, the cold finger holds the last IR filter, its backside is closed off by a Cu cap and the complete assembly is wrapped in super-isolation (MLI), see Figure 5-11.

5.2 The cryogenics sub-system

In order to cool the detector to its operating temperature of ~0.3K, we use a dewar in combination with sorption coolers. The dewar can contain ~12 litres of liquid Helium. An inside view onto the S-CAM3 cold plate is given in Figure 5-12. The coupling to the external optics is on the right hand side. The light will first pass the IR blocking filters before going through the magnet (circular part to the right) onto the detector, suspended in the centre of the magnet. The detector holder is thermally connected via a Cu strap to the ^{3}He sorption cooler.
There are various ways to operate the coolers. The first, which was the standard operational mode in S-CAM2, relies on pumping the liquid helium bath to reach a cold plate temperature of ~1.9K. A ^{3}He sorption cooler provides further cooling to achieve a temperature of 0.32K at the detector holder [113]. The major drawbacks of this method are that it relies on a large external pumping system to reduce the liquid helium's partial pressure to ~20mbar, it reduces the hold-time of the system and requires extensive manual intervention. Additionally, the pump cycle takes a long time to reach equilibrium pressure and therefore reduces the valuable hold-time even further. Finally, the detector's temperature is not particularly stable.

For S-CAM3, we acquired a combination cooler from the CEA in Grenoble [114], which consists of a hybrid ^{4}He–^{3}He sorption cooler. A picture of this system can be seen in Figure 5-13. This combination would in principle avoid having to pump on the bath. Each sorption cooler is a closed cycle refrigerator, which consists mainly of a sorb, a condensor and an evaporator. The sorb contains an adsorbing material and can be either heated to release its helium gas during the 'recycle phase' or thermally connected via a gas-gap heat switch to the bath and function as a pump in the 'operating phase'. From an un-pumped bath temperature of 4.2K, the first, ^{4}He stage will cool to ~2.5–3K. This temperature is required to condense the ^{3}He of the second stage cooler. Once the second stage is recycled, i.e. the ^{3}He has been completely condensed into the evaporator, the first stage cooler typically runs out. There are now two operating modes one can choose from.

In 'mode A', the system is left as is and the second stage cooler goes into its operating phase. In this mode, the equilibrium temperature reached on the detector holder is ~342mK and the hold time 10h15', in the S-CAM3 configuration.

In 'mode B', the ^{4}He stage can be recycled a second time. The base temperature will then reach 315mK. This temperature is maintained for approximately 10h50' after which the ^{4}He cooler runs out again. At this stage the detector holder's temperature will rise to ~342mK for another ~6 hours after which the ^{3}He runs out.

The added beauty of this combination is the fact that the coolers can be easily (remotely and/or automatically) operated via electrical switches, which turn heaters on or off. The only manual intervention is the filling of the dewar with liquid helium. Its hold time of ~17 hours is more than sufficient for a night of observations at a ground-based telescope, without refilling.

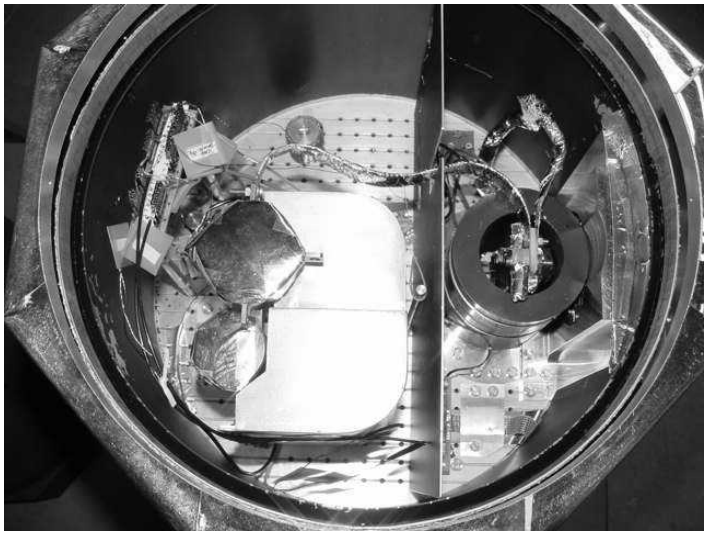

Figure 5-12: Upside-down view of the S-CAM3 cold plate. Light enters from the right through a number of IR blocking filters to reach the detector suspended in the middle of the magnet (circular part on the right-hand side). The detector holder is thermally anchored to the 3He sorption cooler, part of the hybrid cooler seen on the left-hand side.

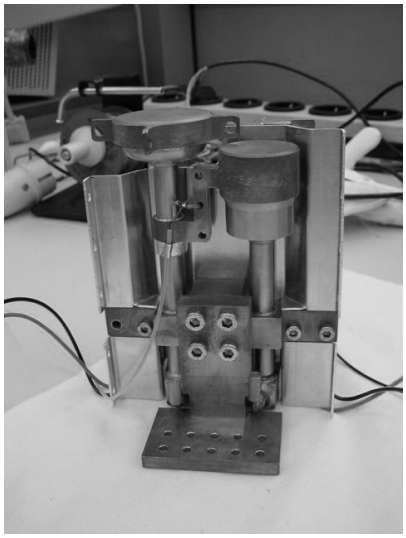

Figure 5-13: Hybrid Sorption coolers from CEA. The large Cu piece in the lower part of the picture serves as mechanical and thermal anchoring to the cold plate. The cups are the evaporators of the ^{4}He (right) and ^{3}He coolers (left). The Cu connections around the middle of the vertical stainless steel tubes are the condensers.

In practice, however, we could not use the system in such a way. It turned out that the large S-CAM3 detector was not sufficiently shielded from the earth's magnetic field by the 110μm thick μ–metal shield internal to the cryostat, which was so successful for S-CAM2. Instead we had to resort to an external double 1mm μ–metal shield to avoid flux-trapping during the cool-down process. If we do not wish to trap a single flux quantum in the detector, one can estimate that the maximum tolerable magnetic field perpendicular to the S-CAM3 detector is ~0.12mG. This requirement will, of course, become ever more stringent for larger arrays.

In order for the previous cooling procedure to work, the dewar would have to be lowered into the shield once a day, for each cooling cycle and then precisely repositioned in the optical beam. Instead, we preferred to adopt a new strategy, whereby the detector would stay superconducting during a complete observation campaign. Only the first cool-down would then require the cryostat to be placed in the μ–metal shield. The cool cycle is now as follows. First, the dewar is filled with liquid Helium and the pump is connected to slowly lower the pressure to ~20mBar. At a He bath pressure of ~150mBar, the sorb heaters are powered until the temperatures reach 60K on the ^{4}He and 40K on the ^{3}He sorbs, after which, the heating power is removed and the gas-gap switches are heated, effectively connecting the sorbs thermally to the Helium bath. When the detector temperature has dropped below 300mK, the pump is switched off and the dewar is refilled with liquid Helium. Then the system is left to stabilize. Using this procedure, the detector temperature never rises above 2K, and re-cycling can take place without the repeated need for the external magnetic shield. The Helium bath will last 17 hours before requiring a refill, while the ^{4}He-^{3}He sorption coolers last for 24 and 27

hours respectively before requiring a recycle. The added advantage is that the detector temperature (292mK) is stable within 1mK throughout a complete observing night and from night to night, providing an extremely stable detector gain. Typical temperature profiles are given in Figure 5-14. This plot includes the first cool down starting at liquid Nitrogen removal at T=0:00 and first liquid Helium fill at T=0:50 and pump down. The sorption pump cycling starts at T=5:24 and the pump is switched-off at T=7:22. The second cycle starts with a LHe refill (T=21:00), pumping (T=21:30) and sorption coolers re-cycling (T=23:15).

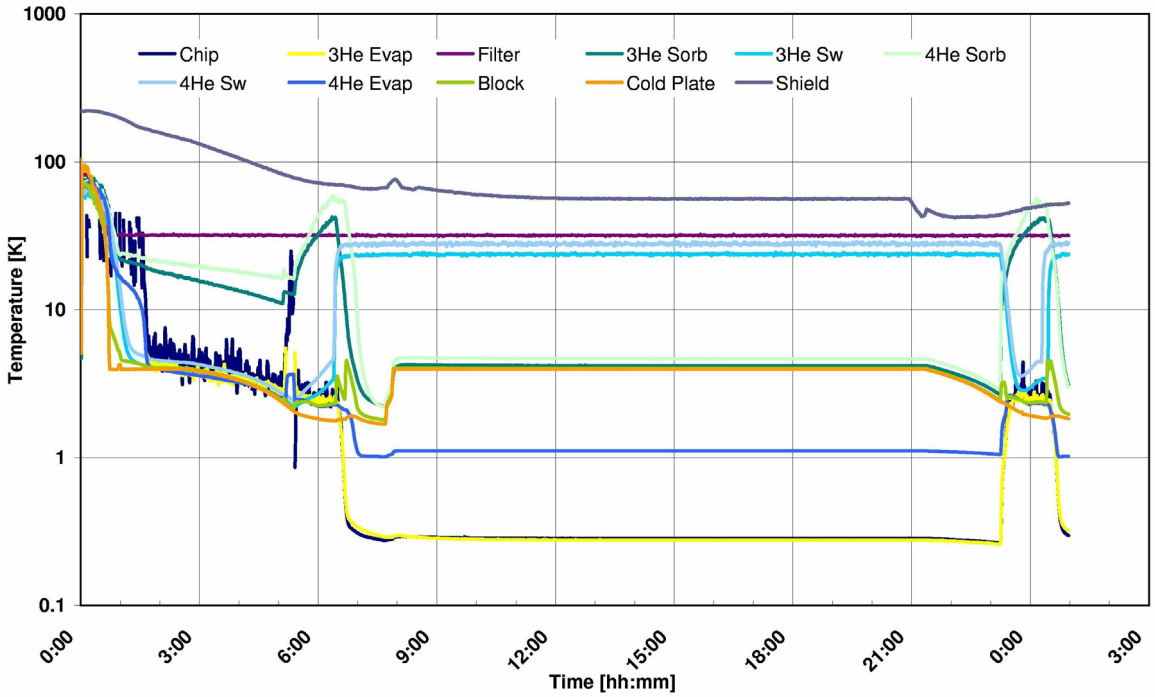

Figure 5-14: Typical temperature profiles for the first cool-down and second cooling cycle.

5.3 The electronics sub-system

The electronics sub-system can be subdivided into three entities:

1. The proximity, or Front-End Electronics (FEE).
2. The back-end electronics.
3. The instrument control and monitoring electronics.

5.3.1 The front-end electronics

The FEE consists of the input amplifiers and are physically mounted on the dewar. They are grouped in sets of 32 channels in individual housings, as shown in Figure 5-1. Each of the groups is connected to a quarter of the detector array with a separate ground return, in order to avoid stability problems. Grounding to the structure is done in the FEE boxes.

The amplifiers are of a similar design as that reported in chapter 4.1. The feedback circuit of the charge sensitive amplifier consists of a 470MΩ resistor in parallel with a 1pF capacitor for normal operation. In parallel to this, we have added a FET in series with a 1MΩ resistor. The FET serves as a switch to activate the lower valued resistor in the feedback. With the FET switched on, the circuit acts like a trans-impedance amplifier and allows to "curve trace" the STJ: by programming the DAC in the bias circuit with a ramp, we can measure directly the current to voltage characteristic of the detector. The system can automatically scan the I–V curves of the 120 channels. Since this scanning method uses the same input circuit as during

normal operations, we use it also to calibrate the amplifiers' offset voltages, which are then compensated digitally.

The offset is mainly determined by the AD549 electrometer (see Figure 4-1), and can be up to ~300μV with a drift of 5μV/°C. In order to maintain a constant bias voltage, each 32-channel amplifier set is temperature controlled separately by a fan and heaters. The control algorithm is implemented in software and temperatures are logged throughout the observations; temperature stability is typically of order 0.1°C.

Noise reduction is of paramount importance in applications like S-CAM. The amplifiers are therefore powered by low-noise power supplies, one for each amplifier box. The amplifiers' buffered differential outputs are routed through a few meters of shielded twisted cables to the pulse processing stages.

5.3.2 The back-end electronics

In the Digital Signal Processing rack (see Figure 5-15), the signals are immediately sampled by analogue-to-digital converters at a programmable rate of up to 40Msamples/s. Note that the digital and analogue parts are well separated and the DSP rack is fibre-coupled to the control PC rack, to avoid ground loops and minimize digital noise injection. The digital samples are passed to a FIR filter which serves as the shaping stage (see section 4.2). The filter's impulse response is very simple in that its tap coefficients are either 1 or –2. By changing the length of the filter (up to 1533 taps) and/or the sampling rate, one can change the effective pulse shaping time over several orders of magnitude. In practice, however, the shaping times are in the range 1-50μs. This allows us to optimize the settings for speed with a short FIR (lower pile-up probability) or better energy resolution with a longer FIR (see section 5.4).

As we have seen in section 4.3.2, the optimum filter is a complex function of parallel and series noise, low frequency microphonic noise, the detector's responsivity and pulse decay time and the level of residual IR radiation and is best appreciated through measurements. In practice, we have chosen 3 operating modes for the instrument. For S-CAM3c/d/e/f, these were: 'Hi-Res' at 24kHz for best possible resolution, 'Med' at 48kHz and 'Fast' at 72kHz for highest count-rate capability. One should note that the implemented filters are bipolar and that both the positive and negative peaks are sampled for each photon. The pulse height amplitude is then evaluated off-line by a weighted sum of both peaks. The weight has been optimized for each operational mode for best resolution. Note that for each detector chip and each FIR setting, we optimized the operating bias voltage and magnetic field as well.

The simplicity of the FIRs, they only require adders and FIFOs, made it possible to integrate them into FPGAs. Further logic in these chips provides for threshold detection, peak search and sampling, time tagging, a digital pulse generator for electronic noise determination, buffering and the required 'glue'-logic. Each event, which passes a programmable threshold, will be detected and the pixel address information with a time tag derived from a GPS receiver is forwarded to a fast buffer. The hardware buffer is then read out by the control PC using a fast PCI parallel port and logged onto disk. The time-tagging accuracy has been calibrated for each individual channel and FIR setting to the level of 1μs (absolute time, see section 5.3.4).

In addition to the above, the DSP rack contains also the low-noise power supply for the magnet and the interface box for all cryogenic temperature sensors as well as the optical unit control. The second rack hosts the fast fibre-optic interfaces to the DSP rack, the GPS receiver, the control PC and the power supplies for the preamplifiers' temperature control.

Figure 5-15: Digital Signal Processing rack. From top to bottom: four DSP modules; Magnet power supply; Temperature monitor and optical unit controller; Four low noise FEE power supplies.

Figure 5-16: Control PC rack. From top to bottom: GPS receiver; LED pulser module; DSP interface module; Control PC; PCI extender; RAID array; FEE heaters power supply; FEE fans power supplies.

5.3.3 Instrument control and monitoring

S-CAM3 is essentially controlled by two PCs; the 'control PC' and the 'GUI PC'. How these fit in the overall S-CAM computer network is schematically represented in Figure 5-17. The hardware is physically connected, through fibre-links, to the Control PC. This computer is the direct interface to S-CAM and contains an array of disks (RAID) which will store the raw event files from the observations as well as all house-keeping files (log-files of temperatures, commands etc.). The graphical user interface (GUI) PC is connected via TCP-IP to the control PC. It is on this machine that the user controls and monitors the state of the instrument. The complete control software is written in National Instrument's LabVIEW language.

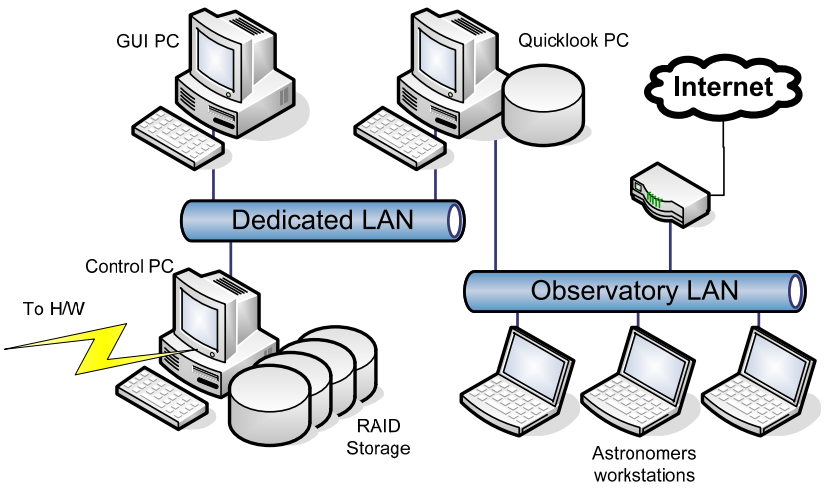

Figure 5-17: Computer network set-up for S-CAM. The Hardware is on a dedicated LAN.

The GUI allows full remote control of the hardware, like e.g. moving the filter wheel position or the calibration sources, setting the FIR filter parameters in the FPGAs and starting data acquisitions. It will also display the various parameters like temperatures but also acquired "live" images and spectra updated every second. In S-CAM3, these analyses tools are implemented in hardware (e.g. FPGAs accumulate spectra and light-curves). The data stream to the GUI can therefore be of low volume and remain well separated from the logging data stream. Also, the Control PC only acts as data router. This has tremendously improved the system's robustness and data handling capability compared to previous S-CAM versions. The maximum event rate is now limited at the 32-channel group level by a glass-fibre interface at 150kevents/s, or 6×10^5 events/s over the whole array. Running at higher count rates will not crash the system, but obviously data will be lost as buffers will overflow.

The quick-look PC shown in Figure 5-17 is inserted between the dedicated S-CAM hardware network and the observatory network, where the users connect to. This computer runs dedicated S/W, to look for new files stored on the Control PC. Once a new raw data file is available, it will copy it to its local repository and convert it into a FITS (Flexible Image Transfer System) format [115], which is a standard data format used in astronomy. These files are then available for download by the users, but can also be analysed in some more detail. In addition to the standard display available on the GUI, the Quick-look S/W can analyse the data offline, apply the gain corrections, select regions of interest, perform more advanced background subtraction or perform Fourier analysis on time series.

5.3.4 Absolute timing calibration

For accurate timing observation as required by e.g. the Crab pulsar observations (see Section 6.2), the system needed also to be calibrated for this aspect. Since high timing accuracy is an essential feature of STJs, we would like to spend some time to explain the calibration procedure.

As we explained earlier, the electronics will attach a 'fine' time tag to each event with a 1μs resolution. Additionally, 'second' time stamps are inserted in the data stream, to provide 'coarse' time. The time is obtained from a GPS receiver and time-tags are derived from the zero-crossing of the FIR filter signal. Since this instant depends on the exact FIR setting and each pixel's decay time, we required a calibration of the time-tag versus photon arrival time delay. The calibration was performed by using the GPS receiver's EVTTRG signal to pulse the red LED in the optical unit. The EVTTRG signal can be programmed to start a pulse train at a programmable date and time and with a given period.

The LED intensity was controlled with the pulse width such that on average 3 photons are detected in each pixel per pulse. In this case, the probability of detecting at least 1 photon in each pulse is almost 100%. Note that the pulses commanding the LED are 1μs long with a 30ms repetition period. Measurements were taken for all relevant FIR frequencies. For each FIR setting, the optimum bias voltages, magnetic fields and threshold settings were used.

In order to find the correct light pulses, the data was selected in energy and raw ratio (negative peak over positive peak); this eliminated most of the noise counts. The limits were optimized for each FIR setting, but were kept constant for all pixels for ease of processing. As a consequence, some LED pulses were not selected for the higher FIR frequencies and lower responsivity pixels. Instead, these pulses were manually checked on an individual basis. Conversely, for the lower FIR filter frequencies, some background light and noise counts are also selected. Examples of the spectra obtained with KJL480.5 and for the 9 and 36kHz FIRs are given in Figure 5-18 and Figure 5-19 respectively.

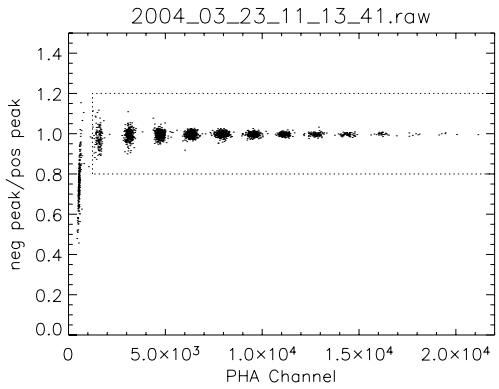

Figure 5-18: Spectrum obtained at 9kHz FIR. The dots are all recorded pulses. The dotted lines represent the selection box.

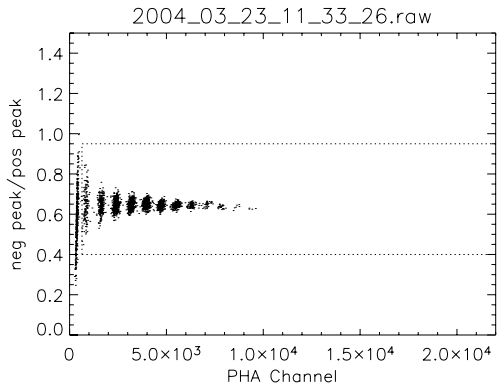

Figure 5-19: Spectrum obtained at 36kHz FIR.

The first check that was performed on each pixel and for each file is the starting time of the first LED pulse. This was confirmed to be identical to the programmed starting date and time on the GPS. We also verified that the GPS was giving absolute times to within its reported 100ns accuracy. Since we did not have an independent time standard, we used a second GPS receiver with its own antenna and verified that both were synchronous to <52ns.

We then investigated the time events in a statistical manner. This allowed verifying that there are no unexpected timing problems or errors and also to evaluate the accuracy with which the times are recorded. To this end, the time tags were folded using the 30ms pulse repetition period and constructed histograms for each pixel, referenced to the programmed GPS start time. A Gaussian fit then provided the mean and standard deviation of the offset for each channel. One such histogram obtained for a specific KJL480.5 pixel, at a 12kHz FIR filter setting is given in Figure 5-20. A zoomed-in version is given in Figure 5-21 together with its Gaussian fit. Note that the offset in the plot is the real delay plus a 31.4μs additional delay, included in the GPS command.

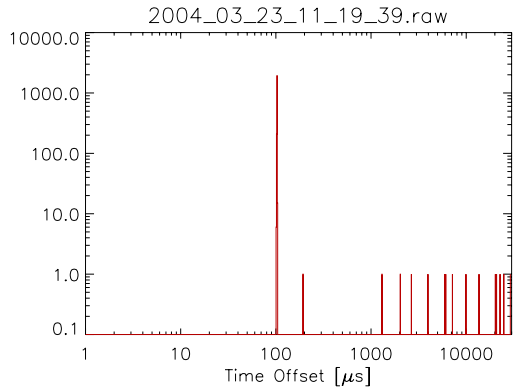

Figure 5-20: Histogram of recorded times for gr0/ch0. Some events have different offsets

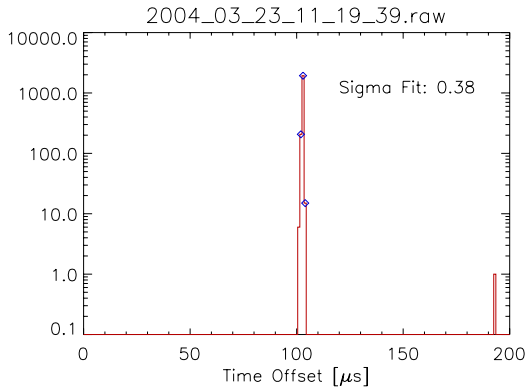

Figure 5-21: Zoomed version of histogram for gr0/ch0. Diamonds are from a Gaussian fit.

Figure 5-22 and Figure 5-23 are similar plots but now constructed with events from all pixels. In order to align the times, the calculated delays were subtracted from each pixel before the histogram was constructed. The alignment is performed using the granularity of the time-tag, i.e. 1μs. In order to estimate the accuracy or noise on the timing values, we take the standard deviations of the resulting Gaussian fit to the histogram distribution.

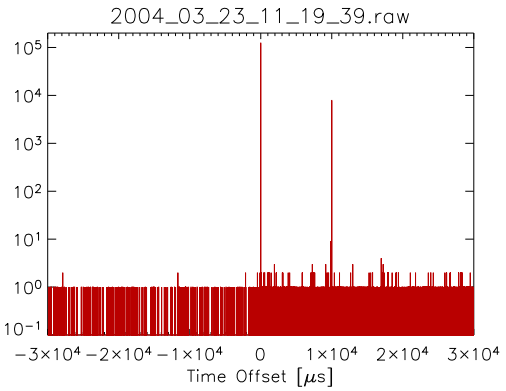

Figure 5-22: Histogram of recorded times for all channels. Some events seem to have wrong time stamps also a second peak is visible (see text).

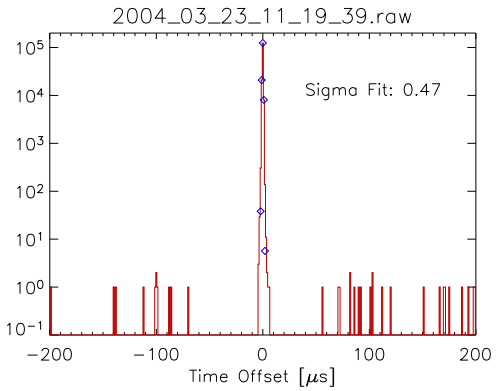

Figure 5-23: Detail of histogram centred around zero (where LED events should be). The diamonds are from a Gaussian fit.

A few features can be deduced from these histograms. First, looking at the histograms containing all channels, there seem to be time events which are negative up to –30000µs, positive up to 30000µs and a secondary peak is present at an offset of 10000µs. The negative offsets all come from events which happen to be in the selection window (most likely stray light) but occurring before the start of the first LED trigger pulse. The positive offsets, outside the two major peaks are identified as stray light events. Firstly, the times are random; secondly, their number is consistent with the background stray light in the laboratory during those measurements. Finally, one can get rid of them by increasing the minimum energy in the selection window. Since most LED events contain more than 1 photon, most of those events are located in PHA channels above the visible range, so the major peak remains visible, however, the stray light is filtered out.

There is also a peak at 10000µs. This one has been uniquely identified to be events with the wrong 1-second time-tag. Investigation revealed that these events only occur in group 2. The sequence of recorded events of group 2 seems to be shifted with respect to the other groups and the 1-second time-tag. Since the 'second' is appended at a later stage in the event processing, these events have an error of +1s. In microseconds, 10^6 modulo $3.10^4 = 10^4$, yielding the peak at 10^4µs. This problem was identified as a hardware failure and subsequently corrected. It should be noted that all investigations seem to indicate that no events are lost nor do they have erroneous fine-times. The histograms obtained after the hardware problem was corrected are given in Figure 5-24 and Figure 5-25. Clearly the anomalous peak at 10^4µs has disappeared.

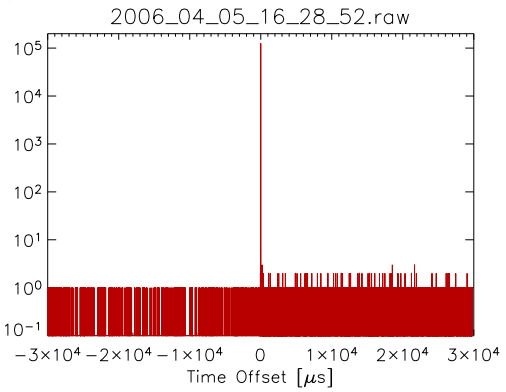

Figure 5-24: Histogram of recorded times for all channels, after correction of group2.

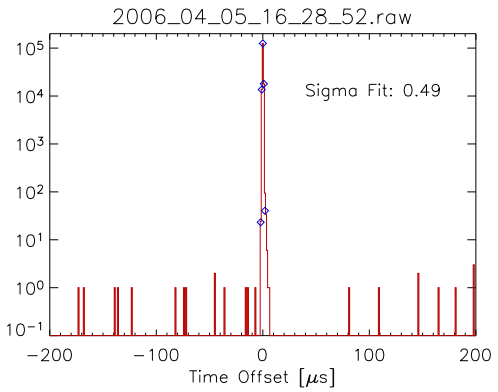

Figure 5-25: Detail of the left histogram.

From the folded histograms, we can also draw some conclusions about the accuracy of the offset determination. From the individual groups, we find that the fitted Gaussian curves have standard deviations ranging from 0.49 to 0.30μs for the lowest and highest FIR frequencies respectively. When merging all groups together, the distributions are all of order 0.5μs. Likely, the results are slightly better for the higher FIR frequencies, but we are limited here by the granularity of the time-tags the LED pulse length, both of 1μs.

A similar analysis was also performed for detector array MUL192.D2. The offsets for each of its pixels and for all relevant FIR filter settings are summarized in Figure 5-26. In order to see the measurement error, the error bars represent 5σ. The average errors on the offset determination range from 0.413±0.001μs at18kHz, to a minimum of 0.367±0.001μs at 36kHz and rising to 0.538±0.001μs at 96kHz; indicating that timing accuracy increases for higher FIR frequencies, but starts decreasing again as the signal-to-noise ratio falls.

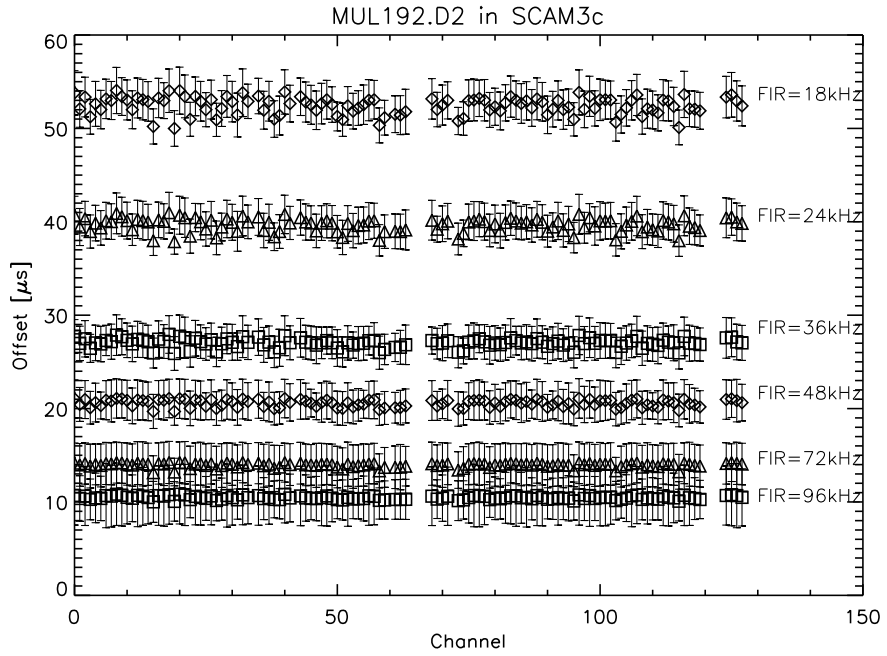

Figure 5-26: Summary of time offsets for each pixel and relevant FIR centre frequencies. Error bars are 5σ.

In order to investigate the influence of the signal-to-noise ratio on the timing accuracy, we selected only the single photon pulses in each channel and performed the same Gaussian fitting. The width of the Gaussian fit is an indication of the accuracy with which one can derive the arrival time of each optical photon. As the signal-to-noise ratio drops, one can easily conceive that the zero crossing of the filter's signal will be affected and thus the timing accuracy will decrease. Figure 5-27 shows the relationship of offset error versus signal amplitude (pulse height amplitude) for all pixels of KJL476.9 taken at a FIR frequency of 24kHz. This chip has the lowest responsivity of all S-CAM detectors and thus the lowest signal-to-noise ratio overall. There is a clear correlation visible; the pixels with highest responsivity giving the best timing accuracy. For comparison, Figure 5-28 is a similar plot for MUL192.D2, also taken at f_{FIR}=24kHz. The pulse height amplitudes have been adapted here to compensate for the lower electronic amplification needed for this chip, so that the PHA channels can be compared to those of the KJL device. Timing accuracy is here limited by the granularity of the measurement. Note that the accuracy of the timing is better than 1μs in all cases.

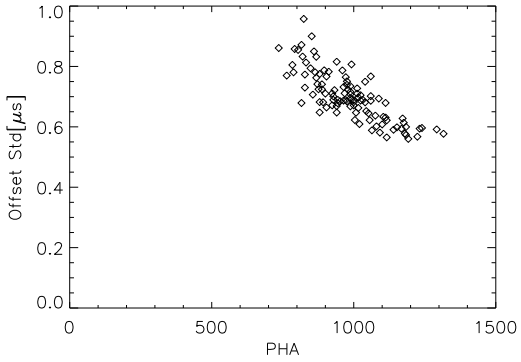

Figure 5-27: Standard deviation of the offset error as function of pulse height for KJL476.9.

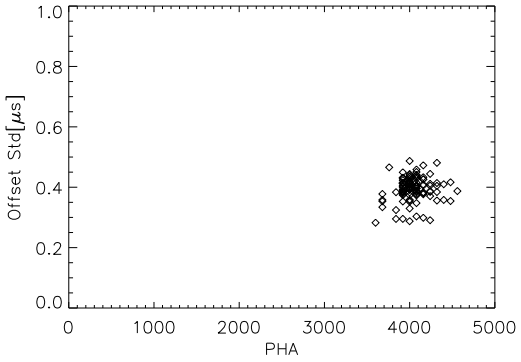

Figure 5-28: Standard deviation of the offset error as function of pulse height for MUL192.D2.

5.4 Pileup

Pileup occurs when two or more photons arrive at the detector in a short period of time and the filter responses overlap. This is illustrated in Figure 5-29, using the exact FIR filter's description (see Section 4.2) and simulated STJ pulses using an exponentially decaying pulse convolved with the amplifier's response. The curves show the output of the FIR filter when two photons, separated in time by a varying amount, Δt, strike the detector. Lets call the main event, the one that occurs at t=0. In the topmost curve, the events are well separated and no pileup occurs. When another event entered the detector 20μs prior to the main event, the latter one will see its positive peak diminished, while the negative peak is almost unaffected. For Δt=0, clearly only the sum signal is detected. For a secondary event occurring after the main event, the negative peak will mostly be affected.

We can now understand the role the positive and negative peak measurements can play. The energy of the incoming photon will be estimated by a weighted sum of the two extrema (the pulse-height), while their ratio will be an indication of the quality of the event. In this way, additional filtering can be applied to the data. Also pile-up can be estimated from plotting the peak-ratio (negative/positive peak) versus pulse-height. Such a scatter-plot is shown in Figure 5-30. Each dot represents a detected photon. The data is from a single detector pixel illuminated by a HeNe laser at a rate of ~1850 photons/s using the Hi-Res mode. The zone marked '1' in the plot corresponds to normal HeNe photons. Zone 2 also corresponds to normal photons, originating from stray light from the laboratory. Zone 3 events correspond to pile-up where another photon preceded the recorded event, while in zone 4 the pileup occurs from an additional photon following the recorded one.

Overlaid on this image is a contour plot (using a logarithmic scale) of the simulation of the pileup conditions of this measurement. The perfect match to the data confirms the correct understanding of the detector and electronics responses.

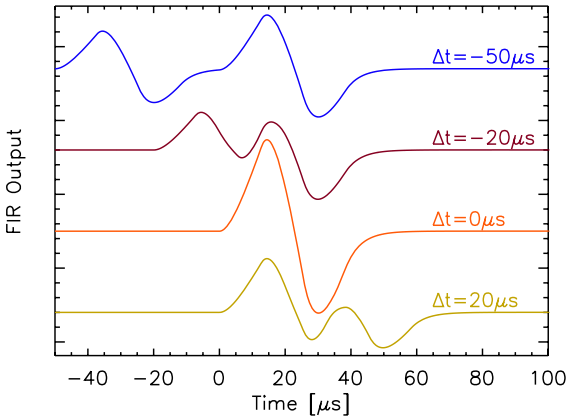

Figure 5-29: Output of the FIR for different times between pulses. In the topmost curve, no pileup is present, while the pulses add up in the case of simultaneous arrival.

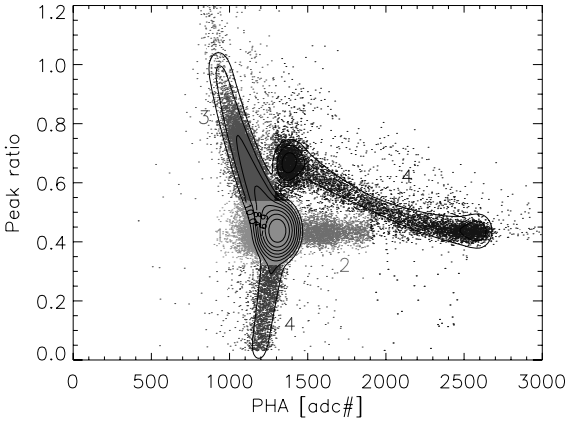

Figure 5-30: Scatter plot of peak ratios versus pulse-height. Zones 1 and 2 are 'normal' events, whereas Zones 3 and 4 correspond to pile-up events. Overlaid is a contour plot of the simulated pileup showing the good understanding of the measurement.

Figure 5-31 is the pulse height distribution of all these events. Overlaid is a fitted Gaussian curve (dashed line), used to determine the energy resolution. Since pile-up events are still rather seldom and distribute the pulse heights over a wide range of values, the Full Width at Half Maximum value of the spectrum is hardly affected and is therefore not a good indicator of pile-up.

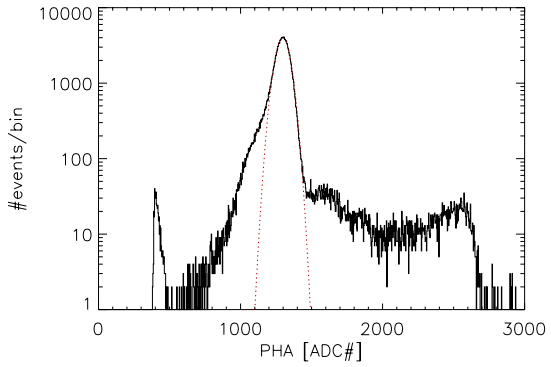

Figure 5-31: Pulse height distribution of pileup measurement. The dotted curve is a Gaussian fit to the data to determine the full width at half maximum resolution, the fitted value gives E/ΔE=11.5

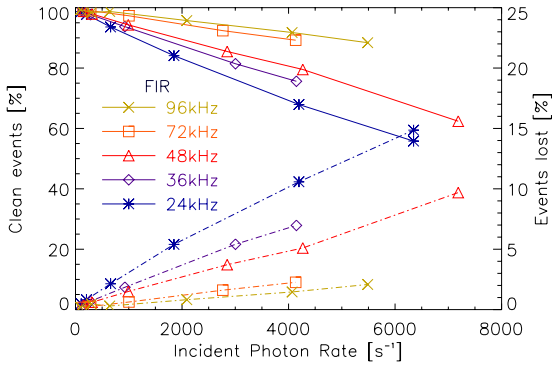

Figure 5-32: Fraction of events not affected by pile-up (solid lines – left vertical scale) and fraction of undetected events (dot-dashed lines – right hand scale) as function of incident photon flux and for various FIR filters.

What will be affected is the number of events which will suffer pile-up and the number of photons that will not be detected (too close to another event). These measurements, as function of incident photon flux, are summarized in Figure 5-32. The solid lines represent the fraction of clean events – not affected by pile-up – for various FIR settings (using the left-hand scale). The lower set of curves is drawn against the right-hand scale and corresponds to the fraction of events which will not be detected. These are important numbers to consider in the case that observations require accurate photometry. As can be expected, the lower FIR frequencies will suffer most from pile-up.

5.5 Gain and resolution stability over time

The stability of the overall system in gain and resolution is limited by all the analogue parts; the preamplifiers, the power supplies, and the detector. Since the sensitive parts of the electronics consist of high precision components and are temperature stabilized, the major contributor to drift is the detector itself. In order to monitor this behaviour, calibration files are acquired at regular intervals and serve as inputs to the post-processing software tools. In the laboratory, this occurs during integrated system tests while during observations, every night is preceded and followed by calibration measurements. Spare time between observations is often also utilized for this purpose.

In what follows, we shall present the gain and resolution measurements of the three detector chips used in S-CAM3 to date. All measurements were taken with the complete S-CAM3 system. The FIR filter was set to 'Hi-Res' mode and all other settings (bias voltage, magnetic field and weighting factor) were optimal for each detector. The arrays were stimulated with a fibre-coupled HeNe laser (632.8nm). A diffuser located in the focal plane uniformly distributes light across the detector and a neutral density filter attenuates the flux to achieve ~300photons.s^{-1}.$pixel^{-1}$. Integration is typically set to 100 seconds in each file. For each of the three detectors, we present the average charge output over the array, in ADC channels, and the average resolving power as function of time.

Figure 5-33 shows the results for KJL480.5, taken over the period March 2004 – May 2005. The FIR filter was set to 3×511 taps and 20MHz sampling frequency, for a 12kHz filter frequency; bias voltage was 190μV and the magnetic field was set to 225Gauss. The jump in signal amplitude during the S-CAM3a campaign is after the replacement of a defective DSP unit, which slightly changed the electronic gain. A linear fit to the data points (after the DSP unit exchange), shows a responsivity degradation of 1.5%/year and a resolution degradation of 2.5%/year.

Figure 5-34 are similar plots for KJL476.9, covering the period September 2005 – February 2006. The FIR filter was also set to 3×511 taps and 20MHz sampling frequency, for a 12kHz filter frequency; bias voltage was 140μV and the magnetic field was set to 230Gauss. The degradation of this chip is considerable, with a (extrapolated) responsivity loss of 11%/year and resolution loss of 12%/year.

The exact origin of this degradation is not understood at this stage. However, it could be related to the Niobium plugs in the base electrode and top contacts. Evidence for recombination traps in the Niobium has been obtained on similar STJ devices produced by the same manufacturer. These results were based on LTSEM scanning of 5keV electrons across a device as well as on DROID structures (see Section 7.1) with a central Nb contact and are reported in [140],[143],[145]. The Niobium, which is intended to confine quasiparticles in the STJ, avoiding diffusion into neighbouring pixels, was found not to act as a pure Andreev reflector, but effectively isolated the pixels also by trap-assisted recombination of quasiparticles. In this context, one could explain the performance degradation, by assuming diffusion of contact material and associated trapping sites into the active device over longer periods of time, leading to shorter quasiparticle lifetimes and, hence, signal loss.

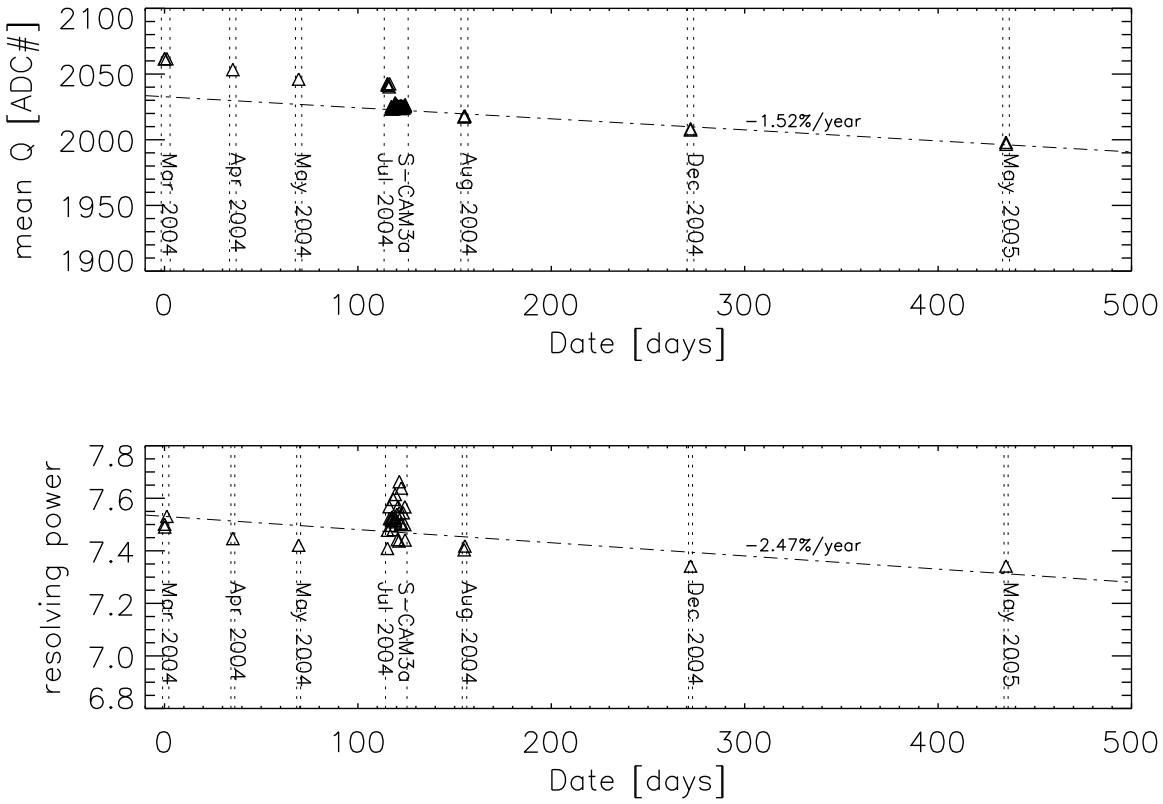

Figure 5-33: Gain (top) and resolution (bottom) stability over time for KJL480.5.

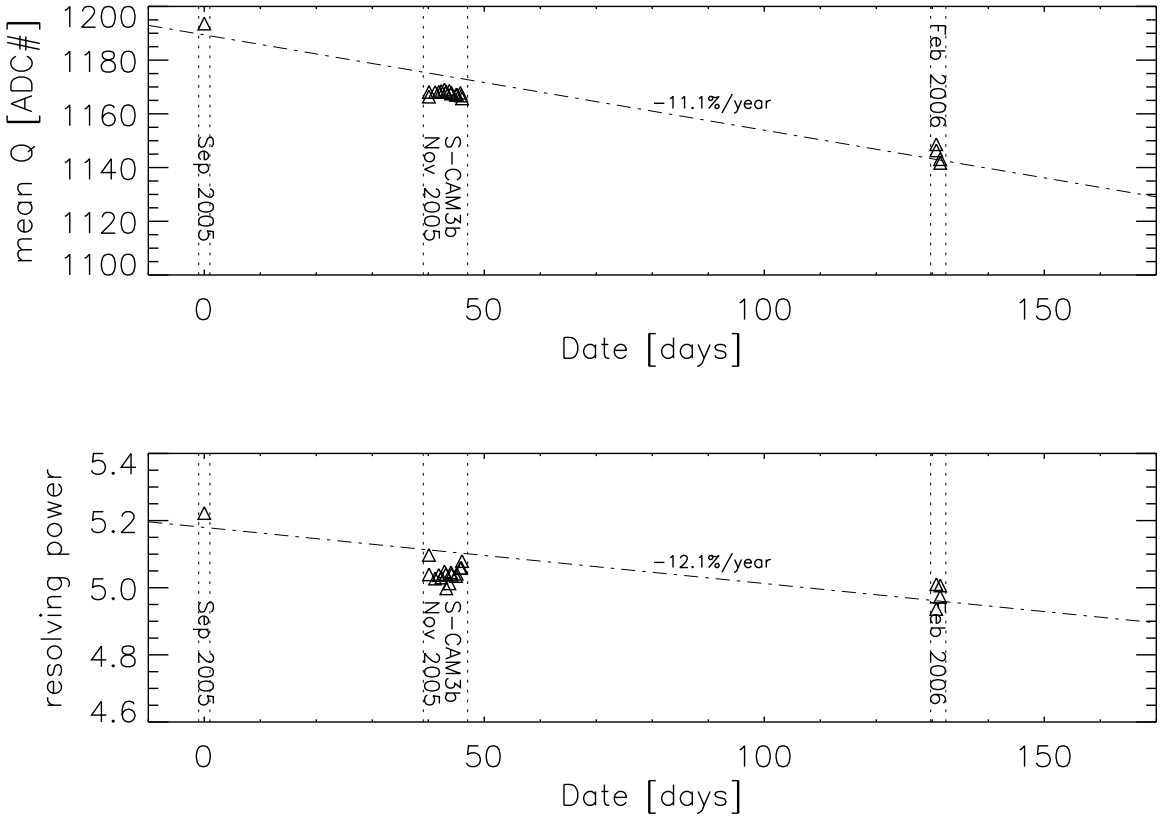

Figure 5-34: Gain (top) and resolution (bottom) stability over time for KJL476.9.

The average array gain and resolution of MUL192.D2 are represented in Figure 5-35. For this detector, the FIR filter was set to 3×511 taps and 40MHz sampling frequency, for a 24kHz filter frequency; bias voltage was 130μV and the magnetic field was set to 231Gauss. The two measurements labelled 'IST run1' and 'IST run3' were taken under slightly different conditions, explaining the lower gain. Over the one and half year time span, there does not seem to be any signal loss over time. Our theory that links traps in the Nb with degradation over time is reinforced here since DROID devices produced by MFab and following similar recipes as MUL192 do not show recombination sites in or near the central Nb contact [144].

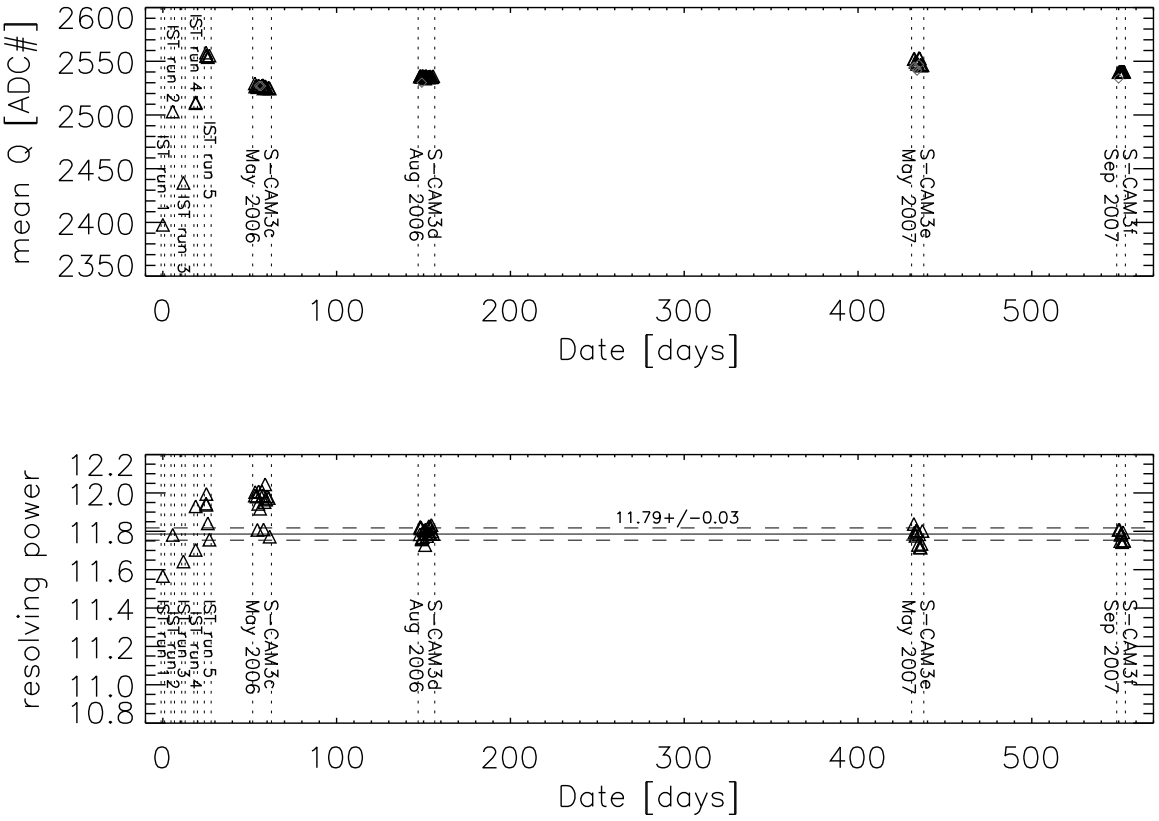

Figure 5-35: Gain (top) and resolution (bottom) stability over time for MUL192.D2.

One can note from Figure 5-35 that gain variations are of order ±0.5% from run to run and does require to be calibrated each time, however the system is particularly stable during a single campaign. To illustrate this, Figure 5-36 gives a detailed look at S-CAM3d campaign. The top panel is again the evolution of the average signal amplitude, but now normalized to the average over the whole campaign. The error bars denote the actual 1σ error in the estimation of the mean gain in each calibration and is of order 0.05%. The variation in average gain over the complete campaign has a standard deviation of 0.023%. There is no obvious day-to-day gain variation linked to the recycling of the coolers and this clearly shows the advantage of keeping the detector below its critical temperature at all times.

The energy resolution, shown in the lower panel, is also rather constant at 11.80±0.03 and consistent for all campaigns (compare to average of 11.79±0.03 obtained for all measurements taken under similar conditions, see Figure 5-35). For comparison we also show the electronic noise, estimated from the Full Width at Half Maximum of the pulse height distribution of a digital pulse injected at a frequency of 300Hz. The overall stability of the system means that in practice, a single calibration set will be used for the data reduction of the complete campaign.

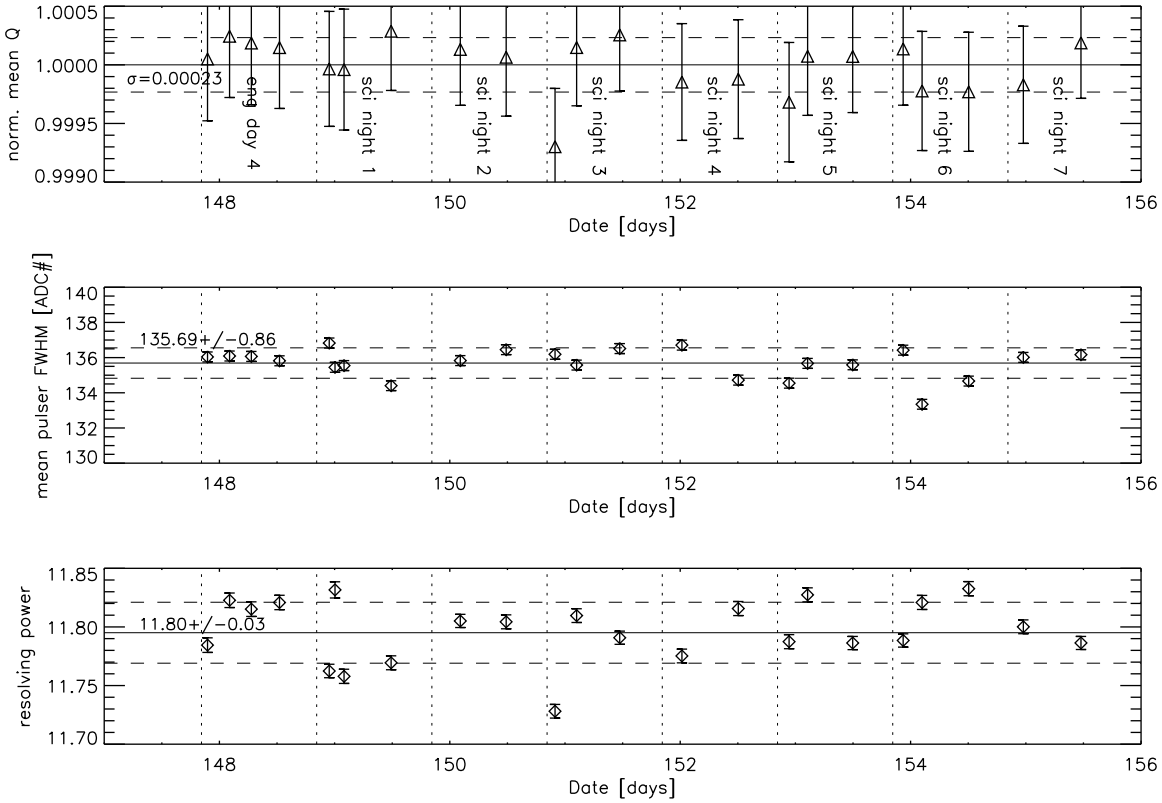

Figure 5-36: Gain and resolution stability during the S-CAM3d campaign. The detector is MUL192.D2 at the standard 'Hi-Res' setting.

Chapter 6

EXAMPLES OF ASTRONOMICAL APPLICATIONS

A number of observing campaigns have already been carried out with S-CAM at both the WHT and OGS telescopes. Although this thesis is not about astrophysics, we would like to present here some examples of the capabilities of a cryogenic photon-counting instrument. Although the data analysis from an instrument like S-CAM is far from trivial, its qualities as photometer, low-resolution spectrometer, and above all, its high timing accuracy will be evident from these results.

6.1 Eclipsing binaries

Figure 6-1 and Figure 6-2 show a measurement taken by S-CAM of the cataclysmic variable UZ-For in the form of broadband pixel-selected and pixel-integrated light curves respectively. Out of eclipse, the objects' brightness is estimated at m_v=17.7-18.1 magnitude depending on the phase. At roughly mid-exposure of the 1800s frame, a ~480s eclipse of the bright white dwarf and the accretion stream originating from the mass-losing companion is evident. During this event, the faint reddish contribution from the main-sequence component remains visible. The V/R and B/V plots in Figure 6-2 show a clear reddening during the eclipse.

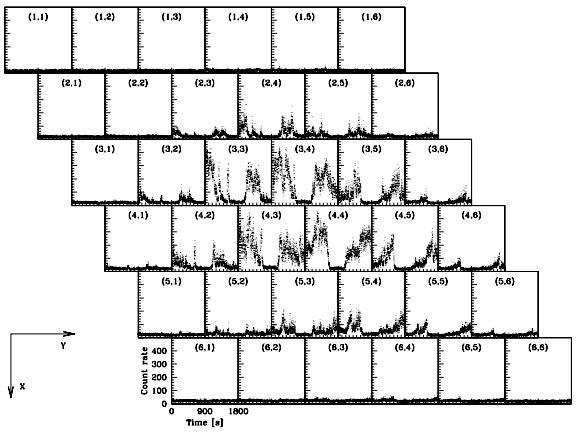

Figure 6-1: Pixel selected light curves of UZ-For, before background subtraction and at a 1s time resolution.

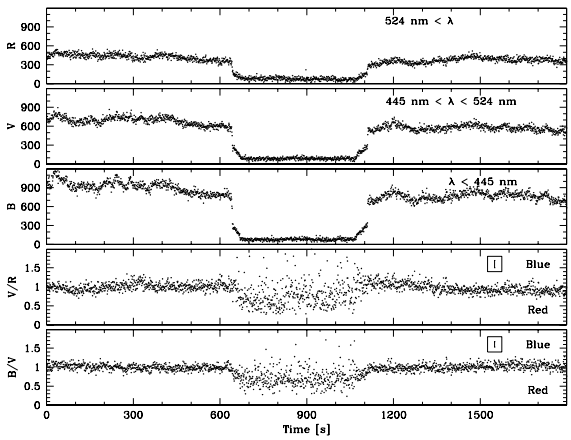

Figure 6-2: Sky-subtracted pixel integrated light curves for three bands (B: blue, V: visible, R: red) and their ratios.

High time-resolution spectrally resolved S-CAM data has provided strong constraints on the geometry of the accretion flow and the location of the accretion spots on the surface of the white dwarf in this system [116],[117],[118]. It was found that there are two small accretion regions, located close to the poles of the white dwarf. The positions of these are accurately constrained and show little movement from eclipse to eclipse. Figure 6-3 gives a schematic view of the system at phases of ingress and egress of spot 1 assuming a mass ratio q=0.2 between the stars. The secondary Roche lobe is projected as a wire model so that the white

dwarf remains visible. The system inclination, i, where i=0° corresponds to pole-on, is inferred to be about 80°. The origin of the coordinate system is at the centre of the white dwarf, with the origin of co-latitude vertically 'up' (so that spot 2 has a co-latitude of close to 0°, while spot 1 is around 150°). The origin of longitude is the coordinate axis joining the line of centres, with increasing longitude in the direction of the third coordinate triad. Ingress or egress of a given spot constrains its instantaneous projected location on the plane of the sky to lie along the limb of the secondary at that instant. The combination of timings of both the covering and uncovering of a given spot then constrain its position in two dimensions.

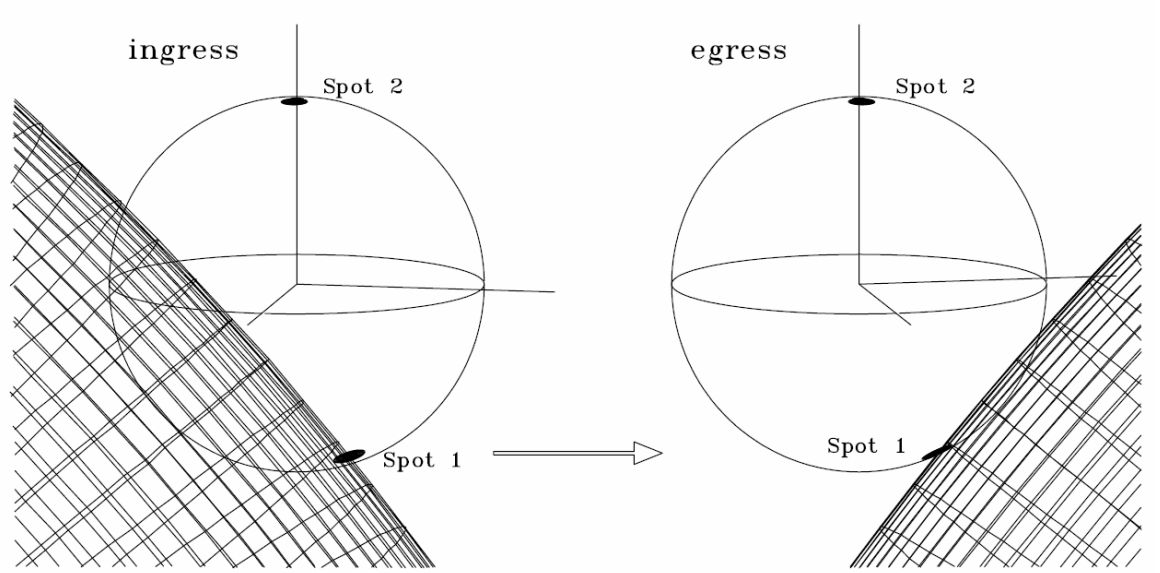

Figure 6-3: View of the system at phases of ingress and egress of spot 1

6.2 Crab pulsar timing

Precise timing of pulsar light curves provide a powerful tool to constrain theories of the spatial distribution of various emission regions, particularly if obtained throughout the electromagnetic spectrum. Recently, it became apparent that the pulses emitted by the Crab Pulsar are not perfectly aligned across different wavelengths. At X-ray and γ-ray wavelengths, the pulses are leading the radio pulses by ~310μs and ~240μs respectively. A 1999 measurement with S-CAM1 [119] was not conclusive at finding a timing difference between the optical pulses and the radio ephemeris. However, for later measurements, in particular during the S-CAM3b campaign [120], particular care was taken at calibrating the instrument's absolute timing (see paragraph 5.3.4). Also the radio ephemeris was more accurate for this observation.

For the analysis, all pulses in each observation were folded using their respective period (P), period derivative ($\dot{P}$) and epoch. The folded and normalized pulses for three S-CAM observations are shown in Figure 6-4, with a zoom on the main peak in Figure 6-5. A clear optical pulse lead of 273±65μs compared to the radio pulses was found in the later two observations. The results are summarized in Table 6-1, where the delays are for the radio pulse to the optical pulse, σ_{radio} is the published uncertainty on the radio ephemeris. The optical time shift is smaller than, but consistent with, the 370±40μs obtained from X-ray measurements which indicates that the optical radiation may be formed ~90km higher in the magnetosphere than the radio emission.

By using the intrinsic spectral resolution of the instrument, we also looked at phase differences between 'red' and 'blue' photons, but no significant difference in arrival times was found.

Table 6-1: Results summary of the radio to optical pulse delays measured with each instrument.

Instr.	Delay [μs]	σ_{radio} [μs]	Separation	P [s]	$\dot{P}$ [10^{-13}ss^{-1}]	Epoch [MFD]
S-CAM1	49±10	80	0.4056±0.0009	0.03349352792448	4.20554737	51224.000000352002
S-CAM2	254±8	160	0.4052±0.0005	0.03351561813489	4.20539152	51832.000000238553
S-CAM3	291±13	90	0.4065±0.0017	0.03358309316492	4.20593301	53689.000000194479

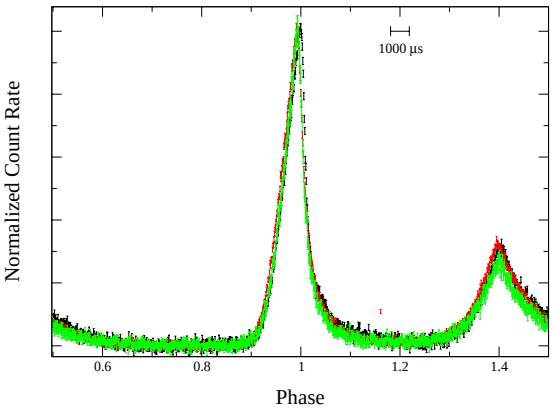

Figure 6-4: normalized pulse profiles for three S-CAM observations. Phase 1 is defined as the peak of the radio ephemeris.

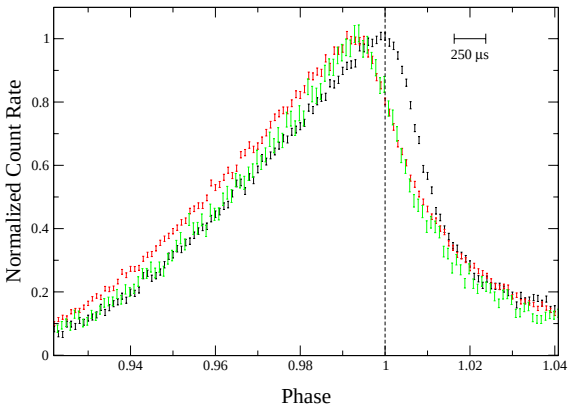

Figure 6-5: Zoom on the main peak. The S-CAM3 observation has higher statistical noise due to the short exposure on a smaller telescope.

6.3 Quasars direct red-shift measurements

The STJs capability to provide colour information has enabled for the first time direct determination of quasar redshifts [121]. During the October 2000 campaign at the William Herschel telescope at La Palma, we observed 11 quasars in the red-shift range z = 2.2–4.1, selected from literature [122]. All targets show strong Lyman-α and C_{IV} emission lines which, at these redshifts, fall in S-CAM's wavelength response range. The observations were carried out in modest seeing (1–1.5" at an airmass $X = 1$) and air-masses between $X = 1.07$–1.82.

Each quasar's redshift was determined by comparing the calibrated observed energy distributions with a single rest-frame composite quasar spectrum based on Hubble Space Telescope Faint Object Spectrograph spectra [121],[123]. The redshifts were then derived by minimizing a standard χ^2 function. The 5 minute exposures resulted in a typical redshift accuracy determination of ~1%. The resulting redshifts are listed in Table 6-2, together with the reported literature values. Examples of the observed and modelled spectra are shown in Figure 6-6. In practice, the Ly-α emission line and associated break at shorter wavelengths contribute most to the redshift determination. Figure 6-7 shows a comparison between reported literature redshifts and our direct determinations. QSO 0127+059 is a clear outlier which, in the literature was tentatively assigned a redshift of ~2.3 [124]. Subsequently a 1200s spectrum was obtained with the Siding Spring Observatory 2.3m telescope. A measurement using the Double Beam Spectrograph showed a z = 3.04, very close to our estimate (within 2%).

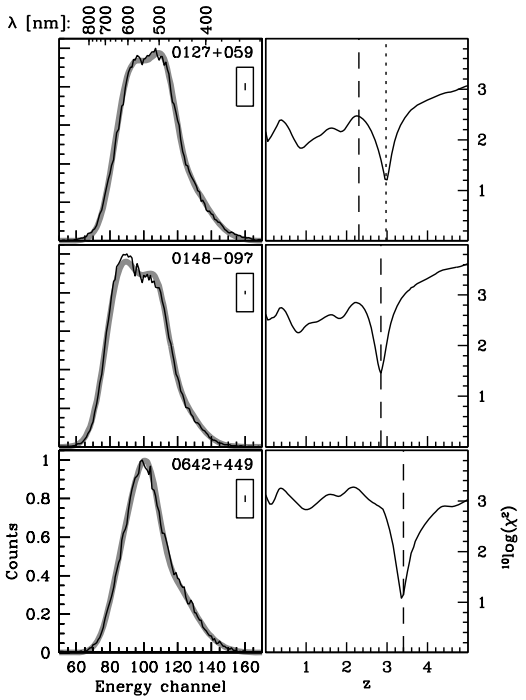

Figure 6-6: Left: the observed (black curves) and modeled (grey curves) energy channel distributions. Right: dependence of χ^2 on z showing clear minima.

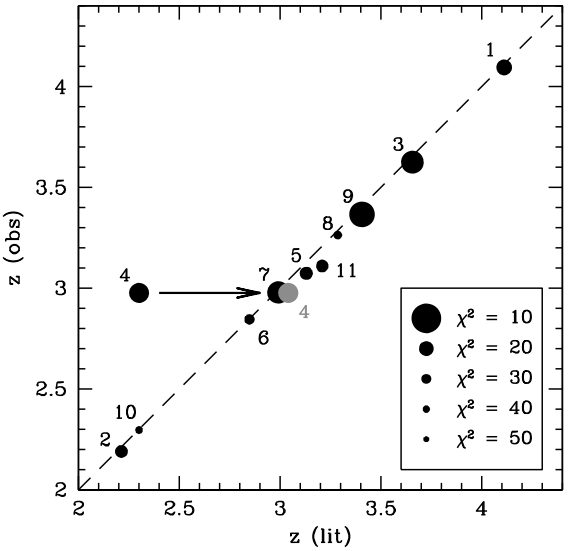

Figure 6-7: Comparison of observed versus literature redshifts. QSO 0127+059 has an incorrect literature reported redshift of 2.30. Our spectroscopic follow-up observation yields z = 3.04.

Table 6-2: Summary of observed redshifts and comparison to literature reported values.

Obs.	QSO Name	V [mag]	z_{obs}	z_{lit}
1	0000–263	17.5	4.095	4.111
2	0052–009	18.2	2.190	2.212
3	0055–264	17.5	3.625	3.656
4	0127+059	18.0	2.976	2.300
5	0132–198	18.0	3.073	3.130
6	0148–097	18.4	2.845	2.848
7	0153+045	18.8	2.978	2.991
8	0302–003	18.4	3.263	3.286
9	0642+449	18.5	3.366	3.406
10	2143–158	21.2	2.296	2.300
11	2233+136	18.6	3.110	3.209

6.4 Direct stellar temperature measurements

In the same spirit as the quasar redshift measurements, S-CAM was used to determine directly stellar temperatures. The traditional method would require photometric filtering or dispersive optics. The intrinsic energy resolution of our superconducting sensor can achieve the same results without having to use inefficient intermediate optical elements. We could demonstrate that a black-body emission profile could be fitted to the data and allow the extraction of reasonable estimates for the effective surface temperatures. In order to validate the method, a set of flux standards were used [125]. The observations and results of the fits are listed in Table 6-3. Spectral types are assigned on the basis of the current SIMBAD entry, while the effective temperatures are derived from literature (all referenced in [125]).

The method of fitting black-body spectra and stellar templates of varying spectral type to observed stellar spectra is a well-known method in X-ray astronomy. In effect the resolution of

S-CAM in the optical wavelength band can be compared to that of gas scintillators used in the 1980's and 1990's for X-ray observations [126],[127]. Figure 6-8 and Figure 6-9 show the results of the black body fit (solid lines) to the observed spectra (crosses) for EV Lac and Feige 25, respectively. The right-hand plots in each figure show the fit statistic χ^2 as function of temperature, T.

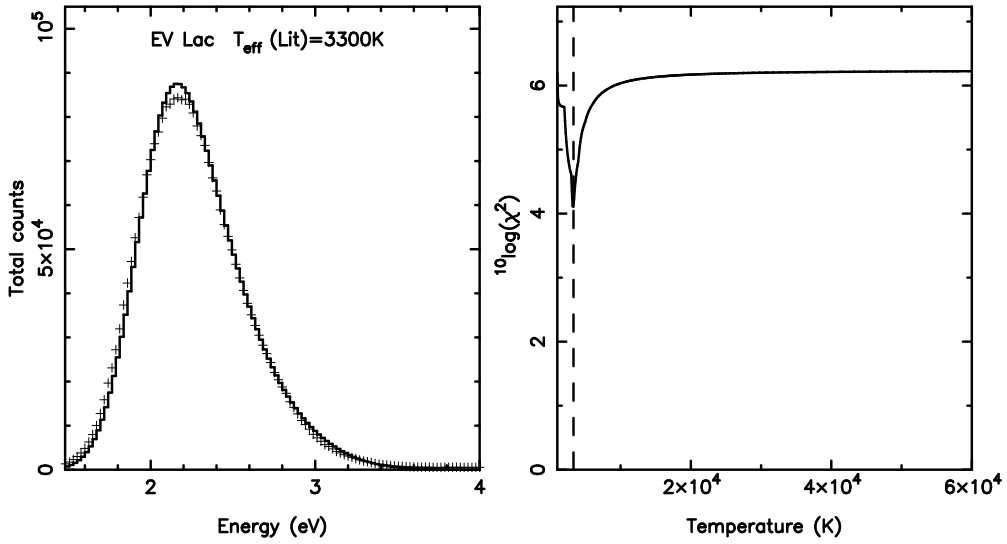

Figure 6-8: Results for EV Lac. Best fit is obtained for a BB temperature of 3200^{3500}_{3100} K, the vertical dashed line corresponds to the literature reported value.

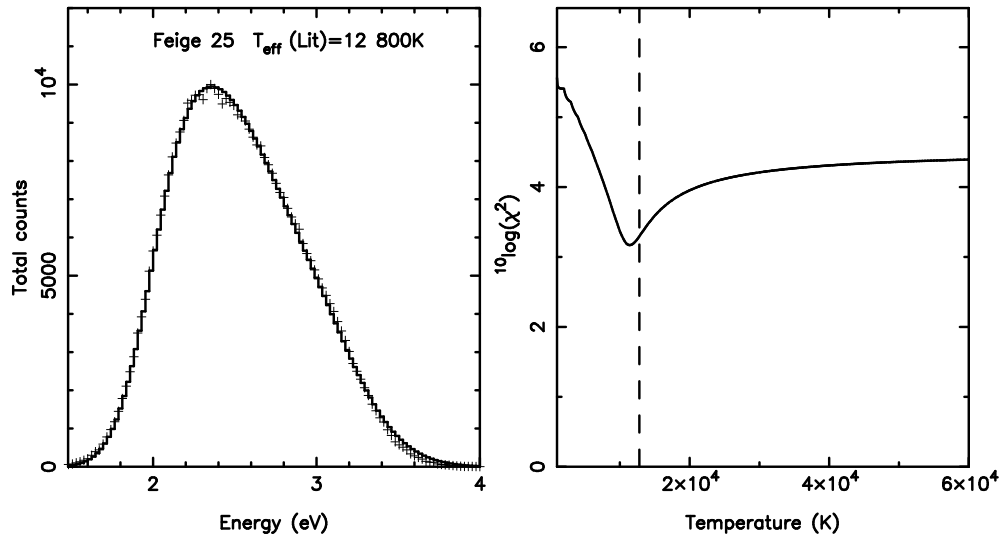

Figure 6-9: Results for Feige 25. Best fit is obtained for a BB temperature of 11400^{14100}_{9950} K.
Some deviations from the predicted emission curve are visible near the peak of the distribution that are most likely related to absorption features and need further analysis.

The results of all nine fits are summarized in Figure 6-10, which compares the observed versus the literature reported temperatures. The horizontal error bars indicate published uncertainties, while the vertical error bars reflect mainly the uncertainties in the instrument's energy calibration at the time of the observation.

Once the principle was established, the same procedure was applied to the accretion regions in several cataclysmic variable binary systems. As a first example, we show HU Aqr., a polar with ~125 minutes period [128]. In such systems, the accretion process is determined by the strong magnetic field, such that the stream is magnetically confined in the vicinity of the

dwarf. Prior to the eclipse, the dominant source of optical emission is the central accretion region. Once this region is occulted by the donor star, cooler components can be studied, such as the rear hemisphere of the donor and accretion stream itself. The light curve of an eclipse of HU Aqr. is shown in Figure 6-11. A sharp ingress of the bright accretion region followed by a more gradual ingress of a component identified with the accretion stream can be recognized. The vertical bars indicate the eclipse of the accretion stream, divided into four 33s intervals and a 200s portion of the mid-eclipse used for background subtraction. A blackbody model fit with T=6600K is shown in Figure 6-12.

Table 6-3: Stellar targets used for temperature determination. Reported literature and S-CAM measured temperatures are listed.

Obs.	Star Name	Type [lit.]	T_{eff} [Lit.; K]	T_{eff} [Obs.; K]
1	AD Leo	M3.5V	3400	$3100\,^{3300}_{3000}$
2	G117-B15A	DA	11500-12620	$13400\,^{16300}_{11200}$
3	Feige 15	A0	10800	$10400\,^{12800}_{9100}$
4	EV Lac	M3.5	3300	$3200\,^{3500}_{3100}$
5	Feige 25	B7	12800	$11400\,^{14100}_{9950}$
6	G138-31	DA8	6300-6870	$7200\,^{8100}_{6600}$
7	HZ 21	DA	48000	$100000\,^{100000}_{40700}$
8	GD337	DA+	9250-15000	$11300\,^{13600}_{9900}$
9	BD+28 4211	Op	82000	$44900\,^{100000}_{26000}$

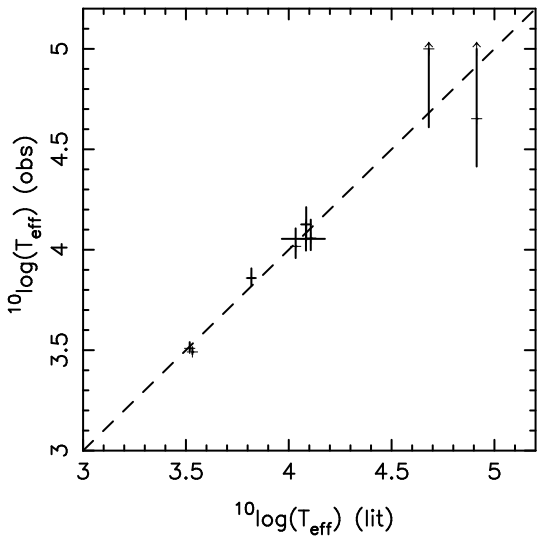

Figure 6-10: Observed versus literature reported temperatures for the nine stellar objects. The dashed line shows the expected one-to-one correlation.

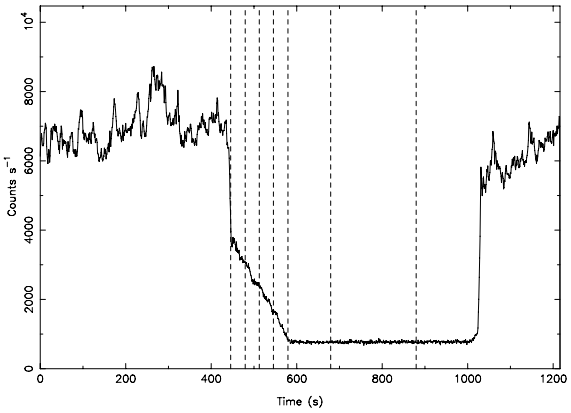

Figure 6-11: Eclipse light curve of HU Aqr.

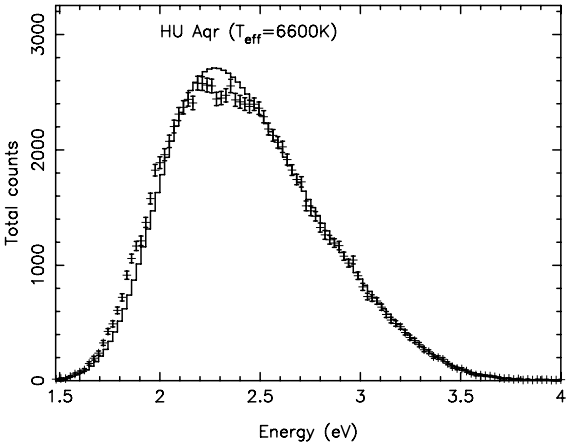

Figure 6-12: Black body model fit to a 33s portion of the stream data in HU Aqr.

As second example, we chose IY UMa, a non-magnetic cataclysmic variable [129]. In this 106.4 minute period system, the accretion proceeds via a disk. The eclipse morphology is significantly more complex (see Figure 6-13) and the geometry precludes an easy selection of an accretion region characterized by a single temperature. However, it is possible to isolate the spectrum of the white dwarf by extracting the difference between the spectrum of the source immediately before and after the rapid eclipse of the compact component. The vertical bars in Figure 6-13 indicate the two 20s eclipse segments used to isolate the spectrum of the white dwarf. Figure 6-14 shows the resulting spectrum and the black body model fit, yielding an effective white dwarf temperature of 16000±3000K.

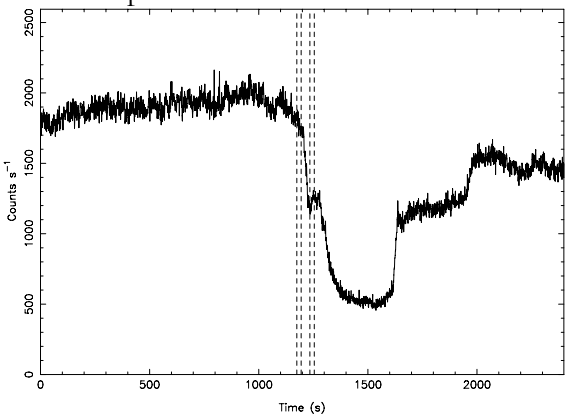

Figure 6-13: Eclipse light curve of IY UMa.

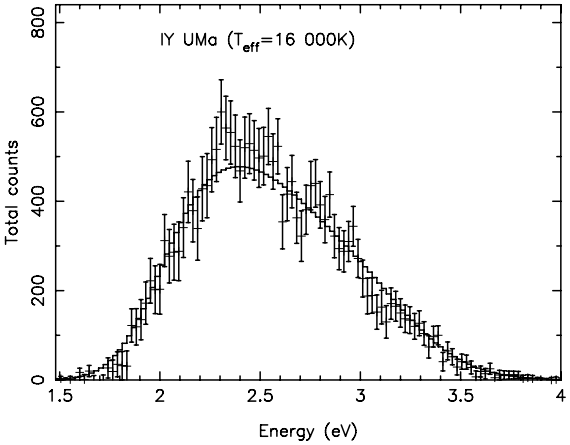

Figure 6-14: Black body model fit to the white dwarf component in IY UMa.

6.5 Planetary transits

In May 2006 we observed the central part and egress of the transit of planet TrES-1b in front of its companion star with S-CAM3 coupled to the OGS telescope [130]. The observed count rate of 12000 counts/sec lead to a light-curve with a time resolution of seconds simultaneously in a number of broad wavelength bands. In addition, we observed HD 149026 in order to establish the S-CAM3 instrument limitations associated with future observations of stars with very shallow transits.

In August 2006 we observed three northern stars (HD 209458, HD 198733, TrES-1) at the predicted times of four planetary transits. The analysis of these light curves will enable us to determine the radius of the planet independently of the size of the host star and may also allow us to study the atmosphere of the transiting planet.

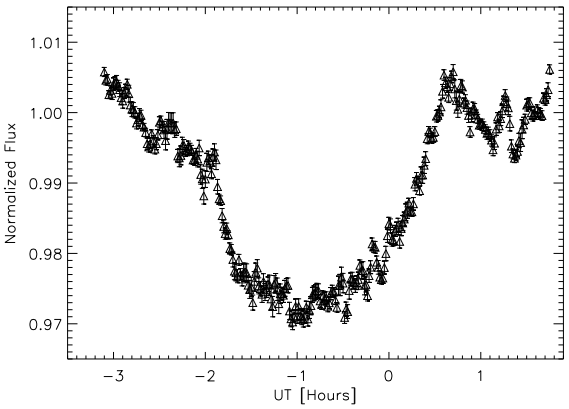

Figure 6-15: TrES-1 light curve obtained with S-CAM3, applying a 1 minute binning.

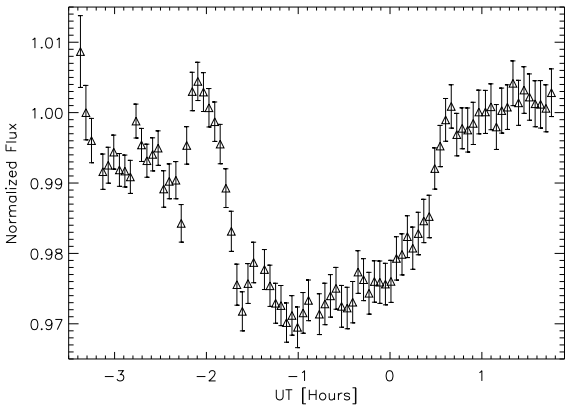

Figure 6-16: Simultaneous observation of TrES-1 with a CCD camera at 3 minute sampling.

For these observations, the S-CAM3 optics was preceded by a beam-splitter, directing ~2/3 of the collected light to S-CAM3 and the remaining 1/3 to a CCD camera. These observations were used to identify the optimum observation procedures and limitations of the system. It showed that apart from photometric sky conditions, good and stable seeing is vital for observations with S-CAM3. The very shallow transit of HD 149026 (0.003%) could not be detected, which is probably due to the unstable sky conditions during the observations.

The ~3% dip which can be observed in the light curve, as planet TrES-1b passes in front of its companion star is easier to observe. Figure 6-15 shows a transit light curve as measured with S-CAM3 during the August 2006 campaign applying a 1 minute time resolution, while Figure 6-16 is a simultaneous observation with an ordinary CCD camera with time steps of about 3 minutes. Although the transit, centred around -1^{h}UT seems to be well defined, the light-curves are varying more than expected outside the transit period. The variations also appear different in the S-CAM3 and CCD camera data. Current work is focussing on calibrating the interaction of the beamsplitter and telescope mirrors to explain this effect. Nevertheless, a direct comparison shows already that the r.m.s error bars in the S-CAM3 data are, at σ=0.1%, only one-third from those obtained with the CCD camera while having a factor of 3 better time resolution.

This planetary transit was observed again during the September 2007 campaign. A screenshot of the 'live' data taken during the transit is shown in Figure 6-17. The bottom part of the picture is the image seen by the detector at 1-sec intervals. The 8×8 grid is a user defined source region, pixels outside this region count as background. TrES-1 is clearly visible in the centre of the image. Total count-rate is about 10000 photons.s^{-1} over the whole array. The background (see upper left curve) is about 17 photons.s^{-1}.$pixel^{-1}$. The S/W calculates in real-time the background subtracted light-curve, just above the middle of the image. In this curve, spanning about 13500s, one can recognize the intensity decrease due to atmospheric extinction (as the object's elevation decreases, intensity decreases as light has to travel through a thicker layer of atmosphere). Nevertheless, the transit is clearly visible, with ingress and egress at ~2250 and ~10750s respectively. This data is currently undergoing detailed analysis.

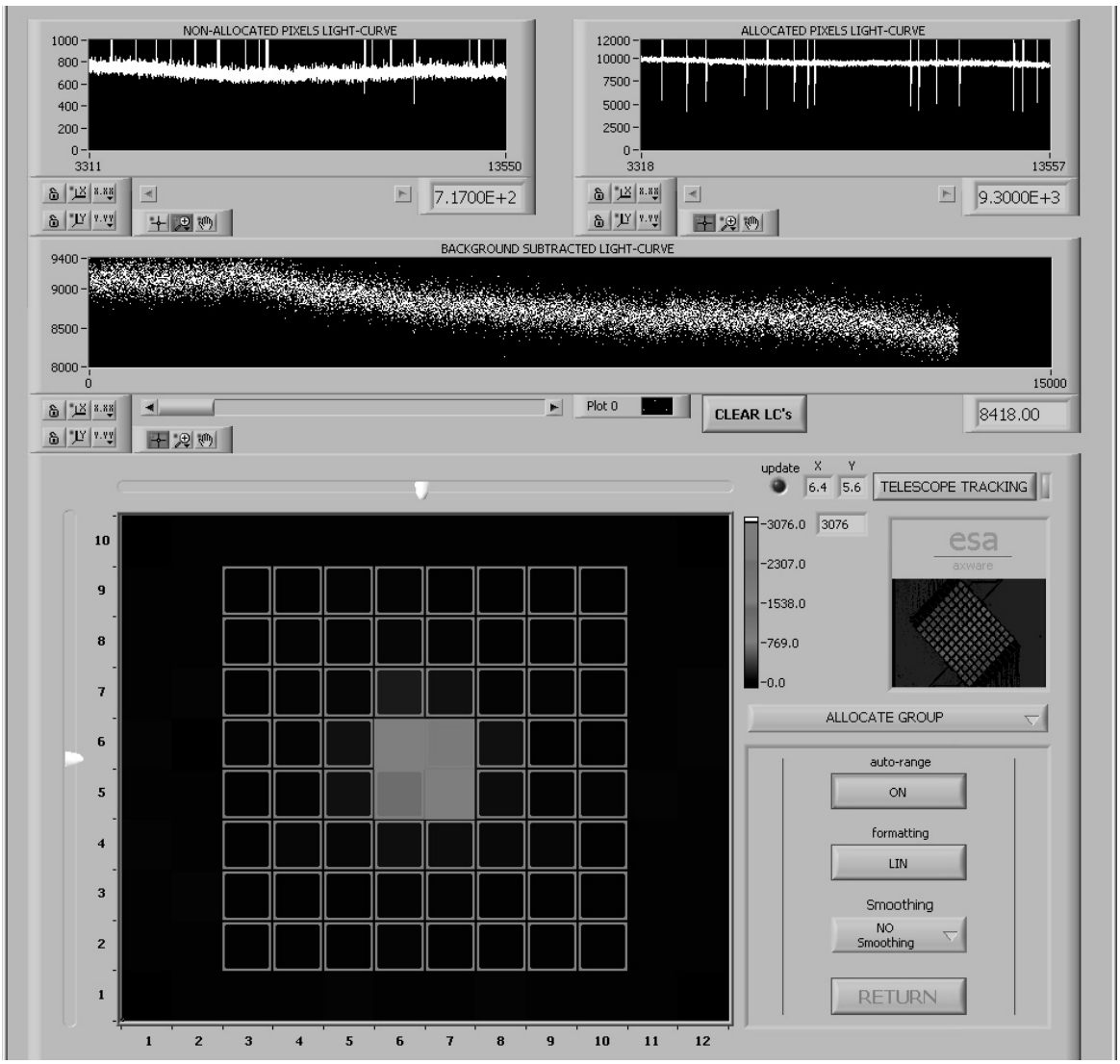

Figure 6-17: Snapshot of (a part of) S-CAM's graphical user interface during the TrES-1 exo-planetary transit observation of September 2007.

Chapter 7

CONCLUSIONS AND OUTLOOK

We set out to design, build and operate an optical spectro-photometer camera based on a superconducting tunnel junction array. Based on previous experience, the goals for this camera were to increase the field of view such that true imaging would be possible whereby the point spread function of the telescope would be fully covered and no light from a point source would be lost from the array. At the same time, a sufficient sampling of the sky background should be possible, for subtraction in the data analysis. We wanted to increase the fill factor of the array and the energy resolution of the tunnel junctions to the limit of the superconducting materials. During the improvement of the devices' quality, we identified a new fundamental source of noise related to statistical energy loss through phonon escape from these thin films. Furthermore, we wanted to improve the throughput of the instrument, while increasing both the bandpass as well as the infrared rejection. Finally, we wanted to make the electronics readout system more flexible, autonomous, faster and more reliable and the cryogenics more stable. All these goals have been met and the instrument was successfully deployed at both the William Herschel Telescope on La Palma as well as the Optical Ground Station on Tenerife, for a total of six observing campaigns to date.

We have clearly shown that such detectors, although requiring more stringent operating conditions then for instance CCDs, can be fabricated and integrated in useful instrumentation. This development has opened the door to future astronomical applications, and ground based or space borne instruments could now be conceived. A number of new developments have already been initiated to increase the capabilities of such instruments. We shall briefly review the four routes that are currently being pursued.

7.1 S-CAM4 – DROID array

As we have seen, the current generation of STJ arrays require a separate readout for each pixel. It is clear that if we would want to increase the number of pixels beyond, e.g. 1000 pixels, a different scheme should be adopted. An alternative method is to rely on two STJs to sample the quasiparticle population created in an absorber strip. These devices, which we call Distributed ReadOut Imaging Devices (DROIDs) were first tested by Kraus et al. [131] and show very promising results. The principle of operation is as follows: an absorbing strip made of superconducting material is ended at both sides by an STJ. For our optical DROIDs, the absorber also forms the base electrode of the STJs. When quasiparticles generated e.g. through photoaborption diffuse outwards from the point of absorption, they will eventually arrive at the STJs. By exploiting the proximity effect, we can lower the energy gap in the junctions and quasiparticles can be captured and retained in the junction area, producing an excess signal current. The sum of the signals from both STJs will give a measure of the photon's energy while their ratio will provide information on the location of the photoabsorbtion site.

Figure 7-1 shows a fabricated DROID array consisting of 60 DROIDs, thus 120 STJs, arranged in four electrically separated banks of 30 devices each. This device can be connected to the S-CAM electronics to provide a field-of view of 20×30 arcsec^2 [132].

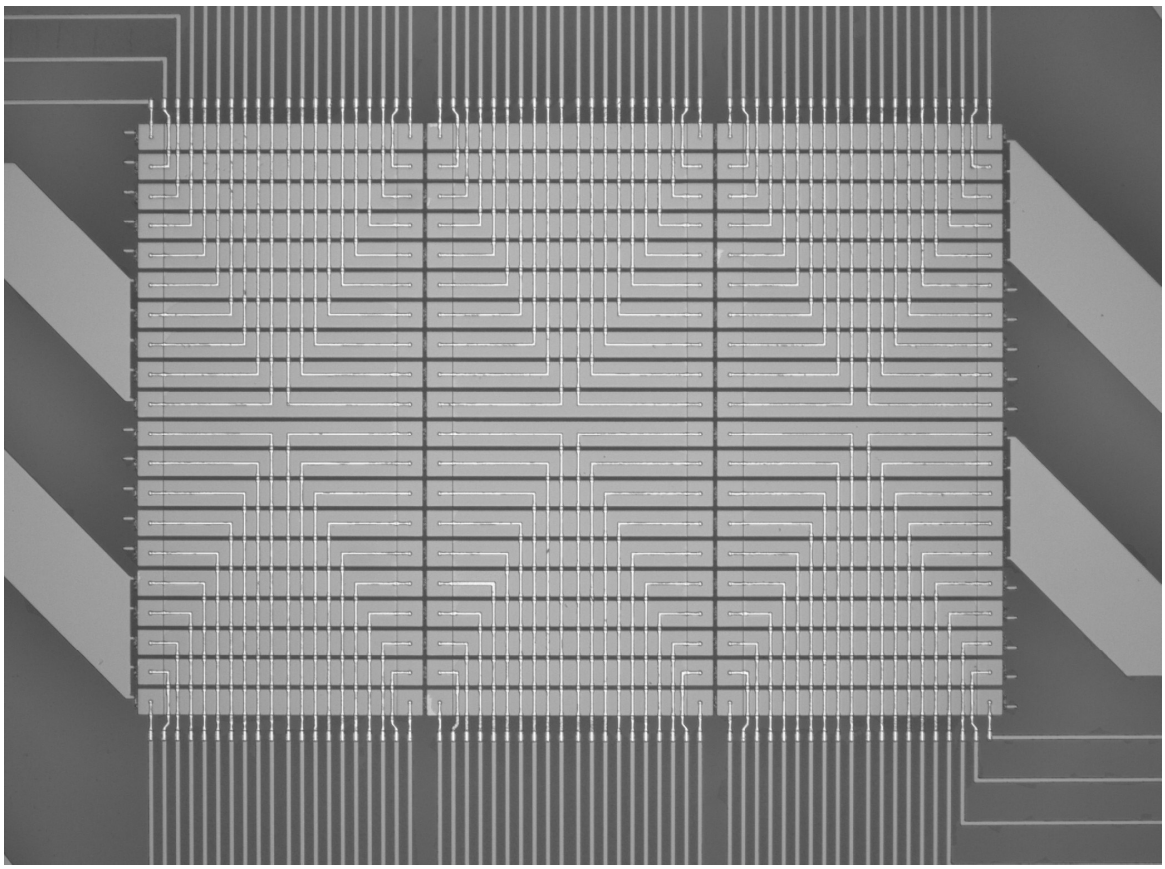

Figure 7-1: Micrograph of one of the first DROID arrays produced by MFab.

7.2 S-CAM5 – Closed cycle cooler

A major disadvantage of our current S-CAM system is the need to use liquid Helium to cool the detector. For fully autonomous operations on ground or indeed for space applications, a mechanical cooler would be more convenient. A number of space instruments are already relying on mechanical cooling machines, e.g. the Planck or James Webb Space Telescope missions will be operating cryogenic sensors using mechanical coolers, which should enable longer lifetimes in orbit and a better exploitation of the investments.

We have started experimenting with a pulse tube refrigerator (PTR) as a first stage cooler. The commercial unit, from Cryomec, has been coupled to a double sorption cooler, similar to our current S-CAM design. The major problem with mechanical coolers is related to the vibrations induced by moving parts. A PTR, although relatively 'noise-free' still has a valve which switches the high pressure Helium gas in a tube, creating standing waves. The switching frequency is unfortunately in the middle of typical shaping filters used for STJ pulse processing. In addition, the high impedance of the sensors makes them very susceptible to acoustic noise. In particular the wiring, capacitively coupled to the structure, will displace charges as they move with respect to a ground potential. These charges are directly measured by the sensitive front-end electronics. STJs are in that sense much more sensitive than the low impedance microcalorimeters, where these coolers are now becoming ubiquitous (e.g. [133],[134]).

In our system, shown in Figure 7-2, we have taken great care to isolate the PTR head mechanically from the cold plate. Also the wiring was laid out such as to minimize acoustic noise pick-up. The dewar has an access port allowing it to be coupled to an external source of radiation, for instance an X-ray beam. Recently we have been able to detect optical photons, proving that low-noise operation is possible in such a set-up.

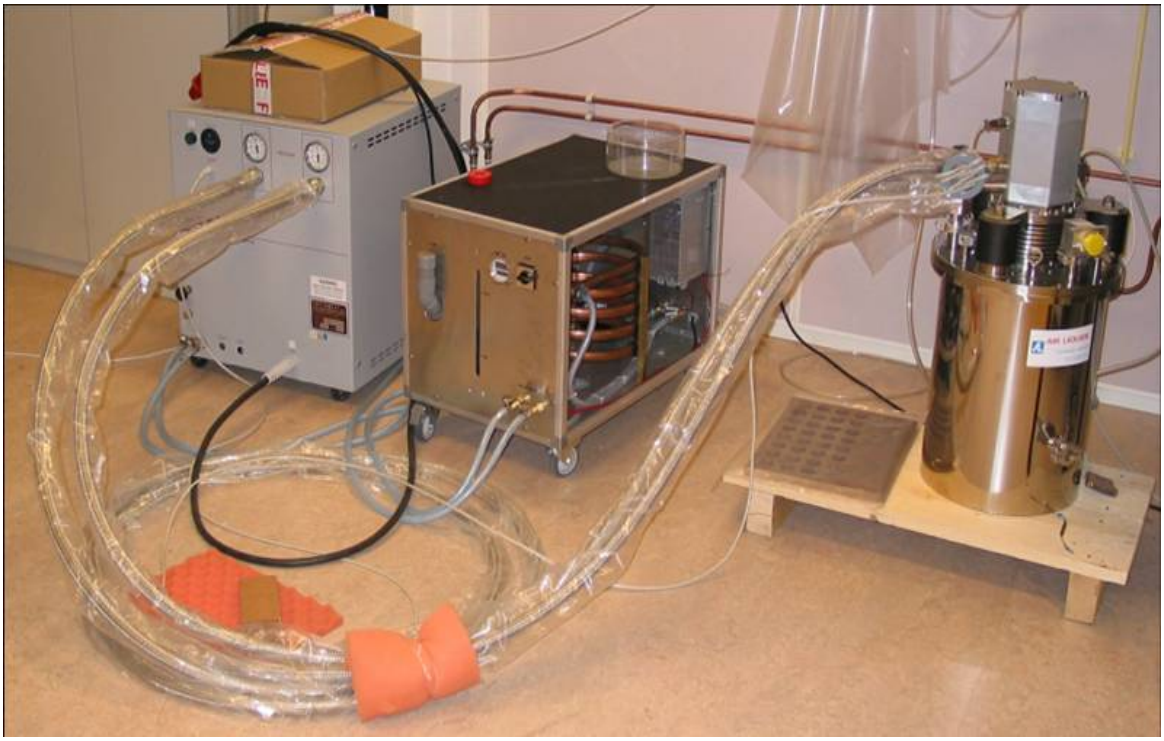

Figure 7-2: Cryostat coupled to a Pulse Tube Refrigerator, model PT503 from Cryomec.

7.3 S-CAM6 – Fibre-fed instrument

One of the most difficult aspects of efficiently coupling an STJ array to an optical ground telescope is the necessity to provide extremely high IR rejection. In our current design, we have seen that various sorts of thick optical glasses are used for that purpose. Their limitation is that the cut-off wavelength is somewhere between 700 and 800nm. Considering only the 300K black-body radiation, one could provide an observing window beyond 1μm without overloading the superconducting detectors with thermal photons.

A possible solution to this problem could be to use 'wet' optical fibres, i.e. fibres containing a high OH concentration. Thermalization of the fibres is done by wrapping a few meters of it inside the dewar, on the cold plate. The OH bands of this cold filter provide effective blocking above 1.7μm wavelength, but allow transmission in the atmospheric windows. The difficulty is in coupling the fibres to the small detectors in a cryogenic environment. The Stanford group has coupled both 50 and 200μm fibres through a grin and spherical lens to a subset of their small TES arrays [135],[136].

Currently we are pursuing two ideas. In the first, the detector consists of two identical arrays, each of which being coupled to a fibre. The fibres are terminated at the telescope's focal plane and sample the target object and the nearby background, respectively. Such a design was already included in the mask set used at MFab and a micrograph of such a device is given in Figure 7-3. The second option is to use the S-CAM as an integral field photo-spectrometer. The detector array could consist of 256 elements, each coupled to its own fibre that is routed to the telescope's focal plane. The instrument would rely on existing fibre units available or being developed at observatories, e.g. INTEGRAL on the WHT [137] or the Fibre Instrument Feed (FIF) at the South African Large Telescope (SALT) [138].

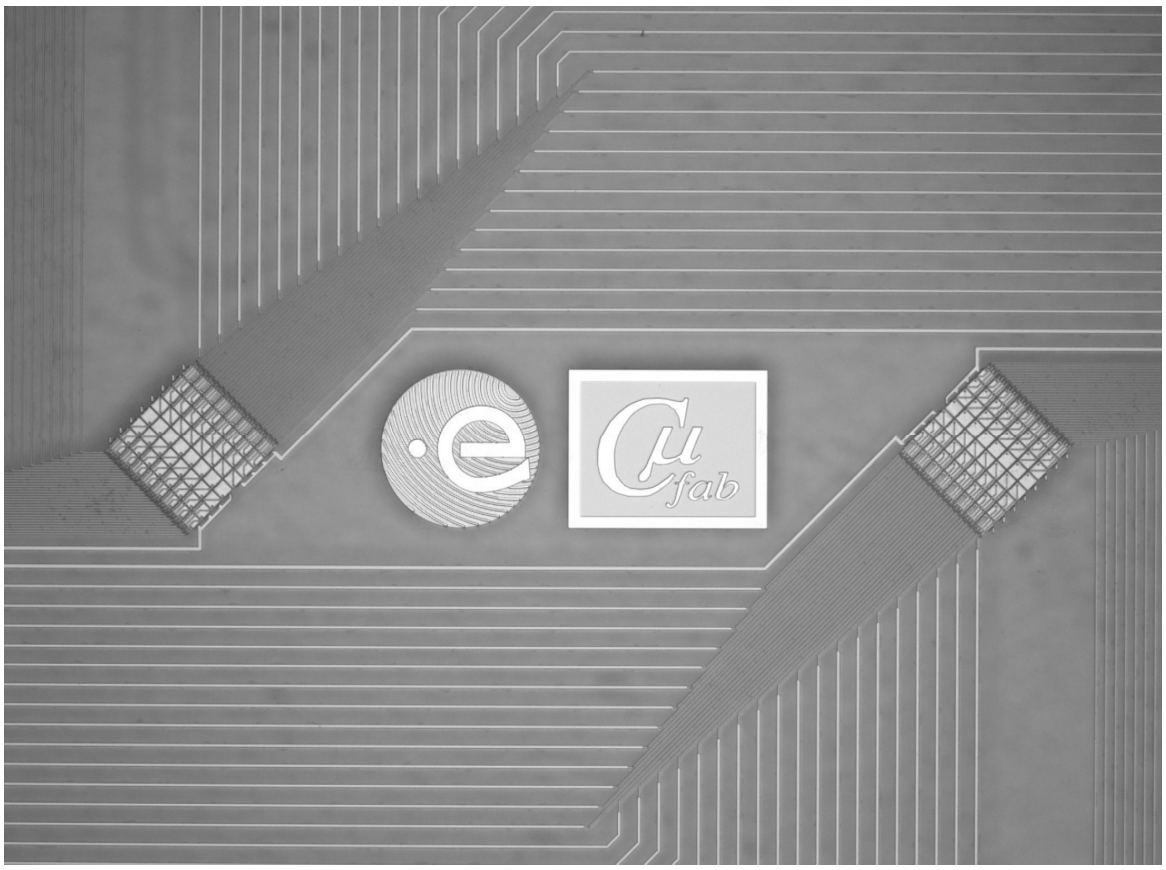

Figure 7-3: Double 8×8 array, which could be used in a double fibre coupled instrument.

7.4 X-ray detectors for the next generation X-ray observatory

The most promising application for STJs is most likely as soft-X-ray detectors for astronomical instruments or material analysis. We are currently focussing on the development of optimized devices that could be used for potential future X-ray observatories like Xeus or Constellation-X.

The major scientific goals for a mission like Xeus are related to the study of very distant, and hence youngest, objects known in the Universe. Specifically, it sets out to measure spectra of objects with redshifts z in excess of 4 with flux levels below 10^{-18}erg.cm^{-2}.s^{-1} which represents a 1000 times improvement in sensitivity to the current instruments onboard XMM-Newton [139]. From the measurement of the red-shift of the spectral lines, one can infer the ages of these objects, otherwise not necessarily possible at optical wavelengths. Furthermore, such a mission should establish the cosmological evolution of matter in the early Universe. This can be inferred form the measurement of heavy-element abundances as function of red-shift. In order to achieve these goals, the mission requires one or two cryogenic instruments, covering a 30×30 arcsec^2 field of view with of order 1000 pixels, ~2-3eV resolution at 1keV and count rate capability in excess of 10^4 counts.s^{-1} combined with a timing accuracy better than 5μs [140].

The focus on the early universe and thus highly red-shifted spectra means that the major K and L emission lines will be below 2keV. Thin superconducting films of order 500nm provide excellent absorption efficiency in this energy range, as an example we show the efficiency for 500nm thick films of Ta, Mo and Re in Figure 7-4, Al is added for comparison

although it is not considered as absorbing material, but could be used as STJ (figures calculated from Henke [141]). DROID arrays could provide the required field coverage, while their energy resolution already approaches the requirements [142],[143].

The developments are now focussed on fabricating different geometries; depending on the way the absorber is coupled to the STJ [144]. Simultaneously, theoretical models are being refined to understand the limitations of those different alternatives, eventually leading to an optimized design [145].

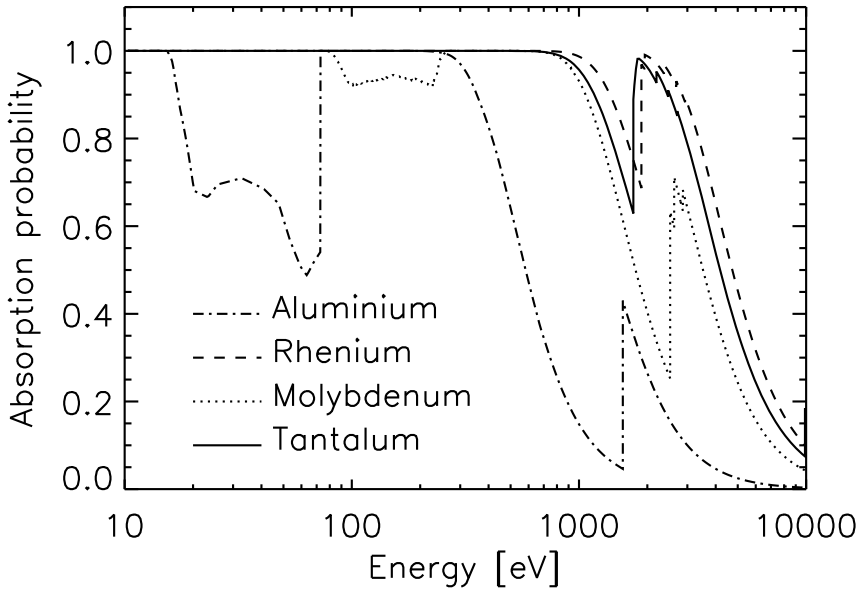

Figure 7-4: Absorption efficiencies for 500nm thick films made of various materials

REFERENCES

[1] I.N. Reid, C. Brewer, R.J. Brucato, W.R. McKinley, A. Maury, D. Mendenhall, J.R. Mould, J. Mueller, G. Neugebauer, J. Phinney, W.L.W. Sargent, J. Schombert, R. Thicksten, Publ. Astron. Soc. of the Pacific **103**, pp. 661-674 (1991).

[2] J.G. Timothy, Proc. of SPIE **1549**, pp. 221-233 (1991).

[3] G.F. Amelio, M.F. Tompsett, G.E. Smith, Bell Syst. Tech. J. **49**, pp. 593-600 (1970).

[4] C.D. Mackay, Ann. Rev. Ast. & Astrophys., **24**, p. 255 (1986).

[5] A. Short, G. Hopkinson, A. Laborie, P. Pouny, C. Vetel, T. Eaton, R. Steward, A. Holland, I. Hutchinson, D. Smith, J. de Bruijne, P. Gare, M. Perryman, G. Sarri, I. Zayer, Proc. of SPIE **5902**, p. 590205 (2005).

[6] V.S. Dhillon, T.R. Marsch, M.J. Stevenson, D.C. Atkinson, P. Kerry, P.T. Peacocke, A.J.A. Vick, S.M. Beard, D.J. Ives, D.W. Lunney, S.A. McLay, C.J. Tierney, J. Kelly, S.P. Littlefair, R. Nicholson, R. Pashley, E.T. Harlaftis, K. O'Brien, Mon. Not. R. Astron. Soc., accepted for publication (2007).

[7] E.R. Fossum, IEEE trans. on Electron Devices **44**, no 10, pp. 1689-1698 (1997).

[8] E.R. Fossum, Proc. of SPIE **1900**, pp. 1-14 (1993).

[9] P.J. Love, K.J. Ando, J.D. Garnett, N.A. Lum, J.P. Rosbeck, M.S. Smith, K.P. Sparkman, Proc. of SPIE **4008**, pp. 1254-1267 (2000).

[10] K. Vural, L.J. Kozlowski, D.E. Cooper, C.A. Chen, G.L. Bostrup, C.A. Cabelli, J.M. Arias, J. Bajaj, K.-W. Hodapp, D.N.B. Hall, W.E. Kleinhans, G.G. Price, J.A. Pinter, Proc. of SPIE **3698**, pp. 24-35 (1999).

[11] P.J. Love, A.W. Hoffman, N.A. Lum, K.J. Ando, W.D. Ritchie, N.J. Therrien, Proc. of SPIE **5499**, pp. 86-96 (2004).

[12] B.J. Rauscher, D.F. Figer, R.J. Hill, P.J. Jakobsen, S.H. Moseley, M.W. Regan, P. Strada, Bulletin of the American Astronomical Society **36**, p. 674 (2004).

[13] B.A. Mazin, R.J. Brummer, Astronomical Journal **120**, issue 5, pp. 2721-2729 (2000).

[14] B.A. Mazin, B. Bumble, P.K. Day, M.E. Eckart, S. Golwala, J. Zmuidzinas, F.A. Harrison, Appl. Phys. Letters **89**, p. 222507 (2006).

[15] J.N. Ullom, J.A. Beall, W.B. Doriese, W.D. Duncan, L. Ferreira, G.C. Hilton, K.D. Irwin, C.D. Reintsema, L.R. Vale, Appl. Phys. Letters **87**, p. 194103 (2005).

[16] J. Beyer, P.A.J. de Korte, C.D. Reintsema, S.W. Nam, M. MacIntosh, G.C. Hilton, L.R. Vale, K.D. Irwin, Trans. on Appl. Supercond. **13**, issue 2, pp. 649-652 (2003).

[17] R.W. Romani, A.J. Miller, B. Cabrera, E. Figueroa-Feliciano, S.W. Nam, Astrophysical Journal **521**, issue 2, p. L153-L156 (1999).

[18] R.W. Romani, A.J. Miller, B. Cabrera, S.W. Nam, J.M. Martinis, Astrophysical Journal **563**, issue 1, p. 221-228 (2001).

[19] R.W. Romani, J. Burney, P. Brink, B. Cabrera, P. Castle, T. Kenny, E. Wang, B. Young, A.J. Miller, S.W. Nam, ASP Conference Proceedings **291**, p. 399 (2003).

[20] M.A.C. Perryman, C.L. Foden, A. Peacock, Nuclear Instruments and Methods in Physics Research Section A **325**, Issue 1-2, pp. 319-325 (1993).

[21] A. Peacock, P. Verhoeve, N. Rando, A. van Dordrecht, B.G. Taylor, C. Erd, M.A.C. Perryman, R. Venn, J. Howlett, D.J. Goldie, J. Lumley, M. Wallis, Nature **381**, pp. 135-137 (1996).

[22] M. Kurakado, H. Mazaki, Nuclear Instruments and Methods **185**, p. 141 (1981).

[23] G. Angloher, P. Hettl, M. Huber, J. Jochum, F. v. Feilitzsch, R. L. Mößbauer, Journal of Applied Physics **82**, issue 2, pp. 1425-1429 (2001).

[24] L. Li, L. Frunzio, C. Wilson, D. E. Prober, A. E. Szymkowiak, S. H. Moseley, Journal of Applied Physics **90**, issue 7, pp. 3645-3647 (2001).
[25] http://constellation.gsfc.nasa.gov/
[26] P.A.J. de Korte, M. Bavdaz, L. Duband, A.D. Holland, A.J. Peacock, L. Strueder, Proc. of SPIE **3766**, pp. 103-126 (1999).
[27] M. Bavdaz, A. Peacock, A. Parmar, M. Beijersbergen, Proc. of SPIE **4497**, pp. 31-40 (2001).
[28] P. Verhoeve, R. den Hartog, A. Kozorezov, D. Martin, A. van Dordrecht, J.K. Wigmore, A. Peacock, Journal of Applied Physics **92**, issue 10, pp. 6072-6081 (2002).
[29] H.K. Onnes, Commun. Phys. Lab **12**, p. 120 (1911).
[30] W. Meissner, R. Ochsenfeld, Naturwissenschaften **21**, p. 787 (1933).
[31] F. London, H. London, Proc. Roy. Soc. **A149**, p. 71 (1935).
[32] J. Bardeen, L.N. Cooper, J.R. Schrieffer, Phys. Rev. **108**, p. 1175 (1957).
[33] A.C. Phillips, *Introduction to Quantum Mechanics*, Chapter 10, John Wiley and Sons, ISBN 0-470-85323-9 (2003).
[34] M. Tinkham, *Introduction to superconductivity*, ISBN 0-486-43503-2 (1996).
[35] N.N. Bogoliubov, Nuovo Cimento **7**, p. 794 (1958).
[36] J.G. Valatin, Nuevo Cimento **7**, p. 843 (1958).
[37] A. Poelaert, *Superconducting tunnel junctions used as photon detectors*, PhD Thesis, ISBN 90-36512867 (1999).
[38] N.E. Booth, Appl. Phys. Letters **50**, pp. 293-295 (1987).
[39] I. Giaever, Phys. Rev. Letters **5**, p. 147 (1960).
[40] I. Giaever, Phys. Rev. Letters **5**, p. 464 (1960).
[41] J. Nicol, S. Shapiro, P.H. Smith, Phys. Rev. Letters **5**, p. 461 (1960).
[42] E.L. Wolf, *Principles of electron tunnelling spectroscopy*, ISBN 0-19-503417-1 (1985).
[43] K.E. Gray, Appl. Phys. Letters **32**, pp. 392-395 (1978).
[44] D.J. Josephson, Phys. Letters **1**, p. 251 (1962).
[45] C.P. Poole Jr., H.A. Farach, R.J. Creswick, *Superconductivity*, ISBN 0-12-561455-1 (1995).
[46] R.L. Peterson, Cryogenics **31**, pp. 132-135 (1991).
[47] M.C. Gaidis, S. Friedrich, D.E. Prober, S.H. Moseley, A.E. Szymkowiak, IEEE Trans. on Appl. Superconductivity **3**, pp. 2088-2091 (1993).
[48] P. Hübner, N. Rando, A. Peacock, P. Videler, A. van Dordrecht, J. Lumley, Proc. of SPIE **2006**, pp. 308-323 (1993).
[49] Yu. N. Ovchinnikov, V.Z. Kresin, Phys. Rev. B **58**, pp. 12416-12421 (1998).
[50] D. van Vechten, K. Wood, Phys. Rev. B **43**, pp. 12852-12860 (1991).
[51] A.G. Kozorezov, A.F. Volkov, J.K. Wigmore, A. Peacock, A. Poelaert, R. Den Hartog, Phys. Rev. B **61**, pp. 11807-11819 (2000).
[52] M. Kurakado, Nuclear Instruments and Methods **196**, pp. 195-197 (1982).
[53] N. Rando, A. Peacock, A. van Dordrecht, C. Foden, R. Engelhardt, B.G. Taylor, P. Garé, J. Lumley, C. Pereira, NIM-A **313**, pp. 173-195 (1992).
[54] C.A. Mears, S.E. Labov, A.T. Barfknecht, Appl. Phys. Letters **63**, pp. 2961-2963 (1993).
[55] D.J. Goldie, P.L. Brink, C. Patel, N.E. Booth, G.L. Salmon, Appl. Phys. Letters **64**, pp. 3169-3171 (1994).
[56] P. Verhoeve, R. den Hartog, A. Kozorezov, D. Martin, A. Van Dordrecht, J.K. Wigmore, A. Peacock, Journal of Applied Physics **92**, issue 10, pp. 6072-6081 (2002).
[57] K. Segall, C. Wilson, L. Frunzio, L. Li, S. Friedrich, M.C. Gaidis, D.E. Prober, A.E. Szymkowiak, H. Moseley, Appl. Phys. Letters **76**, pp. 3998-4000 (2000).
[58] J.B. LeGrand, C.A. Mears, S.E. Labov, P. Jakobsen, P. Verhoeve, M. Bavdaz, A. Peacock, Proc. of LTD-7, Munich, pp.106-107 (1997).
[59] G. Brammertz, *Development of low critical temperature superconducting tunnel junctions for applications as photon detectors in astronomy*, PhD thesis, ISBN 90-365-1970-5 (2003).

[60] G.M Eliashberg, Zh. Eksp. Teor. Fiz. **61**, p. 1254 (1971) [Sov. Phys. JETP **34**, p. 668 (1972)].
[61] J.J. Chang, D.J. Scalapino, Phys. Rev. B **10**, pp. 4047-4049 (1974).
[62] J.J. Chang, D.J. Scalapino, Phys. Rev. B **15**, pp. 2651-2670 (1977).
[63] J.J. Chang, D.J. Scalapino, Phys. Rev. Letters **37**, pp. 522-526 (1976).
[64] V.F. Elesin, Yu.V. Kopaev, Sov. Phys. Usp. **24**, p. 116 (1981).
[65] A.G. Kozorezov, A.F. Volkov, J.K. Wigmore, A. Peacock, A. Poelaert, R. den Hartog, Phys. Rev. B **61**, pp. 11807-11819 (2000).
[66] A.G. Kozorezov, J.K. Wigmore, D. Martin, P. Verhoeve, A. Peacock, Phys. Rev. B **75**, p. 094513 (2007).
[67] S.B. Kaplan, J. Low Temp. Phys. **37**, numbers 3-4, pp. 343-365 (1979).
[68] S.V. Kaplan, C.C. Chi, D.N. Langenberg, J.J. Chang, S. Yafarey, D. Scalapino, Phys. Rev. B **11**, pp. 4854-4873 (1976).
[69] G. Brammertz, P. Verhoeve, D. Martin, A. Peacock, R. Venn, Proc. of SPIE vol. **5499**, pp. 269-280 (2004).
[70] G. Brammertz, A.K. Kozorezov, J.K. Wigmore, R. Den Hartog, P. Verhoeve, D. Martin, A. Peacock, A.A. Golubov, H. Rogalla, J. Appl. Phys. **94**, pp. 5854-5865 (2003).
[71] Oxford Instruments Scientific Research Division, Cambridge UK.
[72] G. Brammertz, A. Peacock, P. Verhoeve, D. Martin, R. Venn, Nucl. Instr. Meth. A **520**, pp. 508-511 (2004).
[73] Cambridge Microfab Ltd., Broadway, Bourn, Cambridge CB23 2TA, UK.
[74] Plansee SE, 6600 Reutte, Austria.
[75] Technical Materials Incorporated, 5 Wellington Rd., Lincoln, RI 02865, USA.
[76] Shipley Co, 245 Santa Ana Ct. Sunnyvale, CA 94086, USA.
[77] M. Sampietro, L. Fasoli, G. Bertuccio, IEEE Trans. on Nuclear Science **43**, issue 4 part 2, pp. 2413-2418 (1996).
[78] E. Gatti, P.F. Manfredi, Riv. Nuovo Cimento **9**, (1986).
[79] F.S. Goulding, D.A. Landis, IEEE Trans. on Nuclear Science **29**, issue 3, pp. 1125-1141 (1982).
[80] D.D.E. Martin, A. Peacock, J. Phys. IV France **8**, 225 (1998).
[81] Z.Y. Chang, W.M.C. Sansen, *Low-Noise Wide-Band Amplifiers in Bipolar and CMOS Technologies*, Chapter 5, Kluwer academic publishers, ISBN 0-7923-9096-2 (1991).
[82] Z.Y. Chang, W. M. C. Sansen, IEEE J. of Solid-State Circuits **25**, No.3, 833-840 (1990).
[83] P.R. Gray, R.G. Meyer, Analysis and Design of Analog Integrated Circuits, ch. 11, 2nd ed. (Wiley, New York, 1984).
[84] J.A. Chervenak, K. D. Irwin, E. N. Grossman, Appl. Phys. Lett. **74**, 4043 (1999).
[85] K.D. Irwin, Physica C **368**, pp203-210 (2002).
[86] D.D.E. Martin, A. Peacock, P. Verhoeve, D.J. Goldie, V. Polushkin, Proc. Wolte-4 (2000).
[87] D.D.E. Martin, A.Peacock, P. Verhoeve, A. Poelaert, R. Venn, Rev. of Sci. Instr. **71**, 9, pp. 3543-3551 (2000).
[88] D.D.E. Martin, A.Peacock, P. Verhoeve, A. Poelaert, R. Venn, NIM-A **444**, issue 1-2, pp. 115-119 (2000).
[89] D.D.E. Martin, P. Verhoeve, A. Peacock, D.J. Goldie, Proc. SPIE **4008**, pp. 328-336 (2000).
[90] N. Haralabidis, K. Misiakos, IEEE Trans. on Nuclear Science **44**, No.3, 370-373 (1997).
[91] P. O'Connor, G. Gramegna, P. Rehak, F. Corsi, C. Marzocca, IEEE Trans. On Nuclear Science **44**, No. 3, 318-325 (1997).
[92] J.B. Le Grand, C.A. Mears, S.E. Labov, P. Jakobsen, P. Verhoeve, M. Bavdaz, A. Peacock, Proc. LTD-7 Munich, 106-107 (1997).
[93] B. Dierickx, Ph.D. dissertation, K.U. Leuven (1999).

[94] P. Merken, Y. Creten, J. Putzeys, T. Souverijns, C. Van Hoof, Proc. of SPIE **5498**, pp. 622-629 (2004).
[95] P.A.J. de Korte, J.J. van Baar, N.H.R. Baars, F.E. Bakker, W.M. Bergmann Tiest, M.P. Bruijn, A. Germeau, H.F.C. Hoevers, M. Kiviranta, E. Krouwer, J. van der Kuur, M.P. Lubbers, W.A. Mels, M.L. Ridder, H. Seppae, R.J. Wiegerink, Proc. of SPIE **5501**, pp. 167-176 (2004).
[96] J.N. Ullom, J.A. Beall, A. Clark, S. Deiker, W. Doriese, W. Duncan, L. Ferriera, G.C. Hilton, K.D. Irwin, N. Miller, C. Reintsema, L.R. Vale, Y. Xu, 2nd International Workshop on Transition Edge Sensor Device Physics, Miami, Florida (2004).
[97] Hypres, 175 Clearbrook Rd., Elmsford, N.Y. 10523.
[98] R.P. Welty, J.M. Martinis, IEEE Trans. on Appl. Supercond. **7**, issue 2, pp. 3415-3418 (1993).
[99] J. Clarke, *The New Superconducting Electronics*, pp. 123-180, Kluwer academic publishers (1993).
[100] C.A. Mears, S.E. Labov, M. Frank, H. Netel, L.J. Hiller, M.A. Lindeman, D. Chow, A.T. Barfknecht, IEEE Trans. on Appl. Supercond. **7**, issue 2, pp. 3415-3418 (1997).
[101] V. Polushkin, D. Glowacka, R. Hart, J.M. Lumley, IEEE Trans. on Appl. Supercond. **9**, issue 2 part 3, pp. 4436-4439 (1998).
[102] M. Podt, D. Keizer, J. Flokstra, H. Rogalla, NIM-A **444**, issues 1-2, pp. 120-123 (2000).
[103] IDEAS, http://www.ideas.no
[104] D.D.E. Martin, A. Peacock, P. Verhoeve, A. Fernández-Léon, B. Glass, G. Mæhlum, NIM-A **520**, issue 1-3, pp. 570-573 (2004).
[105] E. Nygård, P. Aspell, P. Jarron, P. Weilhammer, K. Yoshioka, NIM-A **301**, issue 3, pp. 506-516 (1991).
[106] AMS, http://www.austriamicrosystems.com/index.htm
[107] O. Toker, S. Masciocchi, E. Nygård, A. Rudge, P. Weilhammer, NIM-A **340**, issue 3, pp. 572-579 (1994).
[108] Isaac Newton Group of Telescopes, Roque de Los Muchachos Observatory, La Palma, Spain; http://www.ing.iac.es/.
[109] Optical Ground Station, Teide Observatory, Tenerife, Spain; http://www.iac.es/telescopes/ogs/OGSE.html.
[110] SESO: Société Européenne de Systèmes Optiques, 305 rue Louis Armand, 13792 Aix-en-Provence, France; http://www.seso.com.
[111] Winlight System S.A.: Bâtiments 301-302, Village d'Entreprise de Saint Henry, 13466 Marseille, France; http://winlight-system.com.
[112] Tekdata Interconnect Ltd., Federation Road, Burslem, Stoke-on-Trent, Staffordshire ST6 4HY, UK, www.tekdata-interconnect.com, www.cryoconnect.com.
[113] L. Duband, L. Hui, A. Lange, Cryogenics vol. **30**, pp. 263-270 (1990).
[114] L. Duband, L. Clerc, A. Ravex, Advances in Cryogenic Engineering, AIP Conference Procedings vol. 613, pp. 1233-1240 (2002).
[115] FITS, Flexible Image Transfer System, http://fits.gsfc.nasa.gov/.
[116] M.A.C. Perryman, M. Cropper, G. Ramsay, F. Favata, A. Peacock, N. Rando, A. Reynolds, Monthly Notices of the Royal Astronomical Society, vol. **324**, pp899-909 (2001).
[117] J.H.J de Bruijne, A.P. Reynolds, M.A.C. Perryman, F. Favata, D. Martin, P. Verhoeve, N. Rando, A. Peacock, Galaxies: The Third Dimension, ASP Conf. Series vol. **282**, pp555-565 (2002).
[118] D.D.E. Martin, P. Verhoeve, R.H. den Hartog, Proc. of SPIE vol. **4841**, p. 805 (2003).
[119] M.A.C. Perryman, F. Favata, A. Peacock, N. Rando, B.G. Taylor, Astronomy and Astrophysics vol. **346**, p. 30 (1999).

[120] T. Oosterbroek, J.H.J. de Bruijne, D. Martin, P. Verhoeve, M.A.C. Perryman, C. Erd, R. Schulz, Astronomy and Astrophysics vol. **456**, pp. 283-286 (2006).
[121] J.H.J. de Bruijne, A.P. Reynolds, M.A.C. Perryman, A. Peacock, F.Favata, N.Rando, D. Martin, P. Verhoeve, N. Christlieb, Astronomy and Astrophysics vol. **381**, pp57-60 (2002).
[122] Sargent W.L.W., Steidel C.C. and Boksenberg A., Astrophys. J. Suppl. **69**, pp703-761 (1989).
[123] W. Zheng, G.A. Kriss, R.C. Telfer, J.P. Grimes, A.F. Davidsen , The Astrophysical Journal vol. **475**, pp. 469-478 (1997).
[124] G.M. MacAlpine, S.B.Smith, D.W. Lewis, The Astrophysical Journal Supplement Series vol. **35**, p197 (1977).
[125] A.P. Reynolds, J.H.J. de Bruijne, M.A.C. Perryman, A.Peacock, C.M. Bridge, Astronomy and Astrophysics vol. **400**, pp. 1209-1217 (2003).
[126] D.D. Martin, M. Bavdaz, A.J. Peacock, G. Vacanti, A.N. Parmar, Proc. of SPIE vol. **2517**, pp. 209-222 (1995).
[127] A.N. Parmar, D.D.E. Martin, M. Bavdaz, F. Favata, E. Kuulkers, G. Vacanti, U. Lammers, A. Peacock, B.G. Taylor, Astronomy and Astrophysics Supplement Series vol. **122**, pp. 309-326 (1996).
[128] C. Bridge, M. Cropper, G. Ramsay, M.A.C. Perryman, J.H.J. de Bruijne, F. Favata, A. Peacock, N. Rando, A.P. Reynolds, Monthly Notices of the Royal Astronomical Society, vol. **336**, p. 1229 (2002).
[129] D. Steeghs, M.A.C. Perryman, A. Reynolds, J.H.J. de Bruijne, T. Marsh, V.S. Dhillon, A. Peacock, Monthly Notices of the Royal Astronomical Society, vol. **339**, p. 810 (2003).
[130] R. Schulz, J. Stüwe, D. Martin, A. Stankov, C. Erd, T. Peacock, P. Verhoeve, T. Ho, Presented at Observing Planetary Systems ESO Workshop (March 5-8 2007).
[131] H. Kraus, F. von Feilitsch, J. Jochum, R.L. Mössbauer, Th. Peterreins, F. Pröbst., Physics Letters B **231**, pp. 195-202 (1989).
[132] R.A. Hijmering, I. Jerjen, P. Verhoeve, D.D.E. Martin, A. Peacock, A.G. Kozorezov, R. Venn, Proc. of SPIE **6276**, p. 627619 (2006).
[133] VeriCold Technologies, http://www.vericold.com.
[134] Janis Research Company, inc., http://www.janis.com.
[135] A.J. Miller, B. Cabrera, R.W. Romani, R.M. Clarke, E. Figueria-Feliciano, S.W. Nam, Proc. of SPIE **3764**, pp. 188-194 (1999).
[136] B. Cabrera, J.M. Martinis, A.J. Miller, S.W. Nam, R. Romani, AIP Conference Proceedings **605**, pp. 565-570 (2002).
[137] S. Arribas, D. Carter, L. Cavaler, C. del Burgo, R. Edwards, F.J. Fuentes, A.A. Garcia, J.M. Herreros, L.R. Jones, E. Mediavilla, M.P. i Puig, D. Pollacco, J.L. Rasilla, P.C.T. Rees, N.A. Sosa, Proc. of SPIE **3355**, pp. 821-827 (1998).
[138] D. Buckley, New Astronomy Reviews **45**, Issues 1-2, pp. 13-16 (2001).
[139] ESA SP-1238 (2000).
[140] ESA SP-1273 (2003).
[141] B.L. Henke, E.M. Gullikson, J.C. Davis, Atomic Data and Nuclear Data Tables **54** (no.2), pp. 181-342 (1993).
[142] R. den Hartog, P. Verhoeve, D. Martin, N. Rando, A. Peacock, M. Krumrey, D. J Goldie, NIM-A vol. **444**, Issues 1-2, pp. 278-282 (2000).
[143] R.H. den Hartog, D.D.E. Martin, A.G. Kozorezov, P. Verhoeve, N. Rando, A.J. Peacock, G. Brammertz, M.K. Krumrey, D.J. Goldie, R. Venn, Proc. of SPIE, vol. **4012**, pp. 237-248 (2000).
[144] P. Verhoeve, R.A Hijmering, D.D.E. Martin, I. Jerjen, A. Peacock, R. Venn, Proc. of SPIE, vol. **6276**, p. 627613 (2006).

[145] R. den Hartog, A.G. Kozorezov, J.K. Wigmore, D. Martin, P. Verhoeve, A. Peacock, A. Poelaert, G. Brammertz, Phys. Rev. B, vol. **66**, issue 9 (2002).

SUMMARY

The original S-CAM1 and 2 systems were a first successful demonstration of a camera for optical astronomy based on superconducting sensors. However, a number of shortcomings were identified during the observing campaigns at the William Herschel Telescope at La Palma that triggered this work.

As the plate-scale was chosen to slightly over-sample the telescope's point-spread function under ideal seeing conditions, the average atmospheric conditions at the WHT combined with the limited field-of-view of the early 6×6 array severely limited accurate photometry. Also, the quality of the sensor and the IR background limited the spectral resolution of the instrument. This work was therefore focussed on the further understanding of the fundamental physical limitations of these superconducting tunnel junction sensors, the fabrication and optimization of medium sized arrays and the substantial improvement, implementation, verification, calibration and exploitation of a camera system, called S-CAM3.

We started with the design of a new mask-set for a 10×12 pixel array. The peculiarities of this design were the consequence of optimizing the number of wires crossing the pixels, to the limits of the available photo-lithography, while also separating the pixels into four groups, each with its own return wire and connected to a separate electronics group. The fabrication of these devices was closely followed and allowed limited process optimization. In a first instance, a series of arrays were developed that outperformed the previous results.

During the development, we had to switch manufacturer which allowed a different process optimization and lead to further improvements in device performance. The measured energy resolving power of $E/\Delta E=24$ at 500nm is currently the best result obtained for cryogenic sensors. More importantly, this result also led to the understanding of the physical processes of energy down-conversion and their influence on achievable energy resolving power.

The improved quasiparticle lifetimes enabled on the one hand to solidly confirm that tunnel noise could be partly compensated by adequate signal filtering and on the other hand revealed new features. An effect which had been expected to only lead to some inefficiency in the energy detection was soon found to explain discrepancies of the energy resolving power of Superconducting Tunnel Junctions as function of photon energy, when compared to previous theories. It turned out that after the photon absorption in a superconducting film, the process of energy down-conversion passes through a series of stages, alternatively dominated by electrons and phonons. In a first instance in Ta/Al STJs grown on sapphire substrates, we have shown that energetic phonons can escape the superconductor if they travel within a critical cone towards the substrate. This leads to an energy loss in excess of that due to the energy partition between sub-gap phonons and quasiparticles. This energy loss is more pronounced the closer the photon is absorbed to an interface, as phonons have a lower probability to interact with the condensate before being able to cross the interface. Detailed analysis of the down-conversion process below ~1eV revealed that, beyond the previously known noise factors, two newly identified processes are responsible for further degradation of the capacity of STJs to distinguish photons of different wavelengths. First, the statistical nature of energetic phonons crossing an interface and being lost from the system brings in a variance on the total energy detected. We described this effect as a phonon escape noise coefficient that enters the resolution calculation at the same level as the Fano and Tunnel noise factors. Secondly, the absorption sites of mono-energetic photons are exponentially distributed which leads to a

vertical inhomogeneity factor. The energy dependent absorption depth allowed us to verify this theory elegantly against measurements on our best devices. We believe that this effect will ultimately limit the performance of STJs at X-ray wavelengths.

This effect is of course of a more general nature and was also verified against older data taken with pure Al STJs. In addition, we adapted the theory to also fit the case of tungsten transition edge sensors grown on a solid substrate.

The S-CAM system was then considerably improved and adapted to fit on two telescopes: the WHT (La Palma) and the OGS (Tenerife). The field-of-view increased immediately with the larger array to 10.8"×9" at the WHT and 12.8"×10.7" at the OGS.

The cooling system was changed and optimized, using a combination of ^{3}He and ^{4}He sorption coolers. This configuration allows 24 hours operations, does not require pumping during the measurements, keeps the detector constantly below its critical temperature, and provides a very constant operating temperature, guaranteeing stable detector characteristics.

The electronics system was completely redesigned to allow for digital pulse processing which can be adapted 'on-the-fly' to best fit the observing goals: high count-rate or high resolution. Different preamplifier techniques were evaluated with the objective to simplify the connectivity and complexity associated with the readout of large arrays. On the one hand we introduced a matrix readout scheme where the number of amplifiers is drastically reduced by interconnecting pixels in rows and columns. The principle was verified on a dedicated array using X-ray and optical photons. In a second alternative, a 64-channel preamplifier ASIC was designed, fabricated and tested, allowing for a very compact and low-power amplification and trigger stage. Whereas the new biasing scheme and low-noise performance were both verified, conclusive tests on a real detector could not be conducted. Finally, a SQUID readout was also studied, concluding that although SQUIDs are best suited for lower impedance devices, they could very well be tailored to read out STJs.

For S-CAM3, a more standard approach using room temperature J-FET amplifiers was chosen, however a new pre-amplifier design enabled stable detector biasing and diagnostics while providing low-noise operation. The complete system is fully S/W controlled and the latest implementation even allows fast guiding using the faint target. Particular attention was also given to the absolute calibration of time-tagging of the individual photons, which is now possible at the microsecond level.

The IR rejection filters, present at various stages in the cryogenic enclosure, were optimised. In this way we realized a ten-fold increase in IR rejection, while at the same time we increased the visible throughput by 50%.

The reduced IR induced noise, electronics noise and increased detector responsivity translated into an almost three-fold increase in energy resolving power compared to the previous instrument.

Superconducting detectors are revolutionizing the way we will perform astronomical observations in the near future, in particular in the optical-UV they have already shown to be capable of providing four-dimensional simultaneous imaging, spectral and timing information. At the time of writing, the S-CAM3 system has been deployed for six observing campaigns, to investigate various classes of astronomical objects, such as cataclysmic variables, quasars, pulsars, comets, exo-planets and many more.

SAMENVATTING

De originele S-CAM1 en 2 systemen waren de eerste succesvolle demonstraties van een camera voor optische astronomie uitgerust met supergeleidende sensoren. Tijdens observatiecampagnes met de William Herschel Telescoop (WHT) op La Palma werd een aantal tekortkomingen ontdekt welke hebben geleid tot dit werk.

Voor de optiek werd een plaatschaal gekozen om een lichte overbemonstering te krijgen van de puntspreidingsfunctie van de telescoop onder ideale atmosferische condities. De gemiddelde atmosferische condities op de WHT, gekoppeld met het gelimiteerde gezichtsveld van de eerste 6×6 pixels detectoren, bemoeilijkte het maken van accurate fotometrische metingen. Verder beperkten de kwaliteit van de sensoren en de na onderdrukking nog aanwezige infraroodachtergrond de energieresolutie van het instrument. Dit onderzoek werd zodoende geïnitieerd met drie doelen: (1) een betere beschrijving verkrijgen van de fundamentele fysische begrenzingen van supergeleidende tunnel juncties (STJs), (2) nieuwe, grotere sensoren ontwikkelen, optimaliseren en fabriceren en (3) wezenlijke verbeteringen aanbrengen in een nieuwe camera, S-CAM3, en deze verifiëren, kalibreren en in gebruik nemen.

Er werd begonnen met het ontwerpen van een nieuwe maskerset voor een 10×12 pixels matrix. De eigenschappen van dit ontwerp vloeiden voort uit de optimalisatie van het aantal elektrische verbindingen dat over elk pixel kon worden gemaakt, gelimiteerd door de beschikbare fotolithografie en de noodzaak om vier elektrisch gescheiden groepen te verwezenlijken, elk met een afzonderlijke massaverbinding. De fabricage van deze detectoren werd nauwlettend gevolgd, waardoor beperkte procesoptimalisatie mogelijk was. In eerste instantie werden een aantal series geproduceerd die alle vroegere resultaten overtroffen.

Tijdens de ontwikkeling rees de noodzaak om de productie van sensoren over te brengen naar een nieuwe fabrikant. Dit heeft geleid tot een alternatieve optimalisatieroute en verdere verbeteringen in detectorprestaties. Het gemeten energieoplossend vermogen van $E/\Delta E=24$ bij 500nm is het beste resultaat dat tot nu toe met cryogene detectoren behaald werd. Nog belangrijker echter heeft deze overstap ons een beter inzicht gegeven in de fysische processen van energieconversie en hun invloed op het maximaal haalbare energieoplossend vermogen.

Met de langere leeftijden van quasi-deeltjes kon duidelijk worden aangetoond dat tunnelruis gedeeltelijk onderdrukt kan worden door een geschikte signaalfiltering, hetgeen weer tot de eerder vermelde nieuwe inzichten heeft geleid. Een effect dat voorheen gedacht werd alleen tot een ietwat inefficiëntere energieconversie te leiden, kan nu de gemeten verschillen in energieoplossend vermogen van supergeleidende tunnel juncties als functie van fotongolflengte verklaren. Het blijkt namelijk dat na fotonabsorptie in een supergeleidende dunne laag het proces van energieconversie door verschillende stadia evolueert welke om en om door quasi-deeltjes en fononen gedomineerd worden. Als eerste hebben we in Tantaal/Aluminium STJs op saffier aangetoond dat energetische fononen de supergeleidende film kunnen verlaten als zij zich binnen een bepaalde hoek naar het substraat verplaatsen. Dit leidt dan tot een extra energieverlies bovenop de traditionele energiepartitie tussen laagfrequente fononen en quasi-deeltjes. Dit energieverlies is hoger naarmate het foton dichter bij het substraat wordt geabsorbeerd omdat de fononen dan een kleinere waarschijnlijkheid hebben om met het condensaat te interacteren en dus makkelijker het substraat kunnen bereiken en zodoende verloren gaan. Een gedetailleerde analyse van het conversieproces beneden ~1eV liet toe om, bovenop de voorheen bekende ruisfactoren, twee nieuwe processen te identificeren die verantwoordelijk zijn voor het verder degraderen van de eigenschap die STJs hebben om fotonen met verschillende energieën te onderscheiden. Ten eerste bleek dat de statistische eigenschap van energetische fononen om wel of niet verloren te gaan door via het substraat te

ontsnappen leidt tot een statistische variatie van de gedetecteerde totale energie. Dit effect hebben we beschreven met een fonon verliesruiscoëfficiënt die een vergelijkbare rol speelt in de energieresolutievergelijking als de Fano- en tunnelruisfactoren. Ten tweede zijn de absorptiedieptes van monoenergetische fotonen in elk materiaal volgens een exponentiële waarschijnlijkheidsdistributie verdeeld, wat tot een verticale inhomogeniteitsfactor leidt. Door de energieafhankelijkheid van de gemiddelde absorptiediepte kon deze nieuwe theorie op elegante wijze worden getoetst aan metingen van onze beste detectoren. Onzes inziens zal dit effect het uiterste vermogen van huidige STJs bij Röntgenstralen beperken.

Het zojuist beschreven fenomeen is natuurlijk algemener van aard en we hebben onze theorie dan ook kunnen toetsen aan eerder gedane experimenten met pure Aluminium sensoren. Bovendien hebben we de theorie verder uitgewerkt om ook Wolfraam transitierand detectoren (TESs) te analyseren.

Het S-CAM systeem werd vervolgens grondig verbeterd en aangepast om op twee telescopen te kunnen dienen: de WHT op La Palma en de OGS op Tenerife. Het gezichtsveld werd vergroot door het gebruik van de grotere detector tot 10.8”×9” op de WHT en 12.8”×10.7” op de OGS.

Het koelsysteem werd vervangen en geoptimaliseerd door het gebruik van een gecombineerde ^{3}He-^{4}He sorptiekoeler. Deze configuratie maakt een 24-uurs bedrijfsvoering mogelijk, behoeft niet meer gepompt te worden tijdens metingen, houdt de detector permanent beneden zijn transitietemperatuur en verzorgt een uiterst stabiele temperatuur tijdens observaties waardoor een zeer constante detectorkarakteristiek kan worden gegarandeerd.

Het elektronische systeem werd compleet opnieuw ontworpen en biedt nu een digitale signaalverwerking welke op elk willekeurig moment aangepast kan worden aan de meetomstandigheden zoals een hoge energieresolutie of observaties van heldere objecten. Verschillende technieken voor de voorversterking van het signaal werden uitgebreid getest met het oog op een vereenvoudiging van de connecties en complexiteit die gepaard gaat met grotere detectoren met meer pixels. Eerst hebben we een matrix uitlezing geïntroduceerd waar het aantal versterkers drastisch gereduceerd kan worden door pixels in rijen en kolommen te verbinden. Het principe werd geverifieerd met zowel Röntgen als optische fotonen. Als tweede alternatief hebben wij een 64-kanaals voorversterker ASIC ontwikkeld en getest waardoor een zeer compact en energiezuinig ontwerp mogelijk wordt. Hoewel het nieuwe concept voor detector spanningsverzorging en lage ruis goed werkte, kon een definitieve test met detector nog niet worden uitgevoerd. Als laatste alternatief werd ook een SQUID uitlezing bestudeerd. De conclusie van dit experiment toonde aan dat ook deze versterkers, hoewel ze eigenlijk beter geschikt zijn voor lagere impedantie sensoren, zeer goed aan STJs gekoppeld kunnen worden.

Voor S-CAM3 werd uiteindelijk gekozen voor een traditionele voorversterker, opgebouwd uit discrete componenten en werkend op kamertemperatuur. Dit nieuwe ontwerp geeft een zeer stabiele spanningsverzorging van de detector en tegelijk een zeer lage ruis. Het complete systeem wordt door software bestuurd en de allerlaatste uitbreiding biedt de mogelijkheid om de telescoop direct te besturen en het te meten object feilloos te volgen, al is het nog zo zwak. Uitgebreide aandacht werd ook gegeven aan de absolute tijdskalibratie van het instrument zodat elk foton tot op de microseconde nauwkeurig kan worden vastgelegd.

De infraroodfilters, die op de verschillende trappen in de cryostaat zijn bevestigd en die de straling afkomstig van de 300K omgeving sterk moeten onderdrukken, werden geoptimaliseerd. Hierdoor werd een tienvoudige verbetering in de onderdrukking van infraroodlicht bereikt en werd tegelijkertijd een 50% verhoging in de doorlaatkarakteristiek in het optische gebied bewerkstelligd.

De gereduceerde infraroodruis, de lagere elektronische ruis en de hogere detector respons hebben uiteindelijk tot een drievoudige verbetering in het energieoplossend vermogen van het instrument geleid.

Supergeleidende detectoren kunnen een revolutie teweegbrengen in de manier waarop astronomische waarnemingen in de toekomst gedaan zullen worden. In het optische en nabije ultraviolet hebben deze detectoren al aangetoond vierdimensionale plaatjes te kunnen maken door simultaan de positie, energie en aankomsttijd van elk foton te registreren. Tot op heden is S-CAM3 op zes observatiecampagnes ingezet waarbij verschillende astronomische objecten zoals cataclysmische variabelen, quasars, pulsars, kometen, exoplaneten, etcetera zijn waargenomen.

ACKNOWLEDGEMENTS

This work has been a long-breath exercise as the idea of a PhD already rose in 1990, when I started research in the completely different area of spread-spectrum communications. It turned out that I could only seriously start working towards a thesis more than a decade later.

The work on Superconducting Tunnel Junctions and the instrumentation of the S-CAM3 camera has, by no means, been the work of a single individual and I am in great depth to all my colleagues and friends who made this work possible. First I wish to thank my promoter Prof. Rogalla for giving me this opportunity and for providing the necessary academic environment and guidance, Tone Peacock who initiated the STJ research at the European Space Agency and, as my boss, allowed me and, more importantly even, encouraged me to combine part of my day-time job with research activities and Sasha Golubov as co-promoter who helped me in understanding superconductivity and many of its intricacies along the way.

Special thanks are due to the design team of the S-CAM1 and 2 systems, which have served as a starting point for the present work: Nicola Rando, Solve Andersson and Jacques Verveer, who has also been an endless source of practical ideas throughout this work, pioneered the usage of superconducting devices in optical ground based astronomy. Then comes the S-CAM3 team with electronics designer Axel van Dordrecht, Jacques Verveer again for the cryogenics and mechanics together with Georges Sirbi. Further support was provided by Richard Hijmering for the quick-look analysis tool and Christian Erd who, together with Hans Smit built up all the necessary software tools to control the OGS and provide accurate pointing and flawless tracking of celestial objects. Not to forget Rob and Jeannie Venn, who together with the MicroFab team suggested and implemented substantive process optimizations for the superconducting devices.

No R&D activity has any value without an application and I am thankful to the astronomy teams who understood how to best deploy this instrument and exploit the complex datasets. The first observations were lead by Michael Perryman, who together with Jos de Bruijne and Alastair Reynolds planned and exploited the observations at the William Herschel Telescope. The Optical Ground Station observations were initiated by Rita Schulz, with support by Joachim Stüwe, Tra-Mi Ho, Anamarija Stankov and Tim Oosterbroek.

But all this is dwarfed by the help provided by Peter Verhoeve and Alex Kozorezov. Peter, with his extensive laboratory experience with STJ characterization and his thorough knowledge of these sensors helped in all major issues related to detector development and system assembly and validation. Alex was the key catalyst in the theoretical analysis and interpretation of the measurement results. Both were a tremendous source of inspiration and the endless discussions we had made this whole effort so much more interesting and rewarding.

Of course, I wish to thank my parents who created the environment for me to develop and encouraged me in all my endeavours.

Last, but not least, I will always be thankful to Nathalie, Enrico and Raoul who gave me the liberty to embark on this adventure even at times when family events should have been more important. Their understanding and support in difficult times has meant so much to me that I could not have finished this thesis without them.